

SOME ASPECTS OF THE RADIO MORPHOLOGY
OF QUASARS WITH $Z < 1$

by

John Robin Price
B.Sc., University of Victoria, Victoria, B.C., 1985

A THESIS SUBMITTED IN PARTIAL FULFILLMENT
OF THE REQUIREMENTS FOR THE DEGREE OF
MASTER OF SCIENCE

in the Department
of
Physics

We accept this thesis as conforming
to the required standard

[REDACTED]

ACCEPTED
FACULTY OF GRADUATE STUDIES

Supervisor Dr. A.C. Gower

[REDACTED]

Dr. J.B. Hutchings

[REDACTED]

Dr. J.A. Burke

[REDACTED]

Dr. R. Ring

[REDACTED]

Dr. C.R. Purton

©JOHN ROBIN PRICE, 1989
UNIVERSITY OF VICTORIA

*All rights reserved. This thesis may not be reproduced
in whole or in part, by xerography or other means,
without the permission of the author.*

Jan 25, 1989 DEAN

Supervisor: Dr. Ann C. Gower

Abstract

The Very Large Array synthesis telescope has been used to observe a carefully-selected sample of ~ 100 radio-loud quasars of redshift less than one. The telescope produces high-resolution and high-sensitivity images that allow detailed analysis of the radio structure. The images are presented and discussed. The measurements obtained from these images provide a large data base of quasar radio properties, which have been used to test the sample for evidence of alternating ejection and relativistic beaming of plasma from the quasar nucleus. The outer parts (lobes) of the radio structures appear to be moving with non-relativistic velocities and show some evidence for alternating ejection. Narrow 'jet' structures are observed on only one side of the core in any one quasar, but do not display direct evidence of alternating sides. Within the framework of the models considered, the jets appear to be transporting material at speeds greater than that of the outer lobes, and there is some evidence for bulk relativistic motion in the jet and core components.

Examiners:

[Redacted]

Supervisor Dr. A.C. Gower

[Redacted]

Dr. J.B. Hutchings

[Redacted]

Dr. J.A. Burke

[Redacted]

Dr. B. Bing

[Redacted]

Dr. C.R. Purton

Contents

Abstract	ii
Contents	iii
List of Figures	vi
List of Tables	viii
Acknowledgements	ix
1 Introduction and Sample Selection	1
1.1 The Radio Structure of Quasars	2
1.2 The Sample Selection	5
2 Image Formation	10
2.1 Synthesis Telescopes	10
2.2 Image Restoration using CLEAN	13
2.3 Calibration and Self-calibration	16
3 Observations and Data Reductions	19
3.1 Observations	19
3.2 Image Formation	20
3.2.1 The $u-v$ data	21
3.2.2 The Initial Image	23
3.2.3 Self Calibration	28
3.3 The Images	29

4	Measurements	35
4.1	Morphological Classifications	37
4.2	Image Measurements	37
4.2.1	Core Flux	37
4.2.2	Core Spectral Index	42
4.2.3	Lobe Flux	42
4.2.4	Core-Lobe Distances	43
4.2.5	Bending Angle	44
4.3	Other Measurements	44
4.3.1	Total Flux	44
4.3.2	Absolute Magnitude	47
5	Alternating Ejection	48
5.1	Introduction	48
5.2	The Alternating Ejection Model	49
5.3	Tests for the Alternating-Ejection Model	50
5.3.1	Visual Evidence	50
5.3.2	The Lobe-Length Ratio Test	51
5.3.3	Core-Lobe Lengths	54
5.4	Summary and Problems	54
6	Relativistic Beaming	57
6.1	Introduction	57
6.2	The Alignment Indicators	60
6.2.1	Linear Size	60
6.2.2	Bending Angle	64
6.2.3	Bending Angle/Linear Size Relation	67
6.3	Tests for Relativistic Beaming	68
6.3.1	Lobes	69
6.3.2	Jets	74
6.3.3	Cores	79
6.4	Summary	81

CONTENTS

v

7 Summary	83
References	85
Appendix	87

List of Figures

1.1	Total Luminosity vs. Redshift. Triple (T), Core-Lobe (CL), and Core (C,CE) sources are represented with different symbols as shown in the box. The curves are explained in the text.	6
1.2	Core Luminosity vs. Redshift. The symbols represent different source types.	9
2.1	Schematic of the VLA Synthesis Telescope	11
2.2	Instantaneous VLA $u-v$ coverage for source at $\delta = 30^\circ$. . .	12
2.3	Antenna Beam Pattern or Dirty Beam	14
3.1	$u-v$ plot of 0133+207; 6cm (Flux vs. Antenna Separation) .	22
3.2	The effect of bandwidth smearing on 0222-008; 6cm	25
3.3	Untapered image of 0003+158; 6cm	27
4.1	Total Fluxes from the Dixon Catalogue vs. Frequency . . .	45
5.1	Histogram of Core-Lobe Distance Ratios with Alternating Ejection Model	52
5.2	Difference in Lobe Lengths of Triples(upper) and CL sizes (lower)	55
6.1	Histogram of Core-Lobe Distances	61
6.2	Dependence of Linear Size on a) Redshift and b) $\log P_{core}$.	63
6.3	Histogram of Bending Angles	65

6.4	Bending Angle Dependence on a) Redshift b) $\text{Log}P_{core}$	66
6.5	Bending Angle Dependence on Core-Lobe Distance	67
6.6	Ratio of Lobe Luminosities vs. a) Linear Size b) Bending Angle	70
6.7	Ratio of Lobe Lengths vs. a) CL Distances b) Bending Angle	71
6.8	Test for Beaming in the Lobes (Lobe Length Ratio vs. Lobe Power Ratio)	73
6.9	Histogram of Core-Lobe Distances	75
6.10	Bending Angle dependence on Jets	77
6.11	Core Luminosities for Jet and Non-Jet Sources	78
6.12	Core Fraction vs. Core-Lobe Distance a) 6cm b) 20cm	80
6.13	Core Fraction vs. Bending Angle a) 6cm b) 20cm	82

List of Tables

3.1	Overall image parameters	29
3.2	Image Parameters	31
4.1	Principal properties of the new sample	38

Acknowledgements

It is difficult to imagine a supervisor who would do as much for a graduate student as Ann Gower has done for me. Her enthusiasm for the science, as well as her patience and encouragement when things were not going too well were always a joy to experience. I am also grateful for generous financial support and the chance to observe with major radio telescopes. There is no one I would have preferred to have worked with.

This thesis would not be possible without the tremendous initiative of John Hutchings who designed the project and was able to synthesize so many different aspects of the research. John has also provided useful advice and guidance on career matters and his opinions were always greatly respected. Table 4.1 and figures 1.1, 1.2, 5.1, and 5.2 also appear in a paper written by John and I appreciate him allowing them to be used in this thesis.

The images were produced using facilities at DRAO and the VLA and the hospitality of these institutions is gratefully acknowledged.

When I started my masters I also began to climb. Since that time climbing has become an integral part of my life and my climbing partners have become some of my closest friends. I would like to thank them for continually refreshing my life with trips to the crags and the many hours of climbing talk that always provided new trips on the horizon and sweaty palms. Thanks to the Go(u)rds, Rheinhard, Martin, and Corinne.

It is difficult to get much work done if you do not feel comfortable being at work, so I must thank my fellow graduate students for providing an enjoyable atmosphere for both work and play. Special thanks to Gordon Ross for helping to produce half of the radio images and his overwhelming enthusiasm for both climbing and astronomy.

Chapter 1

Introduction and Sample Selection

This thesis examines the morphology of a large sample of radio-loud quasars of redshift less than one. The project was initiated in 1985 by J.B. Hutchings and A.C. Gower to investigate radio evolution in quasars. The sample was carefully chosen and then observed with the Very Large Array (VLA) in its highest resolution configuration. The observations required over 150 radio images to be produced and my involvement began when, as a summer student, I undertook this task. The project soon became my Master's thesis and is presented so that it emphasizes the aspects of the project with which I was most involved (*e.g.* image processing and data reduction) and discusses topics that I found particularly interesting. Once the data reductions were complete I chose to concentrate on testing two simple models that offer possible explanations for the asymmetries observed in the large-scale radio structure of quasars. Although the models, alternating ejection and relativistic beaming, are also contained in the more complete analysis of the sample presented in Hutchings, Price, and Gower (1988:HPG), they are treated slightly differently in this thesis. The analysis here concentrates on these two models and does not attempt to develop an evolutionary scenario, as HPG does.

This first chapter gives a brief introduction to the radio structure of

quasars and explains how the quasar sample was chosen. Since a large portion of time was spent producing the radio images, chapter 2 outlines the basic theory of image formation using synthesis telescopes, while chapter 3 gives specific details on how the images contained in this thesis were produced. Chapter 4 explains the techniques used in obtaining the relevant source measurements and discusses problems encountered in the process. Evidence in the large-scale structure both for and against alternating ejection is discussed in chapter 5, while chapter 6 examines whether the radio emitting material from the lobes, jets and cores is moving with relativistic velocities or not. The final chapter is a brief summary.

1.1 The Radio Structure of Quasars

This section provides an introduction to extragalactic radio sources by defining pertinent jargon, outlining the basic radio structure and then describing the models that are tested in chapters 5 and 6. To illustrate these ideas references to specific sources in the appendix will be made, using the IAU name of the source and the wavelength of the observation.

Approximately 10% of all quasars are denoted *radio-loud* with luminosities greater than $\sim 10^{23}$ Watts/Hz (Miley 1980; Kellerman and Owen 1988). The quasars in this thesis are all radio-loud and they have radio structure similar to powerful radio galaxies, except they have brighter *core* components and brighter *jets* (Owen 1986). Cores are the point-like sources that coincide with active galactic nuclei (AGN) that are embedded deep within the host galaxy and energize the radio source. Cores are generally unresolved with the ~ 1 arcsec resolution of this survey (*e.g.* 0003+158; 6cm), but can in some cases be slightly extended (*e.g.* 0134+329; 6cm). They can be the sole radio component of a quasar or be accompanied by *lobes* which are generally resolved and located at distances beyond ~ 25 kpc from the core, outside the optical extent of the host galaxy and in the intergalactic medium

(IGM). Single lobes are observed in some sources (*e.g.* 0812+020; 6cm), but it is more common to find them in pairs straddling the core (*e.g.* 1156+631; 20cm). *Hotspots* are the strong point sources that are sometimes observed near the outer edge of lobes (*e.g.* 1509+158; 6cm). Jets are the narrow ridges of emission that are sometimes observed between the core and a lobe (*e.g.* 0812+020; 6cm) and have only been observed on one side of the core in a given quasar. One could continue to enumerate source properties and further refine the classification of source types, but only a rudimentary description is necessary to outline the simple models that will be discussed in this thesis. Before introducing the models, a 'plausible' physical description of extragalactic radio sources will be presented.

The main radiation mechanism associated with extragalactic radio sources is accepted to be synchrotron radiation, which is produced by relativistic electrons spiralling in a magnetic field (see chapter 18 of Longair 1981). The energy source responsible for accelerating the electrons and transporting them to such large distances is the AGN located deep inside the core component. Material, once energized by the core component, moves outward along very well-collimated jets towards the lobes. Where the jet is 'stopped' by the intergalactic medium a shock develops and creates a hotspot (*e.g.* 1509+158; 6cm), followed by much of the material dispersing slowly away from the jet axis and back toward the core. This dispersed material makes up the lobe emission which in some cases reaches all the way back to the core and envelopes the entire source (*e.g.* 0704+384; 20cm). This simple description of extragalactic radio sources is not necessarily correct, but it does provide a basic physical interpretation that will be useful throughout the rest of the thesis.

After a quick flip through the appendix it is apparent that the source description outlined above is far too simple for the incredible variety of source structures. Yet the wealth of morphological information contained

in these images is still not enough to understand these sources, as many fundamental questions remain unanswered. Two questions that this thesis sets out to address are: 1) Is material transported in the jets, cores or lobes at relativistic velocities? and 2) Does the central engine only eject material on one side of the source at a time? There are many other puzzles contained in the radio structure of quasars, but these are both fundamental problems and are well suited for tests using the given sample. The tests performed in chapters 5 and 6 of the thesis are very simple and merely determine if the models suggested play a dominant role; they do not provide irrefutable evidence.

The lobe structure of quasars does not only vary from source to source, but drastic differences also occur between the two lobes on either side of the core of the same quasar (*e.g.* 2353+283; 6cm). The side to side differences in brightness distributions and the one-sided nature of jets prompted the *alternating ejection* model, where the central engine only ejects material on one side of the core at a time. If the material ejected on either side of the core had roughly the same velocity, alternating ejection would create a source where the brightness distribution on either side of the core would systematically interleave if folded about the core (*ie.* the emission on either side would be at different distances from the core). Chapter 5 examines the lobe emission in the context of alternating ejection as developed by Rudnick and Edgar (1984:RE), making simple tests of the model they propose. In HPG this model was developed into an evolutionary scenario where a source begins as just an active core, then ejects material on one side, producing a source with a single lobe, then ejection occurs on the opposite side and the source becomes a *classical double* with a fading core component.

While side-to-side asymmetries can be produced easily by assuming physically different conditions on either side of the core, they can also be observed in sources that are intrinsically very symmetric. In the *relativistic beaming* model (Scheuer and Readhead 1979) material can be ejected

identically on either side of the core and yet appear very asymmetric if the ejection velocities are relativistic. This is the same principle that occurs with a single electron in synchrotron radiation, where the radiation pattern is enhanced in the direction of motion. In radio sources with relativistic ejection velocities, beaming would increase the luminosity of the approaching lobe of a source aligned near the line of sight. The approaching lobe would also appear further from the core because light-travel-time effects cause the observer to see the receding lobe at an earlier epoch than the approaching lobe and hence the receding lobe would be closer to the core. The strongest argument in favour of relativistic beaming is that using this hypothesis it is possible to explain the apparent superluminal motions observed with very high resolution imaging in the radio cores.

1.2 The Sample Selection

The sources presented in this thesis were selected, by J.B. Hutchings and A.C. Gower, to fill the total luminosity/redshift plane as uniformly as possible (figure 1.1). They intended to look for radio evolution in quasars with $z < 1$ and such a sample allows sources within a horizontal slice of the plane to be studied as a function of redshift, independent of luminosity. Similarly, luminosity dependence could be studied using sources contained in a vertical slice of figure 1.1. Being able to isolate the redshift dependence and the luminosity dependence in this manner is critical in devising an evolutionary scenario for radio-loud quasars. Previous studies by Neff (1982) and Bartel (1984) have also attempted to separate these variables and their results suggest that independent luminosity and redshift trends do exist.

The sample was chosen from the quasar catalogue of Hewitt and Burbidge (1980), which provided redshifts, optical positions and absolute magnitudes of the sources. An updated version of this catalogue (Hewitt and

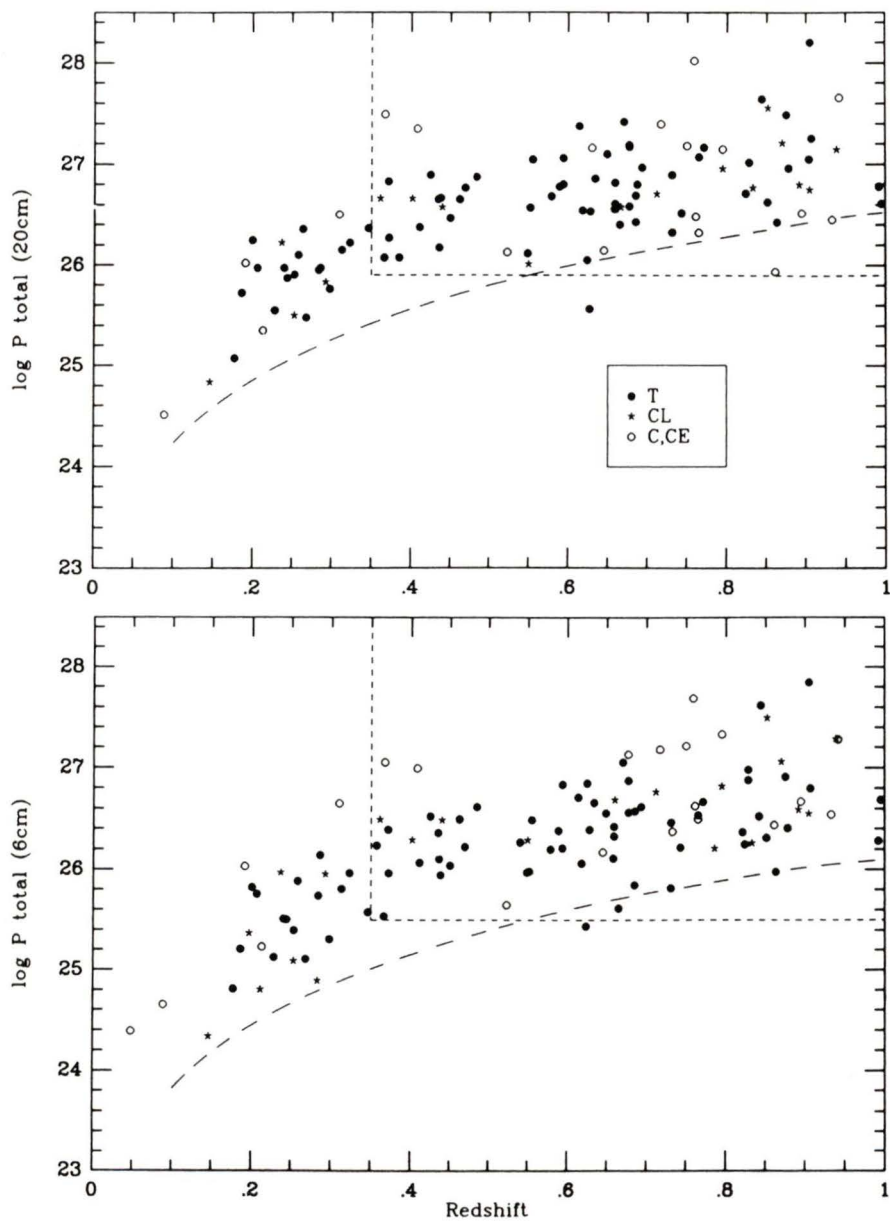


Figure 1.1: Total Luminosity vs. Redshift. Triple (T), Core-Lobe (CL), and Core (C,CE) sources are represented with different symbols as shown in the box. The curves are explained in the text.

Burbidge 1987; hereafter HB) and the ESO catalogue (Veron-Cetty and Veron 1985; hereafter V-V) provided revisions to these data for the final analysis. The radio fluxes used in defining the sample were from the Dixon radio source catalogue (Dixon 1985) which is the best general compilation of radio observations. Explicit details on the use of data from this catalogue are given in section 4.3. Fluxes in the Dixon catalogue are largely from single antenna observations, which measure the total flux of a source, and hence the sample was chosen based on the total radio luminosity of the quasars.

Figure 1.1 shows the sample plotted in the total luminosity/redshift plane, where 20 and 6cm fluxes have been used to determine luminosities in the upper and lower plots respectively. The dashed curves of luminosity increasing with redshift represent flux limits of ~ 200 mJy at 20cm and ~ 100 mJy at 6cm, and are included on the plot for a visual reference to illustrate a flux-limited sample. The vertical and horizontal lines delineate the region of the plane that the sample was chosen to fill uniformly for $z > .35$ and $\log P > 25.5$ at 6cm and $\log P > 25.9$ at 20cm. The sources to the left of the vertical limit of $z \sim .35$ are from an earlier sample (Gower and Hutchings 1984; hereafter GH) which did not adhere to the above sample definition, but are of similar-quality observations and can be included in the sample. The horizontal lines represent approximate lower luminosity limits of the sample, above which sources could be found at all redshifts. There are two obvious selection effects that make it very difficult (perhaps impossible) to populate the boxed region uniformly. Firstly, since low-luminosity sources are more difficult to detect at higher redshifts the bottom right corner of the boxed region is rather sparsely populated. Secondly, because high-luminosity quasars are rare, very few of them will be found in the immediate vicinity (*ie.* at low redshifts), which is why the top left corner of the boxed region is quite blank. Even in this carefully-defined

sample there is a tendency for luminosity to increase with redshift, so care must be taken in untangling the interdependence of these parameters when studying the radio properties. Since the sources were chosen based on their luminosities and redshifts alone, the selection was independent of morphological type, even though some of the sources are extremely well known (*e.g.* 3C48) and detailed images already existed.

Once high resolution VLA observations were available the sample was rebinned and replotted using the 6 cm core luminosity, since this is presumably a better indicator of the present nuclear activity in a quasar. The redefining of the luminosity parameter, from total luminosity to core luminosity, causes a morphology-dependent shift in luminosity. The effect can be seen by comparing figure 1.1 with figure 1.2. The amount by which the luminosity of the quasar changes, due to the new definition, depends on the ratio of the core flux to the total flux (the *core fraction*). The core fraction of the flux obviously depends on the morphological type, in the sense that unresolved sources are clearly much more core dominated than extended sources. Therefore care must be taken in interpreting the distribution of morphological types in figure 1.2.

With the allocation of 24 hours on the VLA, roughly 100 quasars were observed at both 6 and 20 cm, except for those sources that were contained in the Hintzen, Ulvestad and Owen (1983; hereafter HUU) 20cm survey (for which only 6cm data was obtained). Combined with 37 sources previously observed (GH), this sample is probably the largest survey of radio quasars to $z=1$, and although not complete, it allows the study of the radio source structure as a function of redshift and luminosity independently.

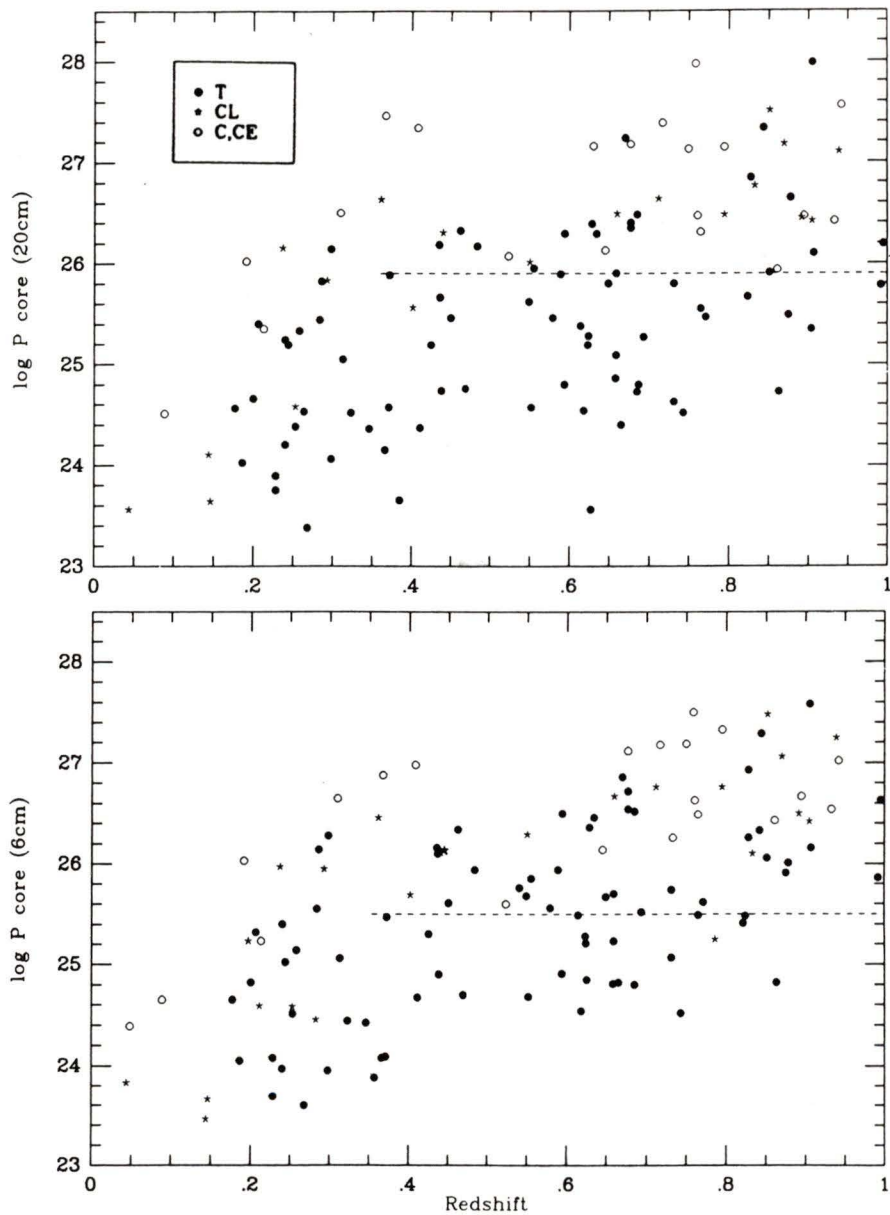


Figure 1.2: Core Luminosity vs. Redshift. The symbols represent different source types.

Chapter 2

Image Formation

Since a large amount of time was dedicated to producing the radio images, a correspondingly large portion of this thesis focuses on image formation. This chapter outlines the basic theory of image formation and chapter 3 gives a detailed description of the techniques used to create the quasar images contained in this thesis. The basic theory in this chapter is taken primarily from a review by Pearson and Readhead (1984), the 'Synthesis Imaging' lecture notes edited by Perley, Schwab, and Bridle (1985), and a similar chapter in C. O'Dea's thesis (O'Dea 1984).

2.1 Synthesis Telescopes

A single observation from a radio interferometer does not contain much information about the detailed structure of a radio source, it is merely a single Fourier component (known in radio astronomy as a complex visibility) of the sky brightness distribution. In order to *synthesize* a large-aperture radio telescope it is necessary to measure visibilities over a wide range of interferometer spacings and orientations. These different measurements correspond to sampling different spatial frequencies across the source, so that each interferometer pair provides new information about the structure of the source.

A synthesis telescope consists of an array of antennas, with each an-

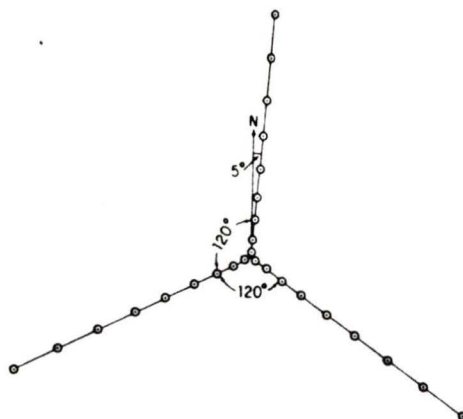


Figure 2.1: Schematic of the VLA Synthesis Telescope

tenna pair acting as an interferometer, so that in an array of N antennas, there will be $N(N - 1)/2$ interferometers. The VLA synthesis telescope, for example, has 27 antennas (see figure 2.1) and measures 351 complex visibilities simultaneously. The complex visibilities are measured in the $u-v$ plane, which is the plane of the radio antennas projected perpendicular to the direction of the source. The points that are sampled in the $u-v$ plane depend only on the relative positions of the antennas. The $u-v$ coverage at any time achieved with a given array of antennas is determined by placing, in turn, each of the antennas at the centre of the plane; the positions of the other antennas then give the points at which visibility measurements are made. The instantaneous $u-v$ coverage by the VLA is shown in figure 2.2 to the same scale as figure 2.1, so a direct comparison is possible. Because only the relative positions of the antennas are used, reflection symmetry about the origin in the $u-v$ plane requires only half of the plane to be sampled.

In order to sample the $u-v$ plane more fully, the relative positions of the antennas need to be altered. The daily rotation of the earth provides a natural way of adjusting the interferometer separations and orientations, since as the earth rotates under the source the relative positions of the antennas change with respect to the source (*ie.* the pattern in figure 2.2

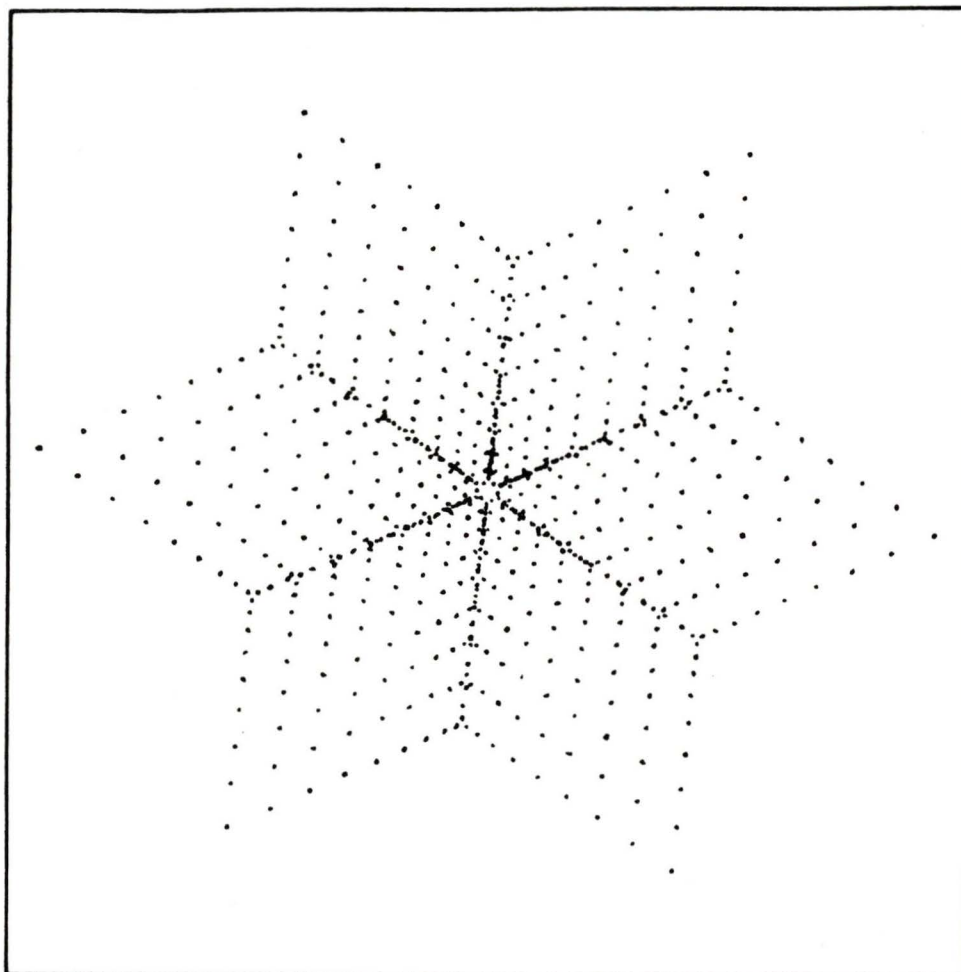


Figure 2.2: Instantaneous VLA $u-v$ coverage for source at $\delta = 30^\circ$

rotates). The u - v plane can then be sampled by simply taking measurements at regular time intervals without actually physically moving any of the individual antennas.

After collecting visibilities with a sufficient number of antenna separations and orientations a map of the sky distribution can be reconstructed by Fourier transforming the measured complex visibilities. The complex visibilities, $\Gamma(u, v)$, are measured in the u - v plane and are related to the source's sky brightness distribution, $I(x, y)$, where x and y are coordinates in the plane of the sky, by the two-dimensional Fourier transform:

$$\Gamma(u, v) \propto \iint I(x, y) \exp[-2\pi i(ux + vy)] dx dy \quad (2.1)$$

This is the fundamental equation of aperture synthesis and it is necessary to invert this equation to reconstruct the sky brightness distribution.

2.2 Image Restoration using CLEAN

With astronomers wishing to obtain high resolution images, the radio antennas tend to be separated by large distances, making it difficult to obtain data for every point in the u - v plane. Having observations that sample the u - v plane at M points, (u_j, v_j) , the inverse Fourier transform of equation 2.1 must be approximated by the sum:

$$I'(x, y) = \sum_{j=1}^M \Gamma(u_j, v_j) W_j \exp[2\pi i(u_j x + v_j y)] \quad (2.2)$$

The image formed by this inversion, $I'(x, y)$, is an initial estimate of the sky brightness distribution, called the *dirty image*. The weighting of the interferometer baselines, W_j , in the inversion is generally a trade-off between sensitivity and resolution, and is discussed in section 3.2. The incomplete and irregular sampling of the u - v plane produces features in the dirty image that tend to confuse and obscure the true structure of the source. This

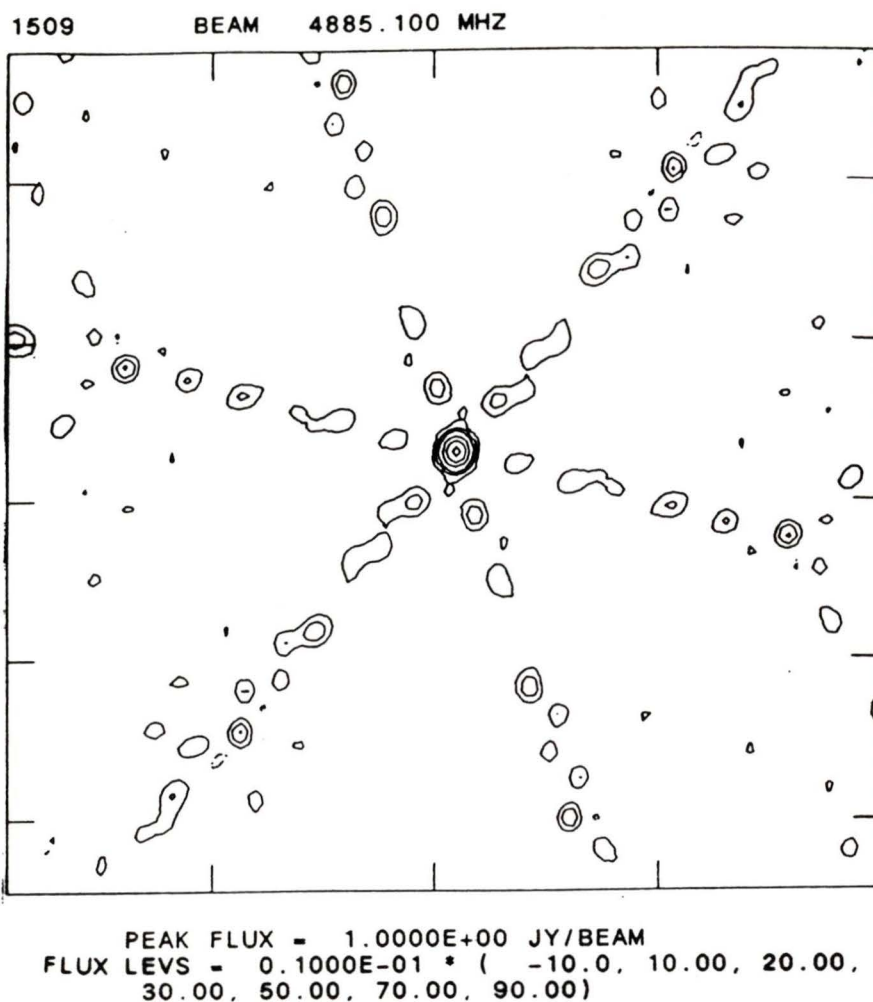


Figure 2.3: Antenna Beam Pattern or Dirty Beam

is illustrated by the observation of a point-source, which produces a dirty image that has unreal sidelobe features (some of which have negative flux values). The image formed by point source observations is called the antenna beam pattern, or the *dirty beam*, and is a function only of the antenna positions in the u - v plane and the weighting applied to the visibility data. The dirty beam formed in the observations of quasar 1509+158 is shown in figure 2.3, with a hexagonal pattern of sidelobes that reach to $\sim 30\%$ of the central peak.

When observations are made of a more complex source the dirty beam pattern, $P(x, y)$, gets convolved with the true sky brightness distribution,

$I(x, y)$, to form the dirty image, $I'(x, y)$:

$$I'(x, y) = I(x, y) * P(x, y) \quad (2.3)$$

Successful removal of the dirty beam from the dirty image would enable the sky brightness distribution to be restored without having to obtain visibility measurements at all points in the u - v plane. Algorithms have been developed that remove the dirty beam pattern by a process that estimates the unmeasured visibilities.

The most widely used algorithm is CLEAN (Högbom 1974; Clark 1980), which is an iterative method of removing or CLEANing the dirty beam pattern from the dirty image. The CLEAN algorithm basically decomposes a dirty image into a number of components, each having the shape of the dirty beam. The algorithm works by repeatedly subtracting a 'weak' beam pattern from the bright regions of the image. This process thereby slowly removes the large sidelobes associated with the bright regions, while leaving the real source structure intact. Each iteration of the algorithm begins by finding the peak of the dirty image. Then a dirty beam, centered on the image peak and having an amplitude of about one-tenth of the peak, is subtracted from the dirty image. The amplitude and position of the beam subtraction (the CLEAN components) are stored and the next iteration begins by finding the peak of the residual image. This iterative process of searching for the residual image peak, subtracting the scaled beam pattern and storing the clean component is continued until either:

1. a specified number of iterations has been reached, or
2. the noise level of the residual image is below a desired level, or
3. the number of negative clean components equals the number of positive ones, at which point the total cleaned flux will be a maximum.

The end products of the process are the list of CLEAN components and the final residual image that contains noise and some low level flux features

of the source. The CLEAN components form an array of delta functions which model the source and which, when Fourier-transformed back into the u - v plane, reproduce the observed visibilities. The final CLEAN image is produced by smoothing the array of CLEAN components and adding in the residual image. The smoothing is done by convolving the CLEAN components with a CLEAN beam. The CLEAN beam is produced by fitting a truncated elliptical Gaussian to the central lobe of the dirty beam, so that the CLEAN beam has the same resolution as the dirty beam but does not have any sidelobes (*ie.* the CLEAN beam is essentially the central component in figure 2.3). The Fourier transform of the final CLEANed image does not reproduce the original visibility measurements, but rather the measured visibilities multiplied by the Fourier transform of the CLEAN beam.

2.3 Calibration and Self-calibration

Before celestial radio waves reach the telescope they pass through the earth's inhomogeneous atmosphere and after they are received they undergo electronic processing. The variable nature of these processes introduces errors, known as gain errors, into the measured visibilities, and calibration of the telescope attempts to monitor and correct for these errors. For the antenna pair m and n the complex gain error, G_{mn} , relates the observed visibility, V_{mn} , to the true visibility, Γ_{mn} , by

$$V_{mn} = G_{mn}\Gamma_{mn} + \text{noise} \quad (2.4)$$

For sources with well-determined structure, strength, and position, the true visibilities can be predicted and so, by observing such sources, corrections to the measured visibilities can be determined and applied to the program sources. These *calibrator* sources are observed roughly every 15–30 minutes, which allows the gains to be estimated on a time-scale of a few minutes.

Using calibration sources enables monitoring of any errors associated with the array electronics which are of a slowly-varying nature.

Gain errors that vary on time-scales faster than this make it impossible to recover the visibilities using this method. Changes in the refractive index in the atmosphere and ionosphere can occur very quickly and they tend to distort the incoming radio wavefront and introduce phase errors into the observations. Such variations that occur extremely quickly require corrections to be made on a very short time-scale.

By assuming the gain errors can be attributed to the individual antennas rather than baselines, the complex gains can be factored into

$$G_{mn} = g_m g_n^* \quad (2.5)$$

where g_m is the complex gain factor of antenna m . With the gains factored in this manner a technique known as 'self-calibration' can be used to correct the short time-scale errors. The self-calibration process uses the source itself as a model which allows the variations in the antenna and atmosphere to be monitored continuously. The basic principle of self-calibration is to allow the antenna gains, g in equation 2.5, to be degrees of freedom in the determination of the sky brightness. If all baselines are correlated there will be $N(N - 1)/2$ complex visibility measurements. By allowing the N complex antenna gains to vary as free parameters there are then $N(N - 1)/2 - N$ 'good' complex numbers remaining available for use as constraints on the true sky brightness distribution. For an array with 6 antennas, such as MERLIN, this loss amounts to 40% of the data, but for the VLA's 27 antennas the loss is only 8%.

Self-calibration is an iterative method that involves repeated Fourier transforming between the image plane (*ie.* the plane of the sky) and the u - v plane (*ie.* the projected telescope plane), while making adjustments in each domain. Each iteration adheres to the following outline.

1. A model of the sky brightness distribution is Fourier-transformed back

into the u - v plane, providing an estimate of the true visibilities, Γ'_{mn} , from which the corrections to the gain errors can be determined. The initial model is the CLEAN components of the calibrated visibilities and subsequent models are the CLEAN components of the previous self-calibration iteration. No negative components are used, thereby eliminating unreal negative flux from the models. CLEAN can also be restricted to search for components inside a defined window of the sky, thus reducing the number of parameters needed to model the source.

2. The mean square difference between the observed and the model visibilities

$$\sum_{m < n} w_{mn} | V_{mn} - g_m g_n^* \Gamma'_{mn} |^2 \quad (2.6)$$

is minimized by adjusting the complex antenna gains g_m and g_n . The w_{mn} term allows greater weight to be placed on the more reliable measurements (*e.g.* the shorter baseline measurements of the faint large-scale structures are often unreliable).

3. Applying the new gains to the observed visibilities enables a new model to be produced. The above procedure is continued until the models are no longer being changed by the process.

No proof of convergence of this method has ever been given, but in practice, given sufficient u - v coverage, tests show that the final image is a good estimate of the correct image. So like CLEAN, self-calibration is another method of improving the quality of the image, this time by correcting the time-varying antenna gains.

Chapter 3

Observations and Data Reductions

This chapter describes the data reduction techniques used in obtaining the images presented in the appendix, focusing on specific details of the concepts outlined in chapter 2. The images themselves are also presented together with tables 3.1 and 3.2 which contain image parameters that describe the ‘limitations’ of the images (*e.g.* resolution, sensitivity, and completeness).

3.1 Observations

To study the morphology of objects as distant as quasars, it is necessary to use a telescope that combines high resolution with high sensitivity. The Very Large Array (VLA) synthesis telescope, (illustrated schematically in figure 2.1) with 27 antennas spread over ~ 35 km, can provide sub-arcsecond resolution and sub-mJy sensitivity after only a few minutes of observing. For the images in this thesis the VLA was used in its A configuration (for maximum resolution) to obtain high-quality images of ~ 100 quasars at both 6 and 20cm. The use of two wavelengths provides complementary views of the sources, as the 20cm images are more sensitive to the extended structure, and the 6cm images, with higher resolution, probe the compact regions (*e.g.* 2325+269). Two wavelengths also allow spectral indices to be

determined for sources that are unresolved at both wavelengths (*e.g.* the core components).

The program sources were observed for roughly 5 minutes at both 6 and 20cm (unless the 20cm data were already available in HUC) and interspersed with 2 minute observations of calibration sources about every 15 minutes. Some of the program sources also happened to be regular VLA calibrator sources and so were used as both program sources and calibrators. The flux density zero-point scale was set by observations of 3C286 during the run. Visibility measurements were taken at 30 second intervals using a 50 MHz bandwidth.

During the observations, four sources were lost due to online computer malfunctions. This problem also ruined observations for some sources at just one of the wavelengths and reduced the integration times of some other sources, thereby increasing the noise level in their final images. This problem occurred while observing sources near right ascension ~ 7 hours.

The data were calibrated using the NRAO software on the DEC10 computer by D. Wunker. This process, as described in section 2.3, estimates the complex antenna gains using the calibrator sources and applies them to the program sources, with the flux zero-point being set by the 3C286 observations. After observation and calibration about 150 sources were ready for imaging. The standard software for reducing VLA data is the Astronomical Image Processing System (AIPS) developed by NRAO and the next section describes the imaging techniques using this package.

3.2 Image Formation

It was at this stage that my involvement in the project began, after the sample selection, observation and calibration had been complete. Thanks to the generosity of the VLA staff, roughly half the images were produced using the VLA facilities and the rest were made using the AIPS software

at the Dominion Radio Astrophysical Observatory (DRAO) in Penticton, to which access was kindly given. The general image formation process remained consistent throughout the data reductions, but as experience was gained and the basic theory of image formation was better understood, the image quality gradually increased. The ability to recognize and correct certain errors, as well as use some of the more subtle features in the software, continually improved the image quality. These improvements are more cosmetic in nature and do not effect the results of this thesis, where the analysis concentrates on the main source properties. The use of tapering may be an exception to this, see section 3.2.2 for details.

The following is a brief outline of the techniques used in producing the images shown in the appendix. The AIPS software was used in image formation, but the details of the software and the use of specific programs are not mentioned directly, as discussion concentrates on the general strategy of the image formation methods used and some variations on the standard methods. For each source, the 20 cm image was produced before the 6cm image to give a more overall picture of the source, since the longer wavelength and lower resolution allow the imaging of a larger area of the sky and also allow the detection of more of the large-scale features in the radio structure.

3.2.1 The $u-v$ data

Before the images are made a few minor manipulations of the $u-v$ data (the calibrated complex visibilities) are necessary. During these processes visual examination of the $u-v$ data can provide insight into the source structure and possibly identify spurious data points. First, the data was concatenated into a single data set and the visibilities were plotted as a function of baseline length, as in figure 3.1. These $u-v$ plots contain useful information on the source structure. For example, the longer baselines are less sensitive to or *resolve out* the extended structure of the source, and therefore

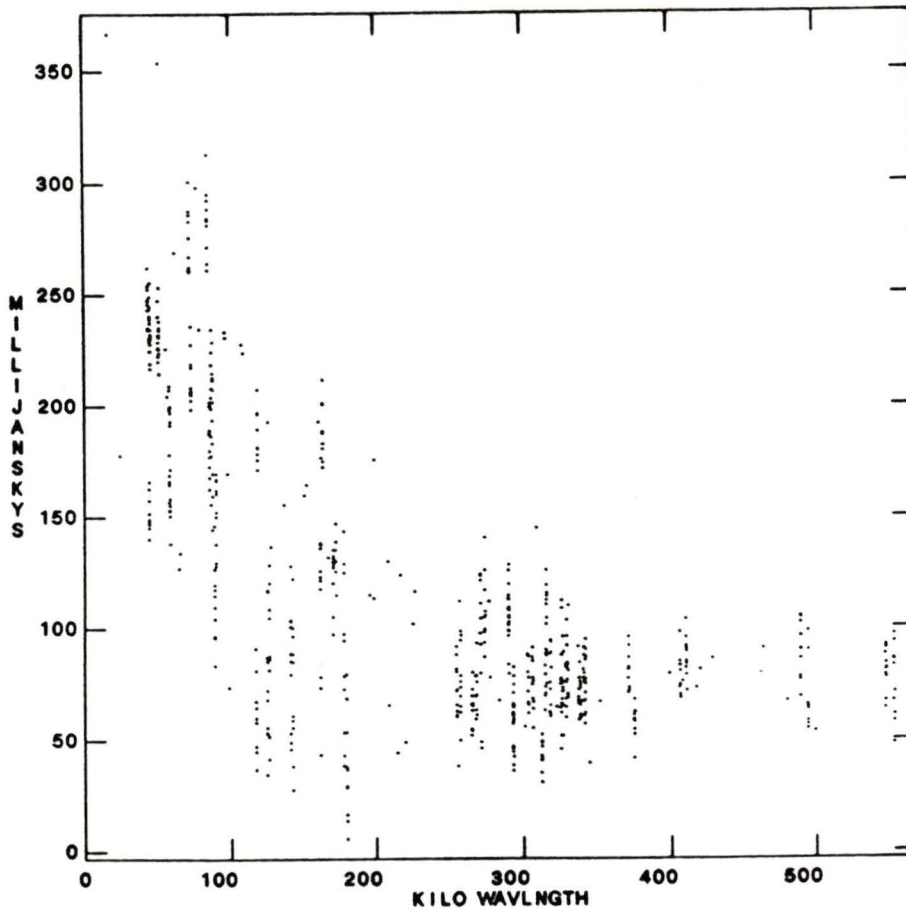


Figure 3.1: u - v plot of 0133+207; 6cm (Flux vs. Antenna Separation)

for extended sources the measured flux decreases with increasing baselines. Point sources, on the other hand, remain unresolved for all the antenna pairs, so the flux stays constant for all baselines. The u - v plot of 0133+207 at 6cm in figure 3.1 displays these features, with the flux decreasing as the baselines increase and leveling off above $\sim 300k\lambda$, where only the unresolved core component is detectable. The average flux beyond $300k\lambda$ is $\sim 75mJy$, which agrees with the core flux measured from the final image. It is also possible to estimate the total observed flux using the flux measured at the short baseline end of the plot. When the flux continues to rise at short baselines it can be expected that the VLA in the A array may have missed

a substantial portion of the flux, and this can be followed up by comparing the observed short-baseline flux with single-dish measurements taken from the Dixon catalogue (see section 4.3). Using this technique it becomes clear that for 0133+207 only 50% of the flux was observed at 6cm, so there is a lot of large-scale lobe structure that is unseen in the image in the appendix. $u-v$ plots are also useful in identifying data points with drastically high or low fluxes as they would stand out on such plots.

The second manipulation of the $u-v$ data is to place the visibility data points on to a rectangular grid. Such gridding allows Fast-Fourier transforms to be used to transform between the $u-v$ plane and the image plane. Since the $u-v$ plane is sampled non-uniformly (see figure 2.2) the weighting of the data has to be determined. For a given interval of time the longer baselines travel further about the centre of the $u-v$ plane, leaving the outer regions of the synthesized antenna more sparsely sampled than the inner regions. A uniform weighting of the gridded data allows an image of high resolution to be produced, while sacrificing signal-to-noise. The *natural* weighting scheme weights the data according to the number of ungridded visibilities that were used to produce each gridded one, which sacrifices resolution for better signal-to-noise. The images contained in this thesis have been weighted uniformly.

3.2.2 The Initial Image

Once the data was examined and gridded it was ready for imaging and CLEANing using an FFT algorithm. CLEANing, as mentioned in section 2.2, attempts to remove the beam pattern, that is convolved with the image, by estimating the complex visibilities in the unsampled regions of the $u-v$ plane. This section discusses the examination of the initial image.

During the initial CLEAN cycle of 500 iterations a 512×512 pixel area was CLEANed which, when using pixels sizes that are approximately

one third the beam diameter, correspond to areas of ~ 200 arcsec and ~ 50 arcsec for 20 and 6cm respectively. The large area of the sky allows one to see the whole source and make decisions on further data reductions. If the source is unresolved and there is no sign of extended structure then no further processing is necessary. For sources that show extended structure, self-calibration can be run on the source using this first image as a model of the source. This initial image then permits boxes to be placed around the regions containing flux so that subsequent CLEAN iterations can be constrained to search only these regions of the sky, increasing the speed of the process.

In cases where the initial position was poor or the source was extremely large, some of the radio emission was outside the CLEANed area and part of a dirty beam pattern that originates outside the area was seen on the initial CLEANed image. For the images with poor positions it was necessary to shift the map centre, while for the large sources (*e.g.* 0007+332) the CLEANed area of the sky had to be increased. Each of these two cases and its implications is discussed in turn below.

Bandwidth Smearing

If, due to an error in the observed position, the source turns out to be far from the map centre used for the observations, an effect known as *bandwidth smearing* causes the source to be elongated radially with respect to the map centre, and the greater the distance from the centre the greater the smearing. Although the map centre can be shifted artificially in analysis (to bring the source to the centre), this smearing effect will remain since it was introduced at the time of observation. An extreme example of this effect can be seen in figure 3.2, where the observed position was 300 arcsec in error. A more subtle example of this effect can be seen in the core of 0810+327 at 6cm, where the core is noticeably elongated in right ascension. The smearing is caused by longer wavelengths in the bandpass bandwidth

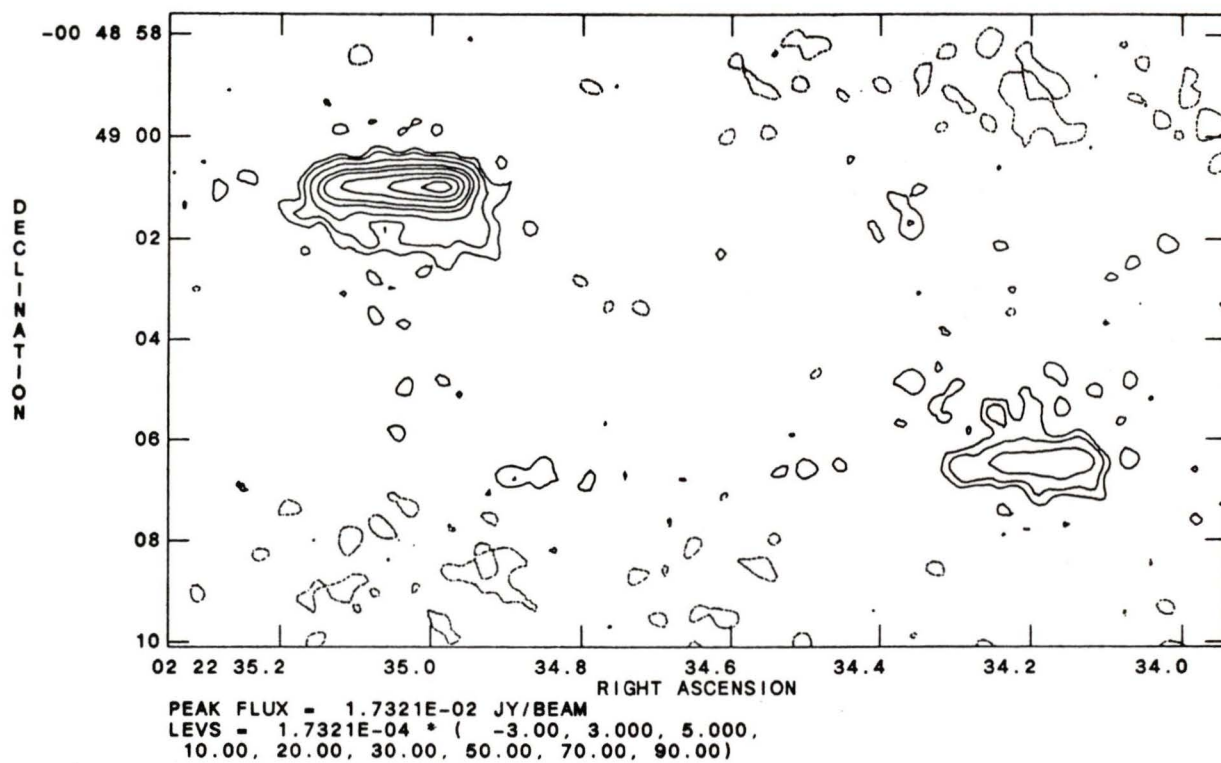


Figure 3.2: The effect of bandwidth smearing on 0222-008; 6cm

focusing further from the image centre than the shorter wavelengths. The difference in the focal points increases with the distance of the source from the centre of the image. The name arises because the effect would not occur for a single frequency and is dependent on the width of the frequency bandpass. This effect is important, since whether the cores are extended or not is an important consideration in the analysis. All the cores of the shifted sources were checked to see if they were extended since the core flux would be diminished by bandwidth smearing and hence be underestimated.

Tapering

In the second case, in order to enlarge the CLEANed area, one technique is to make a larger image, say 1024×1024 pixels in size, but this is rather time-consuming. Another approach is to use *tapering*, where the visibilities are weighted with a Gaussian taper which gives the shorter baselines more weight. This increases the beamsize and the signal/noise ratio for the extended features. This increase in beamsize allows the pixel size to be increased and hence a larger area of the sky to be covered by the 512×512 pixel grid. The increase in the signal/noise ratio for extended features increases the likelihood of detecting faint structures. As discussed in the previous section, the image can be examined in light of the $u-v$ plot. One of the most common disagreements is when the $u-v$ plot suggests extended structure, but it is not apparent in the image; in this case tapering may reveal the extended structure. The use of tapering can be seen by comparing figure 3.3 with the tapered image of 0003+158 in Appendix A. Proper use of this technique in particular did not mature until the second half of the sources were being imaged, so there may be some large scale features that have gone undetected in a few images. The sources that were tapered are listed in column 7 of table 3.2.

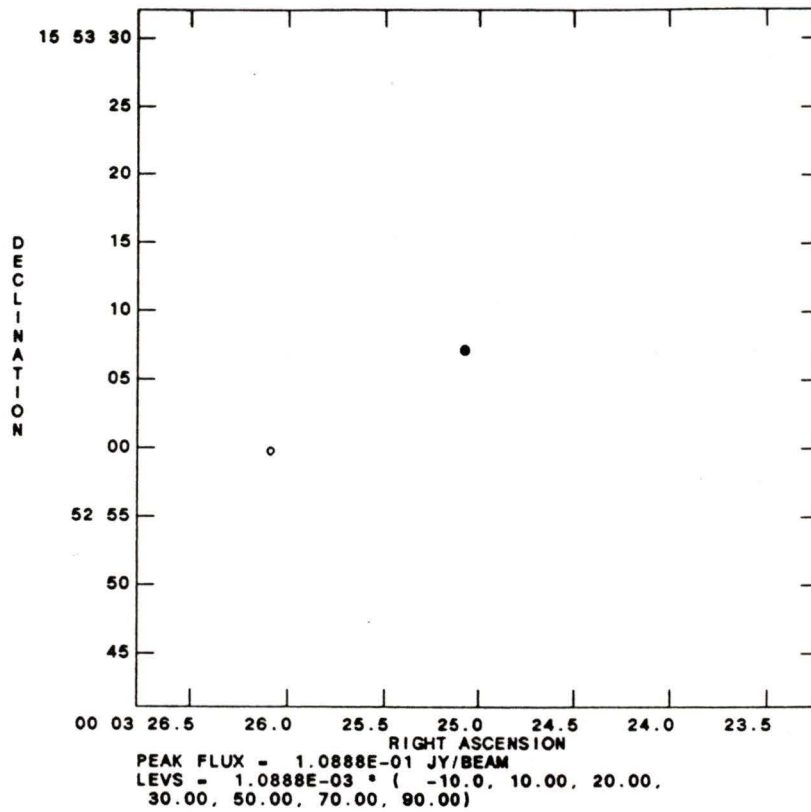


Figure 3.3: Untapered image of 0003+158; 6cm

3.2.3 Self Calibration

The first CLEAN cycle provides an initial view of the source and for bright, extended sources is the first step in the self-calibration process. The initial CLEAN image, up to the first CLEAN component, provides a model of the source for the self-calibration, with the components beyond the first negative component not being used since negative components are obviously unphysical. Baselines shorter than $\sim 100k\lambda$ are also not used in the self-calibration, since the sampling of the large-scale structure is unreliable. This model, which consists of the bright, compact components of the source, is then assumed to be a reasonable estimate of the source structure and the telescope is then 'recalibrated' using the model. The largest gain errors are generally found in the phase of the signal, so for the initial self-calibration cycle adjustments of the phase only are made. The corrections applied to the gains can then be plotted, to check the magnitude of the adjustment (usually less than $\sim 30^\circ$), which may be useful in identifying spurious data.

The above procedures of gridding, CLEANing and inspection are performed again, as they constitute a major portion of the self-calibration process. During each iteration the CLEAN components from the previous self-calibration cycle are used to model the source since they presumably represent the best available model of the source. On all subsequent self-calibration cycles both the amplitude and the phase were adjusted. Once the self-calibration process no longer improves the image (*ie.* the solution has converged), the final image is produced by running CLEAN until the CLEANed flux reaches a maximum. This occurs when the number of negative CLEAN components equals the number of positive ones. The total CLEANed flux at this point should roughly equal the short baseline flux on the $u-v$ plot. The rms noise level of the final image is determined by placing a box around an area that does not appear to contain any source flux, and it should be close to the theoretical limit as determined from equation

Table 3.1: Overall image parameters

	20 cm	6 cm
central frequency	1.4899 GHz	4.8601 GHz
pixel size	0.4"	0.1"
CLEAN beam resolution	$\sim 1.2''$	$\sim 0.4''$
CLEANed image size	200" square	50" square
largest observable structure	$\leq 25''$	$\leq 7''$
theoretical noise level (5 min)	$\sim .27$ mJy	$\sim .18$ mJy
dynamic range	$\sim 300:1$ to $\sim 1000:1$	

16-6 of Perley *et al.* (1986) or the VLA 'Green Book' (Hjellming *et al.* 1982). Examining the mean level of the background can show if there was a DC offset in the flux level or, if it is varying spatially, that large-scale structure may be present which has not been completely mapped.

3.3 The Images

The individual images for all the resolved sources are presented in the appendix. The images constitute one of the largest samples of quasars with $z < 1$. A general summary of the image parameters is presented in table 3.1, while table 3.2 contains image parameters for all the individual sources. The quality of the images is excellent considering the observations were only for a few minutes each. The resolution of roughly an arcsec and sensitivity of less than a mJy, allow precise measurements to be obtained from these images. The theoretical noise levels were generally obtained for the weaker sources, but for the stronger sources a dynamic range limit of $\sim 1000:1$ was reached. The size of the largest observable structure (row 5 of table 3.1) should be noted when the images are studied.

The image parameters for the individual sources are presented in table 3.2. There are two rows for each source, the first row corresponds to 6 cm data and the second row to 20 cm. This table contains data only for the new observations and reference to GH and HUO should be made for the

images of theirs that were used. The table is described here by the column numbers in the table:

- (1) IAU source name
- (2) The right ascension and declination of the radio core component which coincides with the optical position of the quasar (within the errors) in every case. Only the 6 cm position is quoted if the data was available, otherwise the 20 cm position is used. For the cases where no position is quoted no 6 cm data was available, and the HYO paper should be consulted for a core position. There were some sources for which the fit to the core component was poor, so the accuracy in these positions varies from source to source.
- (3) The CLEAN beam parameters are the FWHM major and minor axes in arcsec and the position angle, in degrees, of the major axis measured counter-clockwise from north. Highly elliptical beam shapes occur in sources with low declination. The large beams for some of the 6 cm images correspond to tapered images.
- (4) The rms noise level of the image background is in units of mJy. This was measured by placing a box around a blank patch of the image and then calculating the rms scatter of the flux values contained in the region. It was also useful to plot the the flux distribution to see the scatter and check for an offset of the mean from zero.
- (5) The dynamic range of the image is defined as the ratio of the image peak to the rms noise level. In general it was between 300:1 and 1000:1.
- (6) The fraction of missing flux in an image is the ratio of the total CLEANed flux in the image to the total flux of the source as determined in section 4.3. These values give some idea of the amount of

Table 3.2 Image Parameters

Source (1)	Core Position Right Ascension Declination (2)			CLEAN Beam Pattern (3)			RMS noise level (4)	DR (5)	% flux missing (6)	Comments (7)
0003+158	00 03 25.08	+15 53 07.1	0.87 0.86 42	0.5	230 25	TAP				
			1.23 1.19 34	0.5	290 35					
0007+332	00 07 50.10	+33 12 55.7	0.88 0.84 25	0.3	50 50	TAP				
			1.13 1.08 35	0.3	810 40					
0044+030	00 44 31.41	+03 03 32.7	1.03 1.00 33	0.2	90	TAP				
			1.34 1.23 13	0.2	160					
0056-001	00 56 31.76	-00 09 18.8	0.46 0.38 -1	0.6	2480 0					
			1.56 1.31 -3	1.9	1300 0					
0114+074	01 14 49.51	+07 26 30.1	0.95 0.92 54	2.4	140 0	R6,D13 HUO				
0118+034	01 18 26.13	+03 28 30.8	1.01 0.84 75	0.4	60 65	TAP				
					25 U					
0133+207	01 33 40.41	+20 42 10.4	0.35 0.34 31	1.0	140 50	TAP				
			1.21 1.17 36	1.8	210 40					
0134+329	01 34 49.84	+32 54 20.4	0.36 0.35 34	1.3	2770 0					
			1.17 1.15 39	12.9	1000 0					
0159-117	01 59 30.36	-11 46 59.7	0.51 0.36 -2	0.6	1390 5					
					10 U					
0219+428	02 19 29.99	+42 48 29.8	0.38 0.34 6	0.4	1090 30					
			1.21 1.12 16	1.0	650 10					
0222+000	02 22 34.20	+00 03 35.9	0.44 0.37 3	0.2	470 0					
			1.38 1.26 14	0.3	1000 0					
0222-008				0.2	71	R300 HUO				
					0					
0300-004	03 00 39.56	-00 26 40.1	0.45 0.37 9	0.3	20 10					
			1.43 1.19 8	1.0	490 0					
0310+013	03 10 08.59	+01 22 05.2	0.40 0.35 9	0.7	700 0	D24				
			1.34 1.21 11	0.4	380 0					
0336-019				1.3	1530 0					
	03 36 58.95	-01 56 16.9	1.38 1.16 12	1.5	1370 0					
0340+048	03 40 51.54	+04 48 21.7	0.38 0.35 22	0.1	670 30					
			1.31 1.21 21	1.2	220 15					
0349-146			1.18 1.15 6	0.1	920 45	TAP				
			1.66 1.09 8	1.5	120 30					
0429+415	04 29 07.90	+41 32 08.6	0.40 0.37 53	3.4	1060 0					
			1.37 1.35 46	8.3	980 0					
0440-003			0.44 0.37 4	1.6	810 50					
			1.40 1.16 10	1.0	1420 35					
0518+165			0.39 0.36 24	2.2	1240 0					
	05 18 16.53	+16 35 26.8	1.15 1.11 36	8.9	900 0					
0534-201	05 34 12.88	-20 07 19.2	0.63 0.33 -1	0.2	1090					
			2.00 1.12 1	0.2	430					
0704+384	07 04 08.37	+38 26 57.1	0.34 0.32 31	0.1	480 15					
			1.13 1.05 31	0.2	440 5					
0738+313										
	07 38 00.18	+31 19 02.1	1.23 1.18 32	2.0	1010 0					
0805+579	08 05 58.63	+57 52 37.0	0.36 0.31 23	0.1	280 40					
					0 HUO					
0810+327	08 10 59.56	+32 46 39.8	0.37 0.37 45	0.1	880 25	R32				
0812+020	08 12 47.27	+02 04 12.9	0.42 0.36 8	0.2	870 25					
					5 HUO					
0821+447										
	08 21 50.33	+44 46 14.2	1.01 0.97 39	0.2	740 0					
0827+193	08 27 11.00	+19 20 47.2	0.65 0.58 20	0.1	160	TAP				
			1.20 1.13 32	0.2	540					
0827+243	08 27 54.40	+24 21 07.7	0.38 0.34 15	0.2	4780 5					
			1.26 1.18 26	0.4	1490 25					

Table 3.2: Image Parameters

Table 3.2 continued

Source (1)	Core Position Right Ascension			Declination (2)			CLEAN Beam Pattern (3)			RMS noise level (4)	DR (5)	% flux missing (6)	Comments (7)
	0833+276	08 33	21.93	+27 39	19.3	0.37	0.33	18	0.2	1170			
					1.16	1.11	32	0.4	440				
0903+169	09 03	44.13	+16 58	16.0	0.35	0.34	34	0.1	180	90			
										40	HUO		
0920+313	09 20	48.47	+31 20	48.1	0.33	0.33	38	0.2	1010				
					1.14	1.10	31	0.4	420				
0932+023	09 32	42.93	+02 17	40.9	0.40	0.34	8	0.2	410	50			
										0	HUO		
0937+391	09 37	59.21	+39 07	29.6	0.37	0.31	13	0.1	70	75	R2,D7		
					1.21	1.06	23	0.2	240	15			
0953+254	09 53	59.74	+25 29	33.6	0.37	0.36	29	0.3	1890				
					1.19	1.17	41	0.3	1310	0			
0957+003	09 57	43.80	+00 19	49.2	0.44	0.37	2	0.1	560	0			
										25	HUO		
1012+488								0.2	40	70	U		
1015+227	10 15	00.34	+27 47	05.3	0.38	0.34	1	0.2	680	5			
					1.23	1.09	9	0.5	1220	0			
1022+194	10 22	00.15	+19 27	34.7	0.37	0.33	3	0.8	670	0			
										0	U		
1038+528	10 38	43.15	+52 49	10.0	0.35	0.31	29	0.1	2420	10	R9,D13		
					1.15	1.01	31	0.3	1050	0			
1047+096	10 47	48.93	+09 41	47.1	0.41	0.38	1	0.1	130	25	R29,D6		
										0	U		
1104+167	11 04	36.64	+16 44	16.4	0.38	0.34	3	0.6	590	40	R11,D21		
										30	U		
1118+128	11 18	53.39	+12 52	44.3	0.39	0.33	7	0.1	120	40			
										0	HUO		
1130+106	11 30	24.20	+10 40	16.6	0.41	0.35	3	0.2	630	0			
										0	HUO		
1146+111	11 46	13.37	+11 11	38.9	0.42	0.35	1	0.2	30	50			
										10	HUO		
1151+102	11 51	14.38	+10 12	36.3	0.40	0.33	5	0.4	650	0			
					1.36	1.22	4	0.4	380				
1156+631	11 56	04.65	+63 11	09.7	0.38	0.30	-22	0.1	110	40			
					1.21	1.00	-28	0.3	320	30			
1157+118	11 57	12.60	+11 50	30.7	0.38	0.33	4	0.2	60	50			
										0	HUO		
1222+216	12 22	23.41	+21 39	23.0	0.38	0.34	9	0.5	920	5			
										10	HUO		
1233+108	12 33	32.67	+10 51	19.7	0.39	0.33	5	0.1	100	15	R4,D2		
					1.28	1.16	14	0.2	300	0	R9,D19		
1252+119	12 52	07.72	+11 57	20.8	0.41	0.34	5	0.3	2350	20			
					1.44	1.17	-3	0.8	1080	15			
1253+104	12 53	36.78	+10 25	07.1	0.40	0.34	9	0.1	140	50			
										10	HUO		
1258+287	12 58	04.10	+28 46	18.7	0.37	0.32	10	0.5	380	0			
					1.26	1.10	7	0.3	550	0			
1335-061	13 35	31.17	-06 11	57.1	0.48	0.35	9	0.3	560	30			
										5	U		
1340+289	13 40	42.24	+28 59	12.1	0.37	0.33	1	0.1	1010	20			
					1.25	1.10	2	0.1	1440	5			
1352-203													
	13 52	58.88	-20 23	53.5	2.00	1.10	10	0.3	20				
1415+172	14 15	41.58	+17 17	13.2	0.37	0.35	5	0.3	70	15			
										0	HUO		
1420+326	14 20	21.24	+32 36	47.4	0.36	0.33	-10	0.4	1030				
					1.24	1.12	-15	0.9	440		R7,D7		

Table 3.2 continued

Source (1)	Core Position Right Ascension Declination (2)			CLEAN Beam Pattern (3)			RMS noise level (4)	DR (5)	% flux missing (6)	Comments (7)
1423+242	14 23	34.65	+24 17 32.2	0.37	0.34	-9	0.4	150	25	
									10	U
1442+117	14 42	25.97	+11 44 33.6	0.39	0.34	9	0.2	340	15	
									0	HUO
1458+718	14 58	56.64	+71 52 11.1	0.55	0.36	-62	1.0	2300	15	
				1.90	1.28	-62	2.4	2150	20	
1509+158	15 09	52.34	+15 51 39.2	0.38	0.34	-3	0.3	390	35	
									25	HUO
1510-089	15 10	08.90	-08 54 47.6	0.59	0.39	14	1.0	1580		
1522+155	15 22	22.15	+15 31 53.2	0.41	0.40	-50	0.3	1030	0	
				1.33	1.16	-3			20	
1530+137	15 30	54.23	+13 42 27.8	0.39	0.34	-1	0.3	197	20	R5, D6
									0	HUO
1540+110	15 40	33.03	+11 04 05.0	0.92	0.87	-34	0.3	90	10	TAP
									10	HUO
1548+114	15 48	21.18	+11 29 47.5	0.39	0.35	5	0.3	1450	0	D3
									20	HUO
1606+180	16 06	56.65	+18 04 06.4	0.39	0.33	-2	0.3	50	40	
									40	HUO
1618+177	16 18	07.29	+17 43 30.3	0.93	0.86	-38	1.1	110	55	TAP
									5	HUO
1623+173	16 23	14.00	+17 22 31.5	0.94	0.93	-48	0.3	70	65	TAP, R4, D7
									35	HUO
1637+574	16 37	17.43	+57 26 15.7	0.37	0.35	-37	0.7	2110		
				1.23	1.22	-44	0.7	1710		
1657+265	16 57	22.52	+26 34 03.0	0.36	0.34	7	0.4	1210	0	
									25	HUO
1704+608				0.33	0.32	-42	0.5	320	45	R16, R15
	17 04	03.53	+60 48 31.4	1.09	1.08	44	1.0	1000	25	TAP
1725+107	17 25	32.25	+10 45 21.4	0.37	0.35	23	0.4	190	0	R20, D21
									0	HUO
1741+279	17 41	57.90	+27 54 04.8	0.36	0.33	6	0.2	620	35	
									15	HUO
1819+408	18 19	12.82	+40 50 11.3	0.36	0.33	0	0.2	920	0	
1830+285	18 30	52.38	+28 31 17.0	0.99	0.91	15	1.0	510	35	TAP
									20	HUO
2005-044	20 05	46.29	-04 27 17.0	0.46	0.36	11	0.4	350	25	
				1.47	1.30	11	0.7	180	15	
2044-027	20 44	34.21	-02 47 25.8	0.48	0.37	-4	0.5	1100	5	
				1.43	1.25	-2	0.7	2500	0	
2112+172	21 12	36.72	+17 16 50.5	0.36	0.35	18	0.2	290	15	
									0	U
2142+110	21 42	52.35	+11 01 36.3	0.40	0.38	-26	0.4	960	0	R4, D6
									0	U
2154+100	21 54	45.22	+10 00 05.9	0.38	0.37	33	1.7	200		
				1.28	1.22	28	0.4	590		
2209+080	22 09	32.22	+08 04 26.0	0.38	0.38	36	0.4	670	40	
									20	HUO
2234+282	22 34	01.73	+28 13 23.2	0.39	0.39	47	3.1	530	0	
				1.28	1.26	40	1.0	1080	0	
2251+113	22 51	40.56	+11 20 39.2	0.38	0.36	25	0.2	200	20	
									0	HUO
2251+134	22 51	51.88	+13 25 48.9	0.38	0.37	20	0.4	1460	0	R17
									0	HUO
2314-116	23 14	46.01	-11 38 47.2	0.90	0.87	81	0.2	390	40	TAP
				1.65	1.23	-11	0.3	290	30	

Table 3.2 concluded

Source (1)	Core Position			CLEAN Beam Pattern			RMS noise level (4)	DR (5)	% flux missing (6)	Comments (7)
	Right Ascension	Declination		(3)						
2325+269	23 25 28.55	+26 59 21.6	0.35 0.33 24	0.3	190	20				
2344+092	23 44 03.77	+09 14 05.4	1.19 1.16 35	0.4	1380	0				
			1.28 1.27 30	2.0	720	0				
2349+327	23 49 48.93	+32 47 18.1	0.97 0.87 19	0.4	50	55	TAP			
			1.16 1.11 37	0.4	110	25				
2353+283	23 53 21.36	+28 19 16.3	0.34 0.32 25	0.2	410	10	R6, D9			
						0	HUO			

flux missing from the image due to the poor sampling by the VLA of the large-scale structure or possibly variability of the core component.

(7) This column contains the following notes for individual sources:

- HUO – image is from HUO paper
- U – revised HUO image
- TAP – means the image has been tapered to search for large-scale structure in the image, as discussed in section 3.2.2.
- R or D – refer to any shifts in right ascension, R, and declination, D, that were necessary to center the source in the image. Large shifts, where the values given are in arcsec, imply noticeable radial smearing of the images as discussed in section 3.2.2.

Chapter 4

Measurements

The radio properties of the sample on which this thesis (and HPG) is based are presented in table 4.1. This chapter describes the techniques used to obtain these data. The first section contains a discussion on the morphological classifications, while the second section concentrates on the numerical measurements obtained directly from the images and the third section discusses information not obtained from the images. The measuring techniques used for each property will be described in detail in the text and can be referred to quickly by column numbers, which appear in a bold font in the text. For example, column **(1)** lists the source names by IAU convention followed by a more common name, and column **(2)** lists the redshifts obtained from HB or V-V.

For the HUGO images some of data were measured from their published or revised images (*e.g.* C-L distances and core flux), and when this was not possible (*e.g.* lobe fluxes) their published values were used. For sources in the low redshift region, $z < .35$, the data published in GH were used exclusively and lobe flux measurements were not available.

Before describing the measuring techniques the cosmological parameters and the corresponding equations for linear size and luminosity will be presented. The Hubble constant, H_0 , used was 100 km/sec/Mpc and the deceleration parameter, q_0 , was zero. The luminosity distance, d_L , was then

calculated using:

$$d_L \simeq \frac{cz}{H_0} \left(1 + \frac{z}{2}\right) \quad (4.1)$$

and the equation used to calculate angular sizes, d_A , was:

$$d_A = \frac{d_L}{(1+z)^2} \quad (4.2)$$

as seen on page 485 of Weinberg (1972), where z is the redshift, c the speed of light and the distances are determined in megaparsecs. Evaluating all the numerical constants, luminosities can then be calculated using:

$$L_\nu = 1.076 \times 10^{24} \times S_\nu \times \frac{\left(z + \frac{z^2}{2}\right)^2}{1+z} \quad (4.3)$$

where S is the flux in milliJanskies and the luminosities are in Watts/Hz. The term in the denominator of equation 4.3 is to account for the increase in the bandpass caused by the redshifting of the radiation. The observed frequency of a redshifted object is, $\nu_o = \frac{\nu_e}{1+z}$, where ν_e is the emitted frequency. The emitted bandpass consequently increases with redshift and so the observed luminosity has to be reduced by the factor $\frac{1}{1+z}$. In addition, to reduce the luminosities to the emitting frame it is necessary to apply K-corrections (Weedman 1986), which correct for the effect of the bandpass being redshifted to a different regime of the spectrum; the luminosities should be decreased by the factor $(1+z)^\alpha$. However this correction has not been applied to the sources since for the core components $\alpha \sim 0$, and for the lobe components it was decided that the inaccuracy in the lobe luminosities and the uncertainty in α did not warrant a K-correction. This is not a large error considering that the lobe luminosities are only quoted to within a factor of three and the ratio of the lobe luminosities are used more often in the analysis than their absolute values.

4.1 Morphological Classifications

The sources are classified into the types (column (3)) T, CL, CE, and C, depending on whether the source has two lobes, one lobe, is slightly resolved or unresolved. This simple classification scheme is easy to apply, but it is resolution and sensitivity dependent. With increased resolution, for example, the CE sources may be observed to be CL or T sources and with increased sensitivity low-surface-brightness lobes may be detected. The detection of extended structure may also be redshift dependent, since observing all sources for the same length of time favours detection of lobes in the sources with lower redshifts. With these problems, attempting to classify all the sources with these simple categories resulted in some dubious classifications (*e.g.* 0440-003 as T; 1252+119 as CL; 0310+013 as CL; or 1458+718 as T).

Further morphological classifications are listed in column (18) of table 4.1. These classifications are very subjective, but were necessary for examining the source models in this thesis and HPG. A key for these morphologies is: ECE or CE - core of a CL or T source is extended; J - narrow ridge of emission, or jet, extending from the core towards the lobe (as defined in section 1.1); S - is S-shaped symmetry indicative of precession; A - evidence for continued alternating ejection in the source; Cpx - complex structure in the source.

4.2 Image Measurements

4.2.1 Core Flux

The core flux at 6cm is listed in column (4) and the core luminosities at both 20 and 6cm calculated using equation 4.3 are listed in columns (5) and (6). Where possible the fluxes were measured by fitting a two-dimensional Gaussian to the core component, using the AIPS software. This fit provided

Table 4.1 Principal properties of new sample

1	2	3	4	5	6	7	8	9	10	11	12	13	14	15	16	17	18
Name	z	Type	$S6_c$ (mJy)	$P20_c$ $\log_{10}(W/Hz)$	$P6_c$ $\log_{10}(W/Hz)$	α_{core}	$P20_{l1}$ ---	$P6_{l1}$ $\log_{10}(W/Hz)$	$P20_{l2}$ $\log_{10}(W/Hz)$	$P6_{l2}$ ---	D1 (kpc)	D2 (kpc)	Angle (deg)	M_V	FC 20cm	FC 6cm	Comment
0003+158/4C15.01	0.450	T	125	25.31	25.45	0.28	26.0	25.5	25.5	25.0	62	72	8	-24.5	0.10	0.37	
0007+332/4C33.01	0.743	T	3:	24.28	24.28	0.00	26.0	25.5	26.0	25.0	175	203	2	-23.2	0.01	0.02	
0044+030/PKS	0.624	T	23	25.08	25.01	-0.13		24.5	25.5	24.5	17	36	7	-25.8	0.17:	0.59:	A:,*,Cpx
0056-001/4C-00.06	0.717	C	1510	27.16	26.95	-0.39								-24.7	0.98	0.99	Cal
0114+074/4C07.04	0.861	C	165	25.68	26.16	0.94								-24.4	1.00:	0.98:	†,V
0118+034/4C03.02	0.765	T	26	25.31	25.25	-0.12	27.0	25.5	26.0	25.0	104	107	11	-24.1	0.03	0.09	†
0133+207/3CR47	0.425	T	70	25.04	25.15	0.20	26.0	25.5	26.5	26.0	116	141	4	-22.7	0.02	0.06	
0134+329/3CR48	0.367	CE	<3770	<27.3	<26.8	(-1.1)								-24.2	0.93:	0.67:	ECE
0159-117/3C57	0.670	T	845	<27.0	26.64	(-0.7)		26.5		25.0	7	65	23	-25.6	0.66	0.64	†
0219+428/3C66A	0.440	CL	<418	<26.1	<26.0	(-0.4)	25.5	25.5			16			-25.4	0.54	0.42	*,J:
0222+000/PKS	0.523	CE	<86	<25.9	<25.4	(-0.9)								-22.3	0.88:	0.89:	
0222-008/4C-00.12	0.687	T		24.80			27.0		26.5		30	34	13	-23.1	0.01		†, S
0300-004/4C-00.14	0.693	T	36	25.04	25.30	0.50	26.5	26.0	26.0	26.0	17	22	14	-23.8	0.02	0.08	S,J:
0310+013/OE+017	0.660	CL	566	<26.3	26.45	(0.3)					7				0.86	0.96	V
0336-019/OE-063	0.852	CL	1910	27.25	27.21	-0.06	25.5				26			-24.0	0.90	0.97	V
0340+048/3CR93	0.357	T	4		23.75		26.5	25.0	26.5	25.5	53	60	11	-21.1	0.004	0.02:	S,A:
0349-146/3C95	0.614	T	45	25.18	25.29	0.21	27.0	26.0	26.5	26.0	254	271	7	-25.5	0.01	0.06	S:,A:
0429+415/3CR119	0.408	C	3660	27.19	26.83	-0.71								-20.7	0.98	0.96	
0440-003/OF-067	0.844	T	1260	<27.1	27.02	(-0.1)		25.5		26.0	4	5	15:	-23.2	0.50	0.47	V,ECE?
0518+165/3CR138	0.759	CE	<2710	<27.7	<27.3	(-0.9)								-23.4	0.89:	0.65:	
0534-201/MC 1	0.995	T	177	25.89	26.37	0.85	25.5	25.0	25.5	25.0	28	34	13	-23.4	0.38:	0.88:	
0704+384/4C38.20	0.579	T	61	25.27	25.36	0.18	26.0	25.0	26.5	25.5	48	52	3	-24.0	0.06	0.23	S,A:
0738+313/OI+363	0.630	C		26.95										-24.8	0.99		
0805+579/4C57.15	0.438	T	26	24.58	24.74	0.31					46	52	2	-21.8	0.01	0.09	†
0810+327/B2	0.842	T	140		26.06			25.0		25.0	43	90	12	-24.4		0.64	
0812+020/4C02.23	0.402	CL	196	25.41	25.54	0.26	26.5	26.0			37			-23.5	0.08	0.25	†,J
0821+447/4C44.17	0.904	T		25.07			26.0		26.5		66	68	8	-24.5	0.02		
0827+193/4C19.30	0.658	T	8	24.65	24.60	-0.10	26.0	25.5	26.0	25.0	48	61	6	-23.9	0.02:	0.05:	V,S:,A:
0827+243/OJ+248	0.939	CL	861	26.81	26.95	0.29	26.0	25.0			43			-25.0	0.66	0.92	
0833+276/OJ+256	0.765	C	258	26.07	26.25	0.34									0.96	0.99	V
0903+169/3CR215	0.411	T	18	24.23	24.53	0.59					79	79	18	-22.4	0.01	0.04	†, Cpx

Table 4.1: Principal properties of the new sample

Table 4.1 continued

1	2	3	4	5	6	7	8	9	10	11	12	13	14	15	16	17	18
Name	z	Type	$S6_c$ (mJy)	$P20_c$ $\log_{10}(W/Hz)$	$P6_c$	α_{core}	$P20_{11}$ ---	$P6_{11}$ $\log_{10}(W/Hz)$	$P20_{12}$	$P6_{12}$ ---	D1 (kpc)	D2 (kpc)	Angle (deg)	M_V	FC 20cm	FC 6cm	Comment
0920+313/B2	0.892	CL	177:	<26.0	26.22	(0.1)		25.5			8			-24.6	0.45:	0.80:	V,CE
0932+023/4C02.27	0.659	T	62	25.69	25.49	-0.39	26.0	25.5	26.5		31	188	6	-24.5	0.12	0.19	†
0937+391/4C39.27	0.618	T	5	24.3:	24.34	0.00	26.0	25.0	26.0	25.0	109	127	2	-23.7	0.01	0.03	S,A:,J
0953+254/OK+290	0.712	CL	586	26.41	26.54	0.24	24.5				62			-24.8	0.85	0.99	V,CE,Cal
0957+003/4C00.34	0.907	T	77	25.82	25.87	0.10	26.5	26.0	26.5	26.0	71	100	21	-25.0	0.07	0.23	†,J
1012+488/4C48.28	0.385	T		23.5:			25.5		25.0		190	196	7	-21.5	0.004		†
1015+277/4C27.21	0.469	T	14	24.59	24.54	-0.11	26.5	26.0	25.5	25.0	40	45	0	-23.5	0.01	0.03	S:
1022+194/4C19.34	0.828	T	581	26.59	26.67	0.16					22:	37:	0:	-24.8	0.68	0.89	†, V,S,CE,*
1038+528/OL+564	0.677	T	391	26.18	26.31	0.26	25.5		25.5	24.0	89	96	22	-24.4	0.65:	0.95:	J
1047+096/4C09.37	0.786	CL	14		25.00		26.5	25.5			37			-24.3		0.11	†
1104+167/4C16.30	0.634	T	388	26.09	26.25	0.32	26.0		26.0		93	95	4	-26.1	0.27	0.63	†,J
1118+128/4C12.40	0.685	T	7	24.5:	24.58	-0.13	26.0	25.5	25.5	24.5	43	64	30	-24.0	0.02	0.09	†
1130+106/4C10.33	0.540	T	115		25.58			25.5		25.5	10	10	69	-23.9		0.31	†,S,V,Cpx,J:
1146+111/MC 2	0.863	T	4	24.5:	24.55	0.24	26.0		25.5		41	46	10	-25.4	0.02	0.07	†, S
1151+102/MC 2	0.895	C	260	26.19	26.39	0.40								-23.5	0.90:	1.00:	V
1156+631/4C63.15	0.594	T	13	24.60	24.72	0.22	26.5	25.5	26.0	25.0	115	154	6	-24.8	0.01	0.05	
1157+118/MC 2	0.731	T	11	24.4:	24.83	0.85	25.5	25.0	26.0	25.5	33	89	3	-23.1	0.02	0.18	†
1222+216/4C21.35	0.435	T	480	26.02	26.00	-0.04	25.5		26.0	26.0	34	40	65	-23.3	0.34	0.63	†,J
1233+108/MC 2	0.665	T	8:	24.18	24.61	0.83	25.5	25.0	25.5		197	275	1	-23.4	0.01	0.16	
1252+119/ON+187	0.870	CL	683	26.91	26.79	-0.24	25.5				38			-25.8	0.93:	1.00:	V,Cal
1253+104/MC 2	0.824	T	21	25.41	25.22	-0.36	26.0	25.5	25.5	25.5	61	66	24	-24.3	0.09	0.17	†
1258+287/5C4.105	0.645	C	177	25.92	25.96	0.01								-23.9	0.97:	0.93:	V
1335-061/4C-06.35	0.625	T	10		24.65		27.0	26.5	27.0	26.5	23	29	13	-24.1		0.01	†,Cpx
1340+289/B 2	0.905	CL	141	26.14	26.14	-0.01		25.5			11			-25.5	0.47	0.74	ECE
1352-203/MC	0.627	T		23.4:			24.5		25.0		36	41	3	-21.9	0.01:		
1415+172/OQ+125	0.821	T	18		25.15			25.5		26.0	13	25	71	-24.3		0.11	†,S,*,Cpx,J:
1420+326/OQ+334	0.685	T	368	26.26	26.30	0.07	25.5	25.5	25.5		33	114	16	-24.5	0.61:	0.88:	V
1423+242/4C24.31	0.649	T	59	25.59	25.45	-0.26	26.5	26.0	26.5	26.0	45	53	28	-24.7	0.05	0.13	†
1442+117/MC 2	0.851	T	73	25.64	25.80	0.30	25.5	25.5	26.0	25.5	21	59	10	-24.4	0.19	0.56	†
1458+718/3C309.1	0.905	T	2031:	<27.7	27.30	(-0.8)		26.5		26.5	5	6	34	-25.8	0.60	0.54	CE,Cpx
1509+158/4C15.45	0.828	T	125		26.00			26.0	26.5	26.5	10	39	48	-24.1		0.24	†, V,J

Table 4.1 concluded

1	2	3	4	5	6	7	8	9	10	11	12	13	14	15	16	17	18
Name	z	Type	$S6_c$ (mJy)	$P20_c$ $\log_{10}(W/Hz)$	$P6_c$	α_{core}	$P20_{11}$ ---	$P6_{11}$ $\log_{10}(W/Hz)$	$P20_{12}$	$P6_{12}$ ---	D1 (kpc)	D2 (kpc)	Angle (deg)	M_V	FC 20cm	FC 6cm	Comment
1510-089/OR-017	0.361	CL	1492	26.49	26.33	-0.17		25.0			29			-23.8	0.93:	0.93:	V
1522+155/MC 3	0.628	T	316	26.18	26.15	-0.05	25.0		25.0		36	57	4	-24.3	0.72	0.93	
1530+137/4C13.55	0.771	T	34	25.22	25.37	0.29	26.5	26.0	26.5	26.0	23	36	29	-23.5	0.02	0.09	†
1540+110/MC 2	0.992	T	30	25.47	25.55	0.15	26.0	25.5	26.0	26.0	97	108	1	-22.8	0.10	0.38	†
1548+114/4C11.50	0.436	T	414	25.51	25.94	0.84	25.5		25.0		88	104	58	-23.6	0.31	0.99	†,J:
1606+180/4C18.47	0.346	T	15	24.23	24.30	0.12	25.5	25.5	25.0	24.5	18	24	7	-22.2	0.01	0.07	†
1618+177/3CR334	0.555	T	133	25.76	25.67	-0.19	26.5	25.0	26.5	25.5	75	123	4	-25.0	0.08	0.23	†
1623+173	0.552	T	9::	24.38	24.5:	0.21	26.0	25.0	25.5	25.0	60	76	2	-22.4	0.01	0.05	†
1637+574/OS+562	0.750	CE	1360	26.89	26.95	0.11								-25.2	0.88:	0.94:	V,Cal
1657+265/4C26.51	0.795	CL	437	26.2:	26.51	0.55		25.5			17			-24.3	0.33	0.87	†, V,ECE
1704+608/3CR351	0.371	T	6::	24.44	24.0:	-0.93	26.5	26.0	25.5		92	104	5	-25.1	0.005	0.005	
1725+107/MC 2	0.833	CL	85	<26.5	25.84	(-1.3)		25.5			5			-23.1	1.00	0.69	†
1741+279/4C27.38	0.372	T	<142	<25.7	<25.3	(-0.8)	25.0	24.5	25.0	25.5	16	19	26	-22.7	0.41	0.32	†,V,CE,J
1819+408/4C40.37	0.733	CE	169		26.02						3			-24.1		0.77	
1830+285/4C28.45	0.594	T	496	26.09	26.30	0.40	26.5	26.0	26.0	25.5	64	65	20	-24.6	0.17	0.46	†
2005-044/3C407	0.589	T	142	25.70	25.75	0.10	26.5	26.0	26.0	25.5	31	58	10	-23.6	0.13	0.36	V,J
2044-027/3C422	0.942	CE	510:	<27.3	26.73	(-1.1)								-23.2	0.80	0.55	V
2112+172/4C17.86	0.878	T	<60	<26.4	<25.7	(-1.2)		25.0		25.5	12	23	60	-23.8	0.49	0.40	†, V
2142+110/MC 2	0.550	CL	367	25.83	26.10	0.50					138			-22.4	1.00	1.00	†, V
2154+100/MC 2	0.761	C	363	26.23	26.39	0.32								-23.2	0.96:	1.00:	V
2209+080 /4C08.64	0.484	T	225	<26.0	25.77	(-0.4)	26.0	25.5	26.0	26.0	15	27	15	-23.1	0.20	0.21	†,A:,CE,J
2234+282/B 2	0.795	C	1630	26.90	27.08	0.35								-23.3	1.00:	1.00:	V
2251+113/4C11.72	0.323	T	18	<24.4	24.31	(-0.2)	26.0	25.5	25.5	25.5	12	20	1	-24.3	0.02	0.03	†
2251+134/4C13.85	0.677	T	598	26.1:	26.50	0.72	26.5	26.0	26.5	26.0	11	20	9	-22.8	0.15	0.70	†, V,S,A:,J
2314-116/PKS	0.549	T	91	25.44	25.49	0.10	25.5		25.5	25.0	63	97	17	-23.9	0.32	0.51	A,J
2325+269/3C463	0.875	T	48	25.2:	25.64	0.83	26.5	26.0	27.0	26.5	19	20	5	-25.0	0.01	0.10	S,A:
2344+092/4C09.74	0.677	C	1520	26.96	26.90	-0.12								-26.0	0.97:	0.97:	V
2349+327/4C32.69	0.659	T	21	24.87	25.02	0.28	26.5	25.5	26.0	25.5	119	158	15	-23.4	0.03	0.08	J
2353+283/4C28.59	0.731	T	52	25.57	25.51	-0.12	25.5	25.5	26.5	26.0	20	28	59	-24.3	0.08:	0.19	†,V,J:

See text for detailed explanation of columns.

the peak flux, by interpolating between pixels, as well as the integrated flux of the core component. Since most cores were unresolved, the integrated and peak fluxes were the same and the core flux was estimated using the peak value. For core components that were resolved, (*e.g.* 0134+329; 6cm) the peak flux overestimated the core flux, so the fluxes for these sources are designated as upper limits in table 4.1. Whenever a two dimensional Gaussian could not be fit to a core, due to an asymmetric background (*e.g.* 0219+428) or it being a HUC source, the peak flux of the core was determined either by extrapolating the contours or by printing the pixel values of the core region. The core flux can also be read off the *u-v* plot, as mentioned in section 3.2. For sources where the core is surrounded by emission, (*e.g.* 0044+030; 20cm), the background level was estimated and subtracted from the measured core flux. The core fluxes that are known to be unreliable are tagged with colons in table 4.1.

The 2-D Gaussian fits also deconvolved the CLEAN beam from the core component, thereby providing size and orientation information on the resolved core. For the sources where the map centre needed to be shifted (see table 3.1; column 7), the expected effect of bandwidth smearing (section 3.2) on the size and orientation agreed with the apparently-resolved component. In such cases the extended nature of the core component was due to the bandwidth smearing, so the integrated flux of the smeared core was used for the core flux.

Core flux measurements in most cases are quite simple and reliable. As pointed out above, extended emission around the core and the core being resolved are the major problems in the actual measurements (being more troublesome at 20cm than 6cm). A further problem in using the core component as a measure of quasar luminosity, is that cores are known to be variable. While not all radio cores are variable, some are highly variable, so a single flux measurement is not necessarily indicative of the average core flux. Sources that displayed signs of variability are noted in column (18)

of table 4.1 and the method for detecting variability is discussed in section 4.3.1. The only way around this problem is monitoring the source, which could probably be done with a single antenna, assuming that only the core component is variable. While the variability and measuring of the core flux present problems, it still represents the best measure of the current nuclear activity in a quasar.

4.2.2 Core Spectral Index

The core spectral index, α_{core} in column (7), was determined by fitting a power law relation, of the form $S \sim \nu^\alpha$, to the 6 and 20cm core fluxes. Since the large-scale structure was sampled differently at the two wavelengths, the spectral index can only be determined for unresolved sources. The problems outlined in determining the core flux are the main source of error in the spectral indices as well. Cores that have upper limits on their fluxes generally show steeper spectral indices that are typical of extended diffuse emission. Variability does not affect the sources that we observed at both wavelengths, but for the HVO sources the spectral indices may be unreliable since ~ 4 years elapsed between the two observations.

4.2.3 Lobe Flux

Lobe flux measurements are presented in columns (8) and (9) for the lobe closest to the core, and (10) and (11) for the further lobe, with the 20cm values being listed first in each case. They are measured using the AIPS software, by placing a box around the desired component and integrating the flux within the enclosed region. Lobe fluxes contain all the emission on the given side of the source, including jets and bridges that may connect directly to the core. The lobe fluxes are not determined very accurately and so are rounded off to the nearest .5 in the log or to a factor of three. The main problem is the incomplete sampling of the large-scale

structure with the A array and in many cases a large fraction ($>50\%$ in some cases) of the flux was not detected (see column 6 of table 3.2), as determined by the techniques outlined in section 4.3. While the amount of flux missing in each image was estimated, this does not provide information on where the missing flux belongs and cannot, in general, differentiate between missing flux and variable emission. The incomplete sampling makes it difficult to decide what features are ‘real’, and it can create spurious large-scale patterns in the background of these *snapshot* images. There was a tendency for integrated flux to increase as the box size increased even though no more ‘real’ emission was being included.

4.2.4 Core-Lobe Distances

The core-lobe distances (in kpc) are listed in columns (12) and (13) as D1 and D2, where D1 refers to the lobe closer to the core. The angular displacements of the lobe peaks from the core were measured directly from the final images and converted to linear sizes using the angular distance defined in equation 4.2. The peaks in the lobes were used since they are easily defined and provided a consistent measuring criterion. Using the peak minimizes the sensitivity dependence in the measurement of size, since as long as a lobe is detected the lobe peak can be identified, whereas the size of the source may increase with sensitivity. In the luminosity range of the sources studied here the brightest point in the lobe is usually at the far end of the lobe and therefore provides a good measure of the full extent of the lobe (*e.g.* 0827+193). In *edge-darkened* sources the lobes extend beyond the lobe peak, so the measurements must be interpreted with this in mind. This technique was checked by remeasuring the HUC sources and finding good agreement with their measurements, where they fit parabolas to each lobe to define the positions. The use of core-lobe distances instead of lobe-lobe distance allows the T and CL sources to be compared directly and it

prevents the triple sizes from being bending-angle dependent.

4.2.5 Bending Angle

The bending angle of a triple source, listed in column (14), is defined as the angular displacement from collinear of the two lobes and the core. The measurements, made from the final images using the core and lobe peaks, are quite accurate and agree well with the values determined by H_{UO}. A possible problem is the position of the peak with respect to the rest of the lobe emission, where the hotspot may not be central in the lobe.

4.3 Other Measurements

4.3.1 Total Flux

The total flux is an important measurement that does not appear explicitly in table 4.1, but was necessary in determining the core fraction, f_c , which is the ratio of the core flux to the total flux, given in columns (16) and (17). It is also necessary in determining the variability (column (18)) and the percentage of missing flux in each image (column 6 of table 3.2). To determine the total flux the Dixon catalogue of radio sources (Dixon 1985) was searched for flux measurements at all wavelengths, for each source. It is believed that the observations contained in this catalogue are mostly made with a single antenna or short-baseline interferometer and provide a reasonable estimate of the total flux. The fluxes were then plotted against frequency (figure 4.1) and a straight line was hand drawn through the points to interpolate the total flux at 6 and 20cm. The number of Dixon fluxes per source varied between 1 and 20, with an average of about 5 and with the brighter sources generally having more measurements. The plots were quite diverse, ranging from a large number of points in a tight power law with $\alpha \sim -0.7$ (e.g. the right hand plot of figure 4.1), to sources with

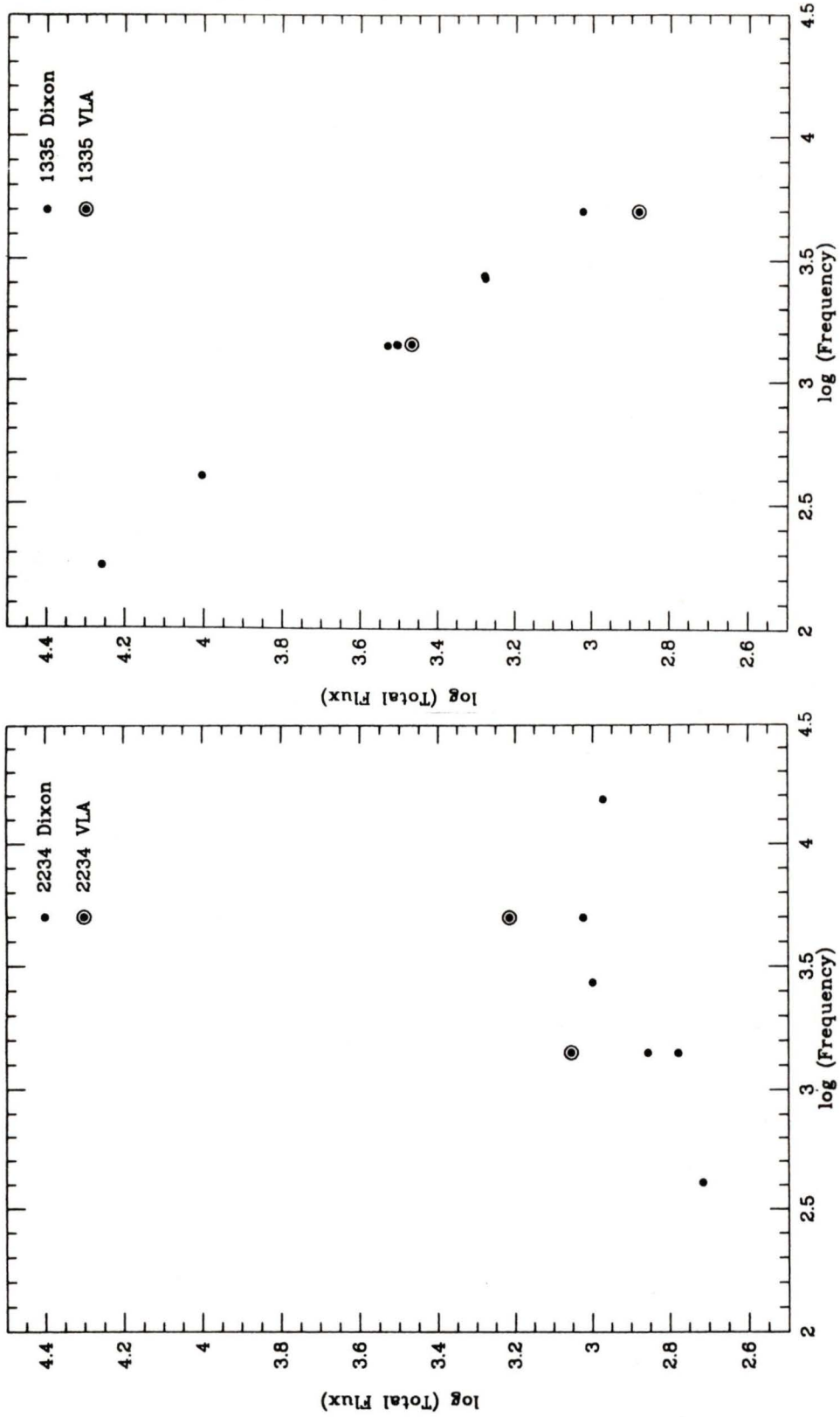


Figure 4.1: Total Fluxes from the Dixon Catalogue vs. Frequency

points scattered about a roughly horizontal line (*e.g.* the left hand plot of figure 4.1). In most cases the plots were well behaved enough to estimate the total flux of the source at both 20 and 6 cm. Extra flux measurements at 6 and 11 cm found in the V-V catalogue were also added to the plots and proved to be especially useful for sources where there were only a few measurements in the Dixon catalogue.

The total CLEAN flux measured by the VLA was also placed on the plots (the circled points in figure 4.1). In general the VLA data points fell below the total flux values (right hand plot) and allowed the fraction of the total flux missing from the VLA images to be estimated. Knowing the amount of missing flux can be helpful in deciding whether faint large-scale features in an image are ‘real’ or not. In the instances where the VLA measured more flux than the total flux power law (left plot of figure 4.1), these sources were assumed to be variable (denoted by V in column (18)). Detecting variability in this manner finds only those sources whose flux has increased and it can be estimated that at least twice as many variable sources exist in the sample, since sources that have become fainter cannot be distinguished from those with missing flux. The amount of scatter in the plots was also used to identify possible variable sources. However, this technique has limitations since the points on the plot were obtained with many different telescopes of different beam sizes which may have either sampled the source differently or included flux from confusing sources.

To do a proper job of getting the fraction of the flux in the core and the percentage of the flux that is missed by the VLA, single dish observations at 6 and 20 cm should be obtained simultaneously. This would eliminate having to deal the variability of the sources and allow a *zero-spacing* flux to be added to the *u-v* data for better images.

4.3.2 Absolute Magnitude

Absolute magnitudes in column (15) were calculated by J.B Hutchings using V band apparent magnitudes from HB and V-V and the cosmology presented at the beginning of the chapter.

Chapter 5

Alternating Ejection

5.1 Introduction

With the data base presented in table 4.1 of the preceding chapter the main properties of the radio structure of the quasar sample can be examined. A more comprehensive analysis of the data is presented in HPG, where an evolutionary scenario is developed. The analysis in this thesis compares the basic radio properties with predictions of two simple source models. In this way trends in the data that are consistent with each model can be recognized and counter examples can be identified. The mere consistency nature of the tests and the examples of counter evidence demonstrate that neither of these simple models can account for all the observed characteristics present in radio quasars. During the analysis it is important to remember that the sample was chosen only to fill the redshift/luminosity plane uniformly (see figure 1.1), so no previous knowledge of the source structure was available.

The two models examined in this thesis are alternating ejection and relativistic beaming. Both are very basic models that attempt to explain the asymmetric nature of the large-scale structure found in radio quasars. The alternating-ejection model produces asymmetries by having a central engine that ejects material on only one side of the core at a time and switches sides on which the ejection occurs (see for example RE). The

relativistic-beaming model has material leaving the core on both sides simultaneously, but at relativistic speeds so that the material ejected on the side approaching the observer appears brighter and further from the core than the material ejected on the receding side (see for example Scheuer and Readhead, 1979). Each of these models in its purest form produces distinct morphology that is observed in only a few sources, so the sample as a whole must be studied to discern whether the models play an important role or not. While it seems unlikely that the observations will fit either of these highly idealized models, reasonable agreement with either model may help determine whether the speed of the large-scale structures is relativistic or not. This remains a very fundamental problem in the large-scale structure of radio quasars (Owen 1986, Bridle and Perley 1984). This chapter outlines the basic model of alternating ejection, checks for consistency with the sample and discusses the implications of the model. Chapter 6 deals with the relativistic-beaming model in a similar fashion.

5.2 The Alternating Ejection Model

The alternating-ejection model is used to explain the side to side asymmetries in the radio structure of powerful extragalactic radio sources. It suggests that the asymmetry is produced by a source ejecting material (non-relativistically) on only one side of the core at a time. Assuming the material travels at similar speeds on either side of the core, the morphology produced by such a model would have emission at different distances from the core on either side. In the next section a number of tests will be described to test this hypothesis. The sample will be examined individually for side-to-side asymmetry in the positions of the lobe peaks, as well as in the extended features of the lobe emission. The distribution of the ratio of lobe lengths will also be examined for consistency with the model. And in a third test, the distribution of differences in the lobe lengths of the

triples will be compared with the distribution of the CL lobe lengths. The one-sidedness of jets is also consistent with the alternating model and may provide insight into the speed at which material is transported in the jets relative to the lobe speed.

5.3 Tests for the Alternating-Ejection Model

5.3.1 Visual Evidence

Evidence for alternating ejection can manifest itself in both individual sources and the overall properties of the sample. In this subsection, structures contained in individual sources are examined for side to side asymmetries that are suggestive of alternating ejection. The techniques used are simple. The structure on one side of the lobe is sketched and then rotated or reflected about the core, depending on the source symmetry, and the amount of overlap is determined, as well as any systematic patterns. By examining all the triple sources it was found that the brightest lobe features on either side of the core are generally not at the same distance from the core (*ie.* they display *avoidance*). In roughly half the sources when the two lobes were overlaid there was no overlap of structure at all. This shows the basic asymmetry present in the large-scale radio structure of quasars in contrast to the simple symmetry seen in the early low-resolution images. In this determination of asymmetry the lobe sizes, shapes, and brightnesses were not considered, only whether or not the lobe emission was at the same distance from the core.

The next step in looking for alternating ejection was to search for sources whose emission alternates sides with increasing distance from the core. In fact the discovery of such sources was a major incentive for the development of the alternating ejection model, and examples are presented by RE and Robson (1981). In the model, material is ejected on alternating sides with roughly the same velocity so that the distance of the features from the core

reflects the time at which they were ejected, with the most recent ejections being closest to the core. The sources with traceable emission between the core and the lobes have been examined for such structure and have been tagged with an 'A' in column 18 of table 4.1; questionable examples are tagged with an 'A:'. None of these are extremely convincing but one good example is 2314-116.

If all the possible examples of this phenomenon are included, it appears as though a rather large fraction of the sample could be deemed as having alternating structure. (This is surprising since alternating ejection is an idealized model and it is unreasonable to expect to find perfect examples of the alternating structure in observations, especially considering how easily an inhomogeneous IGM could destroy the the alternating pattern.) On the other hand, counter examples exist where the structure is very symmetric about the core (*e.g.* 0704+384) and some others contain small, isolated lobes at large distances from the core which exhibit no sign of continuous alternating ejection (*e.g.* 0007+332). Furthermore, jets are generally fairly long and continuous, in some cases extending all the way from core to lobe (*e.g.* 2209+080), and in no case does the jet structure alternate sides.

This subsection has presented radio quasars as being fairly unsymmetric, but the structure does not necessarily alternate neatly from side to side.

5.3.2 The Lobe-Length Ratio Test

While the previous subsection examined individual sources for evidence of alternating ejection, the next two subsections look at properties of the entire sample to check for consistency with the ejection model. Plotted in figure 5.1 is a histogram of the ratio of core-lobe distances, D_1/D_2 , for all sources (including GH quasars). The data are from columns 12 and 13 of table 4.1 and since by definition D_1 is the shorter lobe, the ratio is

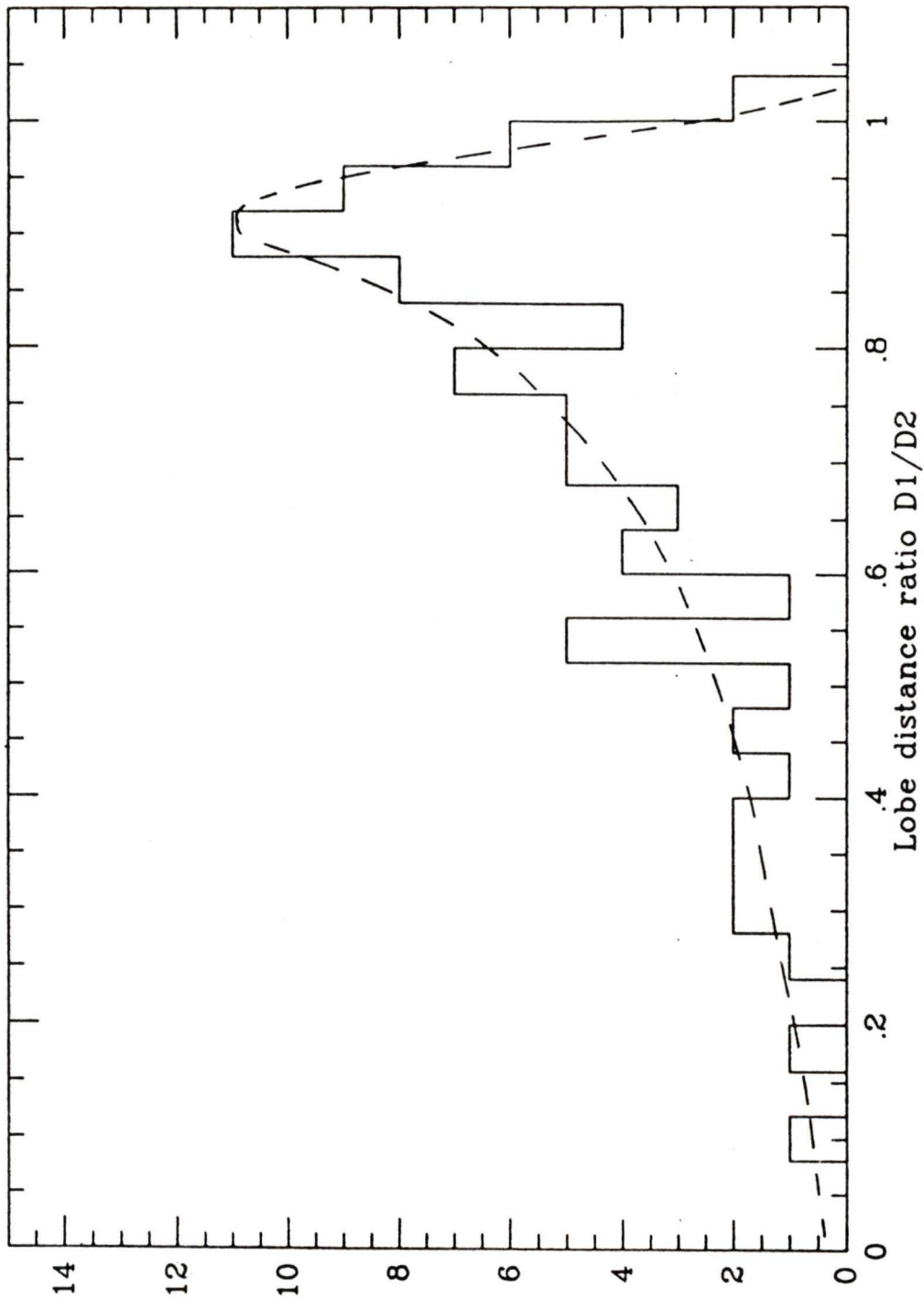


Figure 5.1: Histogram of Core-Lobe Distance Ratios with Alternating Ejection Model

always less than or equal to 1. There is a definite dip in the histogram at 1, where sources with equal lobe lengths would be found. The existence of this dip has been disputed in the literature, where Longair and Riley (1979), Ingham and Morrison (1975) and RE have observed a dip, and Kapahi and Saikia (1982) and Ensman and Ulvestad (1984;EU) did not detect such a dip. In most cases these samples were smaller than the present sample and of lower resolution so the arm lengths obtained are less accurate. The EU data set used the HUU 20cm images and half of their sample is contained within our sample. In most cases our 6cm images enabled us to obtain more accurate arm lengths than could be measured from the HUU images, as our images have higher resolution and less obscuring large-scale structure. The histogram has a peak at .9 implying that it is most common for quasars to have a 10% difference in lobe lengths. Lower resolution images would smear this peak and possibly fill in the dip.

A simple model of alternating ejection is shown with a dashed line on figure 5.1 and seems to fit this distribution rather well. Other models such as light-travel-time effects, random distribution of arm lengths, and Gaussian distribution of arm lengths were found not to fit the observed distribution (see RE and EU). Details of the alternating-ejection model are discussed in RE and EU. The model assumes that the speed of all radio emitting material in a given quasar is the same, so that the distance of a lobe from the core is proportional to its age. The number distribution of source ages was assumed to decrease exponentially with age and the only free parameter in fitting the data was the number of reversals of the ejection direction. In figure 5.1, the central engine has reversed sides 6 times for a characteristic source and this simple model provides a remarkably good fit.

The histogram in figure 5.1 only contains data for the triple sources, as it plots the ratio of the arm lengths. However, knowledge of the number of reversals (6 in the best fitting model) and the distribution of source ages

allows the prediction of the number of sources that have not yet reversed sides (*ie.* CL sources); for 6 reversals the model predicts 15% of the sources should be one-sided. In our sample 17% of the sources with extended structure are CL types, in good agreement with the prediction, giving additional support to the alternating-ejection hypothesis. Following the model further, the core sources are sources that have not begun to form lobes and the CE sources are just sprouting their first lobes.

5.3.3 Core-Lobe Lengths

More evidence for alternating ejection can be seen upon further examination of the core-lobe distances. Figure 5.2 plots (upper histogram) histograms of the difference between the lobe lengths ($D_2 - D_1$) of the triple sources and the lobe lengths for the CL sources (lower histogram).

In the alternating-ejection model the difference in the lobe lengths of the triple sources reflects the size of the source when ejection began on the second side. This is because the model assumes that the ejection velocities are the same on either side of the core and remain roughly constant, thereby preserving the initial lobe-length difference when the second lobe is born. Figure 5.2 shows that for the CL sources all but three are smaller than 45 kpc and ninety percent of the triple sources have lobe-length differences of 45 kpc or less. These distributions are consistent with the alternating-ejection model and suggest that the initial side reversal occurs before the sources reach 45 kpc.

5.4 Summary and Problems

The last section has presented interesting evidence in favour of the alternating-ejection model. The most convincing evidence for the model is: 1) the one-sided nature of jets, 2) the lobe-ratio test and 3) the lobe-length difference histogram. However, in the search for sources where emission

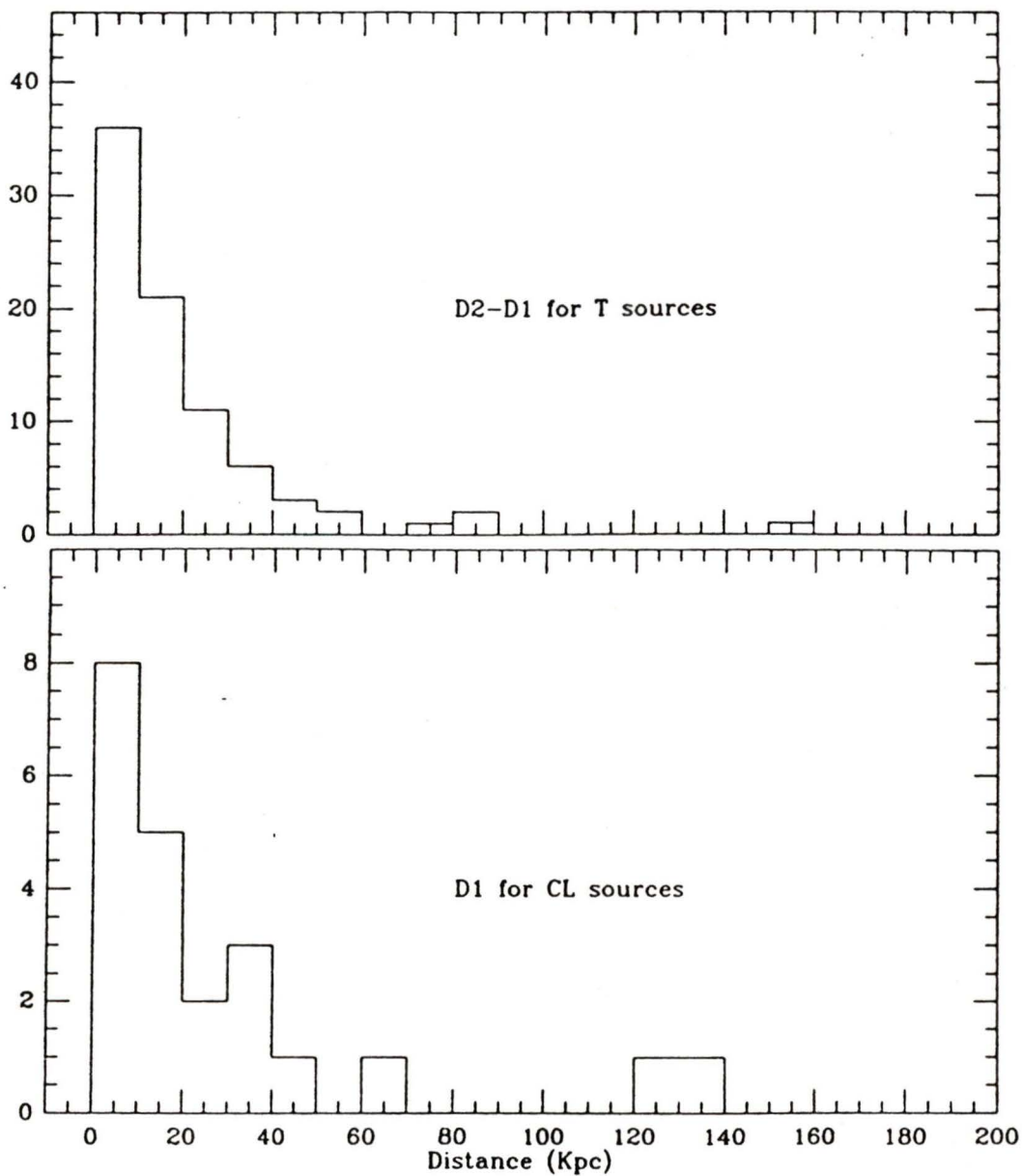


Figure 5.2: Difference in Lobe Lengths of Triples(upper) and CL sizes (lower)

alternates from side to side as the distance from the core increases, only weak evidence is found, as well as some counter examples. This implies that the lobe peaks seem to show signs of alternating ejection, yet the material between the core and peak in general does not. It is possible that the lobes in a given quasar are formed at different times, but move outward with roughly the same velocity on each side, thereby preserving their initial length difference. The material moving toward the lobes, along jets, may be travelling at higher velocities and so jets may extend all the way from the core to the lobes and not be expected to show side-to-side avoidance, yet only be seen on one side at a time. Jets could then energize a lobe upon hitting the hotspot and convert most of their kinetic energy into local turbulence and radiation rather than increasing the lobe's outward motion. From the above analysis this appears to be the most plausible scheme for an alternating-ejection model.

Lastly, a few of the problems with the alternating-ejection model should be mentioned. Theoretically it has not yet been possible to produce a central engine that can alternate the sides on which it ejects material and most theoreticians concentrate on symmetrical models (see RE). Inhomogeneities in the IGM that surround extended radio sources would tend to disrupt any obvious patterns produced by a central engine that alternates sides. The constraints of roughly equal and constant velocities may be too stringent for the IGM (and the interstellar medium, through which the material also has to pass). Further, when superluminal components are seen in sources they occur on the same side of the core as the large-scale jet, which provides support for the relativistic beaming explanation of the one-sided nature of jets. A search for relativistic motion in the quasar sample is the subject of chapter 6.

Chapter 6

Relativistic Beaming

6.1 Introduction

The radio-emitting plasma associated with radio galaxies and quasars is thought to be energized in the active nuclear region and then travel outwards towards the lobes. In this chapter the various components of the radio structure are examined for signs of relativistic motion away from the nuclear or radio core region. At present no technique exists for measuring the velocities, so indirect methods must be adopted. In this chapter some basic tests are performed on the data presented in table 4.1, which attempt to identify bulk relativistic motion in the various source components.

To test for relativistic motions it is necessary to know where and when the effects should occur. When radiating material moves relativistically the radiation pattern becomes *beamed* in the direction of motion. Relativistic beaming will then enhance the emission of the approaching side of a source aligned close to the line of sight, while diminishing that of the receding side. The degree that the approaching lobe is enhanced depends on the bulk velocity, v , the angle of the motion to the line of sight, θ , and the spectral shape of the continuum, α , in the following form $(\gamma(1 - (\frac{v}{c})\cos\theta))^{\alpha-3}$, where $\gamma = (1 - (\frac{v}{c})^2)^{-\frac{1}{2}}$ (Scheuer and Readhead 1979). In this way the approaching lobe is relativistically *beamed* towards the observer.

There is also a geometrical effect since for a source with bulk relativistic motions aligned near the line of sight the observer will receive light from the approaching lobe before the receding lobe. In an intrinsically symmetric source, this causes the approaching lobe to appear further from the radio core. By incorporating these ideas into simple tests the quasar sample in this thesis can be examined for signs of relativistic motion in the extended structure.

Before presenting the results a brief review of previous work on beaming will be given. The most convincing evidence for beaming is seen in the superluminal sources (see Zensus and Pearson (1987) for an up-to-date review) where blobs of emission appear to move away from the core at speeds greater than light speed. This can be explained by having the blob ejected from the core at a small angle to the line of sight and with a velocity approaching the speed of light. While this is a possible explanation of the phenomenon, it is not the only one, and superluminal motion is being found in many cores including ones that are thought to be aligned in the plane of the sky (Barthel 1987).

Relativistic beaming in the unresolved (core) component of sources is difficult to test and there are two main approaches that have been attempted. Firstly, there is the unified scheme (Orr and Browne 1982) where all sources are assumed to transport material relativistically. In this scheme the flat-spectrum core sources are beamed towards the observer, while the steep-spectrum, extended sources are in the plane of the sky. By assuming a random distribution of alignment angles and adopting bulk velocities found in superluminal sources ($\gamma \sim 5$) the relative number of cores to extended sources can be predicted and compared with observations. Secondly, if sources have extended structure this structure may be used to determine the alignment of the source relative to the line-of-sight. Then if the core is beamed towards the observer the core fraction of the source will increase as the alignment angle decreases. This second method has been used by

Saikia (1984a) and Kapahi and Saikia (1982) and is the method used in this thesis. So far both of these methods have produced mixed results and astronomers continue to explore both methods.

Relativistic velocities in the large-scale structure have been suggested to explain the one-sided nature of jets observed in powerful extragalactic radio sources. For a source that has two lobes and only one jet it is proposed that there may be two relativistic jets, but the receding jet remains undetected while the approaching one is beamed towards the observer. Suggestive evidence for this is the continuous geometrical connection between superluminal motion and the large-scale jet in sources such as 3C120 (Walker (1985)). On the other hand, it may be that the one-sided nature of the jet structure is an intrinsic property of the source as they have often been found in very large radio sources which are thought to be in the plane of the sky as opposed to along the line of sight.

Bulk relativistic motion in the lobe structure is the simplest to test for and has been studied quite often by comparing the relative lobe lengths and brightnesses (Longair and Riley 1979, EU, RE, Saikia (1984b), Padrielli *et al.*1988). It is generally concluded that relativistic motion does not play a dominant role in determining a lobe's length or brightness. This seems to be a reasonable conclusion since in powerful sources, which have bright hotspots near the outside edge of their lobes, it is thought that the jet is being 'stopped' by the IGM and releasing its bulk motion into accelerating electrons, which then emit intense synchrotron radiation. The hotspot then may be nearly stationary and the lobe itself could contain material that is actually flowing backward towards the core and radiating isotropically without being beamed. The jets and core on the other hand are transporting material out from the central engine and the speed at these points could be very fast. Therefore, tests should be performed for relativistic velocities in the lobes, the jets, and the core separately.

6.2 The Alignment Indicators

To look for the effects of relativistic beaming in the sample sources it is necessary to have some measure of the angle at which a source is aligned to the line of sight. This section provides a detailed examination of the distribution of linear sizes and bending angles, θ (as defined in chapter 3), so that they may be used as alignment indicators. They are useful as alignment indicators since they depend on the projection of a source. The observed source size is a projection of the intrinsic source size onto the plane of the sky and so a source close to the line of sight will appear small. While it is easy to confuse large sources that have been reduced by projection with intrinsically small sources, sources that have very large observed sizes are likely to be close to the plane of the sky.

For sources close to the line of sight, the observed bending angle is likely to be much larger than the intrinsic bending angle, due to the hotspots being projected very close to the radio core. For sources in the plane of the sky, however, the observed bending angle will be more indicative of the intrinsic angle. While variations in the intrinsic bending angles may dominate the distribution, projection effects still may be important. Before using the linear sizes and bending angles as alignment indicators their dependence on redshift and core luminosity will be examined.

6.2.1 Linear Size

Throughout this chapter core-lobe distances will be used as linear size indicators as opposed to the total source size. This allows a direct comparison between the single-lobed CL sources and the double-lobed T sources (which would otherwise be very much larger). It also eliminates the dependence of T sources on their bending angles, which would greatly decrease a source's size for large bending angles. For those CL sources in which a second undetected lobe may be beyond the sensitivity of this survey this

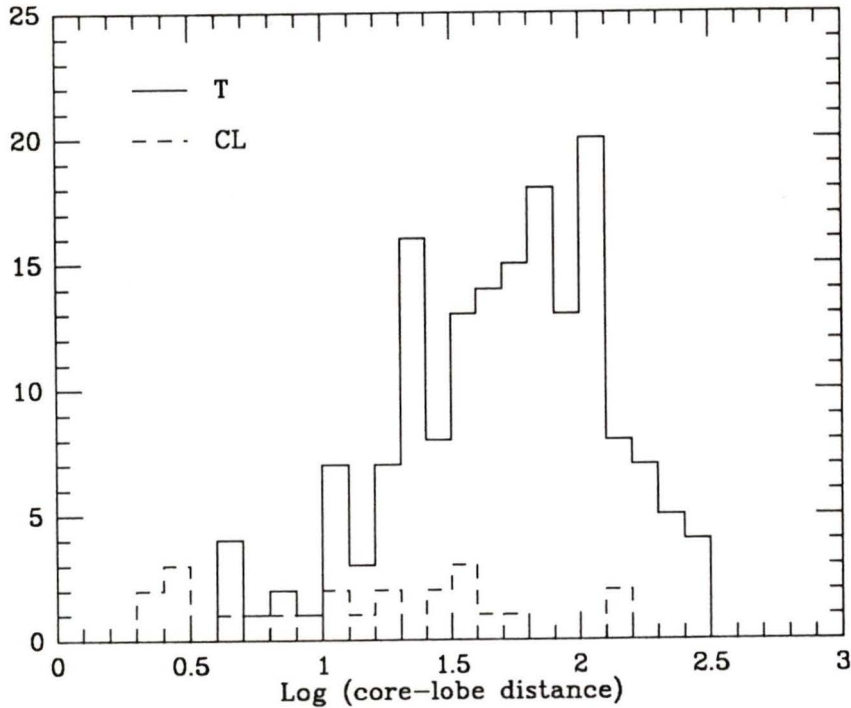


Figure 6.1: Histogram of Core-Lobe Distances

method still allows them to be compared with the triple sources.

Histograms of the projected core-lobe distances for the triple and CL sources are presented in figure 6.1. The T source histogram shows an increase in the logarithmic distribution up to ~ 120 kpc. There is then a strong decrease with very few sources larger than ~ 150 kpc. The CL source histogram contains much less data since there are fewer CL sources and each one has only one core-lobe distance measurement. The logarithmic distribution is quite flat between 2 and 50kpc and has a median value of ~ 16 kpc, roughly three times smaller than the T median of ~ 50 kpc. The spread in these distributions is not that expected from projection effects alone. There must be an intrinsic spread in source sizes, as concluded in HPG, since there are so many small sources and very few large sources.

But it is certain that projection has to play a role in determining the size in *some* sources and still can be used as an alignment indicator.

Figure 6.2a shows the distribution of core-lobe distances against redshift. The plane is filled rather uniformly, which is expected if at any given redshift there is a variety of orientations and intrinsic sizes. This produces a continuum of projected sizes, with the largest sources being the ones aligned close to plane of the sky. At redshifts larger than .8 there are no sources larger than 100 kpc, which has been interpreted by HPG as evolution with time of the source size of quasars. One may argue that this is caused by the survey being less sensitive to large-scale structure at larger z , since we observed each source with the same exposure time and hence the same flux limit, which samples to lower luminosities at lower redshifts. The method used to determine sizes of sources used the lobe hotspots (see section 4.2), so the size of the arms will not change with increasing sensitivity as it would if the overall size (defined by the lowest believable contour) was used. Using the lobe peaks to define sizes is only a function of sensitivity in the sense that weak lobes would not be detected in the sources at higher redshifts. This type of selection effect may be apparent in our sample in that the fraction of core and core-lobe sources increases with redshift.

Whether the core-lobe distance depends on core luminosity also needs to be examined. Figure 6.2b shows that for a core luminosity between $10^{23.5}$ and $10^{26.3}$ a source could have a projected size that ranges from near zero to over 200kpc. Beyond $10^{26.3}$ there are no sources larger than ~ 70 kpc. This represents a small number of sources though and is probably tied to the redshift dependence found previously, since the high redshift sources are slightly more luminous (see figure 1.2).

In summary, there are no large sources beyond $z=.8$ or among the highest core luminosity sources, but in general there is not an obvious dependence of source size on these parameters. This is fortunate since the sample

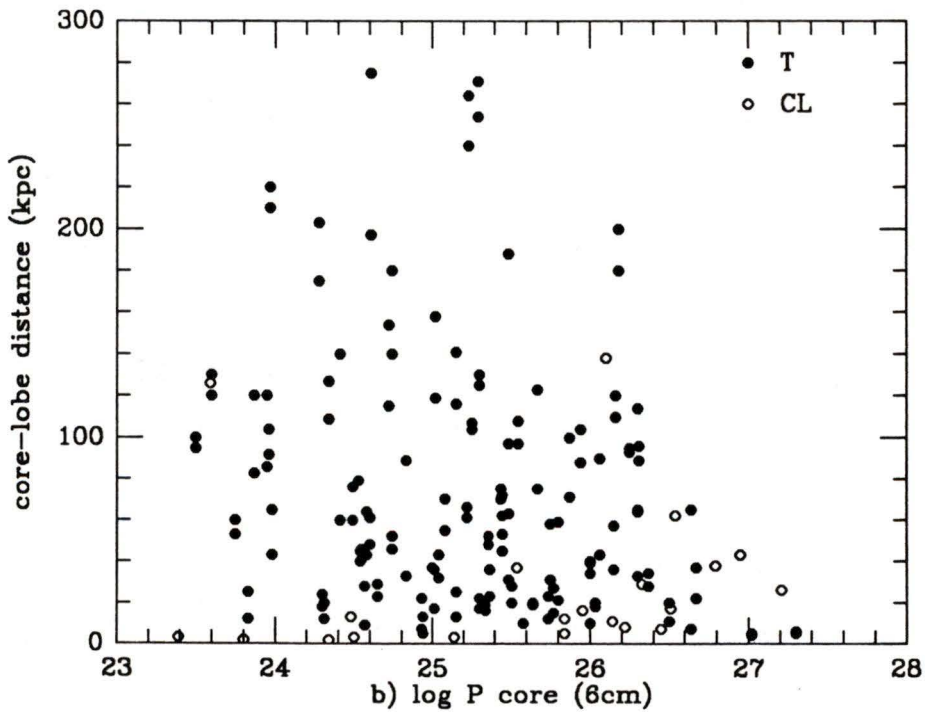
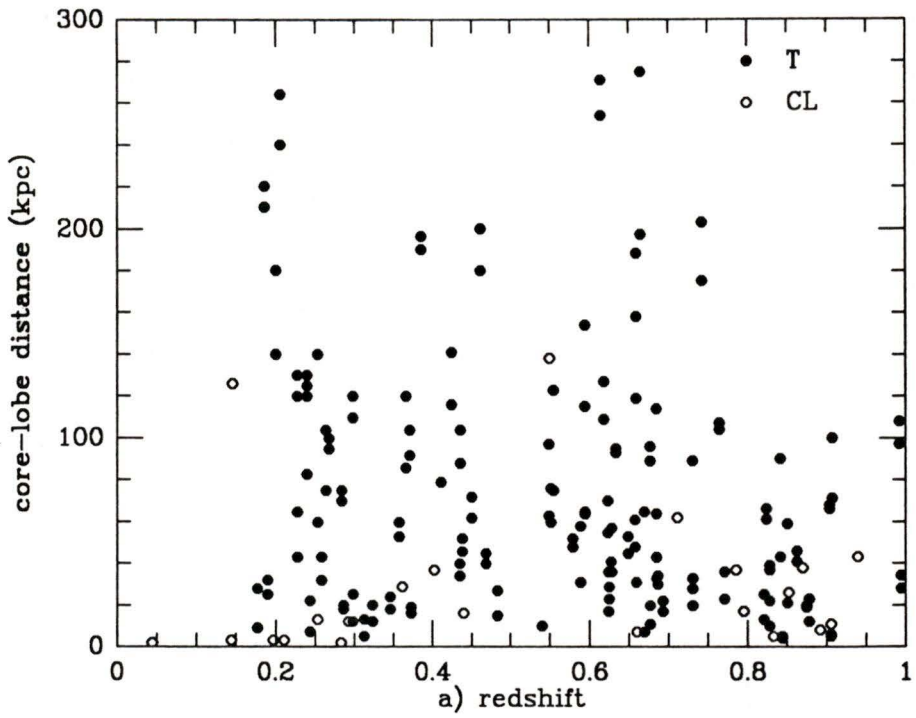


Figure 6.2: Dependence of Linear Size on a) Redshift and b) $\log P_{\text{core}}$

chosen to cover a large range of redshift and luminosity and any dependence on these parameters would hinder the use of the alignment indicators. For a randomly distributed sample whose sizes are determined only by the amount they are projected, most of the sources would be near the plane of the sky, producing a high fraction of larger sources. Such a distribution of sizes is not observed so there must be a large variation in the intrinsic source size. While this greatly fogs the use of linear size as an alignment indicator, projection effects will still play a large role in determining the size of some sources and causes part of the spread in figure 6.2.

6.2.2 Bending Angle

The distribution of bending angles, θ , of the triple sources is shown in figure 6.3. The majority of sources have $\theta < 25^\circ$, and if the few large bending angles are due to projection then the intrinsic bending appears to be less than $\sim 25^\circ$. This implies that most sources are fairly straight (at least in terms of the way ‘bending’ has been defined; using the lobe hotspots).

Bending angle plotted against redshift (figure 6.4a) shows there is basically no dependence, as the plane is filled rather uniformly and the upper envelope remains roughly constant with redshift. It appears that bending angles are redshift independent for $z < 1$ quasars. Others, such as Barthel and Miley (1988), Neff and Brown (1984) and HUO, have found that bending angle does increase with z , where their surveys contain sources out to $z = 3$. The increase of bending angle and decrease of linear size with redshift has been interpreted as being due to a denser IGM at earlier epochs that impedes the outward growth of a source and is more likely to bend the source. This suggests that linear size and bending angle should be correlated in the same sense as they would be if projection effects dominated. This is discussed in the next subsection.

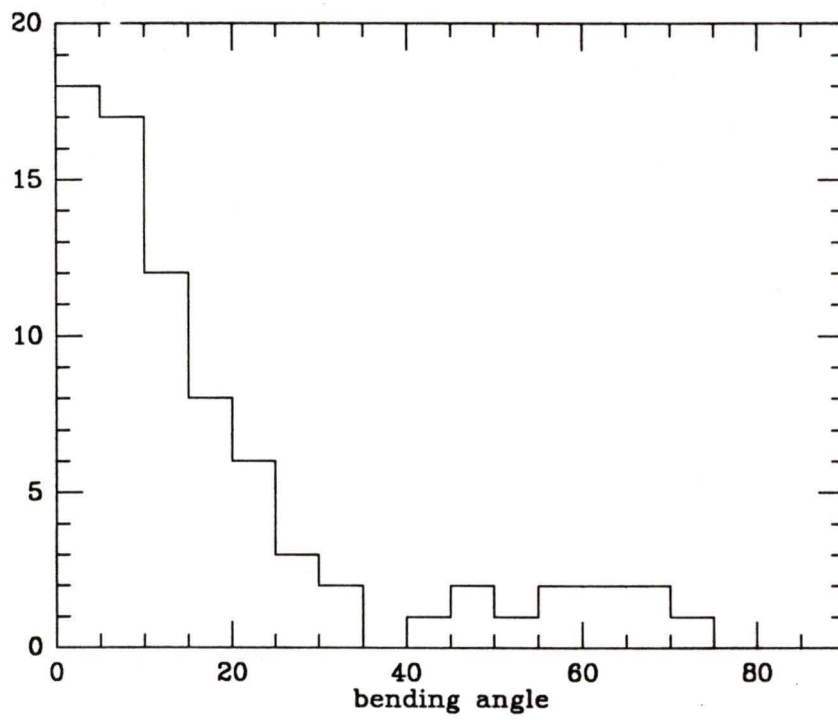


Figure 6.3: Histogram of Bending Angles

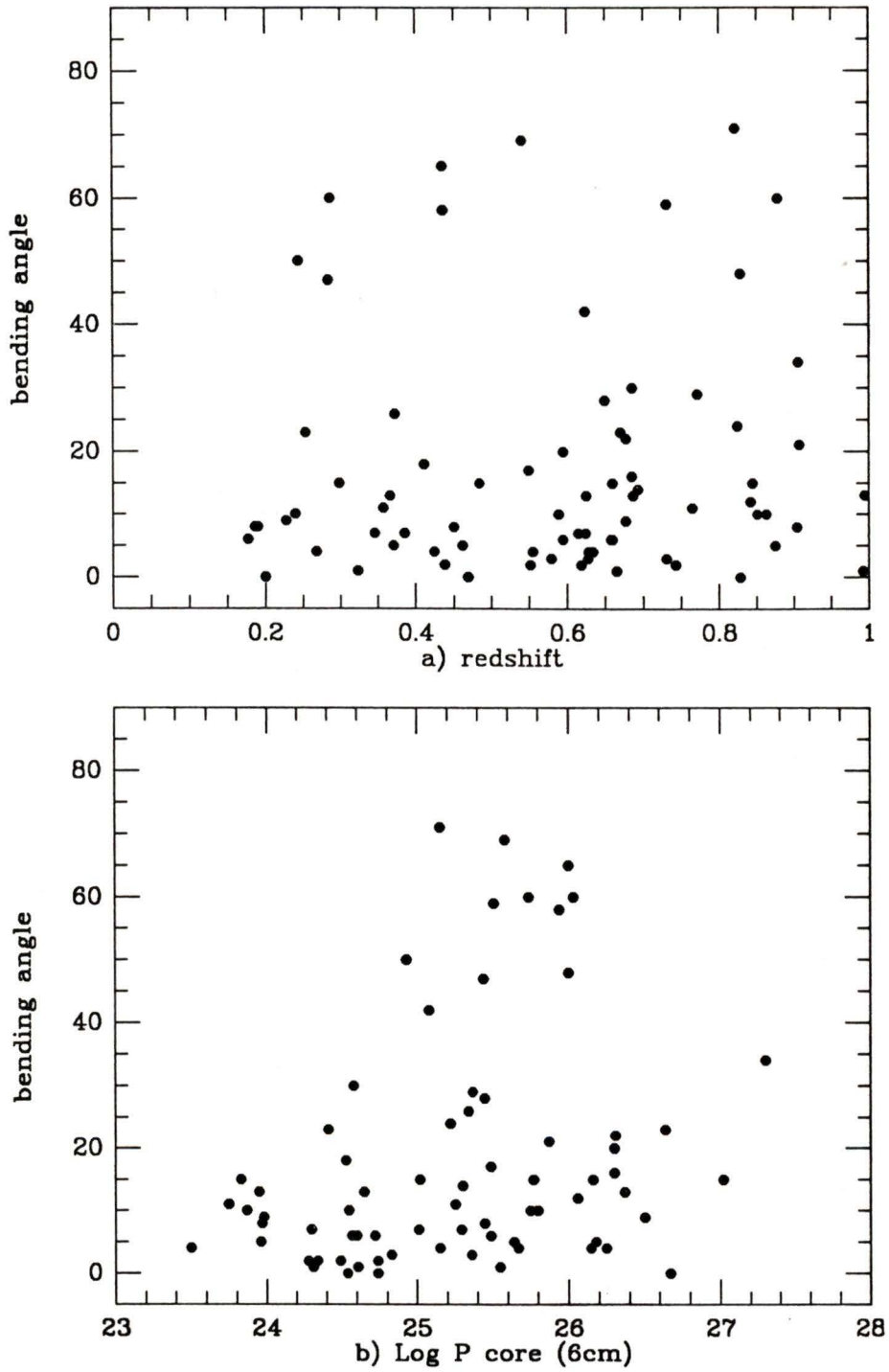


Figure 6.4: Bending Angle Dependence on a) Redshift b) $\text{Log}P_{\text{core}}$

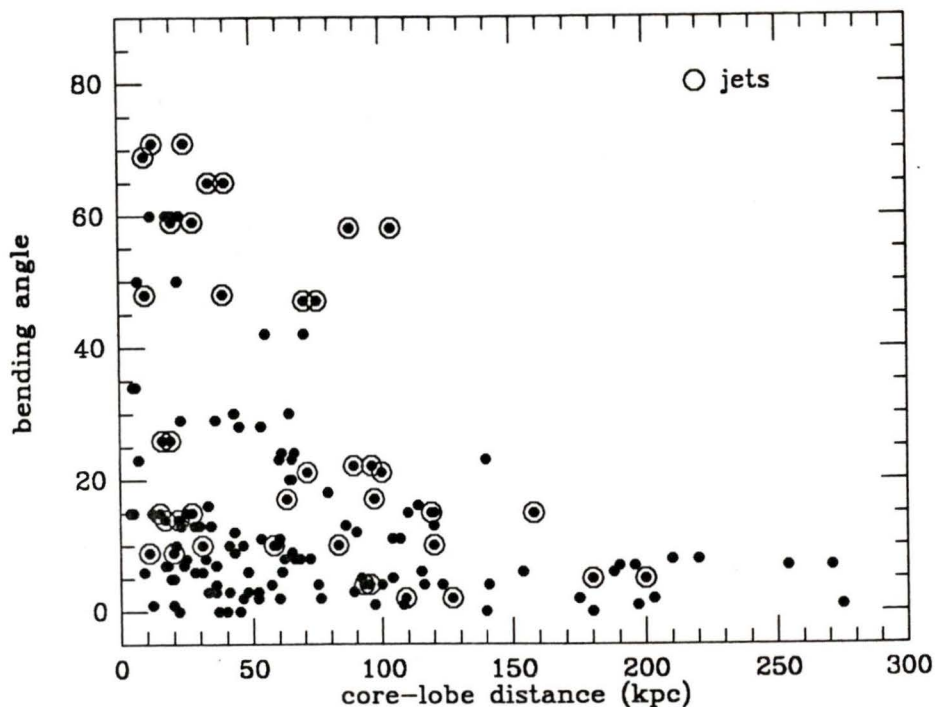


Figure 6.5: Bending Angle Dependence on Core-Lobe Distance

Bending angle does not appear to have a clear dependence on core luminosity, as seen in figure 6.4b where the sources with largest bending angles are those with moderate core luminosity. Barthel and Miley (1988) found that bending increased with luminosity, but our data shows a definite scarcity of highly bent sources with $\log(P_{core})$ greater than 26.

Summarizing, bending angle shows no obvious dependence on either redshift or core luminosity and most sources are quite straight.

6.2.3 Bending Angle/Linear Size Relation

Figure 6.5 shows that the bending-angle upper envelope decreases as the projected linear size of a source increases. This is consistent with a denser IGM both impeding the source growth and bending the source. HUO and

Barthel and Miley (1988) adopt this interpretation along with an increase in the IGM density with redshift. In figure 6.2 the source size upper envelope was found to decrease beyond $z = .8$, but the bending angle distribution for $z > .8$ is quite uniform, not dominated by highly bent sources. The bending/size relation could still be due to density enhancements, where the enhancements may be just local ones and not redshift dependent.

The bending/size relation is also consistent with a projection interpretation in which the size is decreased and the bending angle may be enhanced. Then sources with large size are near the plane of the sky and their bending angles have not been enhanced by projection. In figure 6.5 any source larger than 150kpc has a bending angle less than $\sim 10^\circ$ and ones with bending angles larger than 25° are all smaller than ~ 100 kpc.

From the above discussions it appears that linear size can best be used as an alignment indicator for large sources where the source is probably in the plane of the sky. For small sources the situation is less clear, since they could be either sources with small intrinsic size or projected sources near the line of sight. In using bending angles as alignment indicators the few sources with large angles have the best chance of indicating alignment, where they will be interpreted as being near the line of sight.

Lastly, it is unfortunate that these alignment indicators apply only to sources that have extended structure, since core sources or cores with small extensions are strong candidates for beaming.

6.3 Tests for Relativistic Beaming

Now that alignment indicators have been established simple tests can be performed to see if the sources near the line of sight show signs of beaming relative to the sources that are in the plane of the sky. Sources close to the line of sight should show large side-to-side asymmetries of any component that has bulk relativistic motions. If the lobes and/or the jets

are relativistic they should be brighter on the approaching side and appear further from the core due to light travel time effects. Material that leaves the core and moves relativistically towards the observer will be enhanced in intensity relative to the rest of the source, producing a high core flux fraction. Tests for relativistic motion in the lobes, core and jet will be considered separately in the following subsections.

6.3.1 Lobes

Plotting the ratio of lobe power (at both 6 and 20cm) against linear size and bending angle respectively, should show distinct patterns if relativistic velocities are present and the sources are intrinsically symmetric. Without specifying which of the lobes is approaching, it is expected that the sources near the line of sight will have the largest difference in lobe luminosities, while those near the plane of the sky should have nearly equal lobe luminosities. Of course these relations will be smeared out by intrinsically different lobe luminosities. Figure 6.6a does not exhibit strong beaming characteristics, as sources with large sizes do not have nearly equal lobe luminosities. For the sources with small observed sizes, any possible relation is blurred by the fact that small sources may be either intrinsically small sources in the plane of the sky or larger sources aligned near the line of sight. On the other hand, in figure 6.6b, sources with large bending angles do tend to have fairly large differences in lobe luminosities which is consistent with beaming.

The ratio of lobe lengths plotted against the alignment indicators in figure 6.7 present mixed results for the core-lobe distances being affected by relativistic effects. The largest sources are predominantly of roughly equal length, as expected if they were in the plane of the sky and thus not influenced by light-travel-time effects. The small sources which probably contain intrinsically small sources as well as line-of-sight sources, contain a continuum of lobe length ratios. In general the plot is consistent with the

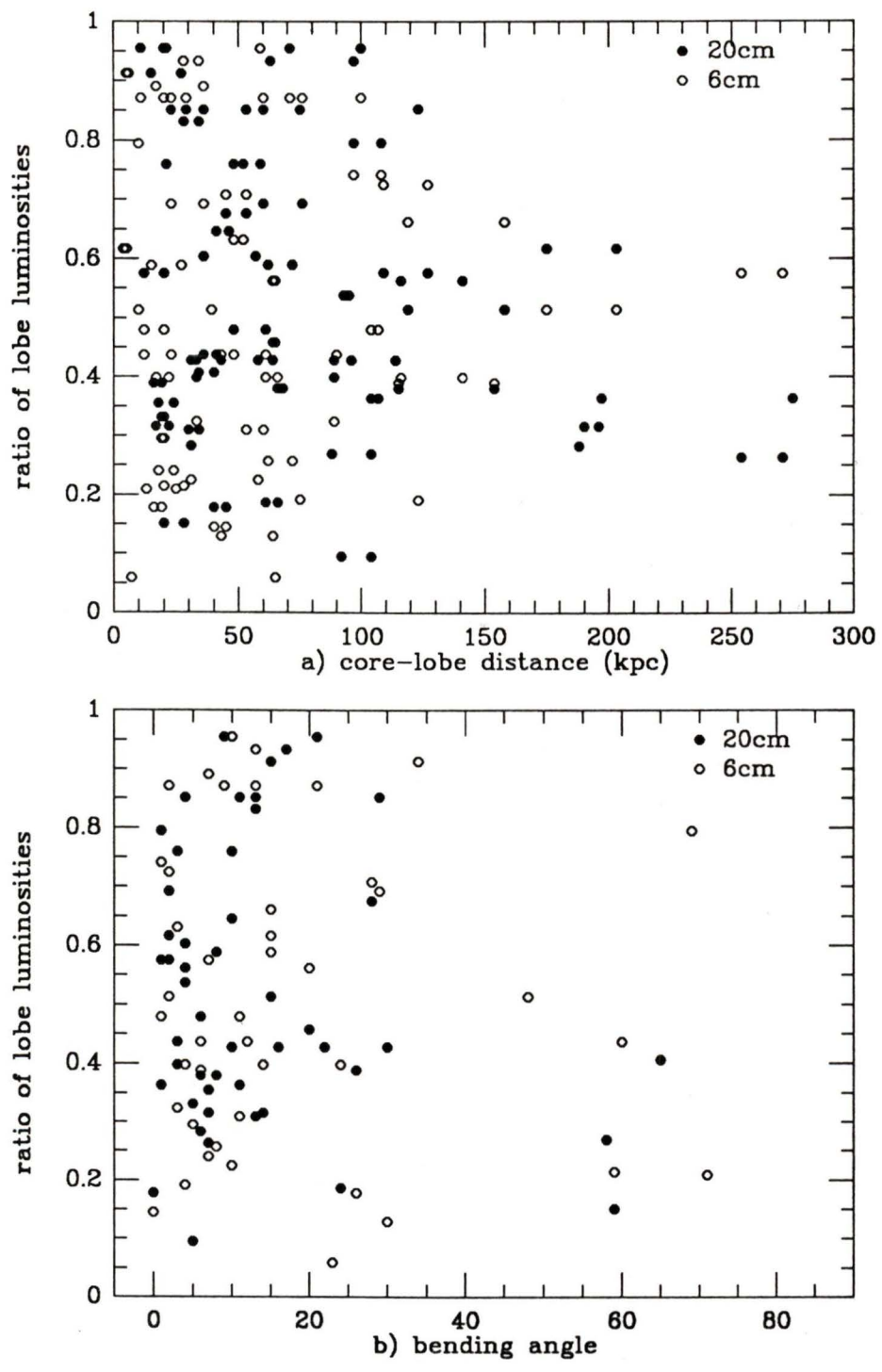


Figure 6.6: Ratio of Lobe Luminosities vs. a) Linear Size b) Bending Angle

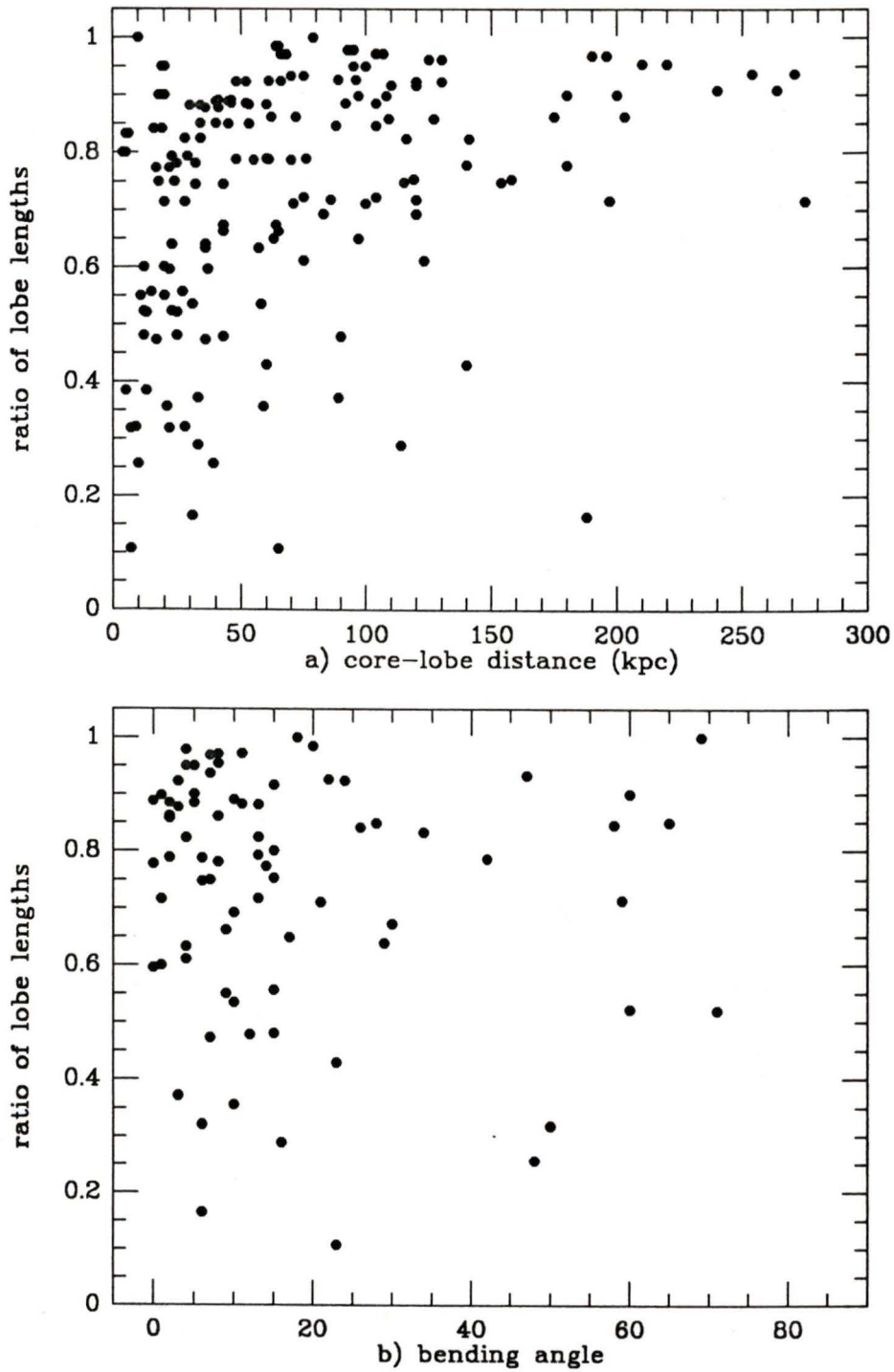


Figure 6.7: Ratio of Lobe Lengths vs. a) CL Distances b) Bending Angle

relativistic beaming scheme, but does not present overwhelming evidence. The sources with large bending angles, on the other hand, if produced by projection, should have very different core-lobe distances. Plot 6.7b shows these sources to vary in lobe length ratio, with a significant fraction having nearly equal lobes, which is inconsistent with the beaming model.

Above in section 6.2.2 it was argued that the intrinsic bending of sources was fairly small, roughly less than $\sim 25^\circ$. If the radio sources are intrinsically fairly straight and the bulk velocities of the lobes away from the core are relativistic, then the lobe distance from the core should correlate with lobe brightness. The brighter lobe would be the one travelling toward the observer and would be further from the core due to light travel time effects. Using these ideas, a test for relativistic beaming in the lobes can be performed that combines the previous two tests. In figure 6.8 the ratio of core-lobe distances for triple sources is always less than one (ie. the receding lobe divided by the approaching one) and yet the lobe luminosities are both less than and greater than one. This clearly shows that the lobe further from the core can be either brighter or dimmer than the nearer lobe. Thus the intrinsic variation in lobe properties does not appear to be dominated by relativistic effects in all sources, so the expansion of the lobes away from the core are not highly relativistic. There is a slight excess (lower left region) of sources with small size and luminosity ratios which are consistent with beaming. Could beaming possibly only play a role in some sources?

Lastly, the ratio-of-lobe-lengths histogram in chapter 5 (figure 5.1) was found to be consistent with alternating ejection and not with the light-travel-time effects predicted by the relativistic beaming model. The shapes of this histogram suggested by the beaming model can be seen in Rudnick and Edgar (1984) and Ensmann and Ulvestad (1984). Histograms such as these have in the past been used to estimate bulk velocities of $\beta \sim .2$ (Lon-

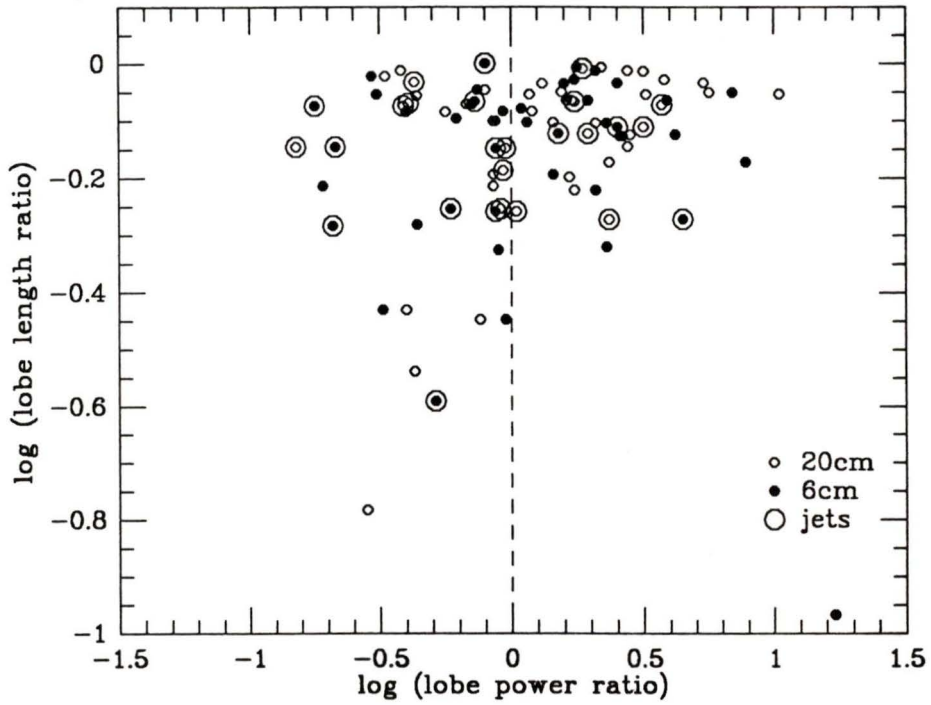


Figure 6.8: Test for Beaming in the Lobes (Lobe Length Ratio vs. Lobe Power Ratio)

gair and Riley 1979). Recently with more and better data it has been found that this method cannot be used since the observed distribution is not as the theory predicts (see RE).

The above tests show that relativistic beaming is not a significant effect in determining the core-lobe distances or lobe brightnesses.

6.3.2 Jets

Determining whether the jets transport energy to the lobes at relativistic speeds or not remains one of the most important problems in the large-scale structure of radio sources. While the lobes appear to be expanding away from the core fairly slowly, they may be being fed by relativistic jets. In powerful radio galaxies and quasars, jets are only seen on one side of the core and it is thought that doppler boosting of the approaching jet could cause only one jet to be detected. Comparing properties of the sources in which jets are found with those for which jets are not detected allows a few simple tests for relativistic velocities in the jet. With the use of the alignment indicators to search for beaming in the jets this analysis is similar to that of Saikia (1984a).

Sources with a narrow ridge of emission between the core and lobe or emanating from the core are designated as jets in the main table (table 4.1). Of the 128 sources, 17 were designated as having jets and 8 more listed as possibly having jets. In the plots of this chapter all of these were considered as having jets and not distinguished separately. In each case, only one jet per source was detected, and all the sources containing jets are triples except for 2 which are CL sources.

The histogram of core-lobe distances (figure 6.9) shows that jet sources are slightly smaller than non-jet sources, but probably not significantly. The median sizes of the two distributions are 40 kpc for the jet sources and 50 kpc for the non-jet sources. If the jet sources were aligned close

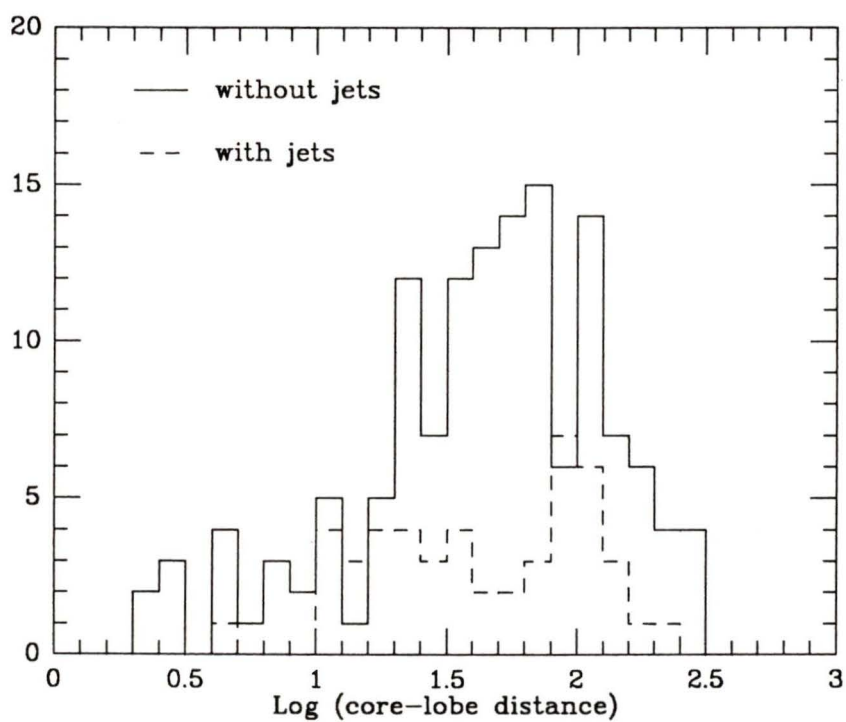


Figure 6.9: Histogram of Core-Lobe Distances

to the line of sight and beamed it would be expected that they would be significantly smaller in projected size. Only a slight size difference between jet and non-jet sources was also found by Saikia (1984a) and the large size of some sources that do contain jets has always provided a strong argument against the beaming of jets (Wardle and Potash 1982, Owen and Puschell 1984, Barthel 1987). The jets were found on the source side with the more distant lobe twice as often as on the shorter side, and for the sources for which lobe luminosities were available the jet was on the brighter side in all sources but one. This relation between the jets and the lobe distance and brightness may not necessarily be because of doppler favouritism since it didn't appear that the lobes were beamed. Instead the jet side may be the active side at the present epoch, feeding the lobe and pushing the hotspot further from the core.

The bending angle of sources may also indicate the alignment of a source (section 6.2), and figure 6.10 shows that a large fraction of the sources with jets also have large bending angles. 35% of the jet sources have bending angles greater than 40° , while only 7% of the non-jet sources have such large bending angles. The position of jet sources in the bending angle/linear size plane are designated with large circles in figure 6.5. It shows that jet sources are much more likely to be both small and highly bent than sources for which jets were not detected. Of the jet sources that are highly bent (*ie.* $\theta > 40^\circ$) lobe luminosities are available for six of them and the lobe further from the core is brighter in five cases. In all 6 cases the jet is on the side of the more distant lobe, as would be expected if both the jet and the lobes were beamed. When jet sources are indicated in the lobe differences plot (figure 6.8) the further lobe is brighter about twice as often as the closer lobe. These properties imply that beaming may play a role in the these sources, especially the ones that are small with large bending angles. The lobe emission may then also be beamed in some sources, as mentioned

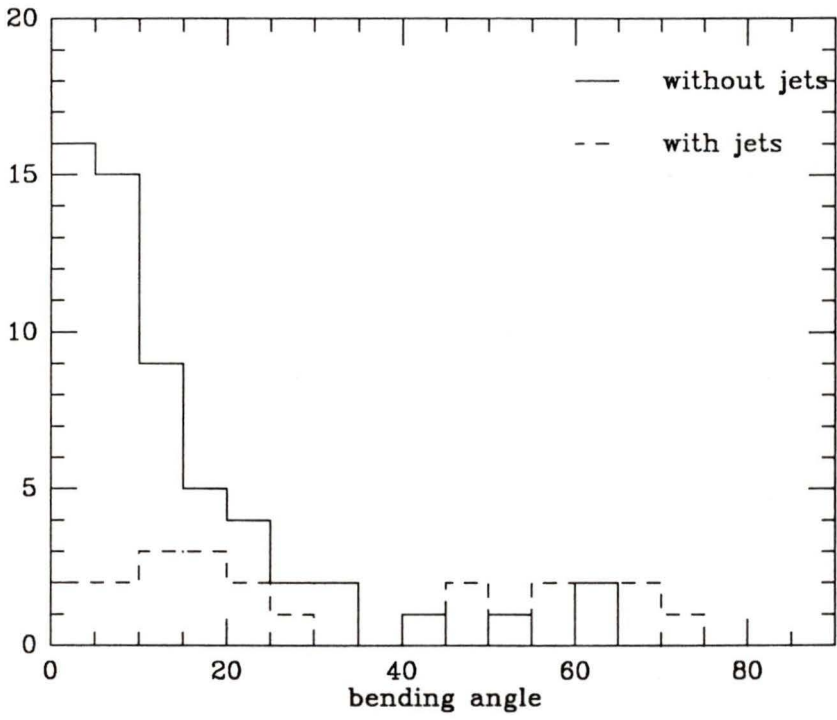


Figure 6.10: Bending Angle dependence on Jets

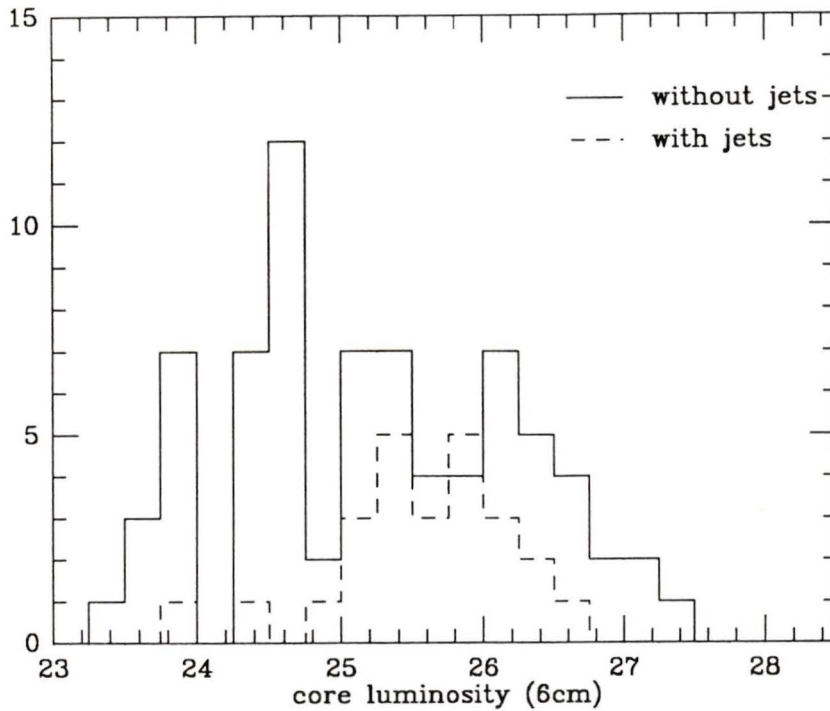


Figure 6.11: Core Luminosities for Jet and Non-Jet Sources

in section 6.3.1, but the lobe on the jet side could also be brighter and further because of the recent energy input from the jet.

If beaming plays a role in the appearance of jets in sources, and if they emerge from the core at a small angle to the line of sight, it is reasonable to expect that the radiation from the core itself will also be beamed. Figure 6.11 shows histograms of the core luminosity for sources both with and without jets. The two histograms have fairly similar distributions above 10^{25} , but below this luminosity there are almost no jet sources as compared to about half of the non-jet sources. The median core luminosity of the sources with jets is $\sim 10^{25.6}$ about four times the non-jet median of $\sim 10^{25}$. This is consistent with the beaming scheme, but it may also reflect an evolutionary epoch in the life of these objects. For example, at some stage

in a quasar's life the core may be very active and transport a lot of material towards the lobes along the jet.

The jet sources appear to be consistent with the beaming model on almost all accounts, except for their sizes. There may also be evidence for beaming in the cores and lobes of these sources as well.

6.3.3 Cores

It is deep inside the radio cores of the images seen in the appendix that superluminal motion has been observed. This is the best evidence in favour of relativistic beaming and observations of superluminal motion are becoming fairly ubiquitous, to the point where it is suspected that, if this hypothesis is correct, a large fraction of cores emit beamed radiation. In the last subsection it was seen that the cores of sources with jets are brighter than those without jets, and it was speculated that possibly both components were beamed. Here, to investigate the beaming of core radiation, the core fraction (ratio of core flux to total flux, f_c) will be plotted against the alignment indicators. Beamed cores would show up as having a high core fraction and should be in sources that are aligned along the line of sight.

Figure 6.12 plots core fraction against core-lobe distance for both 6 and 20cm. The plots show that the large sources are lobe dominated, while the smaller sources span the whole range of core fraction. This is consistent with beaming if the large sources are in the plane of the sky and the small sources have a variety of orientations. It is also interesting that the CL sources are both smaller than the triples and generally have quite high core fractions. Is this because they are beamed towards the observer and the second lobe is not seen due because it is receding relativistically? Alternately, the CL sources could be younger and have only ejected material in one direction so far and their bright core will dim as the source ages, as proposed in HPG.

The plots of core fraction against bending angle are less supportive of

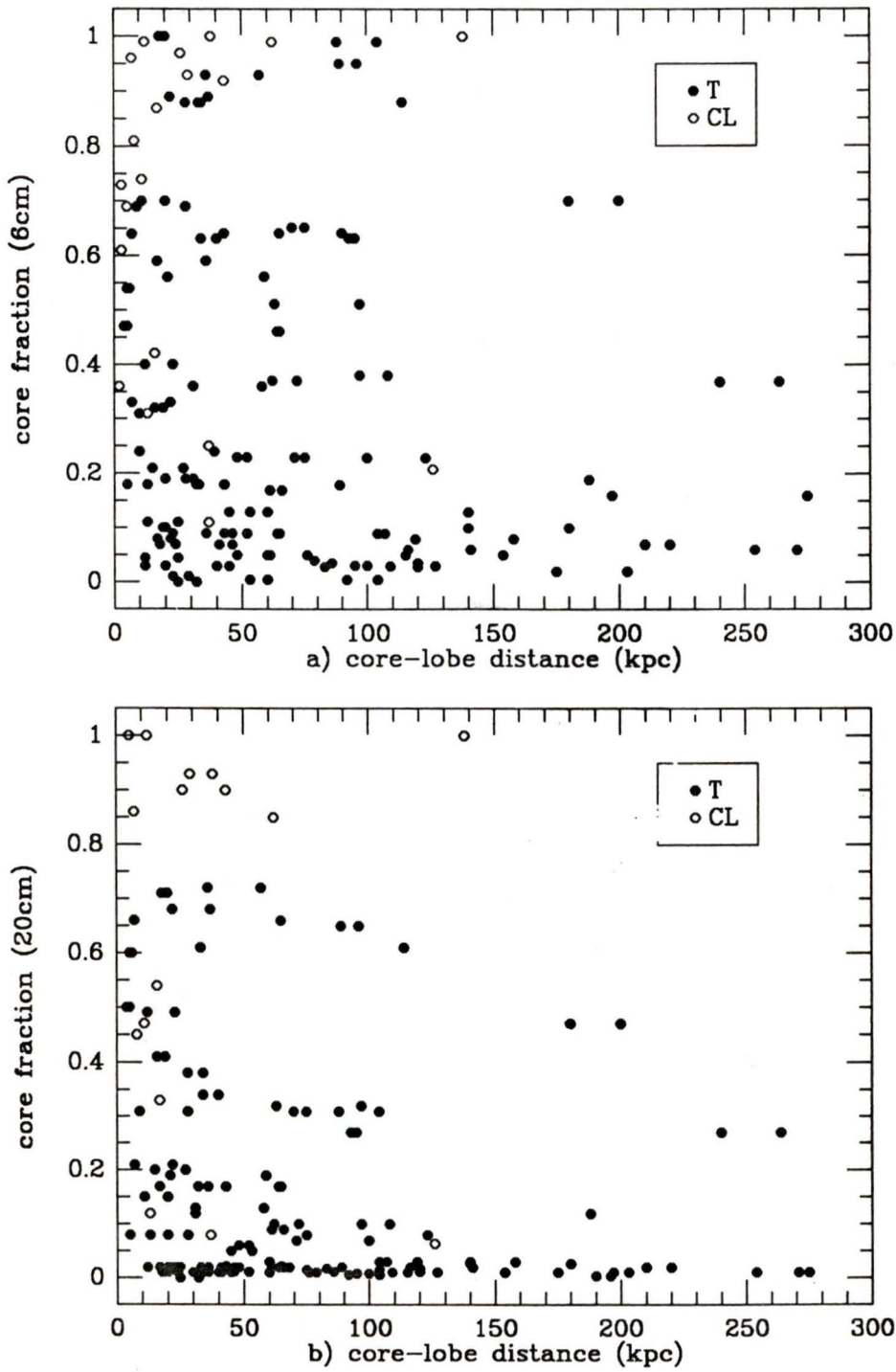


Figure 6.12: Core Fraction vs. Core-Lobe Distance a) 6cm b) 20cm

the relativistic beaming model. Both the 6 and 20cm plots show the more bent sources to have a large range of core fraction, while beaming predicts it should be high. In fact the 20cm plot shows that no sources are core dominated, since $f_c < .8$ for all sources. For sources with small θ (where the small bending angle implies the source lies near the plane of the sky and hence should not be beamed), there is a full range of f_c , but there is a high concentration with $f_c < .1$.

6.4 Summary

This section has performed some basic tests to determine whether the motion of material from the central engine of radio-loud quasars is relativistic or not. Each component was examined separately and in each case there appeared to be properties that were consistent with beaming, while others were inconsistent. There is strong evidence against beaming in the lobe structures, while beaming appears to play a role in the jet and core components. However, the evidence is still tentative and each plot could be interpreted in several different ways using various other models for the radio emission.

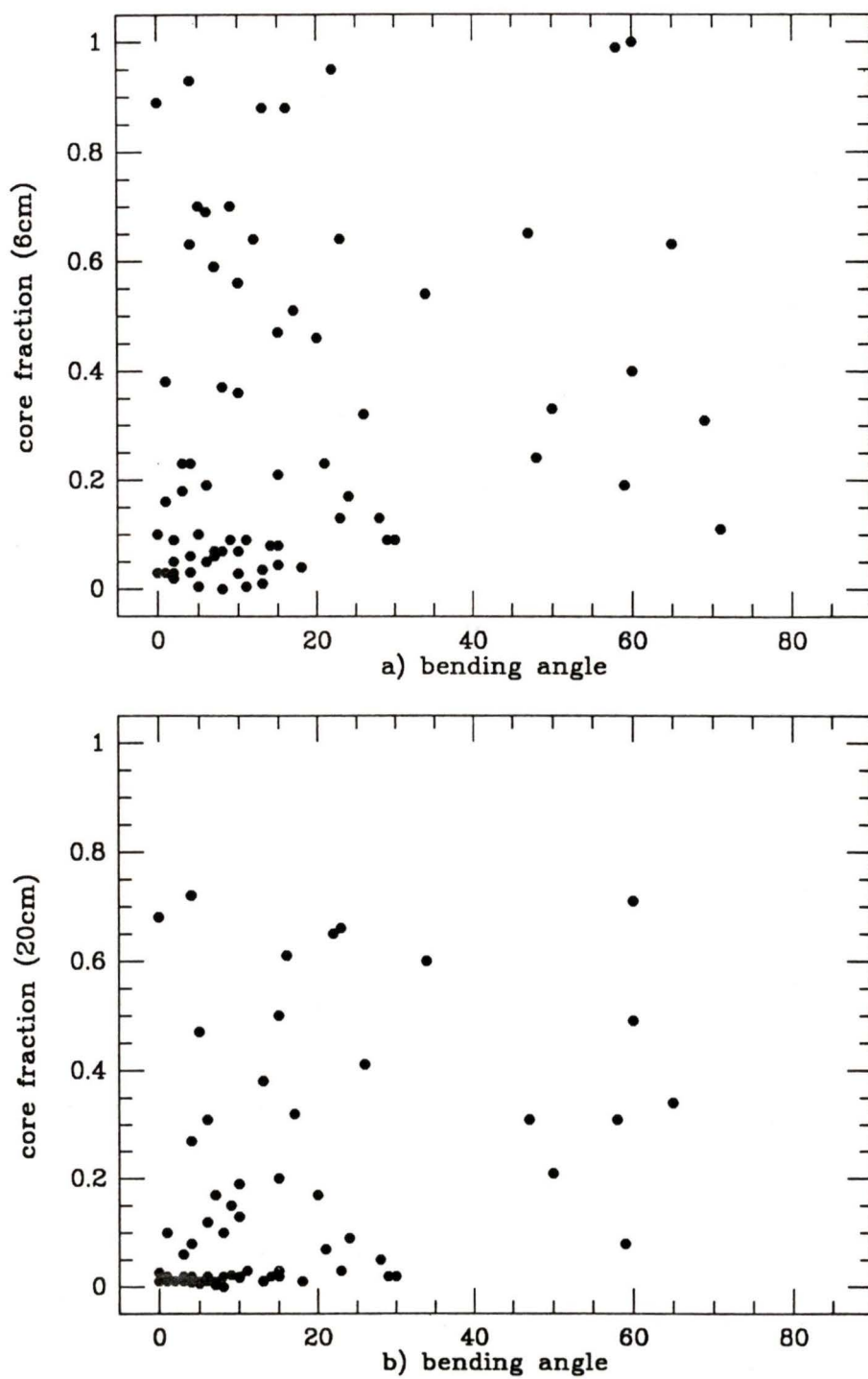


Figure 6.13: Core Fraction vs. Bending Angle a) 6cm b) 20cm

Chapter 7

Summary

This thesis examined the main properties of a large sample of radio-loud quasars and attempted to determine if alternating ejection and/or relativistic beaming play a role in the large-scale structure morphology. The sample was chosen only to fill the redshift/luminosity plane uniformly, without any knowledge of the morphology and without any known biases for morphological types. The final sample consisted of 128 quasars with $z < 1$ and was imaged with sub-arcsecond resolution and $< 1 \text{ mJy}$ sensitivity using the VLA at both 6 and 20cm. Images of sources with extended structure are presented in the appendix and the main source properties are contained in table 4.1. These data were used to test the alternating-ejection and relativistic-beaming models in this thesis and used in the analysis of HPG, where an evolutionary scenario was developed.

The alternating-ejection model has a central engine that ejects material from the core on only one side at a time. Support for this model was found in properties of the source lobes, which were at different distances from the core within a given source, and the lobe-length ratio histogram could be satisfactorily fit with a simple model of alternating ejection. The distribution of lobe-length differences of the triple sources was similar to the CL lobe-length distribution, which suggests that the CL sources are young sources which have so far ejected material on only one side. The

appearance of jet structure on only one side of the core is also consistent with alternating ejection, but it also implies that the central engine does not alternate sides on as short a time scale as it takes the jet to travel to the outer lobe. This has been interpreted as meaning that material in the jet travels much faster than the lobe material.

The relativistic-beaming model has material ejected by the central core at relativistic velocities, so that relativistic effects alter the intrinsic radiation pattern of the source. The effects are largest when a source is aligned near the line of sight, and linear size and bending angle were used to indicate the alignment of a source. Evidence for beaming was found in the jet and core components, but not in the lobes. The jets were one-sided and contained in sources that appeared to be near the line of sight and have a higher-than-average core luminosity. The lobe-intensity ratio distribution and the lobe-length ratio distribution were found to be inconsistent with relativistic lobe velocities.

In conclusion, an attempt will be made to synthesize the above results in the light of these two models. The lobes show signs of alternating ejection, but when a jet is seen between the lobes and the core it does not appear to be alternating sides. The jet and core components may be beamed, while the lobes are travelling non-relativistically. This means that the fast-moving material in the jets can transfer energy from the core to the lobes. This energy input allows the lobes to contain energetic hotspots, but the outward velocity of the lobes cannot be significantly altered, since the alternating-ejection scheme requires that their velocities must remain fairly constant on either side of the core. The energy must be converted into particle acceleration and turbulent motion in the lobe. The lobe positions are then determined by the conditions under which they were born as they drift outwards with roughly constant velocities, maintaining their initial lobe-length difference. The lobe luminosities then will depend on more recent conditions, such as how recently the jet was active on that side of the core.

References

- Barthel, P.D. 1984, Ph.D. Thesis, Leiden University.
- Barthel, P.D. 1987, in *Superluminal Radio Sources*, ed. J.A. Zensus and T.J. Pearson, (Cambridge: Cambridge University Press), p. 148.
- Barthel, P.D. and Miley, G.K. 1988, *Nature*, **333**, 319.
- Bridle, A.H. and Perley, R.A. 1984, *Ann. Rev. Astr. Ap.*, **22**, 319.
- Clark, B.G. 1980, *Astr. Ap.*, **89**, 377.
- Dixon, R.S. 1970, *Ap. J.*, **169**, 791 (*Ap. J. Suppl.*, **20**, [1970]; updated version [1985] available from author).
- Ensmann, L.M. and Ulvestad, J.S. 1984, *A.J.*, **89**, 1275 (EU).
- Gower, A.C. and Hutchings, J.B. 1984, *A.J.*, **89**, 1658 (GH).
- Hewitt, A. and Burbidge, G., 1980 *Ap. J. Suppl.*, **43**, 57.
- Hewitt, A. and Burbidge, G., 1987 *Ap. J. Suppl.*, **63**, 1 (HB).
- Hintzen, P., Ulvestad, J.S., and Owen, F. 1983, *A.J.*, **88**, 709 (HUO).
- Hjellming *et al.* 1982, *An Introduction to the Very Large Array*, (Greenbank:NRAO).
- Högbom, J.A. 1974, *Astr. Ap. Suppl.*, **15**, 417.
- Hutchings, J.B., Price, R., and Gower, A.C. 1988, *Ap. J.*, **329**, 122 (HPG).
- Ingham, W. and Morrison, P. 1975, *M.N.R.A.S.*, **173**, 569.
- Kapahi, V.K. and Saikia, D.J. 1982, *J. Ap. Astr.*, **3**, 465.
- Kellerman, K.I. and Owen, F.N. 1988, in *Galactic and Extragalactic Radio Astronomy*, ed. G.L. Verschuur and K.I. Kellerman, (Second Edition), (New York: Springer-Verlag), p. 563.
- Longair, M.S. 1981, *High Energy Astrophysics*, (Cambridge: Cambridge University Press).
- Longair, M.S. and Riley, J.M. 1979, *M.N.R.A.S.*, **188**, 625.
- Miley, G. 1980, *Ann. Rev. Astr. Ap.*, **18**, 165.
- Neff, S.G. 1982 Ph.D. Thesis, University of Virginia.

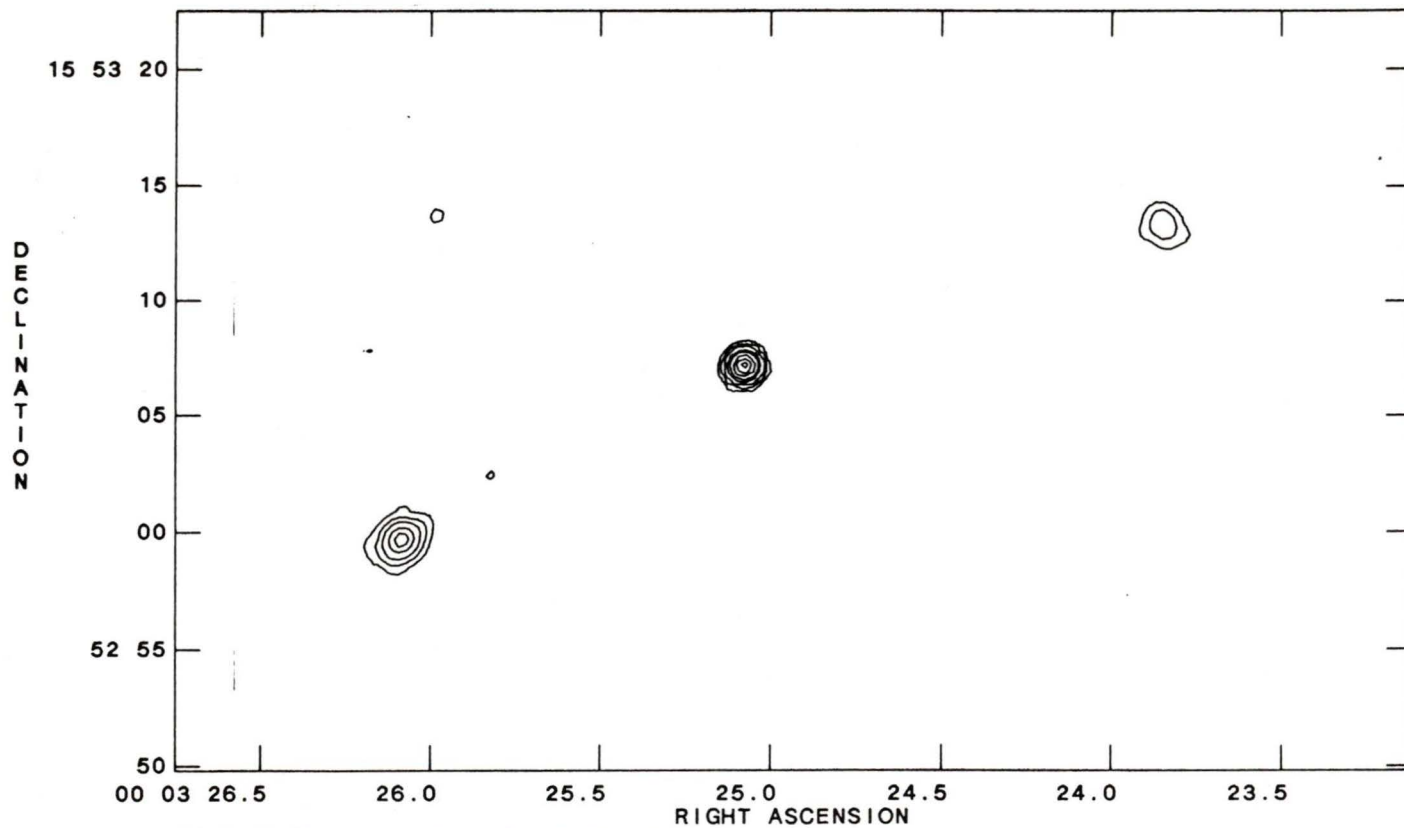
- Neff, S.G. and Brown, R.L. 1984, *A.J.*, **89**, 195.
- O'Dea, C. 1984, Ph.D. Thesis, University of Massachusetts.
- Orr, M.J.L. and Browne, I.W.A. 1982, *M.N.R.A.S.*, **200**, 1067.
- Owen, F.N. 1986, in *Quasars*, ed. G. Swarup and V.K. Kapahi, (Dordrecht:Reidel), p. 173.
- Owen, F. and Puschell, J.J. 1984, *A.J.*, **89**, 932.
- Padielli, L., Rogora, A., and de Ruiter, H.R. 1988, *Astr. Ap.*, **196**, 49.
- Pearson, T.J. and Readhead, A.C.S. 1984, *Ann. Rev. Astr. Ap.* **22**, 97.
- Perley, R.A., Schwab, F.R., and Bridle, A.H. 1986, *Synthesis Imaging*, (Greenbank: NRAO).
- Robson, D.W. 1981, *Nature*, **294**, 59.
- Rudnick, L. and Edgar, B.K. 1984, *Ap.J.*, **279**, 74 (RE).
- Saikia, D.J. 1984a, *M.N.R.A.S.*, **208**, 231.
- Saikia, D.J. 1984b, *M.N.R.A.S.*, **209**, 525.
- Scheuer, P.A.G. and Readhead, A.C.S. 1979, *Nature*, **277**, 182.
- Veron-Cetty, M.-P. and Veron, P. 1985, *ESO Sci. Rept.*, No. 4 (Garching: ESO).
- Walker, R.C. 1984, in *Physics of Energy Transport in Extragalactic Radio Sources*, ed. A.H. Bridle and J.A. Eilek, (Greenbank: NRAO), p. 20.
- Wardle, J.F.C and Potash, R.I. 1984, in *Physics of Energy Transport in Extragalactic Radio Sources*, ed. A.H. Bridle and J.A. Eilek, (Greenbank: NRAO), p. 30.
- Weedman, D. 1986, *Quasar Astronomy*, (Cambridge: Cambridge University Press).
- Weinberg, S. 1972, *Gravitation and Cosmology*, (New York: Wiley).

Appendix

VLA radio images of all quasars in the sample in which resolved structure was detected are presented here. Chapters 2 and 3 provide a detailed description of the imaging process and final image parameters. Measurements obtained from these images and used in the analysis are presented in table 4.1.

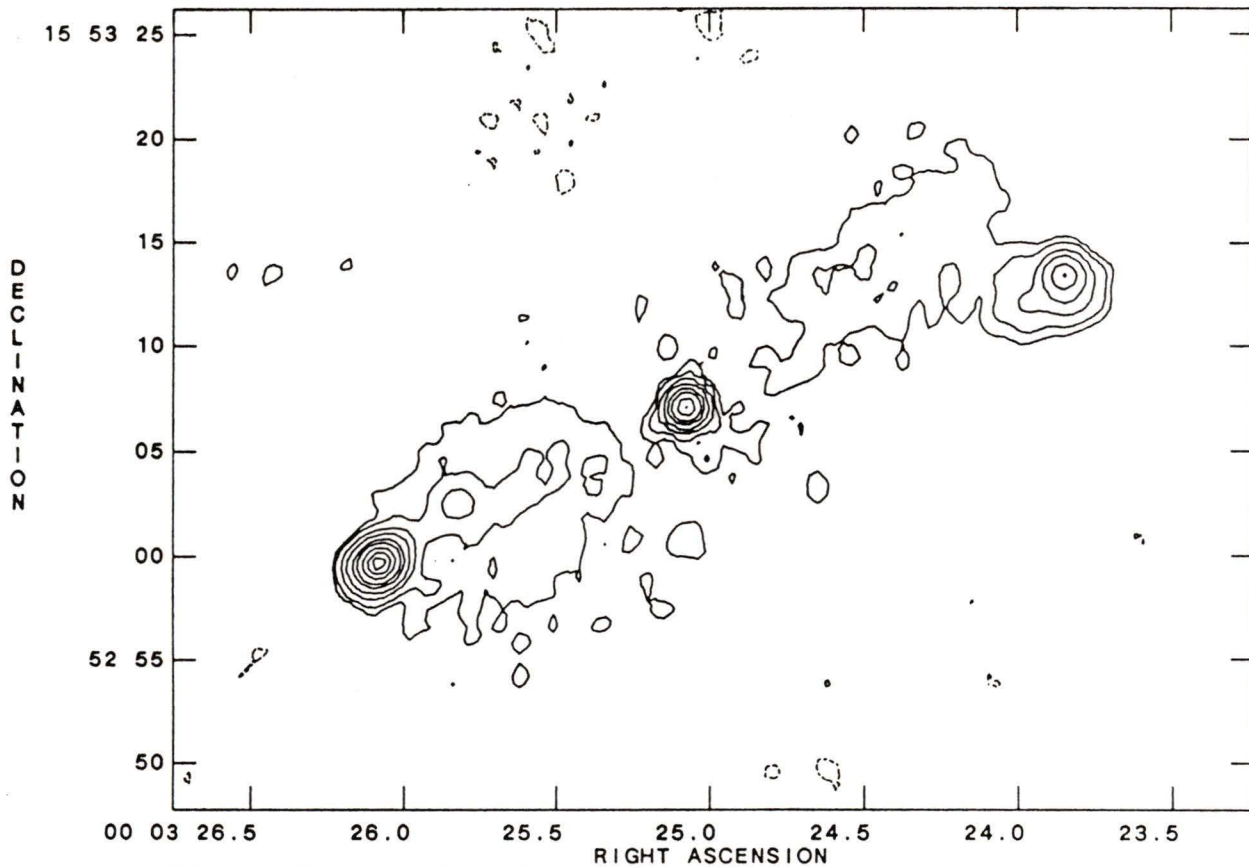
Each source has been CLEANed for a few thousand iterations and self-calibration has been performed on most sources. The resolution is ~ 0.4 arcsec at 6cm and ~ 1.2 arcsec at 20cm, while the limiting noise level is a few tenths of a mJy. The dynamic range varies from a few hundred to a few thousand to one. The largest visible structure is ~ 25 arcsec at 20cm and ~ 7 arcsec at 6cm, so care must be taken in interpreting the large-scale structure. The image parameters are listed in table 3.2 for each source and in every case the optical position of the quasar coincides with the radio core position listed in the table to within the accuracy of the measurements. The contours on each image correspond to percentages of the image's peak flux and are listed below each plot.

0003+158 6cm



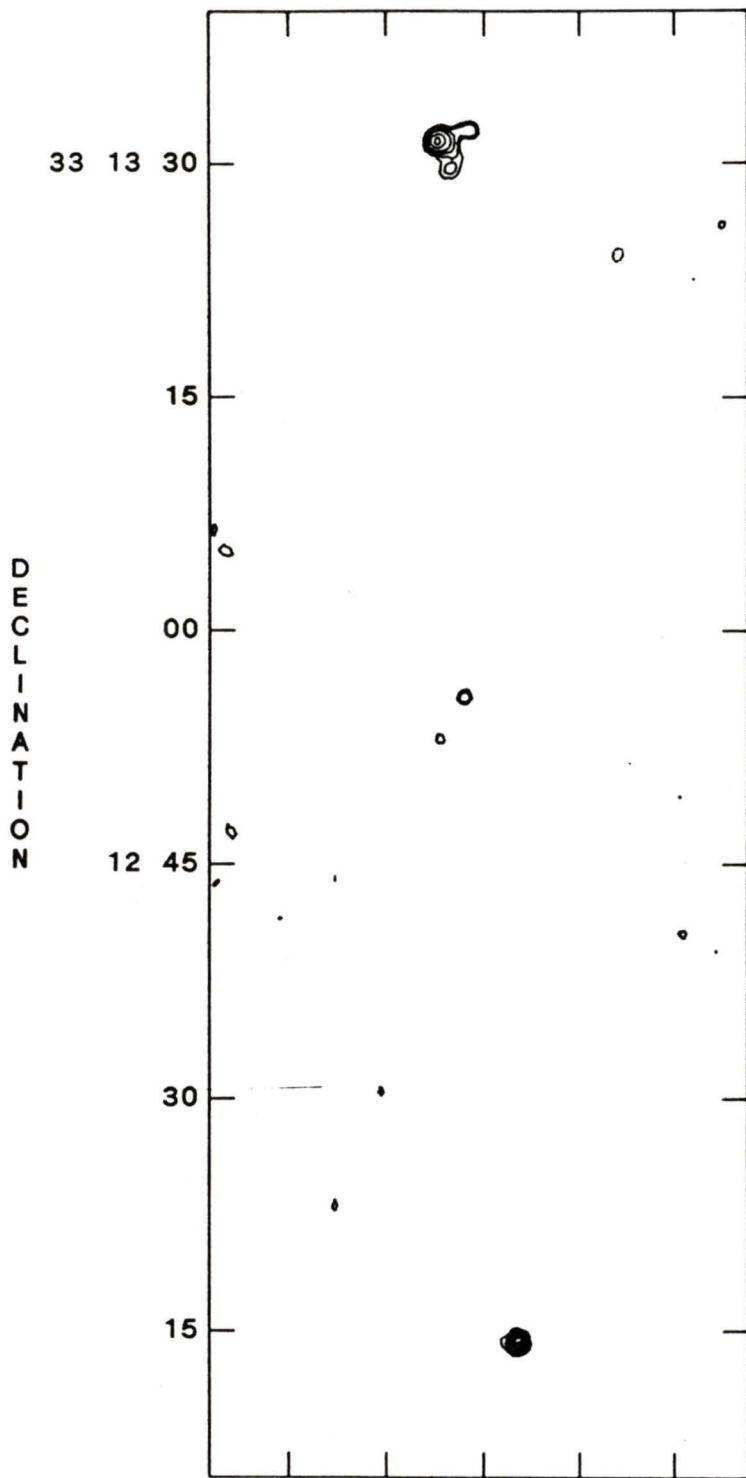
PEAK FLUX = 1.2241E-01 JY/BEAM
LEVS = 1.2241E-03 * (-2.00, 2.000, 5.000,
10.00, 20.00, 30.00, 50.00, 70.00, 90.00)

0003+158 20cm



PEAK FLUX = 1.3162E-01 JY/BEAM
LEVS = 1.3162E-03 * (-1.00, 1.000, 2.000,
5.000, 10.00, 20.00, 30.00, 50.00, 70.00,
90.00)

0007+332 6cm

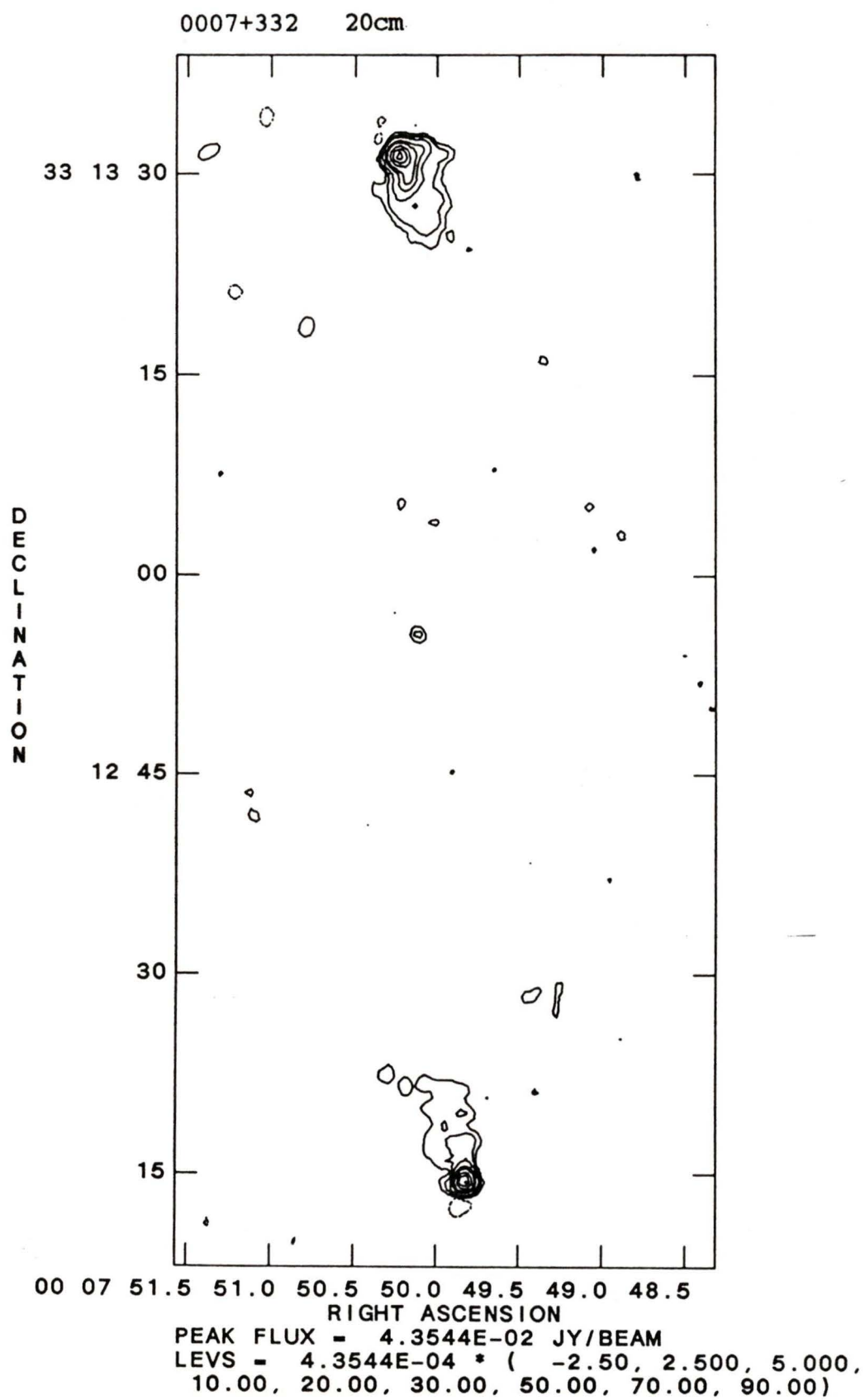


00 07 51.0 50.5 50.0 49.5 49.0

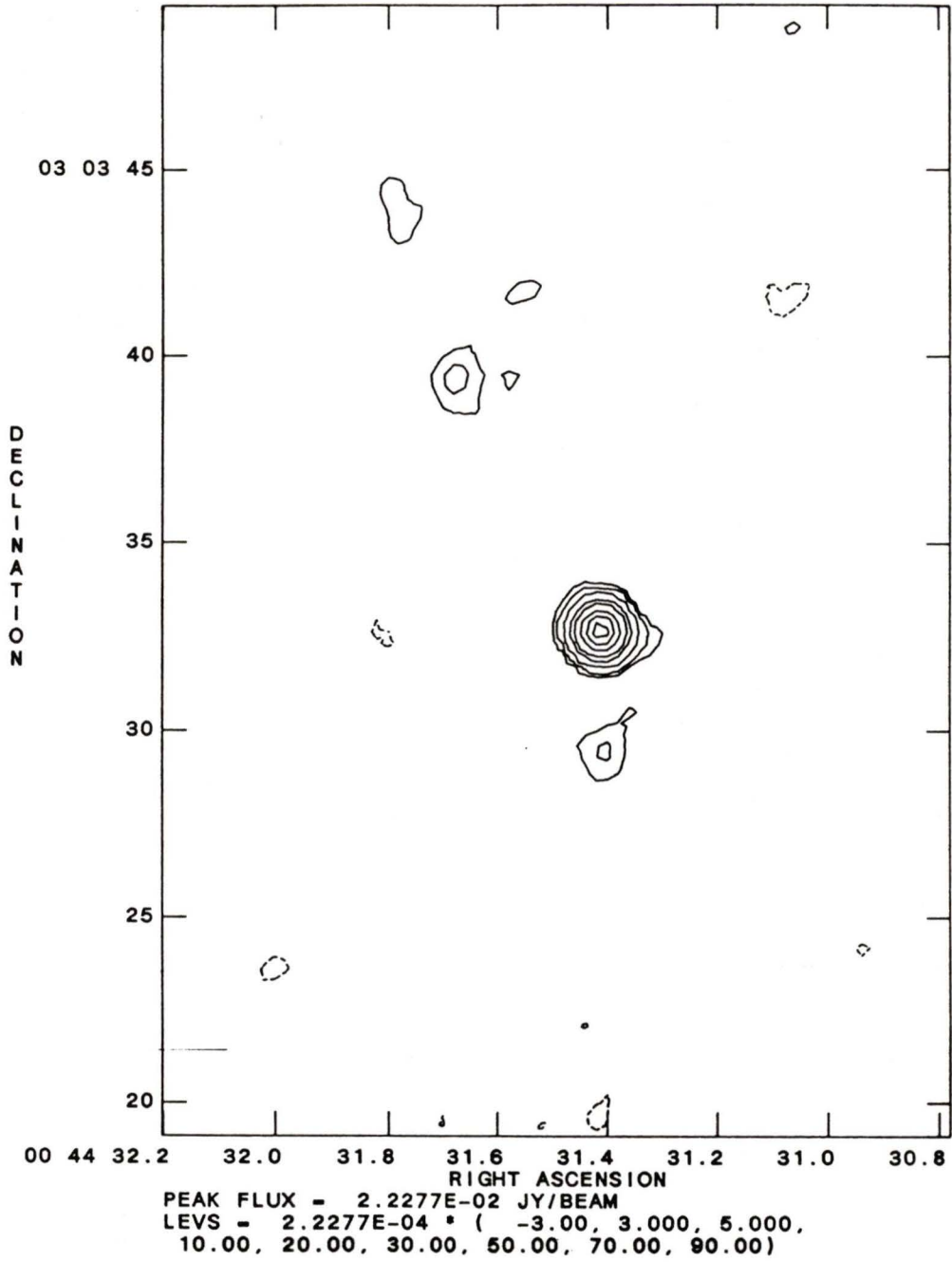
RIGHT ASCENSION

PEAK FLUX = 1.6434E-02 JY/BEAM

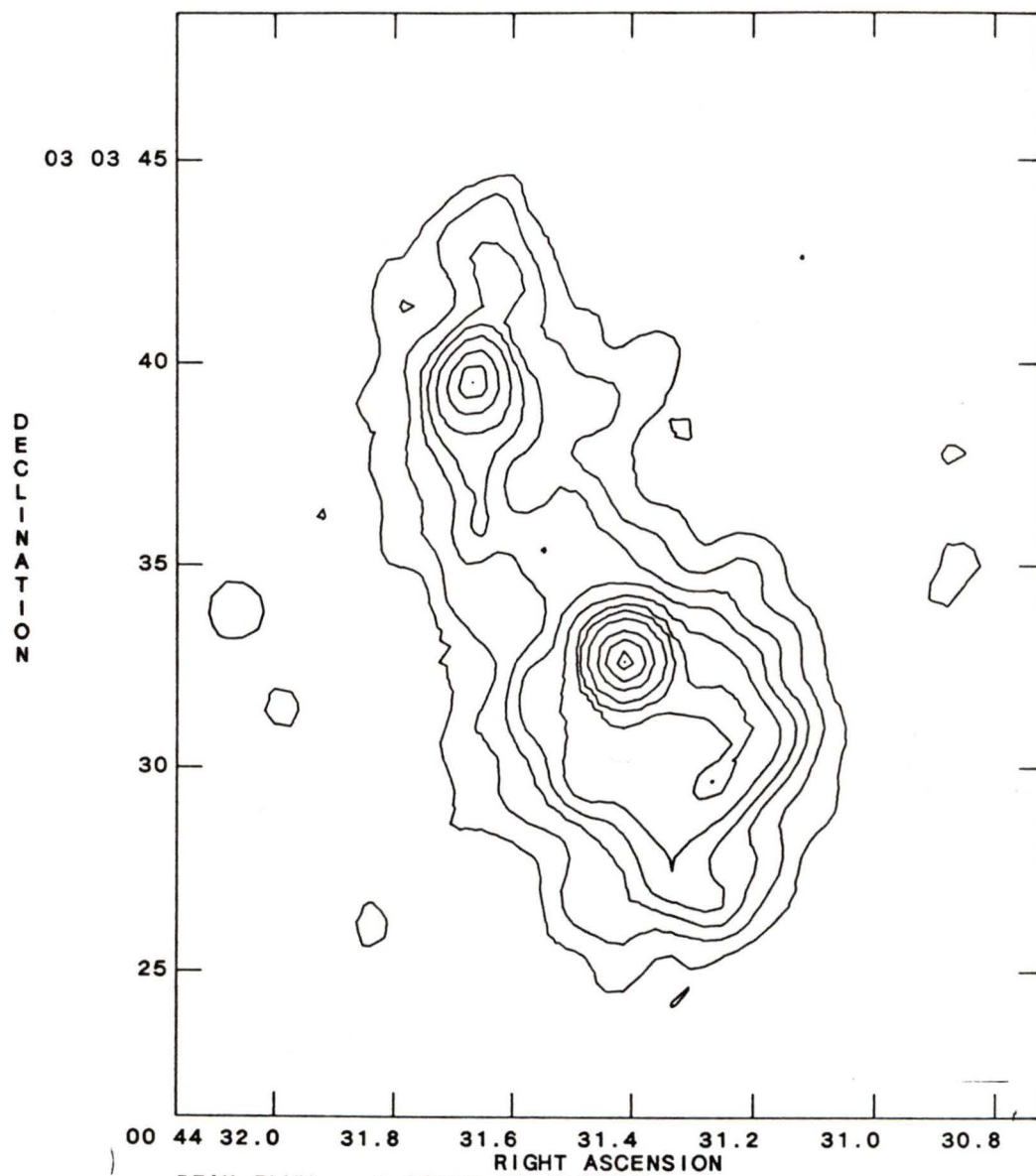
LEVS = 1.6434E-04 * (-8.00, 8.00, 12.00, 20.00, 30.00, 50.00, 70.00, 90.00)



0044+030 6cm

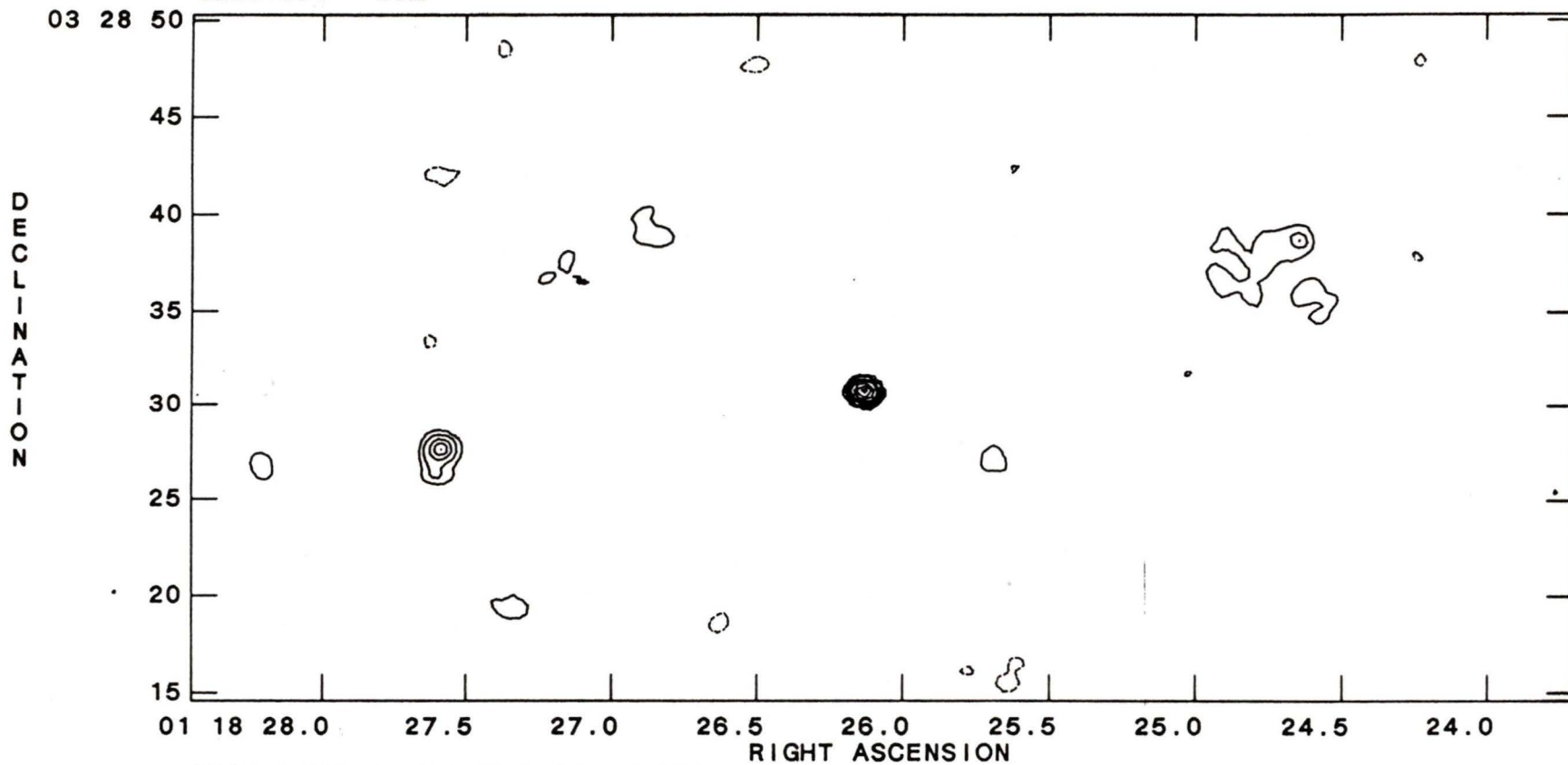


0044+030 20cm

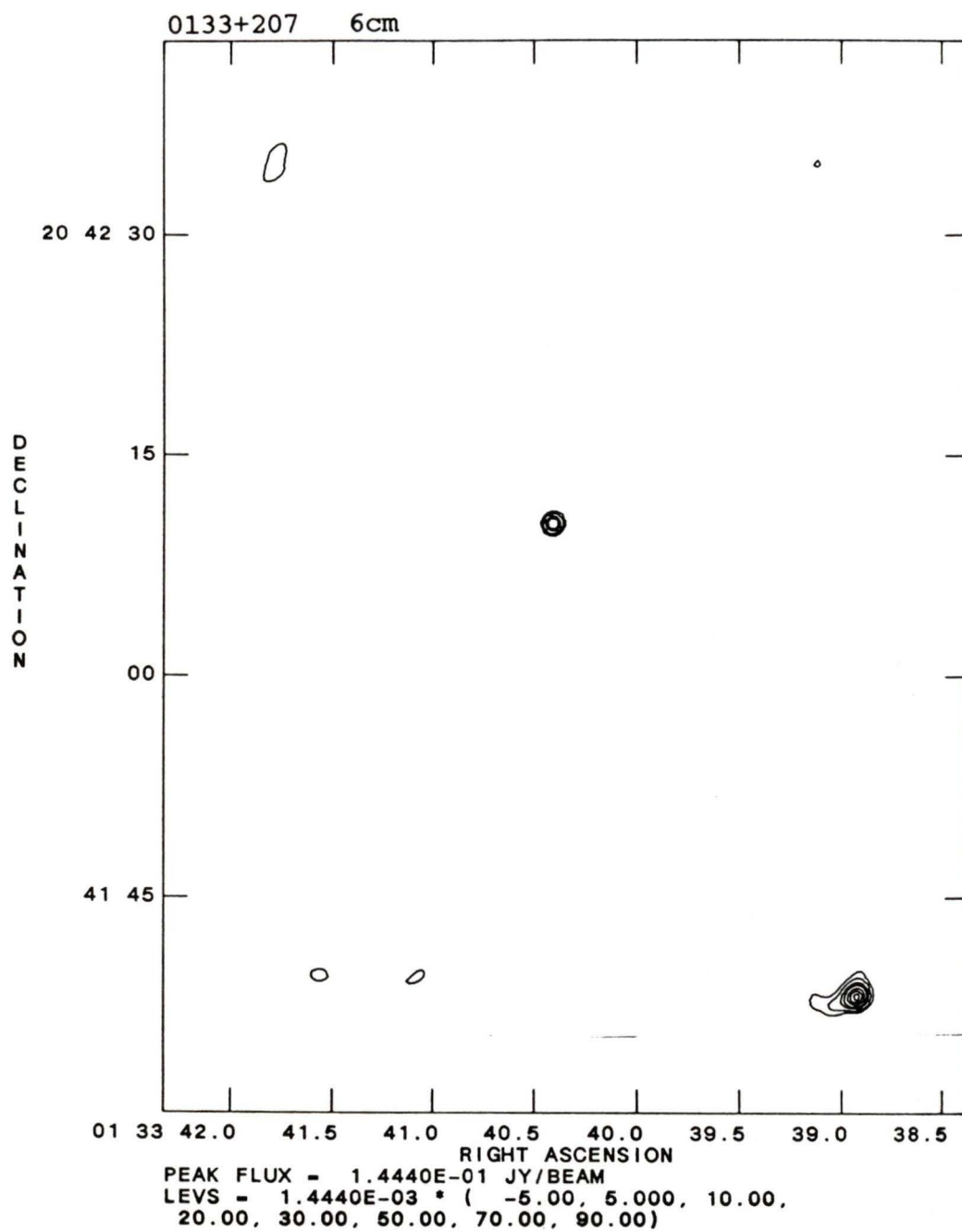


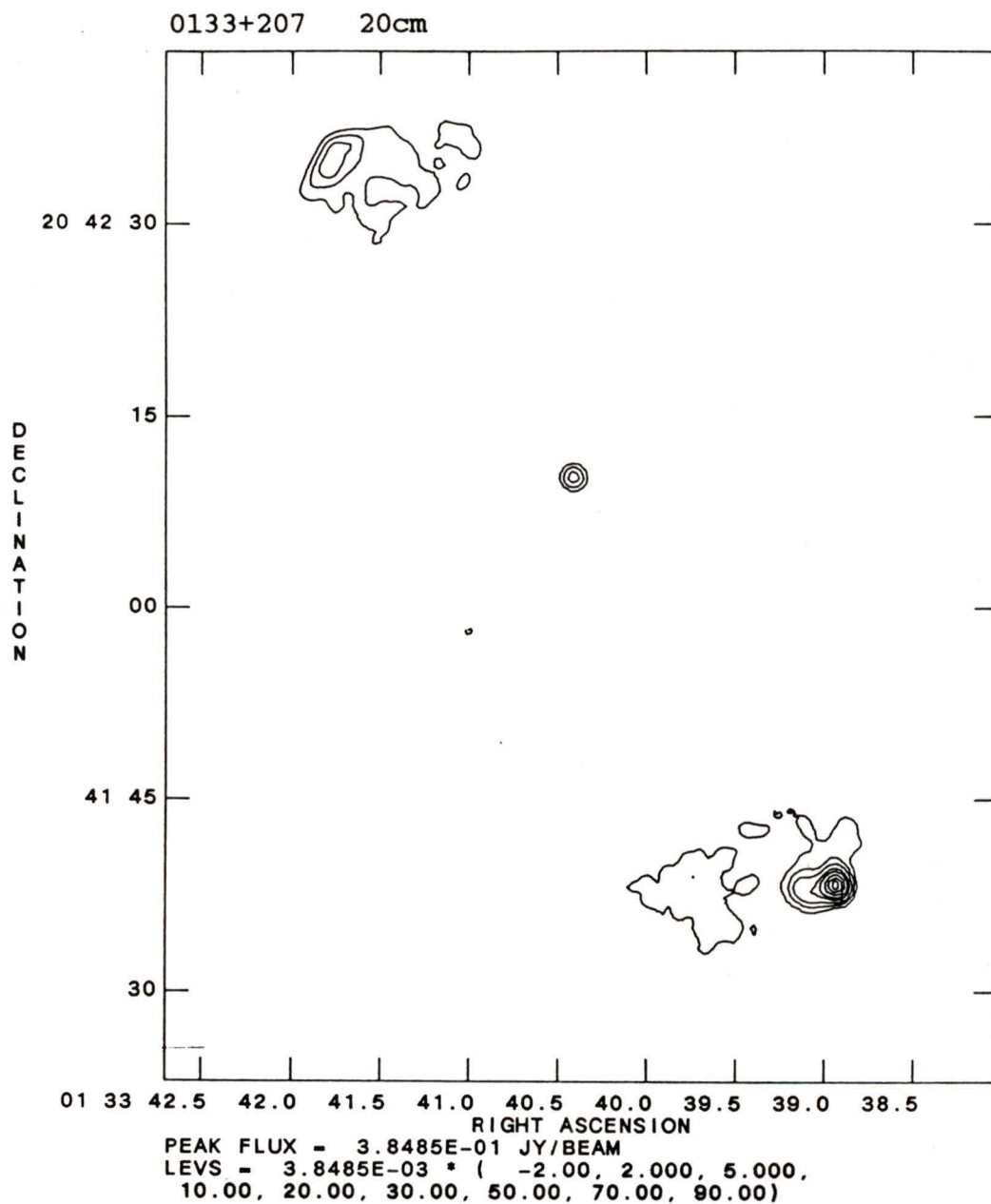
PEAK FLUX = $2.9637\text{E-}02$ JY/BEAM
LEVS = $2.9637\text{E-}04$ * (-1.50, 1.500, 3.000,
5.000, 7.000, 10.00, 15.00, 20.00, 30.00,
50.00, 70.00, 90.00)

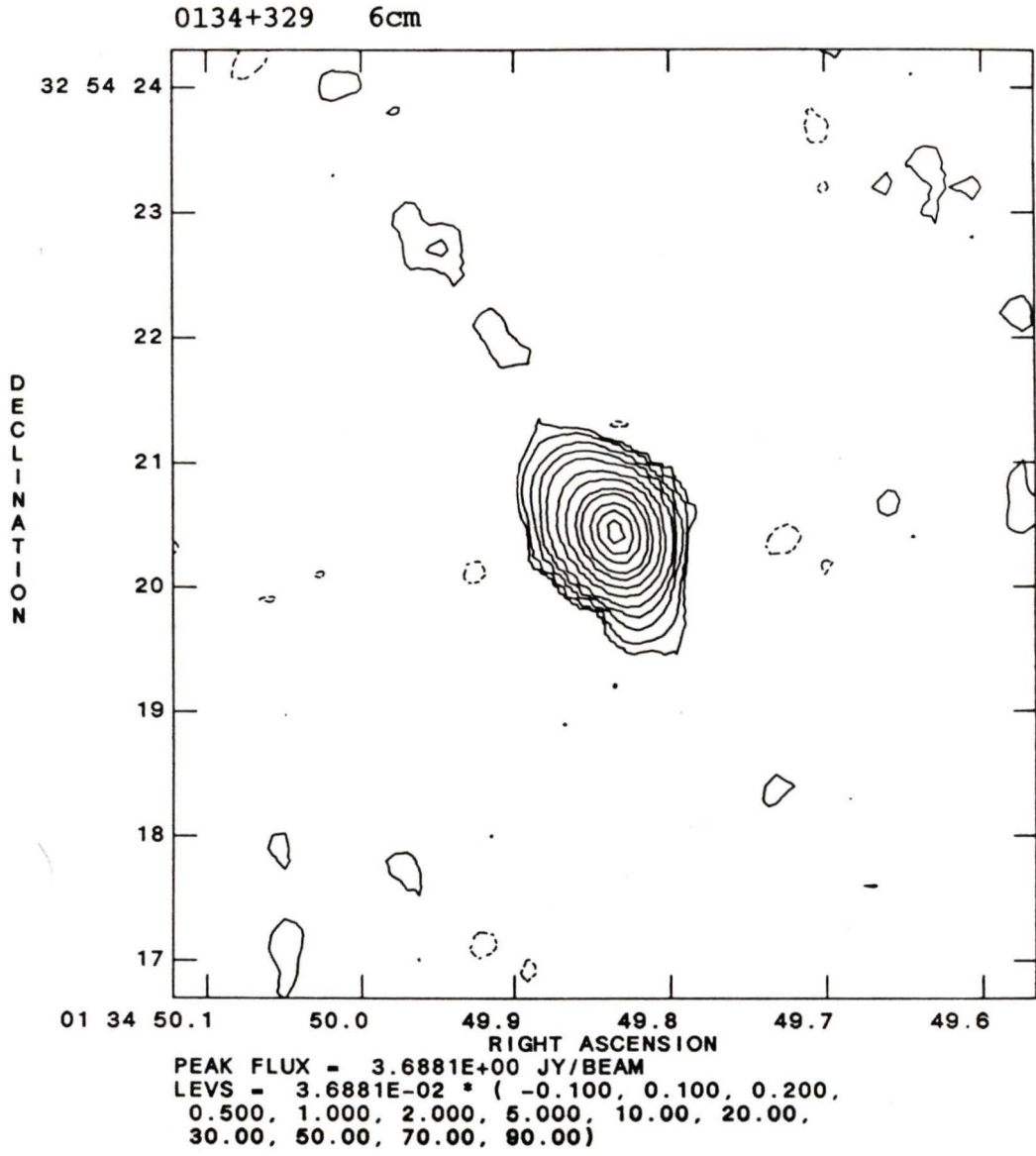
0118+034 6cm

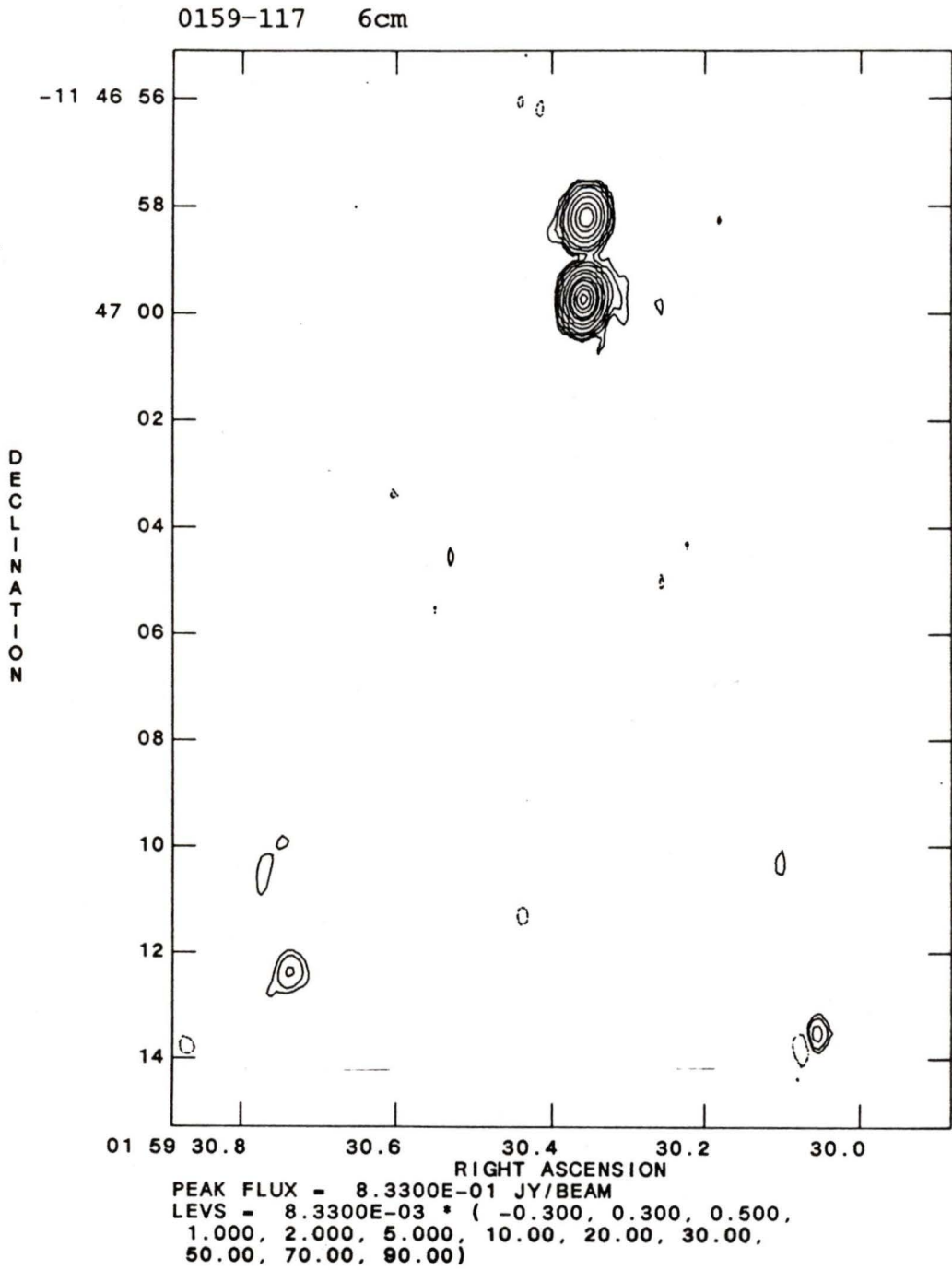


PEAK FLUX = 2.5382E-02 JY/BEAM
LEVS = 2.5382E-04 * (-5.00, 5.000, 10.00,
20.00, 30.00, 50.00, 70.00, 90.00)

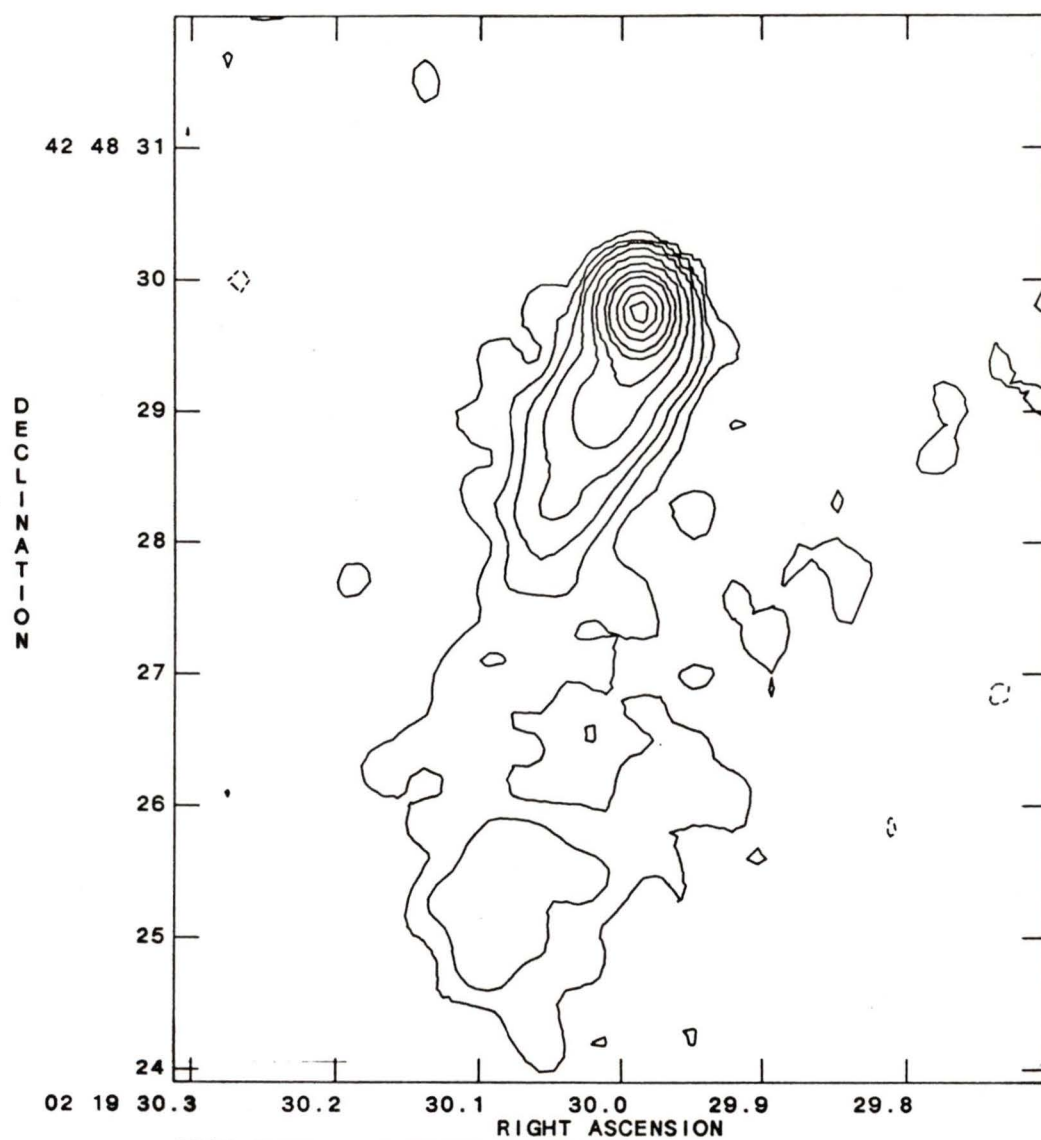






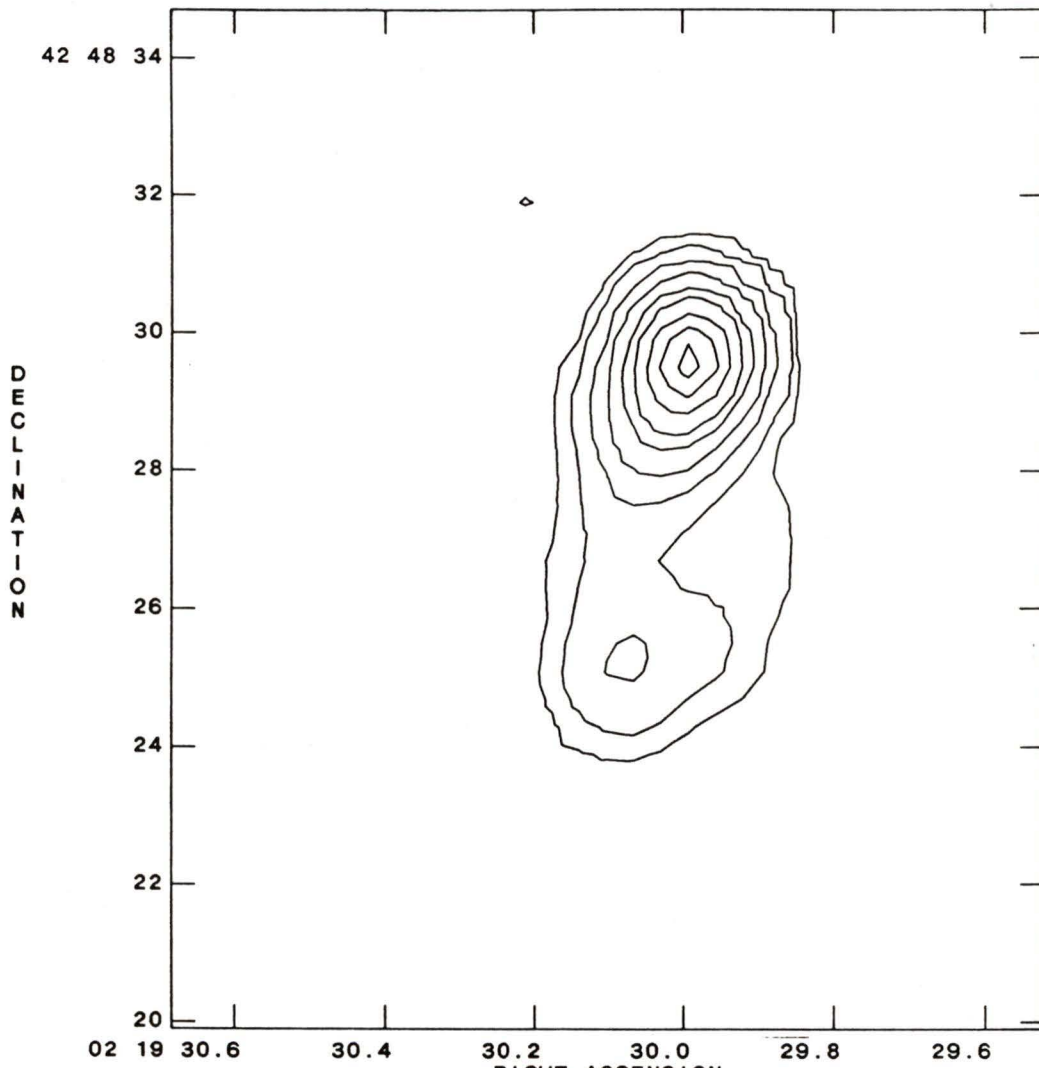


0219+428 6cm

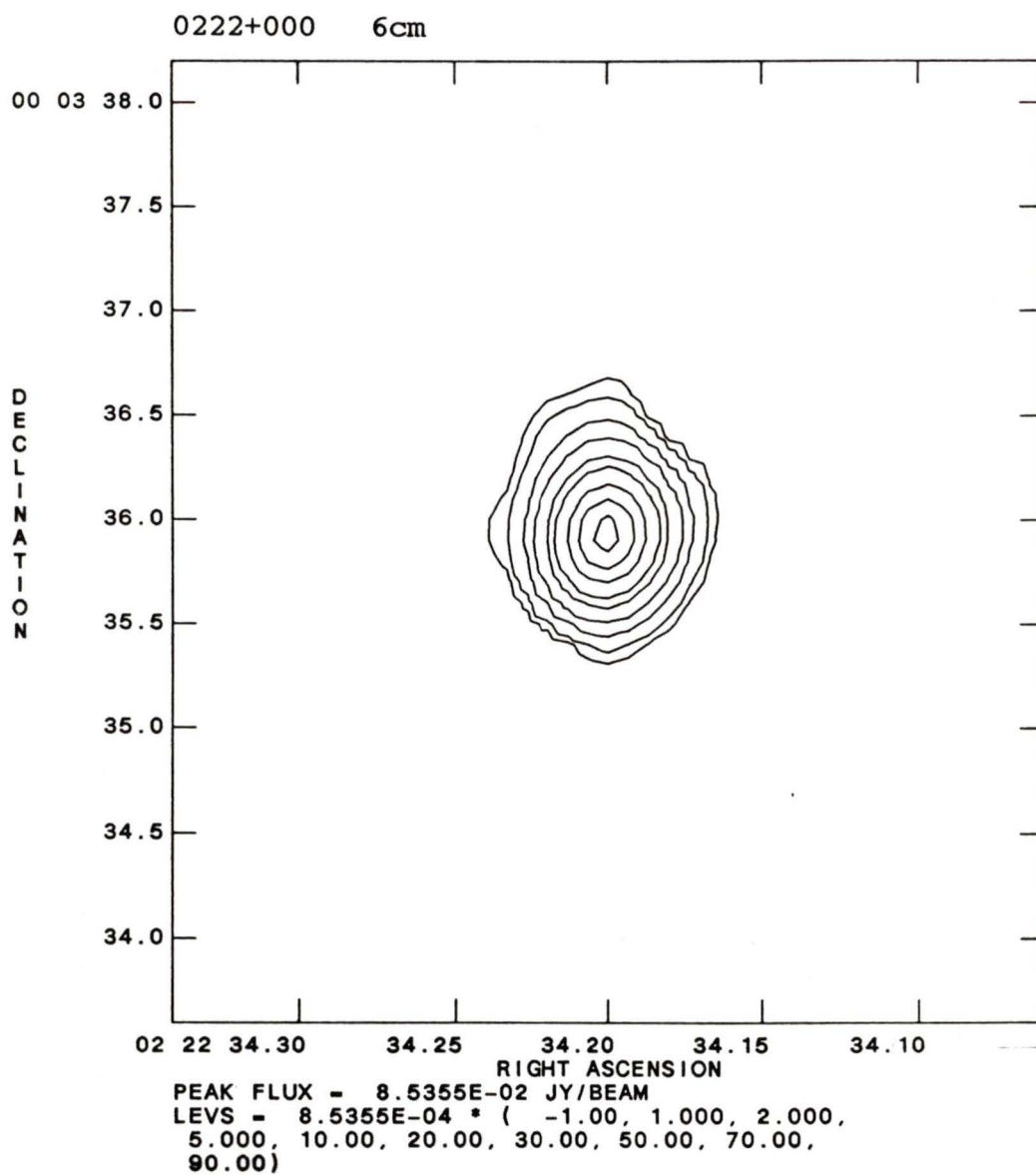


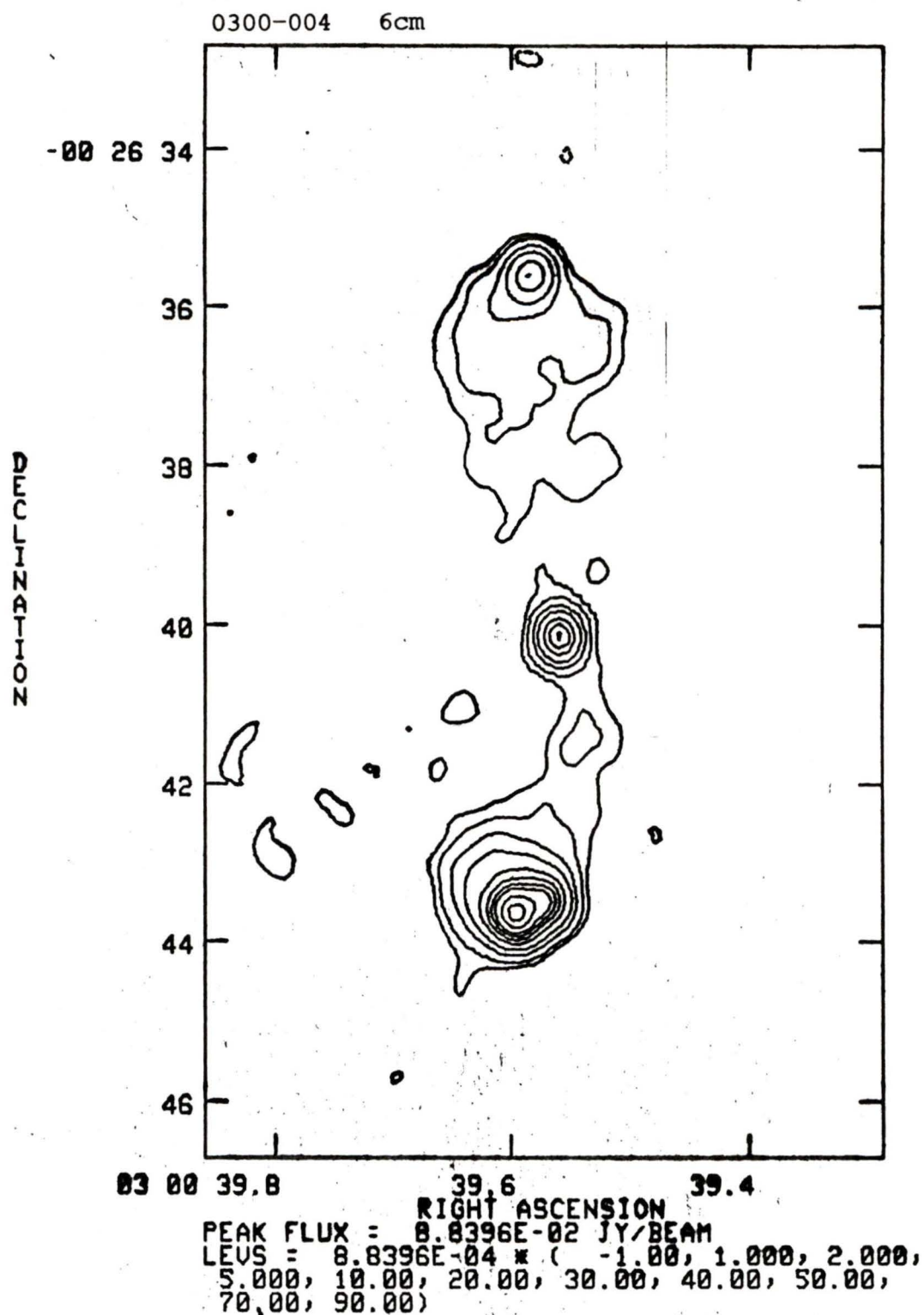
PEAK FLUX = 4.2345E-01 JY/BEAM
LEVS = 4.2345E-03 * (-0.200, 0.200, 0.500,
1.000, 2.000, 5.000, 10.00, 20.00, 30.00,
50.00, 70.00, 90.00)

0219+428 20cm

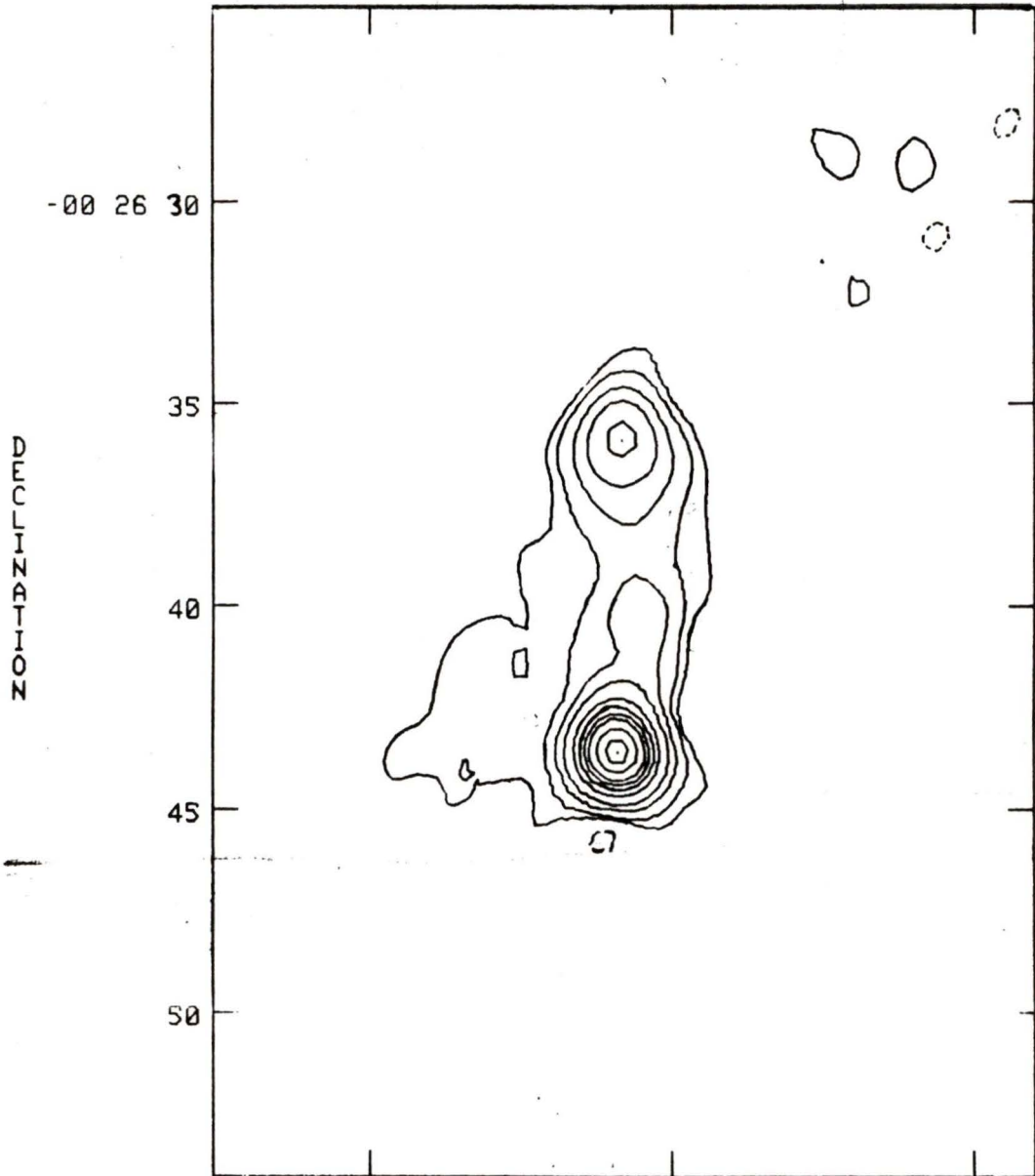


PEAK FLUX = 6.5807E-01 JY/BEAM
LEVS = 6.5807E-03 * (-1.00, 1.000, 2.000,
5.000, 10.00, 20.00, 30.00, 50.00, 70.00,
90.00)

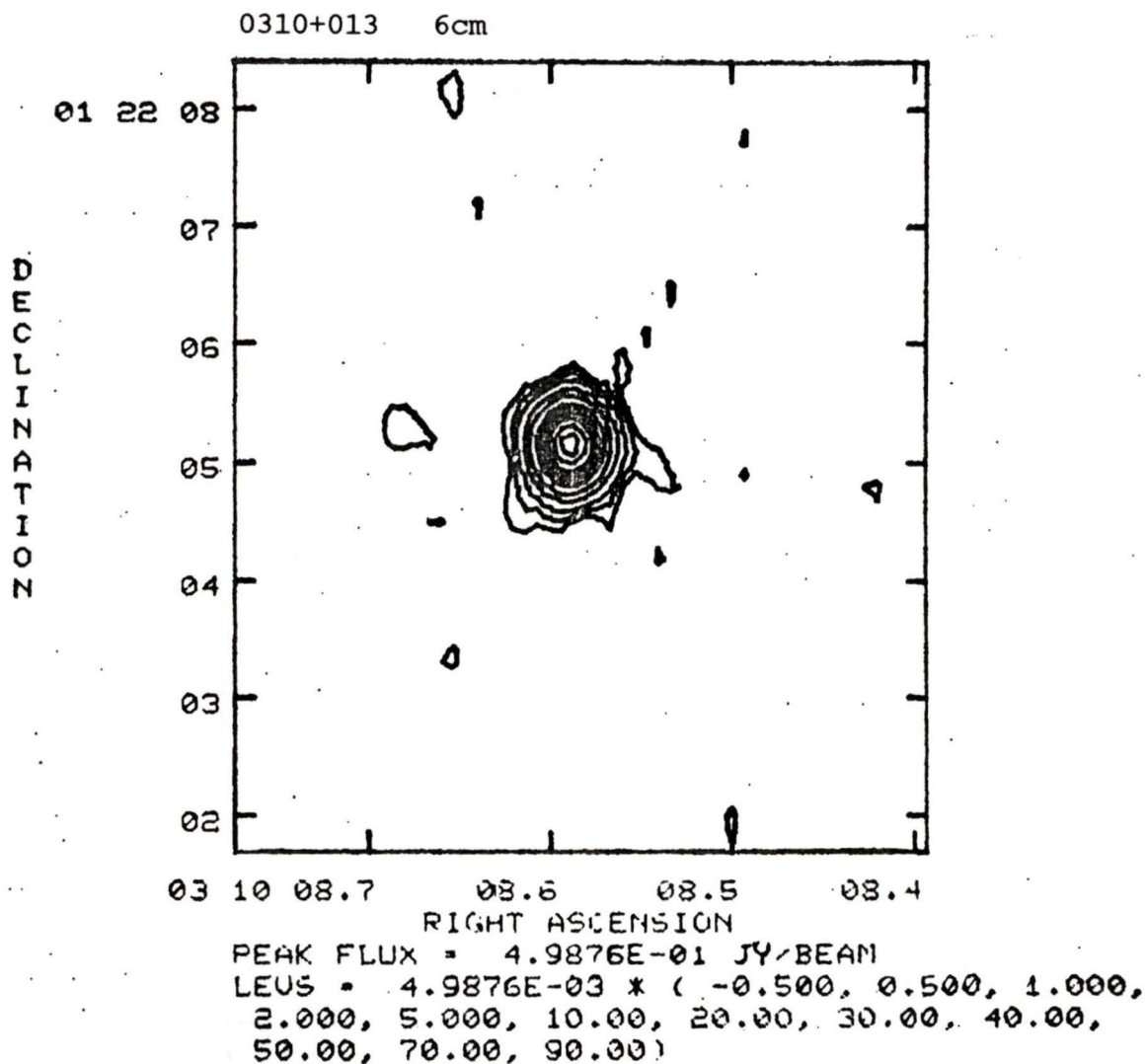


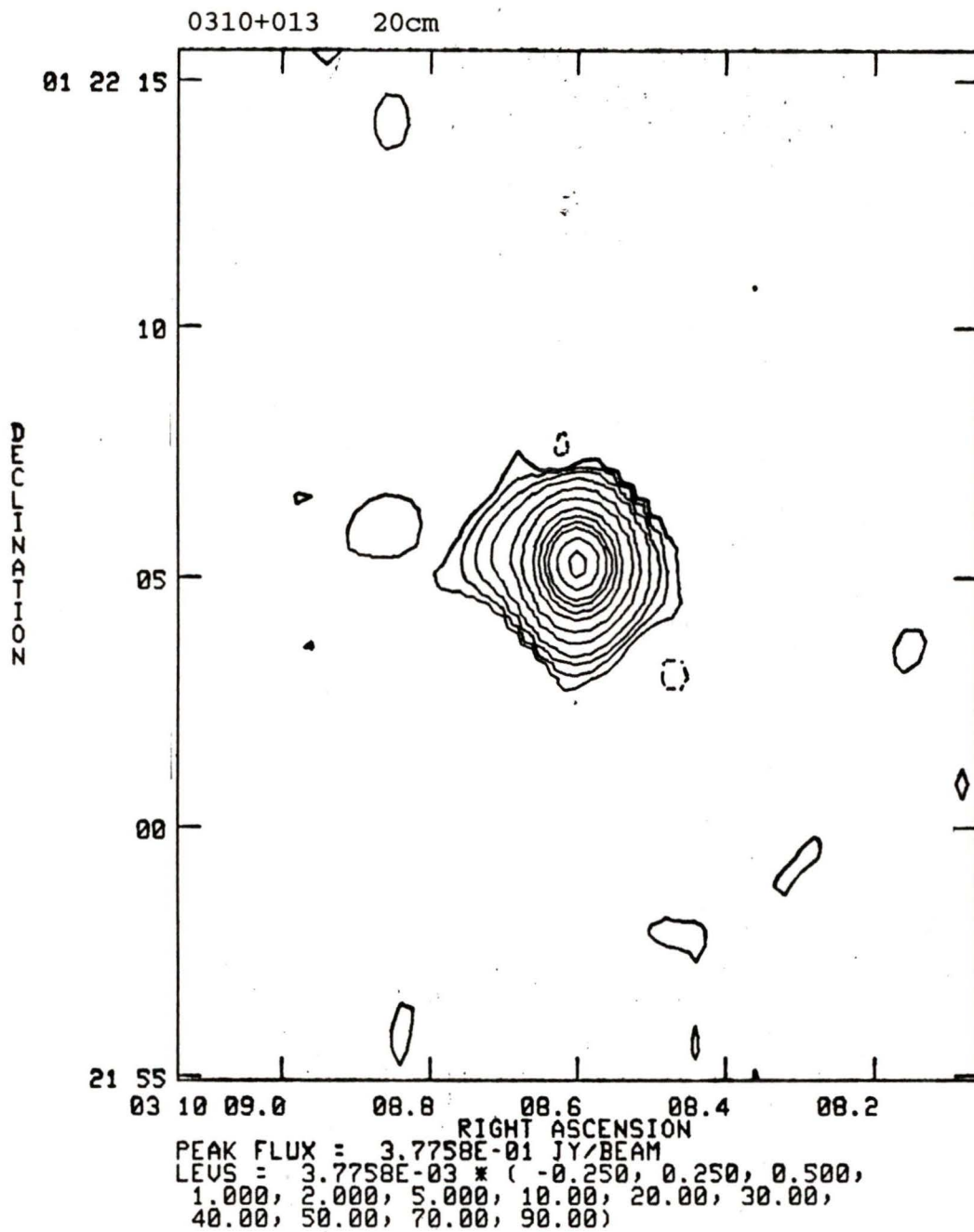


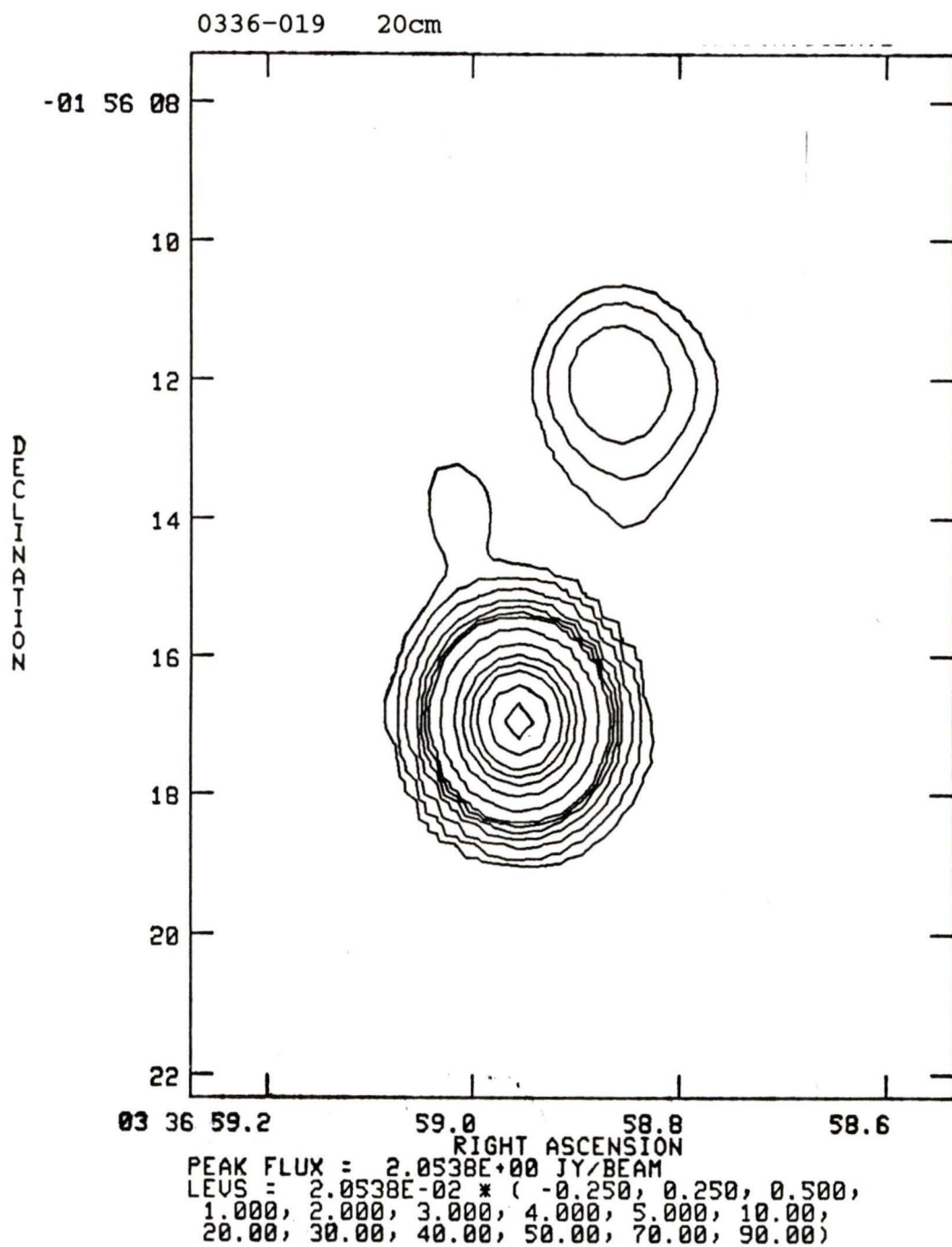
0300-004 20cm

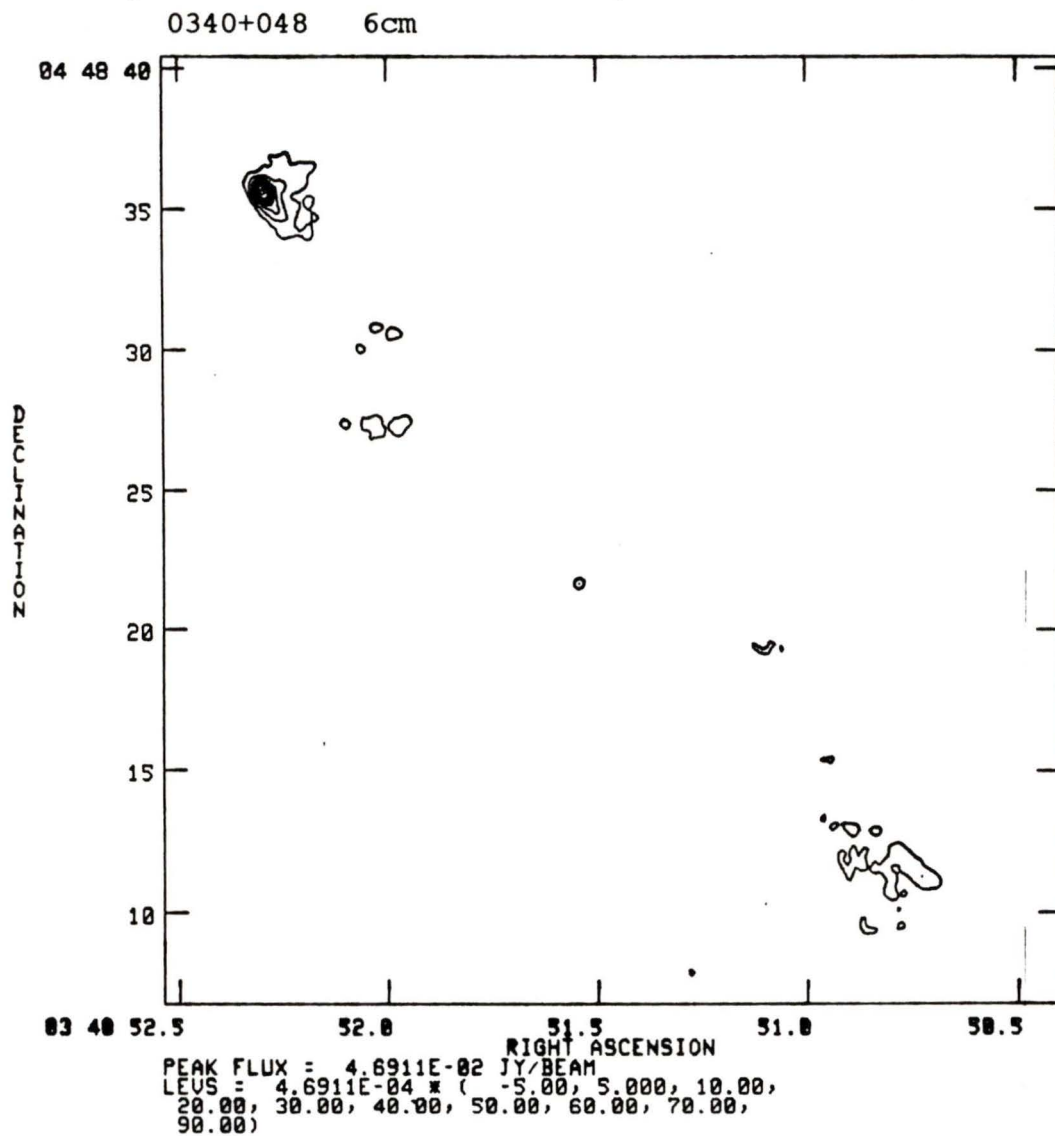


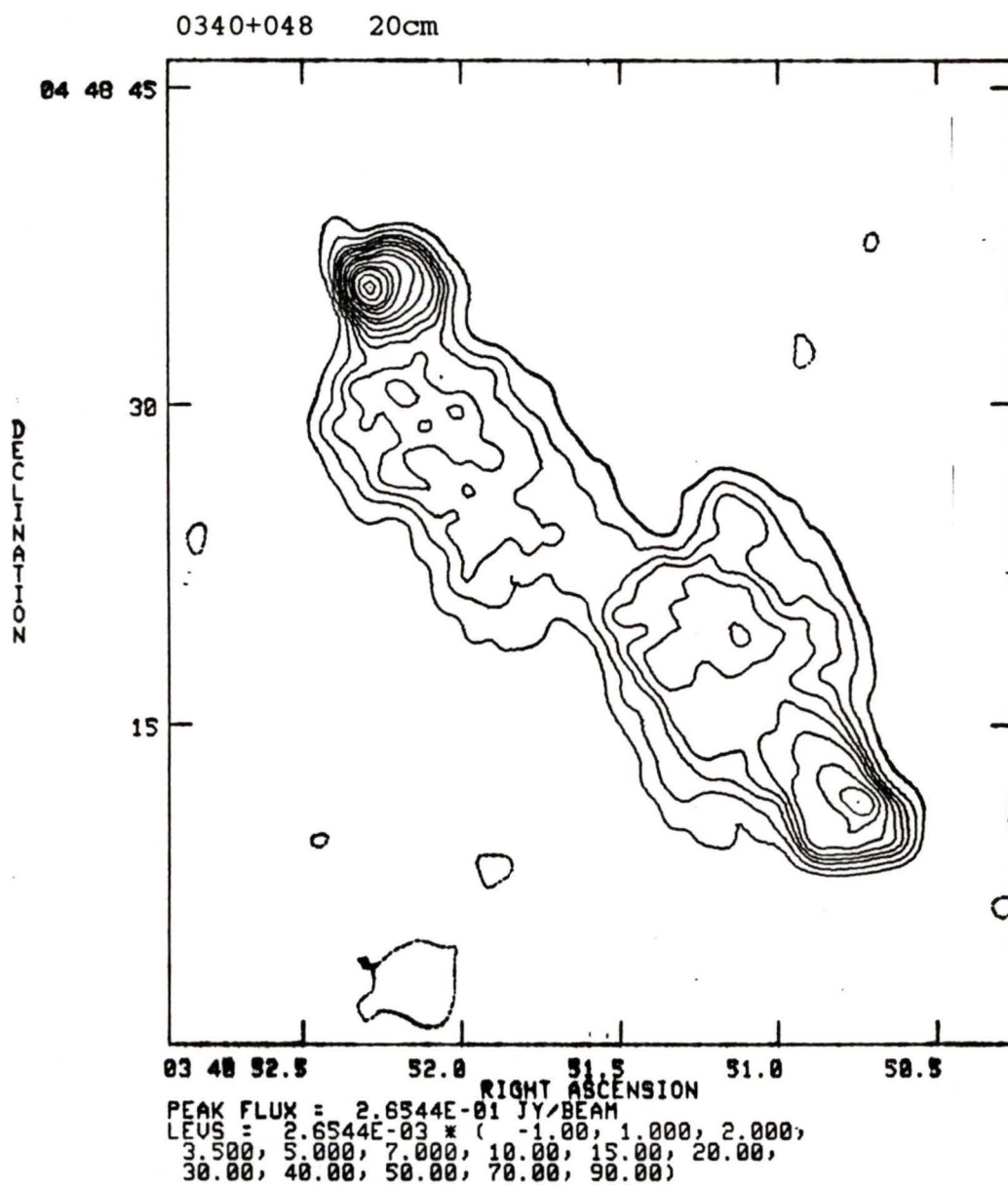
03 00 40.0 39.5 39.0
 RIGHT ASCENSION
 PEAK FLUX = 5.0560E-01 JY/BEAM
 LEVS = 5 0560E-03 * (-1.00, 1.000, 2.000,
 5.000, 10.00, 20.00, 30.00, 40.00, 50.00,
 70.00, 90.00)

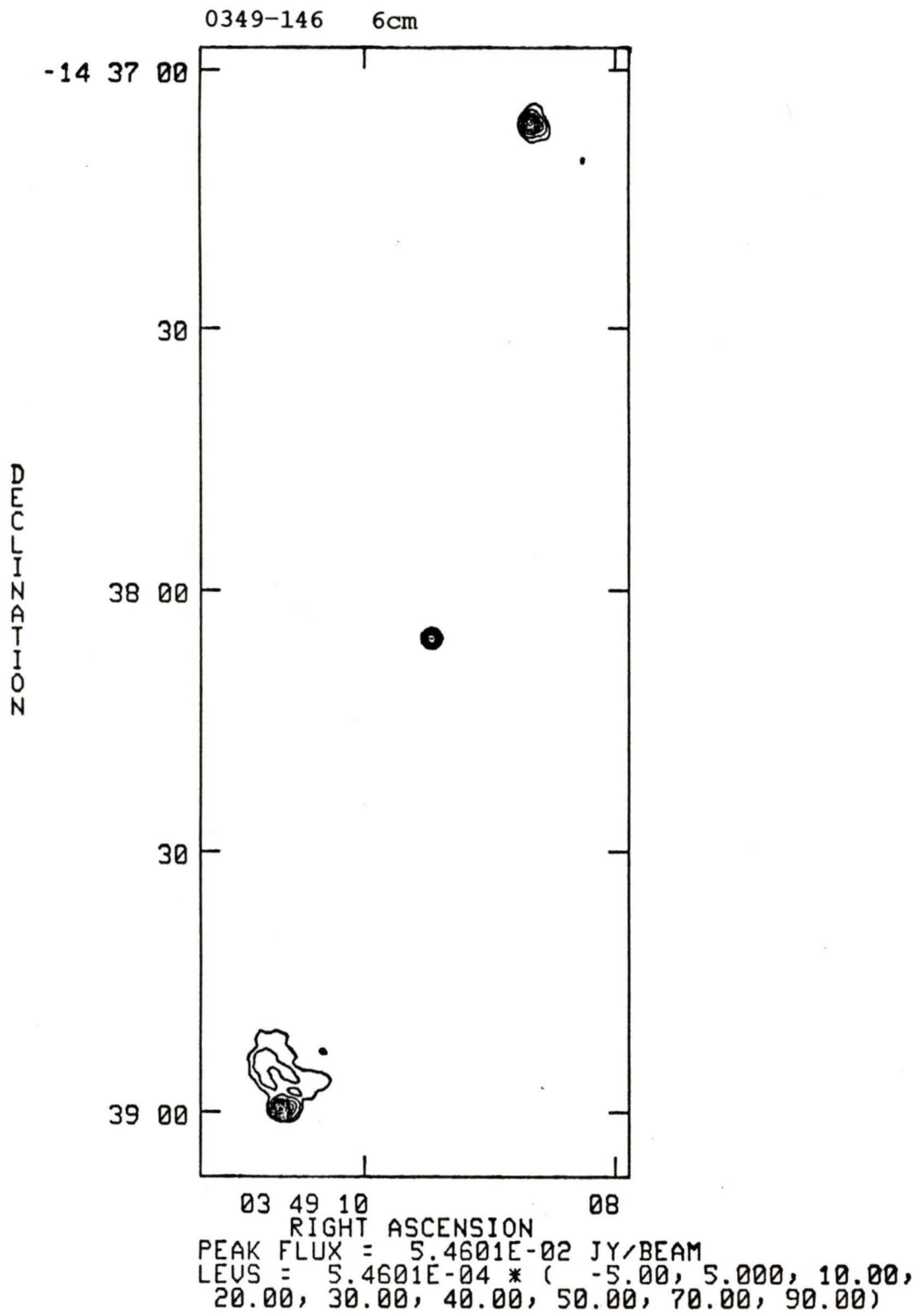




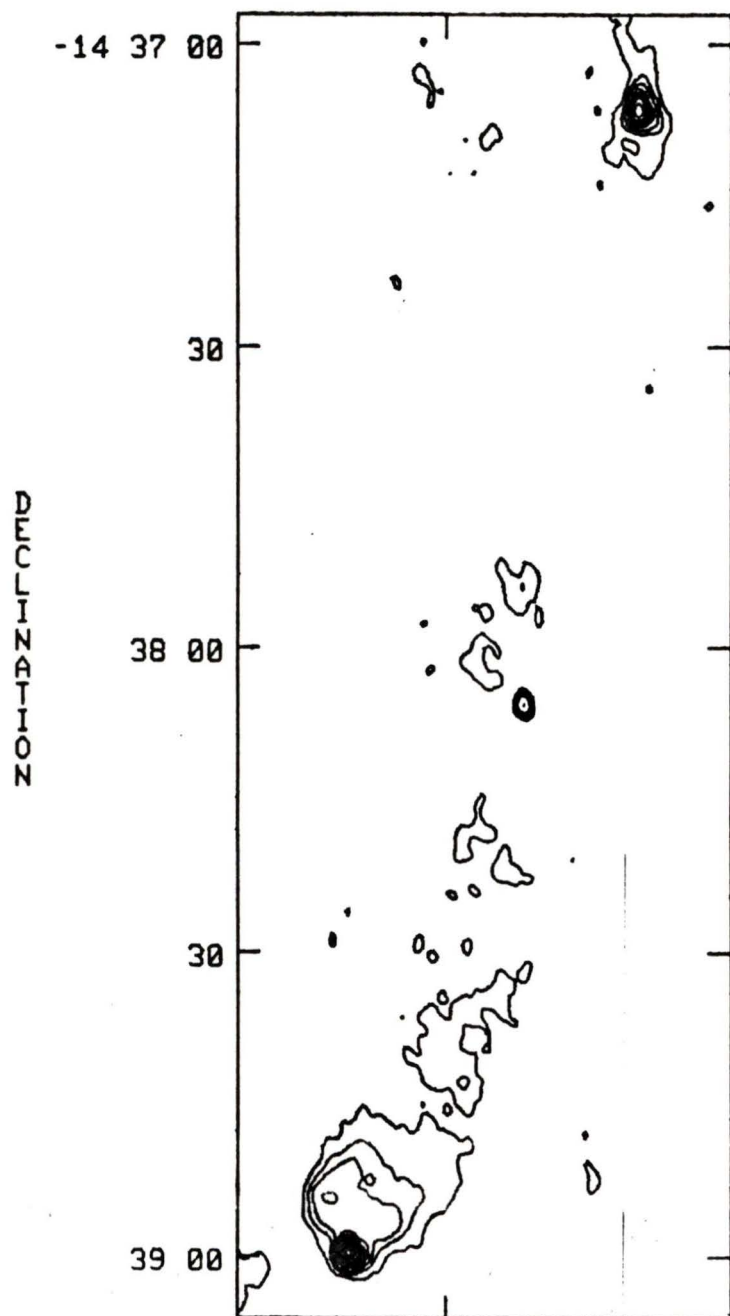








0349-146 20cm



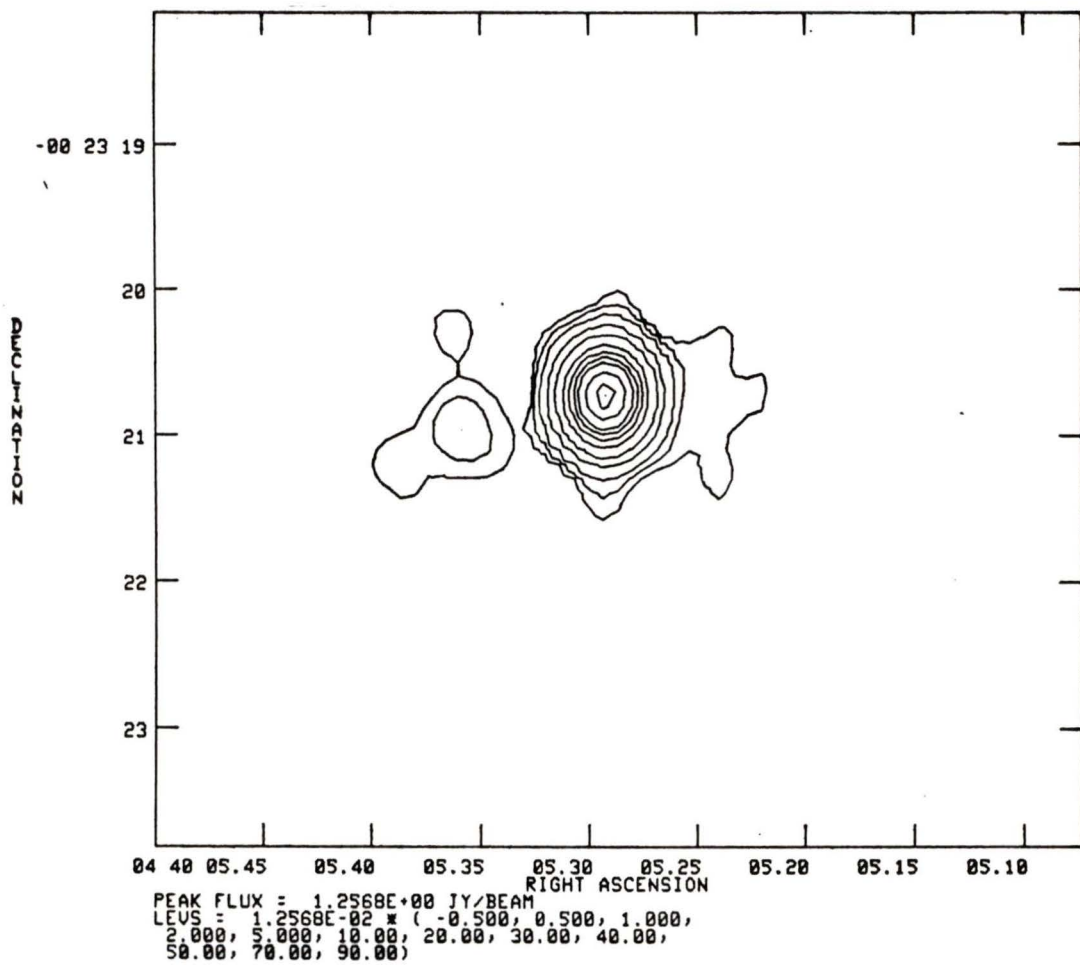
03 49 10

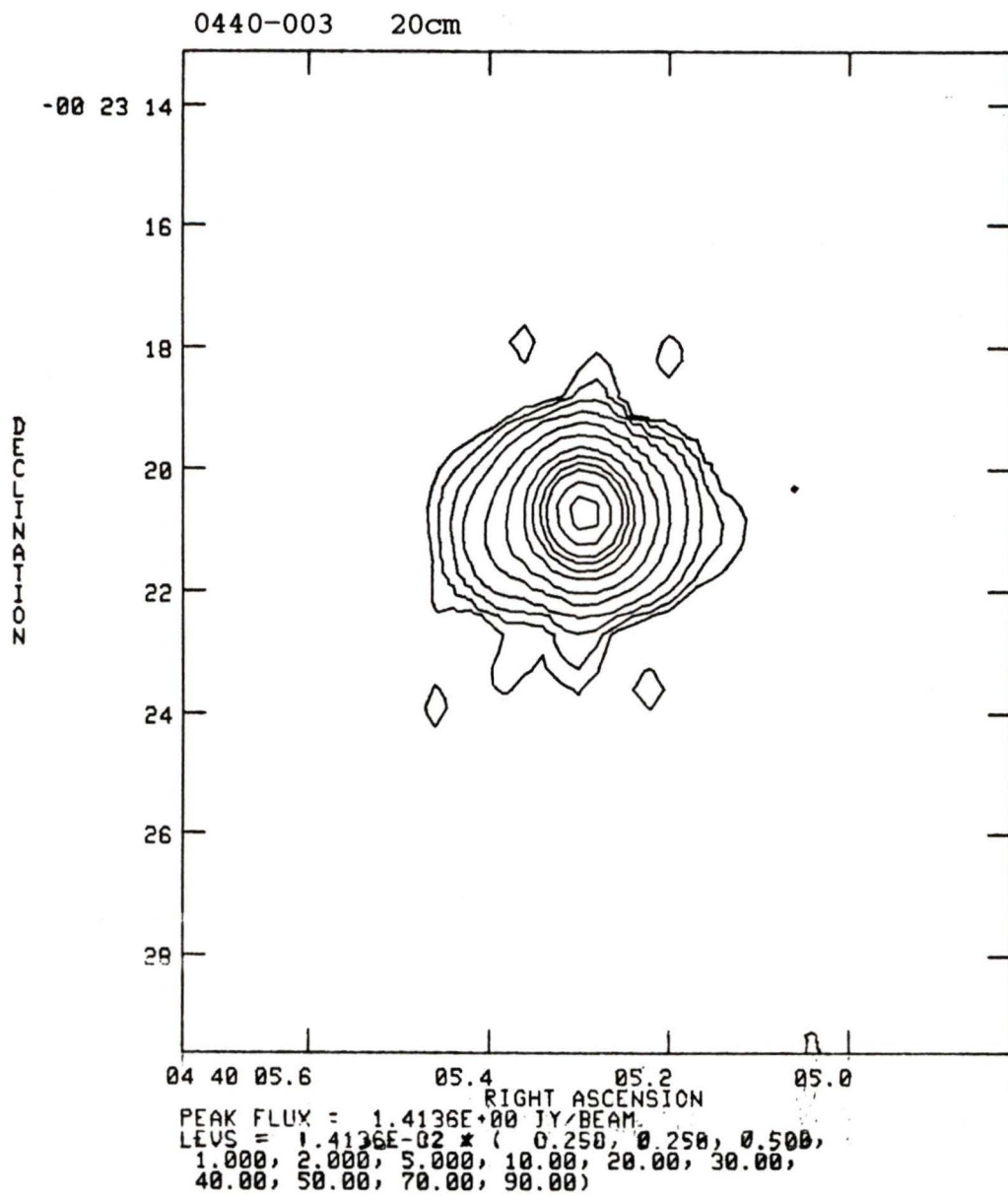
RIGHT ASCENSION

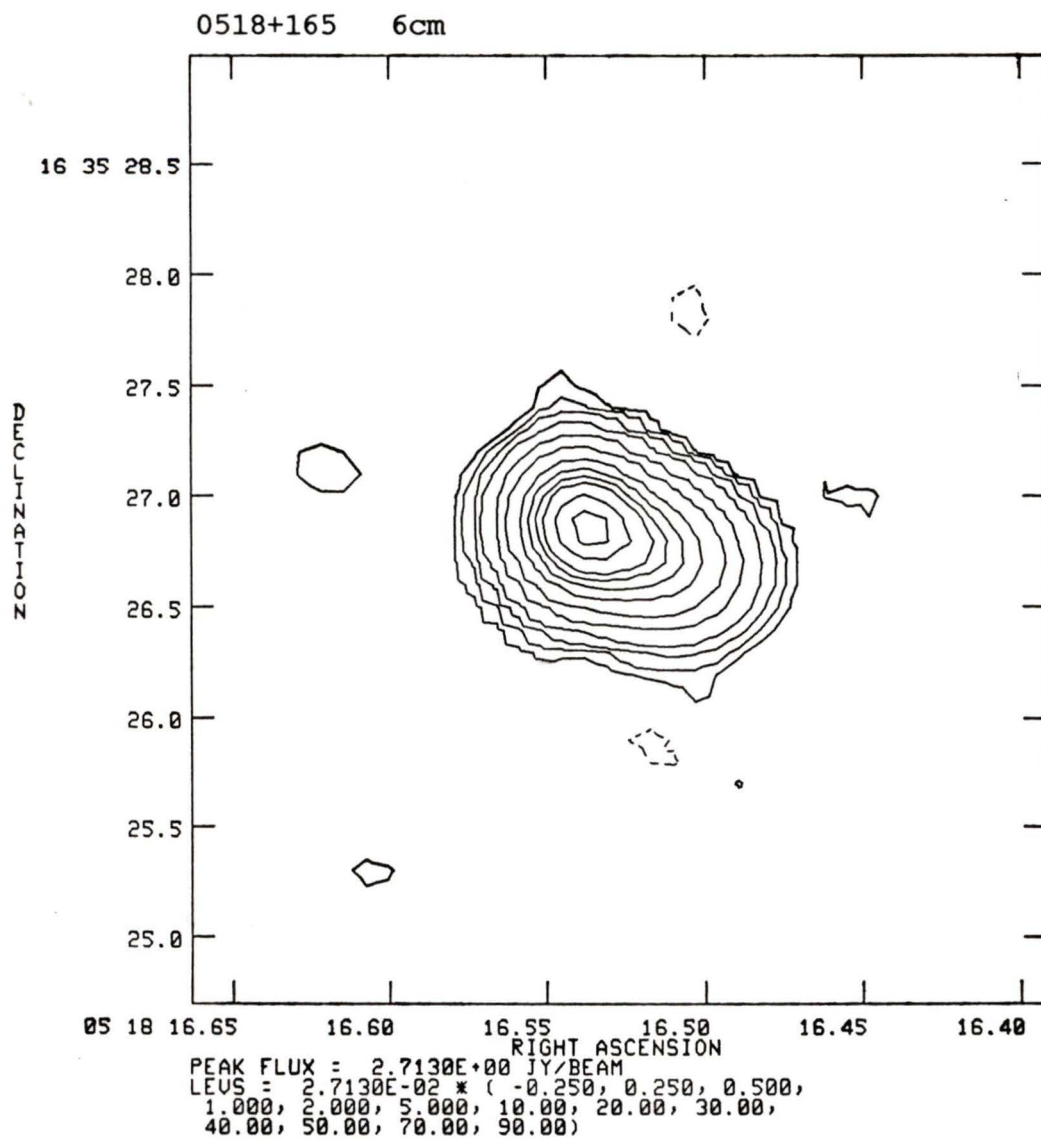
PEAK FLUX = 1.7582E-01 JY/BEAM

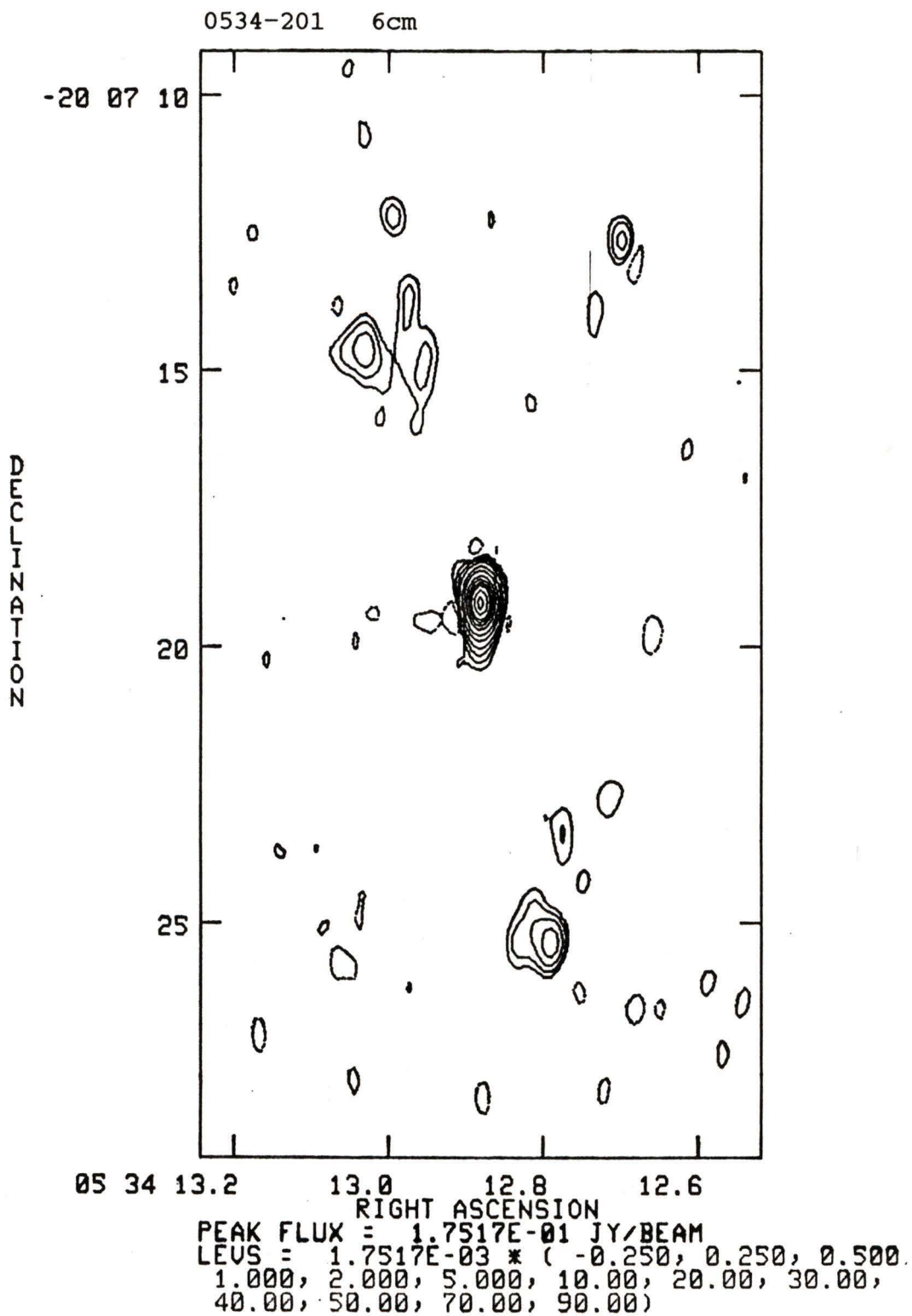
LEVS = 1.7582E-03 * (2.00, 2.000, 5.000
10.00, 20.00, 30.00, 40.00, 50.00, 70.00,
90.00)

0440-003 6cm

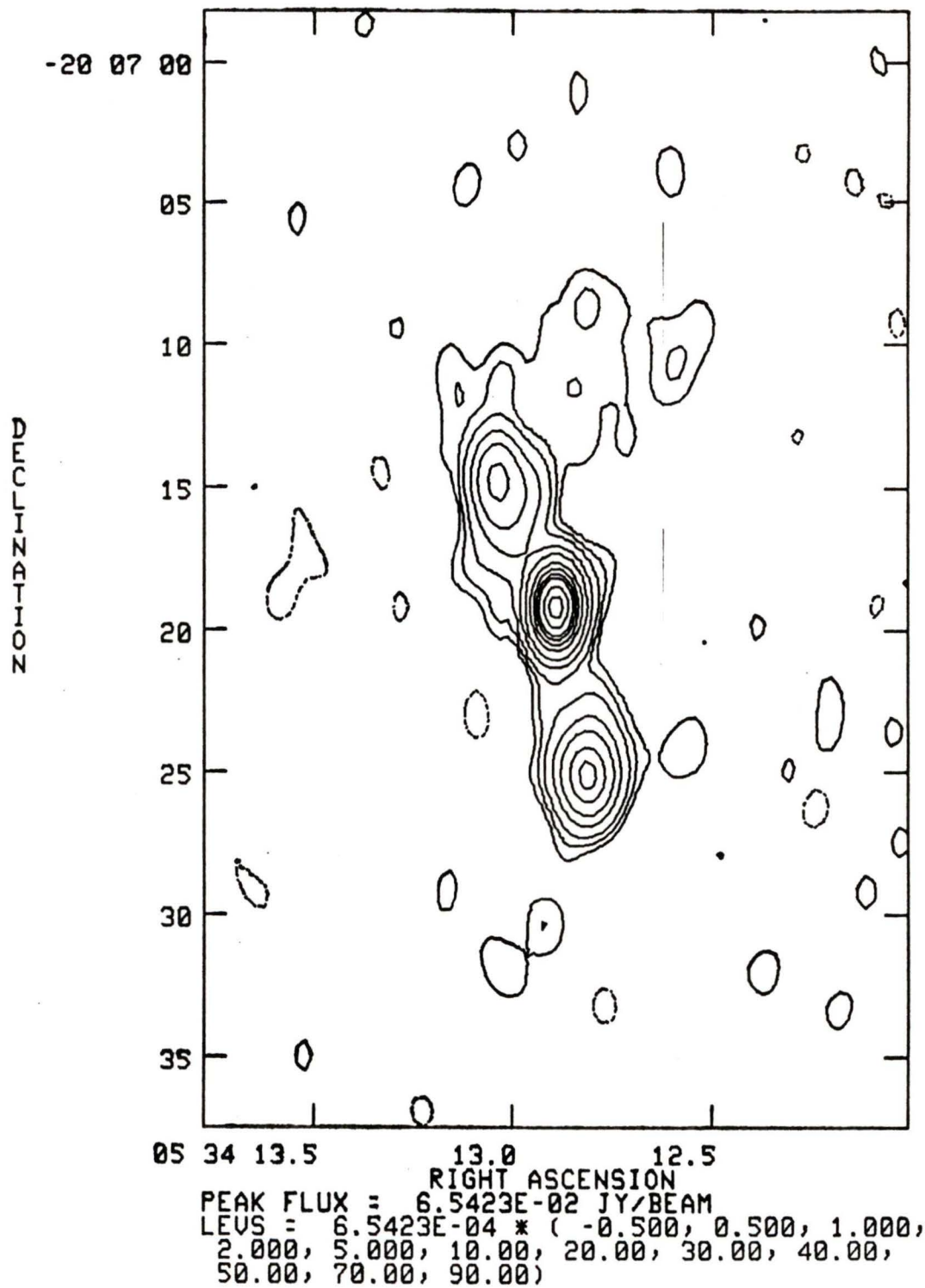




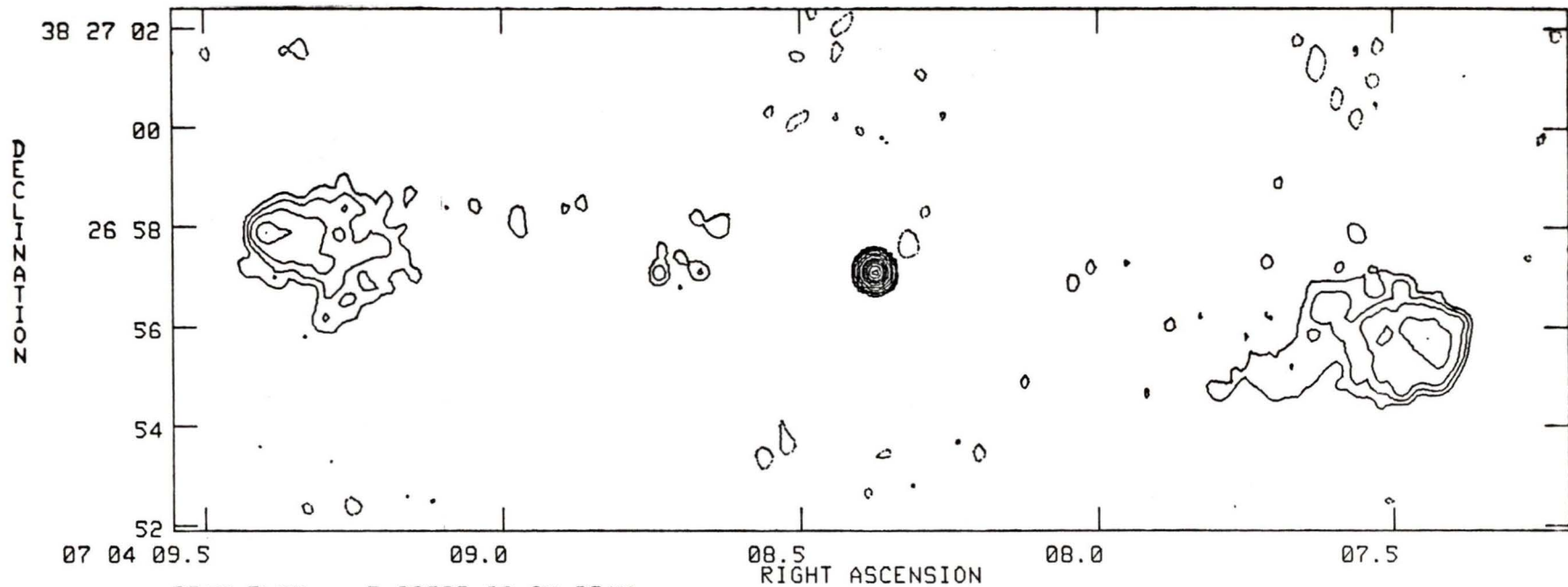




0534-201 20cm

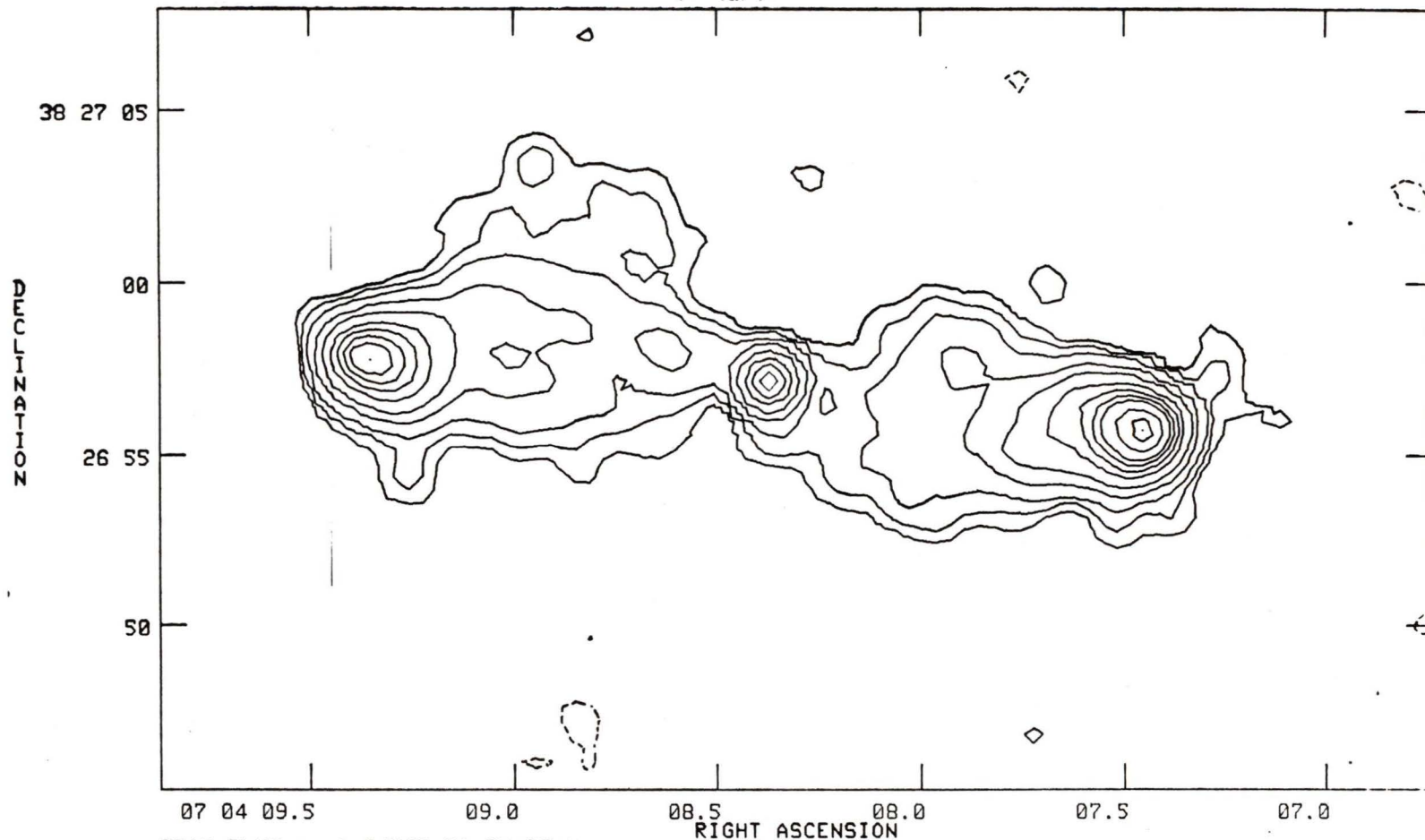


0704+384 6cm



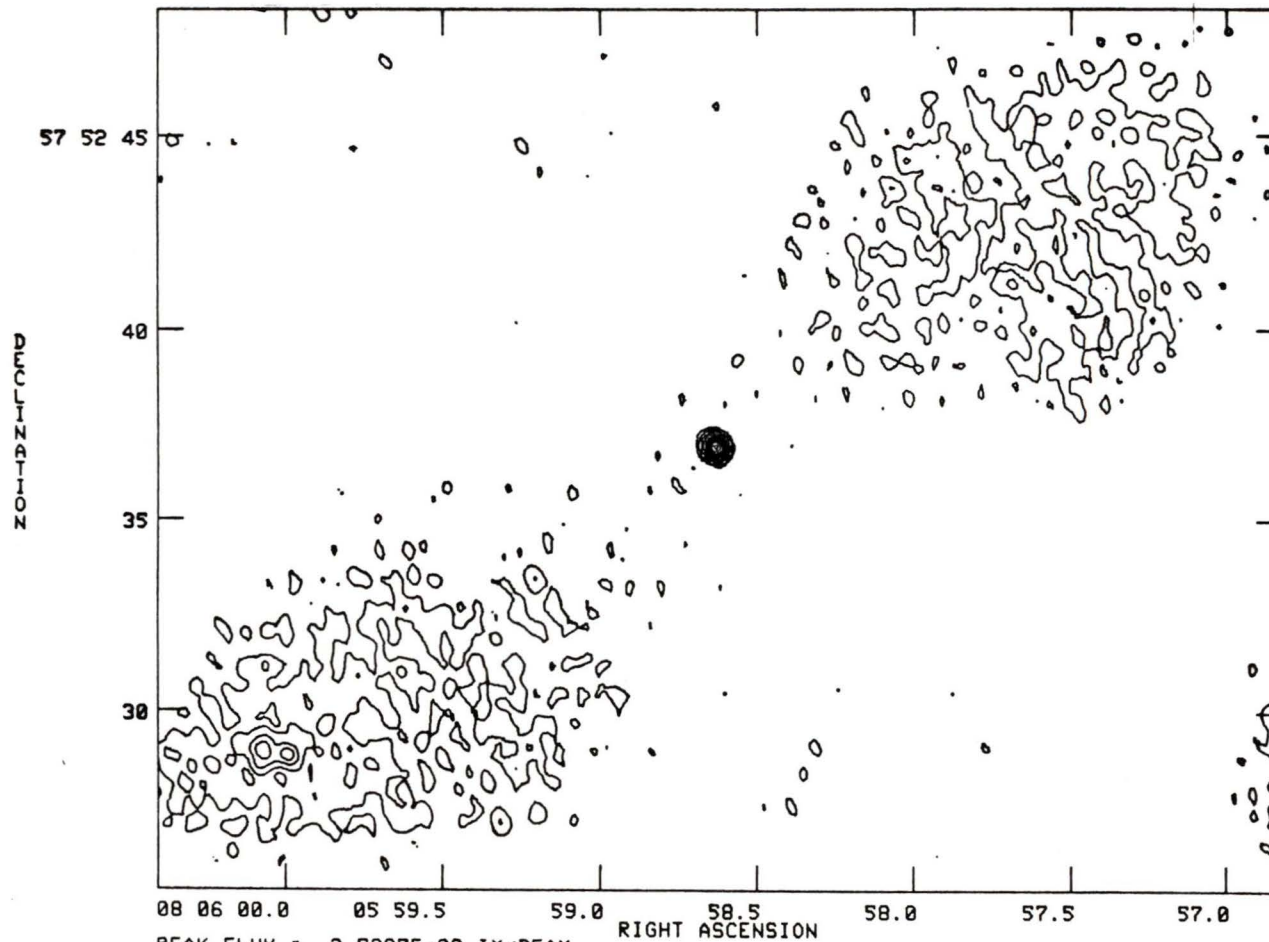
PEAK FLUX = 5.8379E-02 JY/BEAM
LEVS = 5.8379E-04 * (-0.500, 0.500, 1.000,
2.000, 5.000, 10.00, 20.00, 30.00, 40.00,
50.00, 70.00, 90.00)

0704+384 20cm



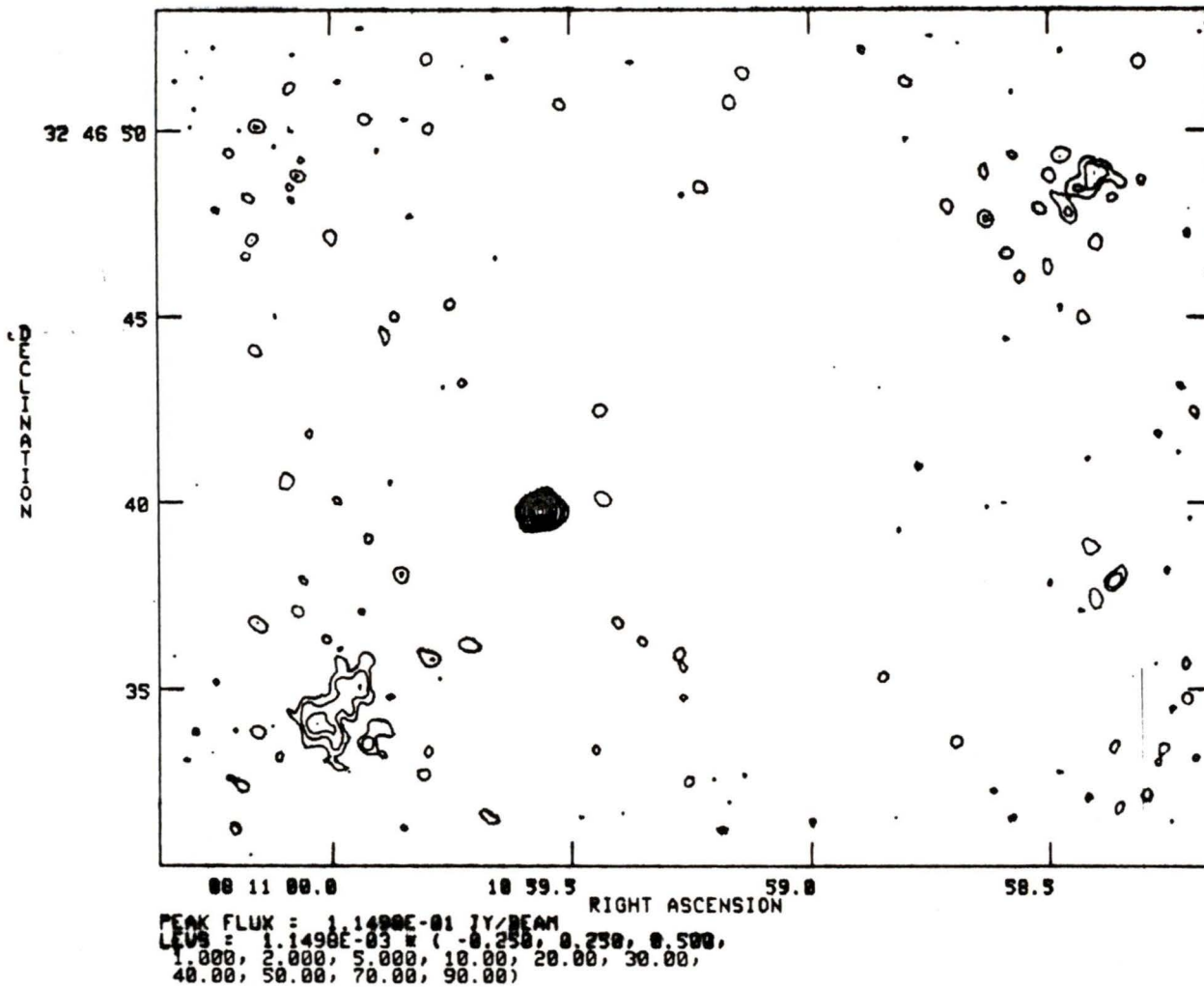
PEAK FLUX = 1.0456E-01 JY/BEAM
LEVS = 1.0456E-03 * (-0.500, 0.500, 1.000,
2.000, 5.000, 10.00, 20.00, 30.00, 40.00,
50.00, 70 00 90 00)

0805+579 6cm

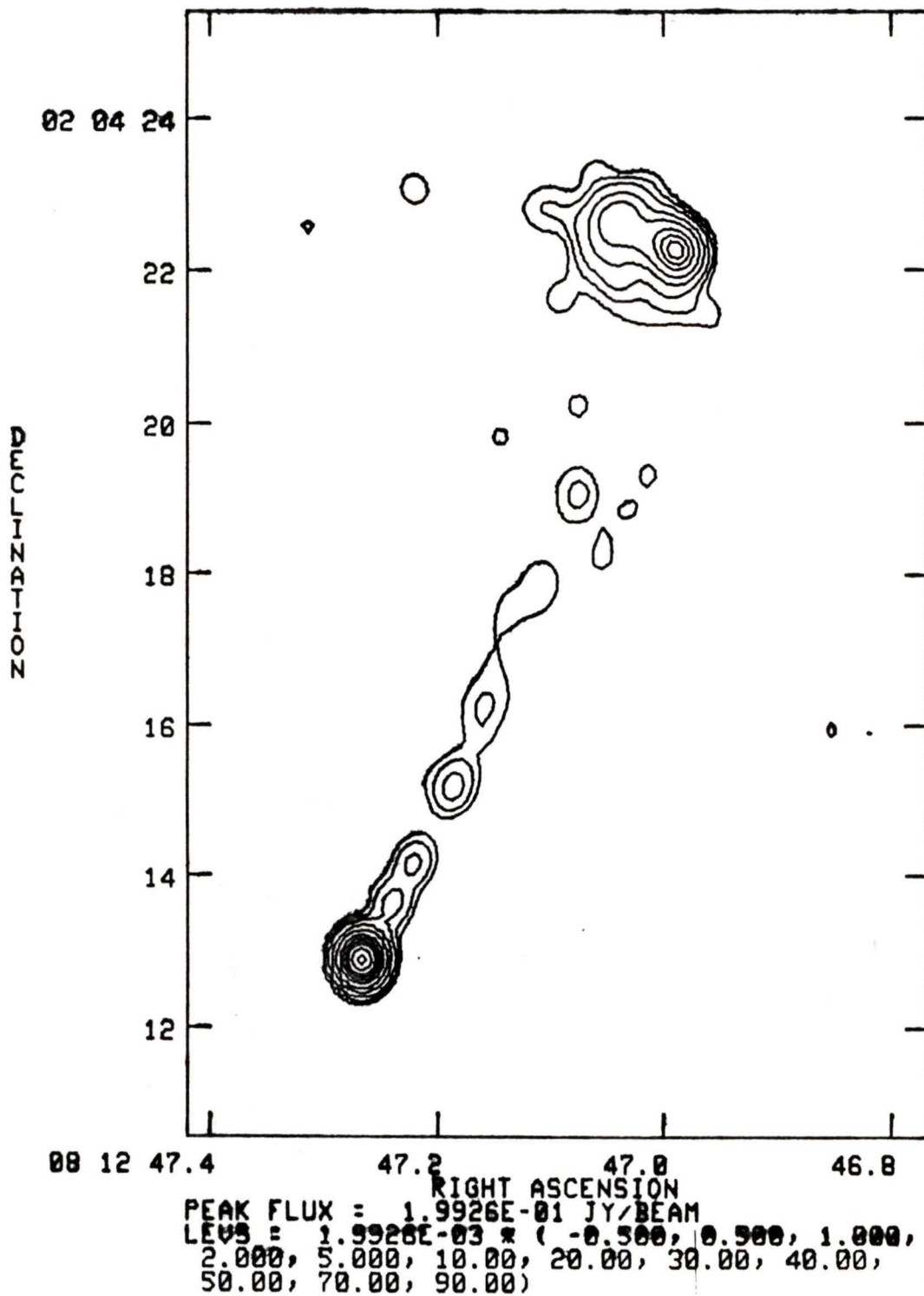


PEAK FLUX = 2.5287E-02 JY/BEAM
LEUS = 2.5287E-04 x (-1.00, 1.000, 2.000,
5.000, 10.00, 20.00, 30.00, 40.00, 50.00,
70.00, 90.00)

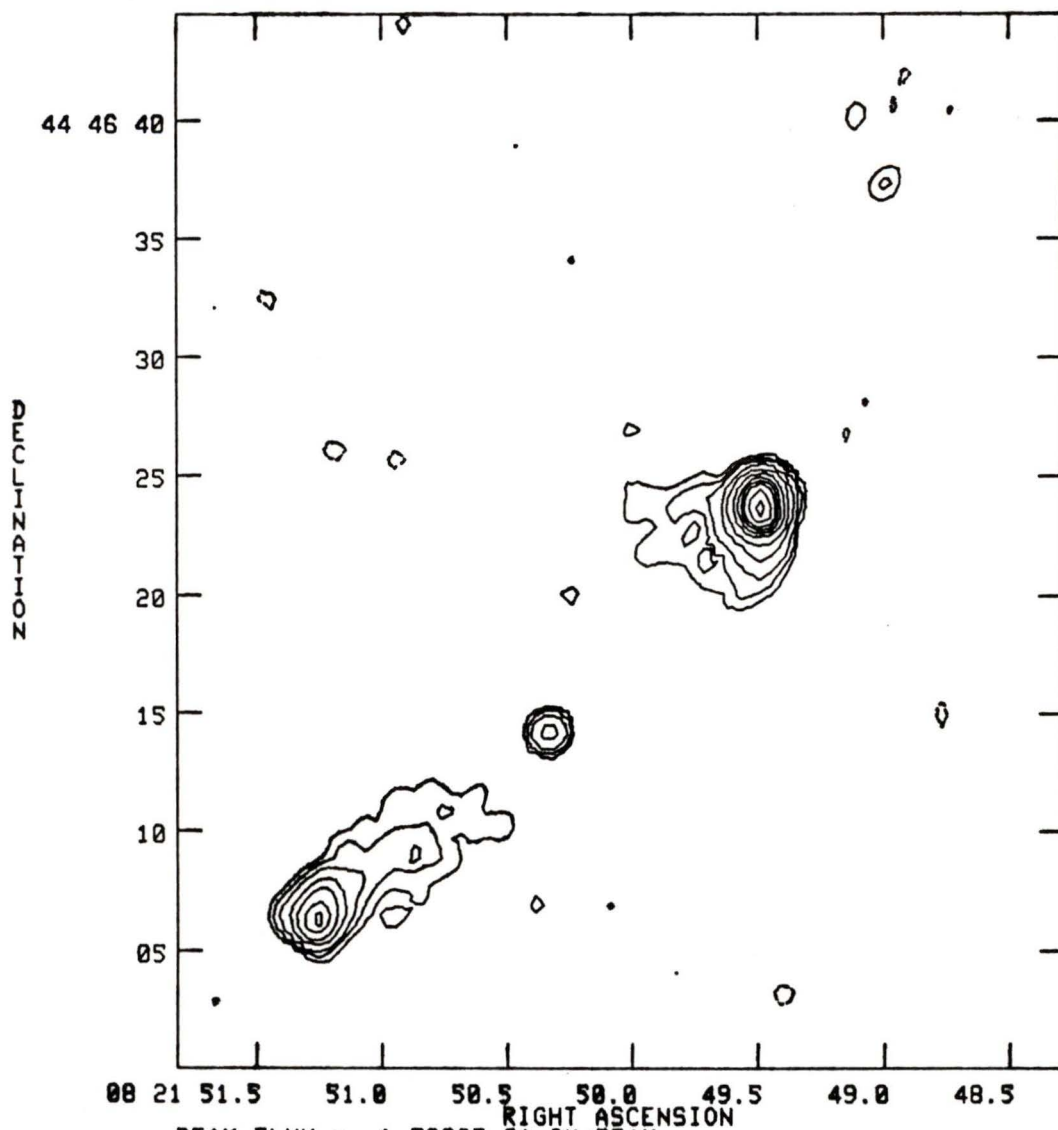
0810+327 6cm



0812+020 6cm



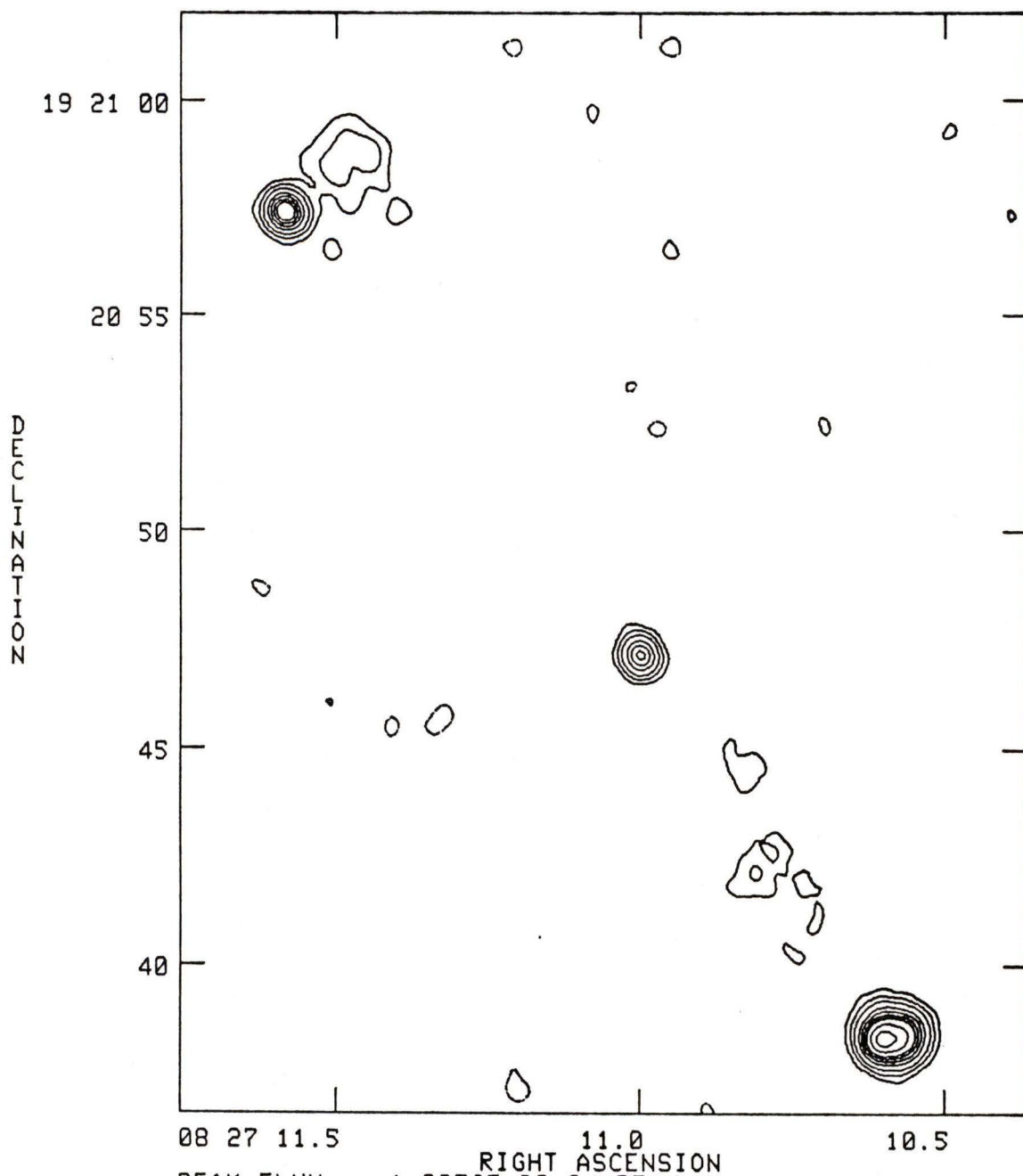
0821+447 20cm



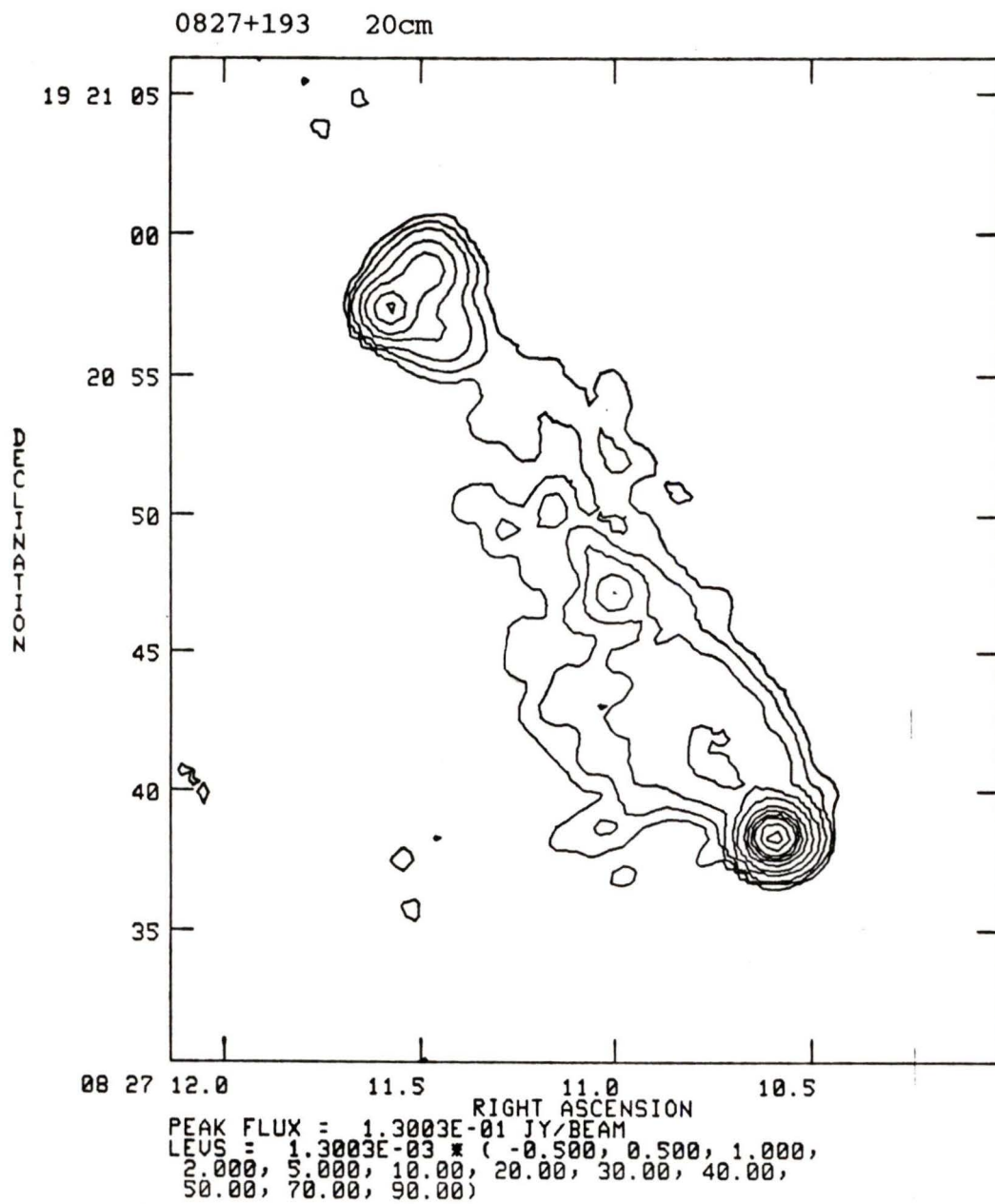
00 21 51.5 51.0 50.5 50.0 49.5 49.0 48.5
RIGHT ASCENSION

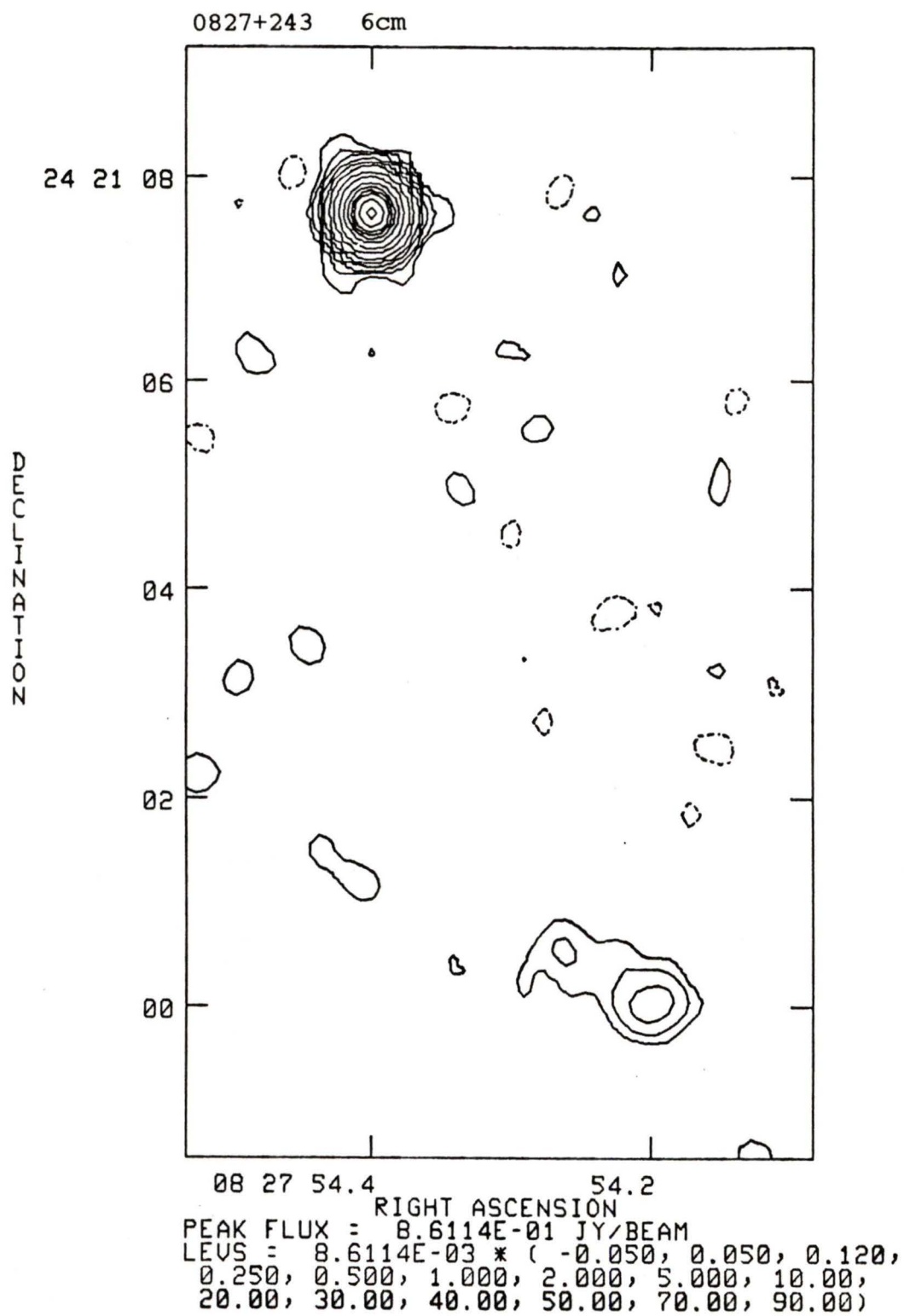
PEAK FLUX = 1.7002E-01 JY/BEAM
LEUS = 1.7002E-03 * (-0.500, 0.500, 1.000,
2.000, 5.000, 10.00, 20.00, 30.00, 40.00,
50.00, 70.00, 90.00)

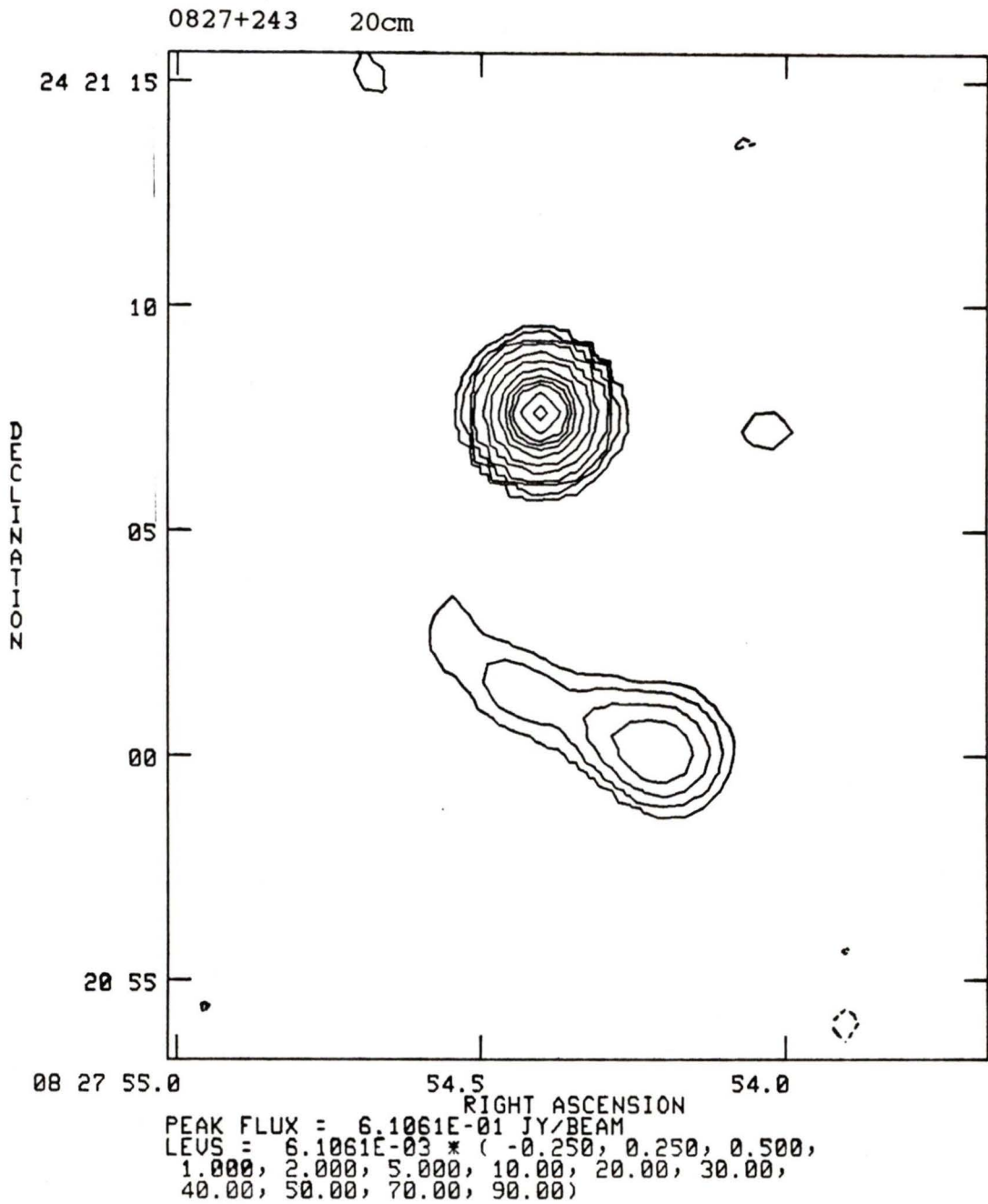
0827+193 6cm



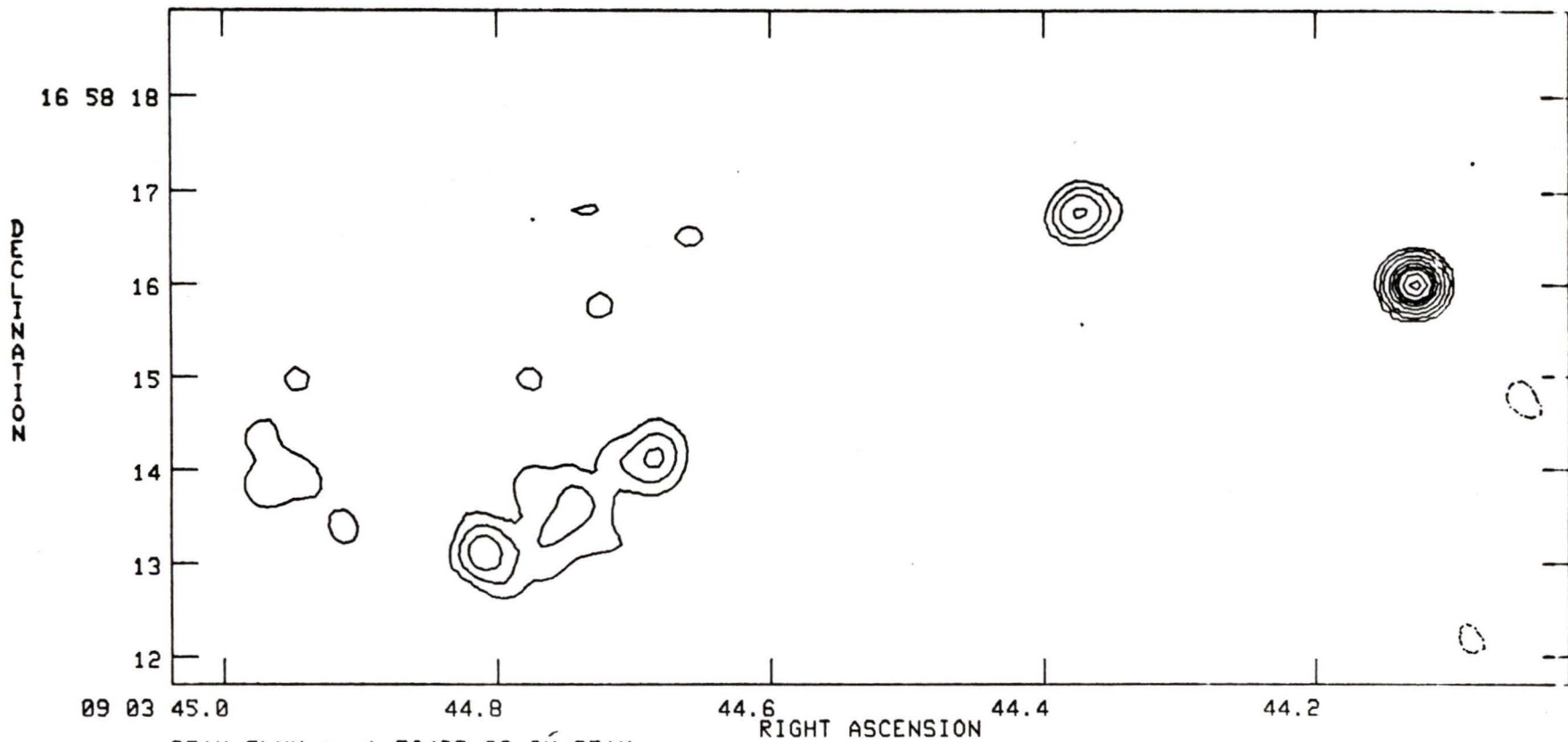
PEAK FLUX = 1.8056E-02 JY/BEAM
 LEVS = 1.8056E-04 * (-2.00, 2.000, 5.000,
 10.00, 20.00, 30.00, 40.00, 50.00, 70.00,
 90.00)



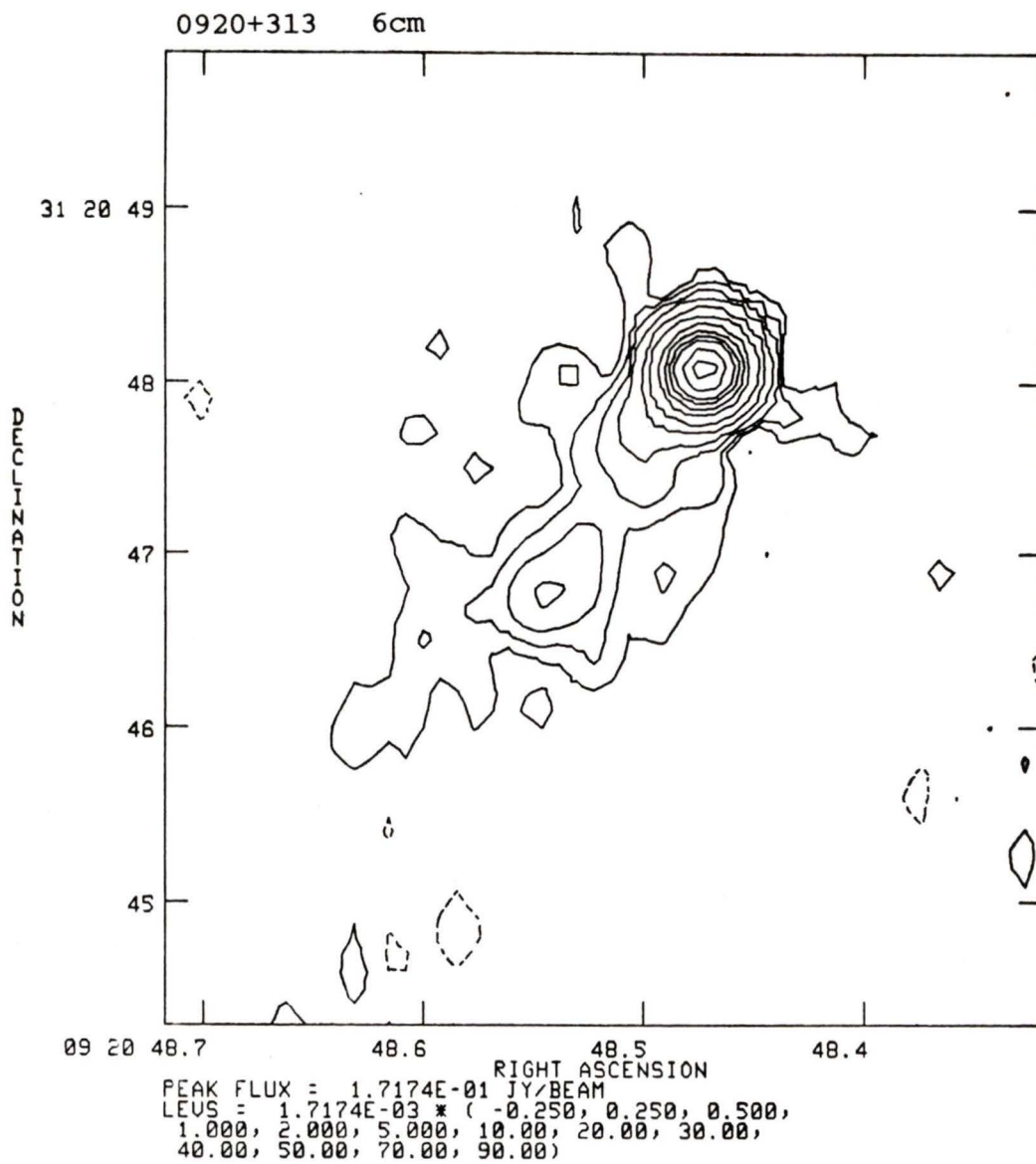


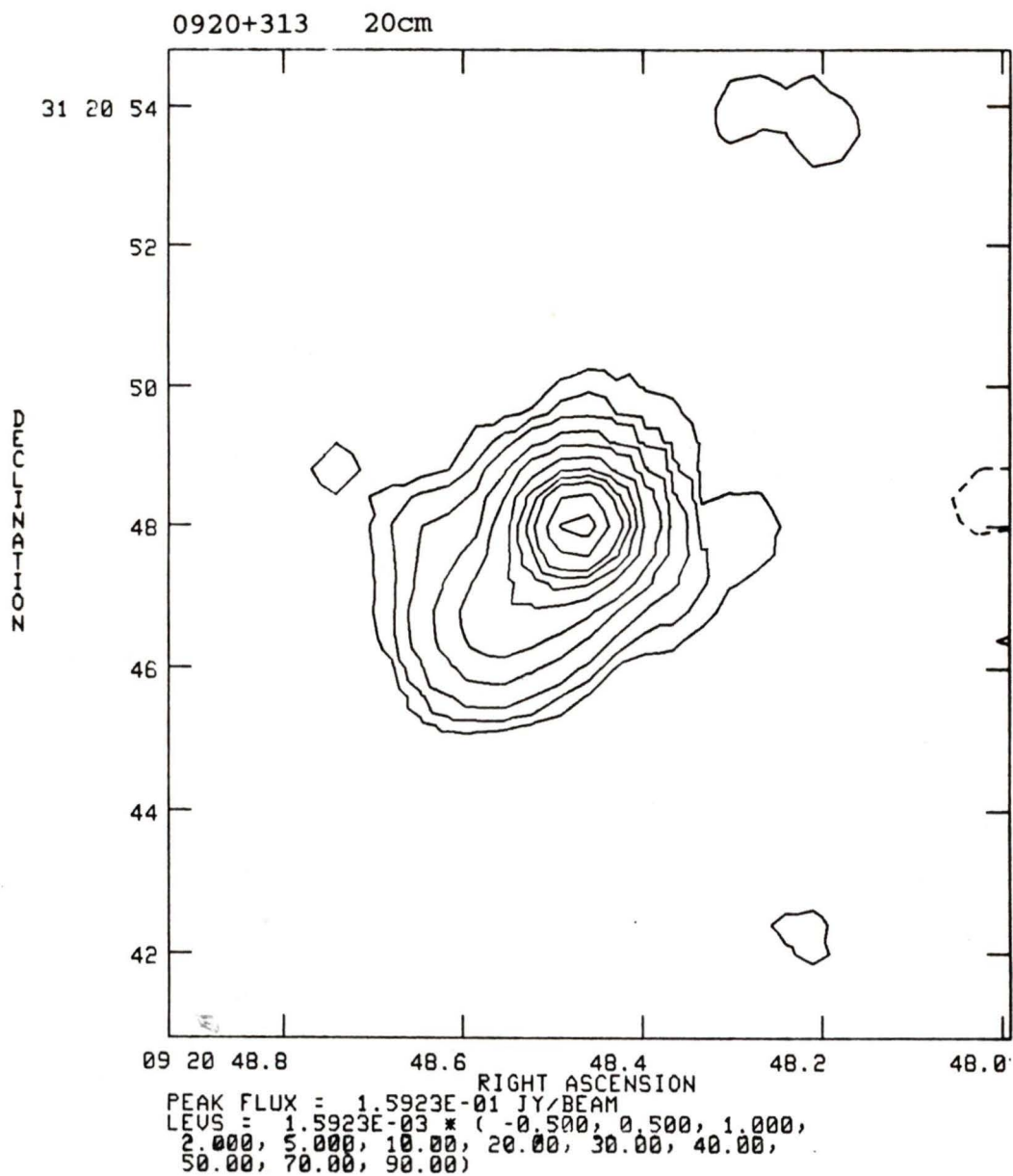


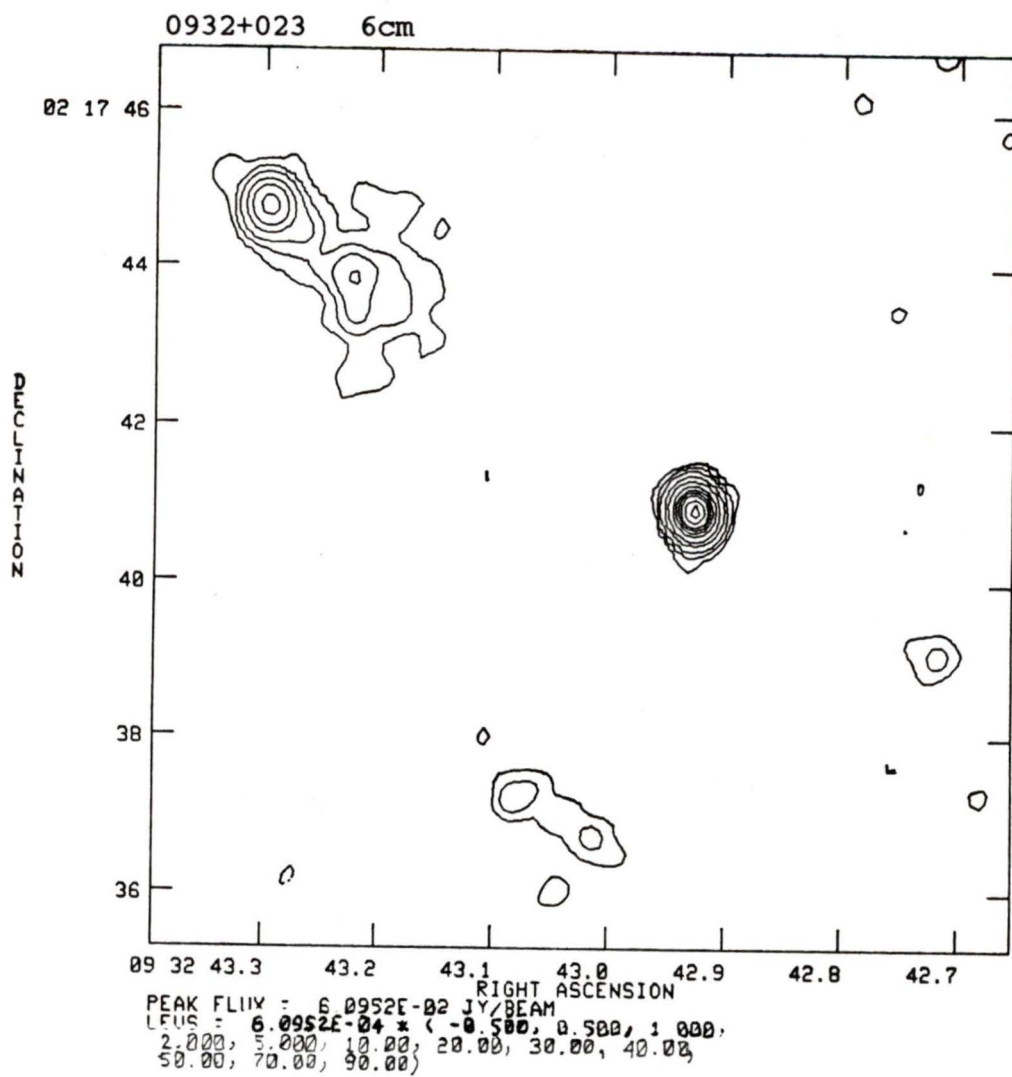
0903+169 6cm



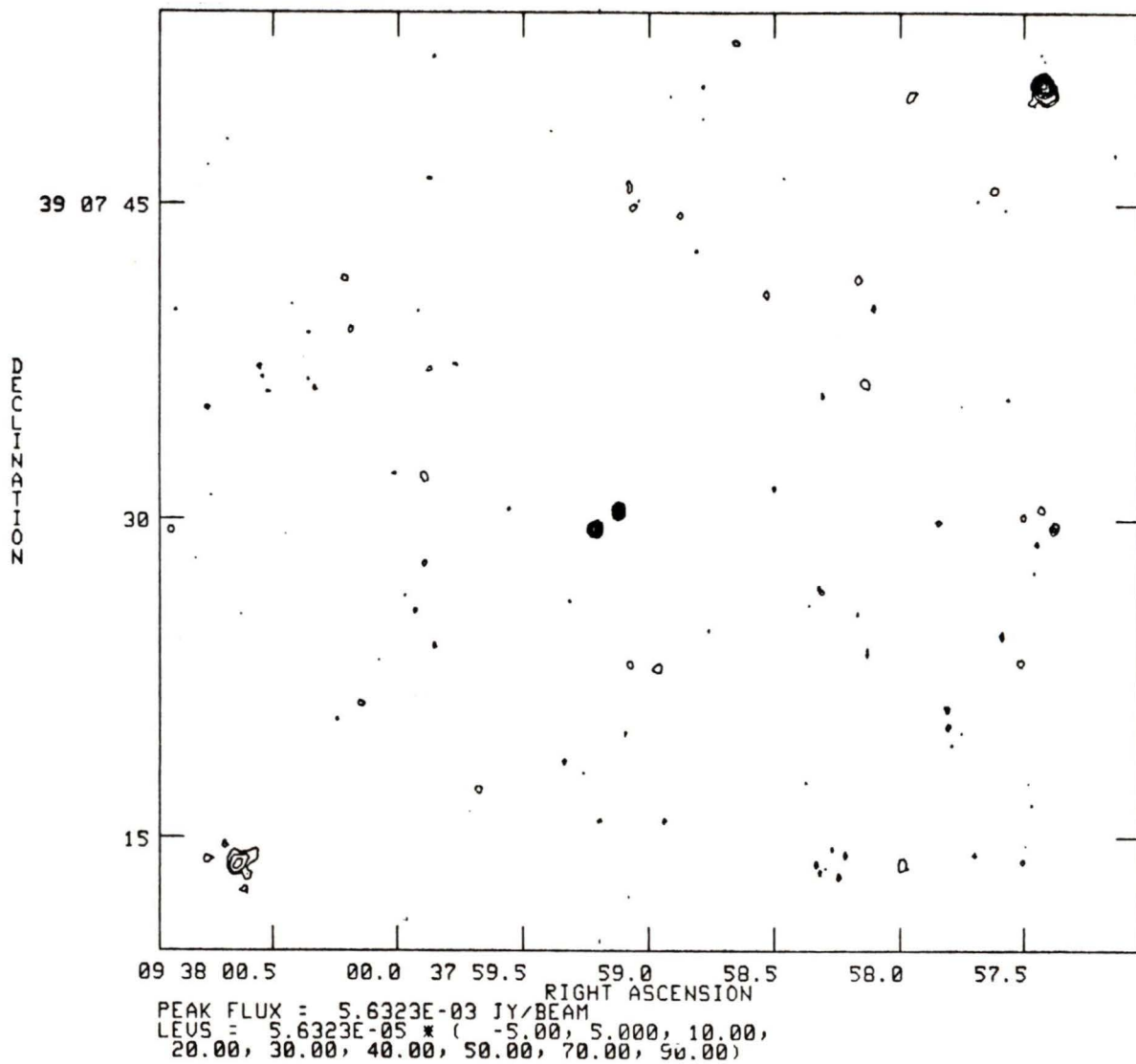
PEAK FLUX = 1.7642E-02 JY/BEAM
LEVS = 1.7642E-04 * (-2.00, 2.000, 5.000,
10.00, 20.00, 30.00, 40.00, 50.00, 70.00,
90.00)

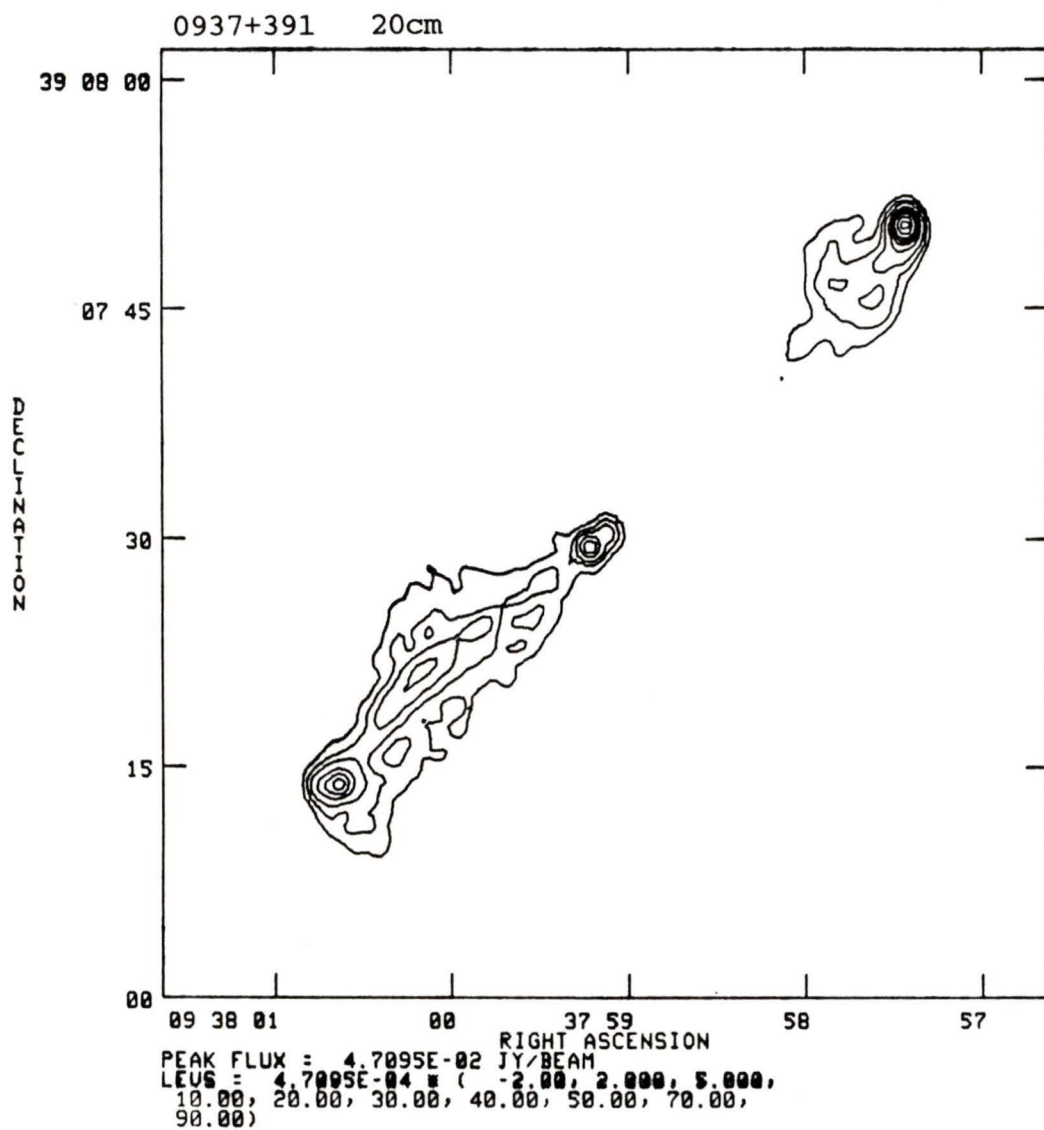




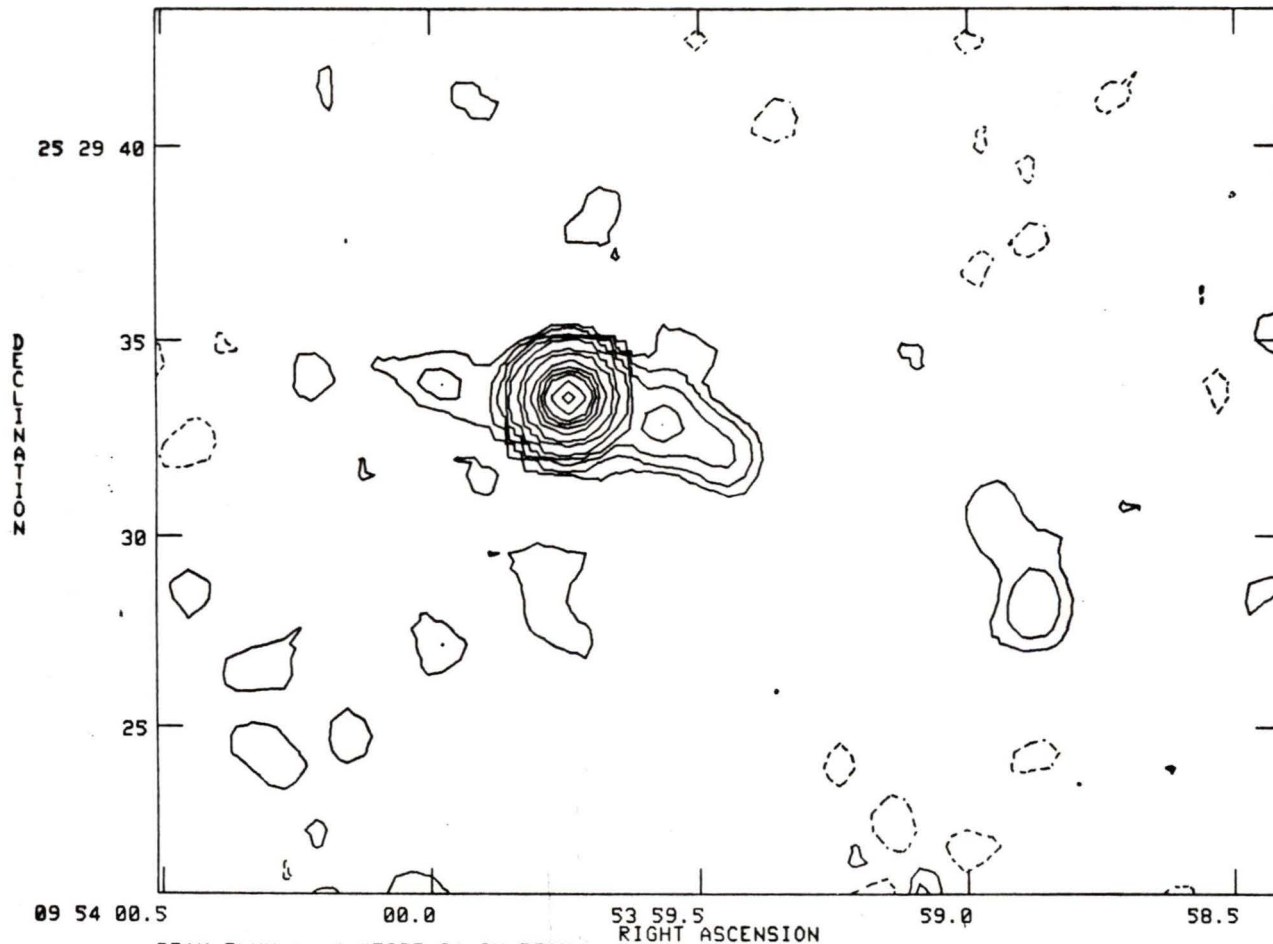


0937+391 6cm



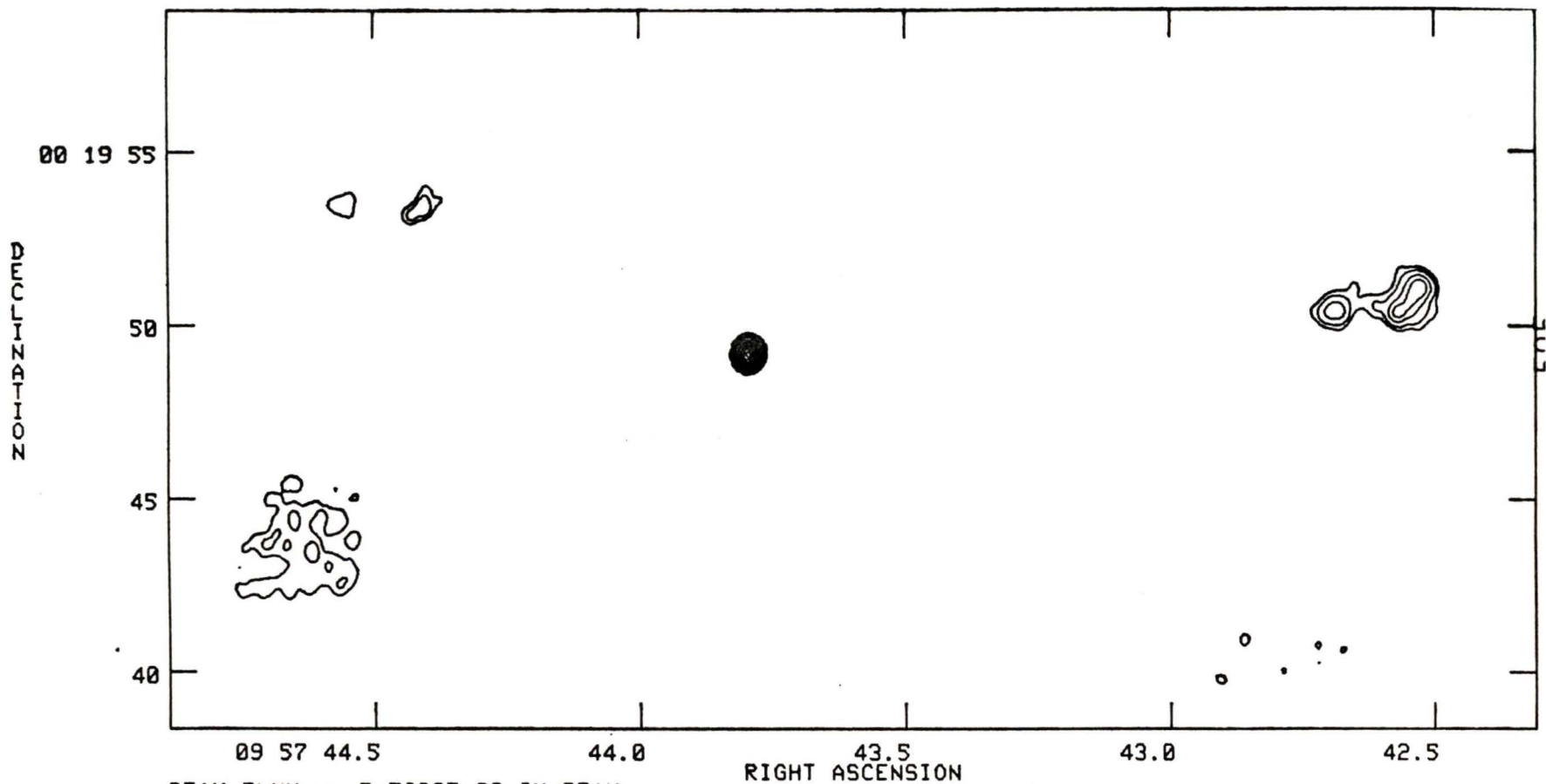


0953+254 20cm



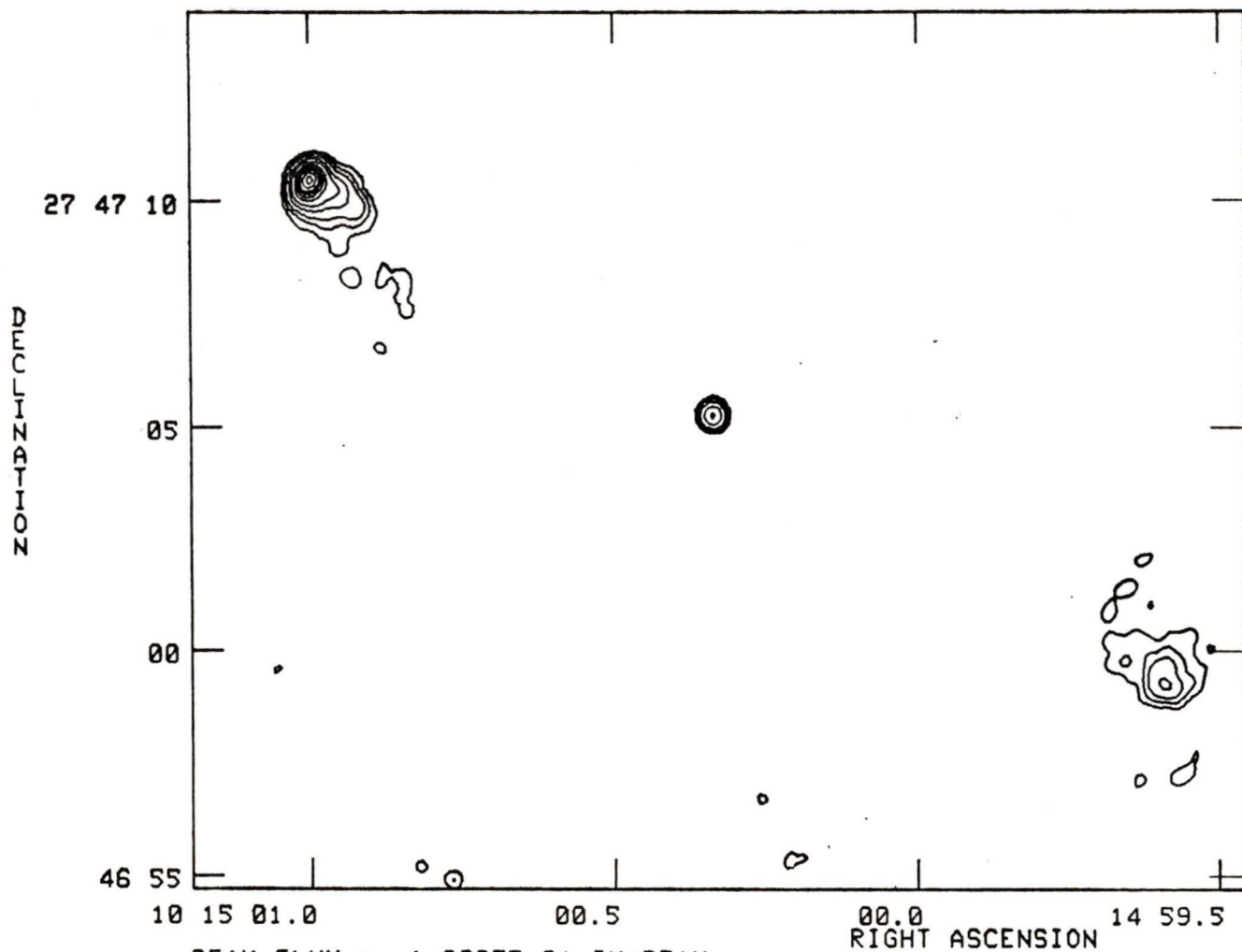
PEAK FLUX = 4.4533E-01 JY/BEAM
LEVS = 4.4533E-03 * (-0.125, 0.125, 0.250,
0.500, 1.000, 2.000, 5.000, 10.00, 30.00,
50.00, 70.00, 90.00)

0957+003 6cm



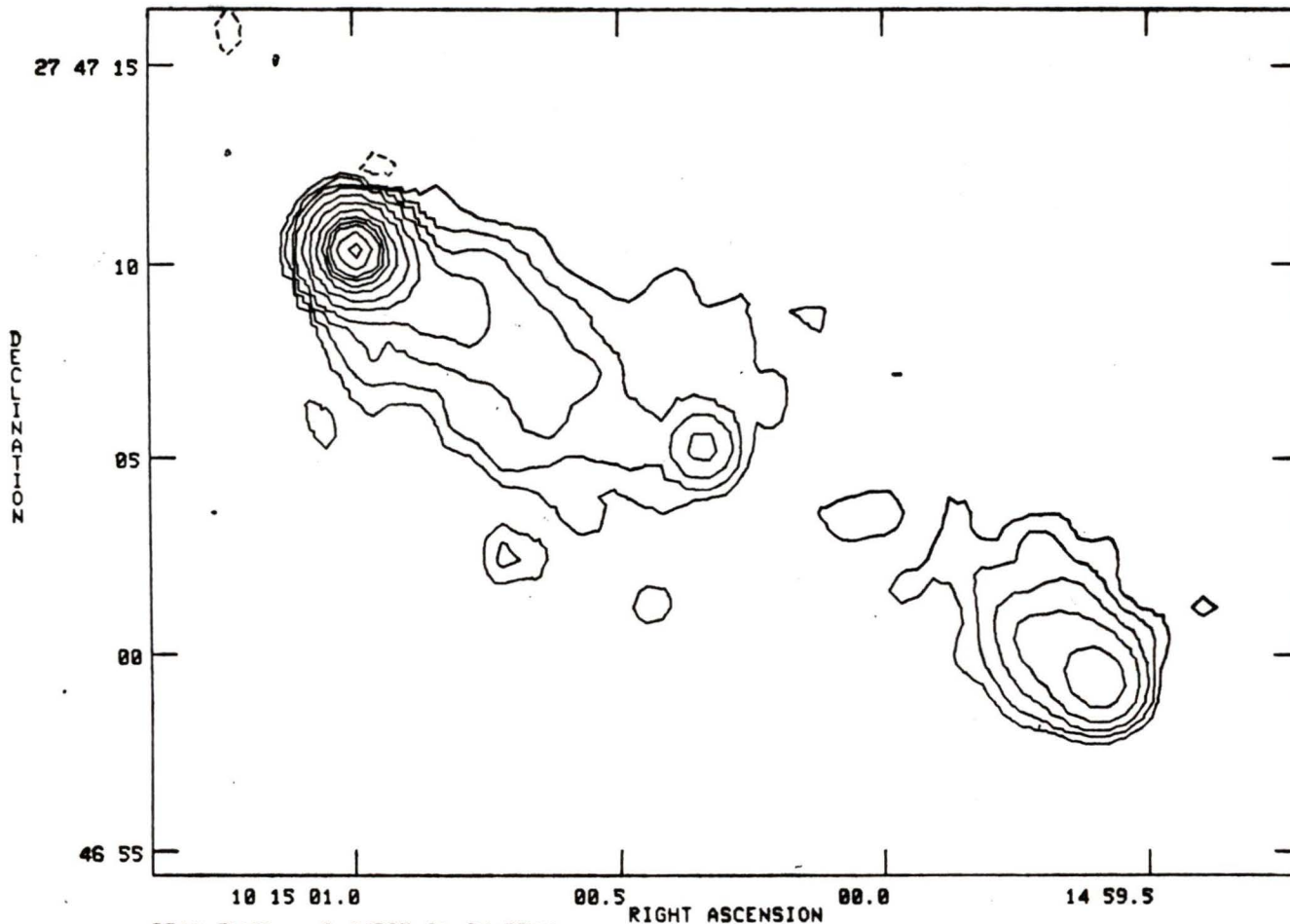
PEAK FLUX = 7.5693E-02 JY/BEAM
LEVS = 7.5693E-04 * (-1.00, 1.000, 2.000,
5.000, 10.00, 20.00, 30.00, 40.00, 50.00,
70.00, 90.00)

1015+277 6cm

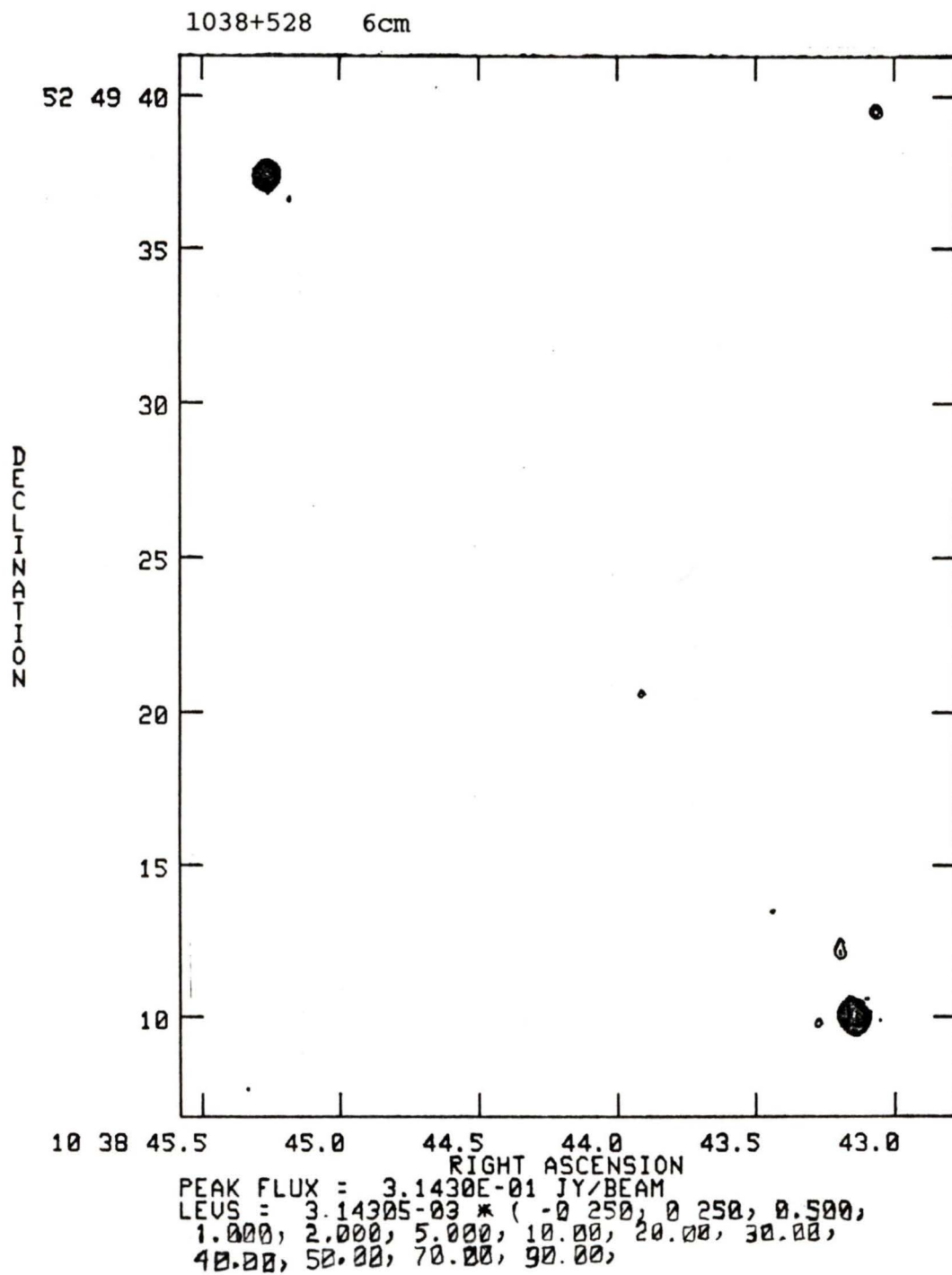


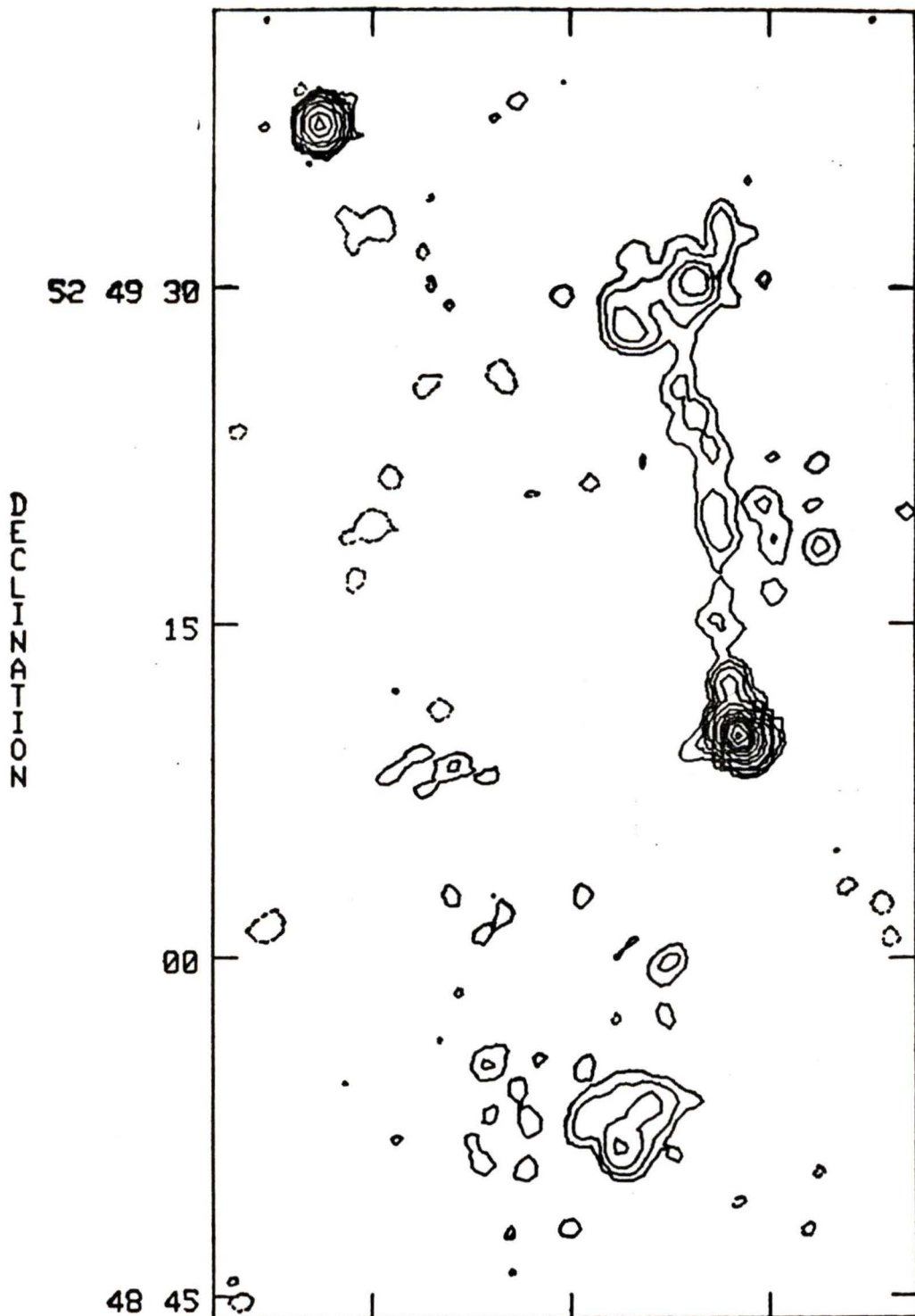
PEAK FLUX = 1.2295E-01 JY/BEAM
LEVS = 1.2295E-03 * (-0.500, 0.500, 1.000,
2.000, 5.000, 10.00, 20.00, 30.00, 40.00,
50.00, 70.00, 90.00)

1015+277 20cm

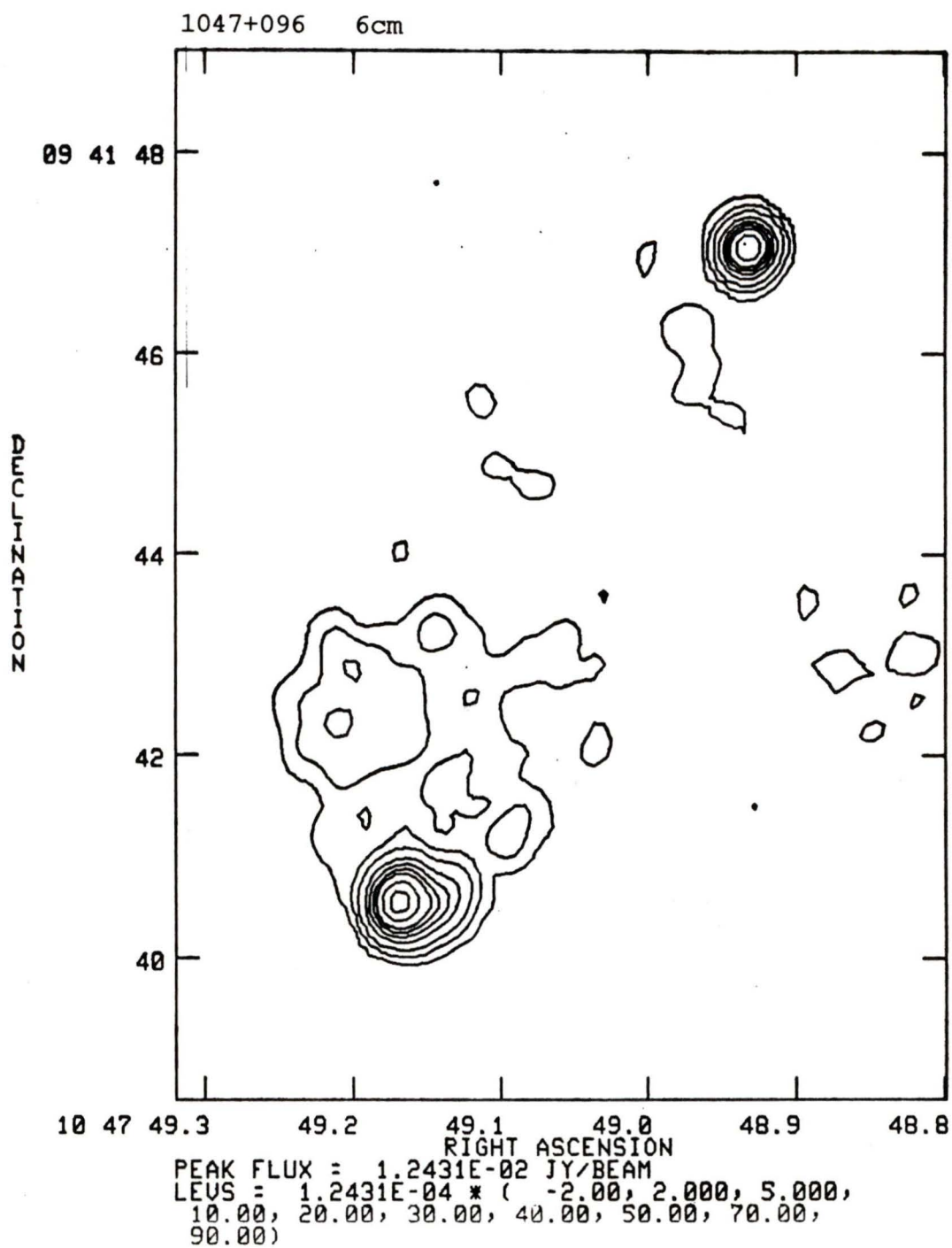


PEAK FLUX = 6.4453E-01 JY/BEAM
LEUS = 6.4453E-03 * (-0.250, 0.250, 0.500,
1.000, 2.000, 5.000, 10.00, 20.00, 30.00,
40.00, 50.00, 70.00, 90.00)

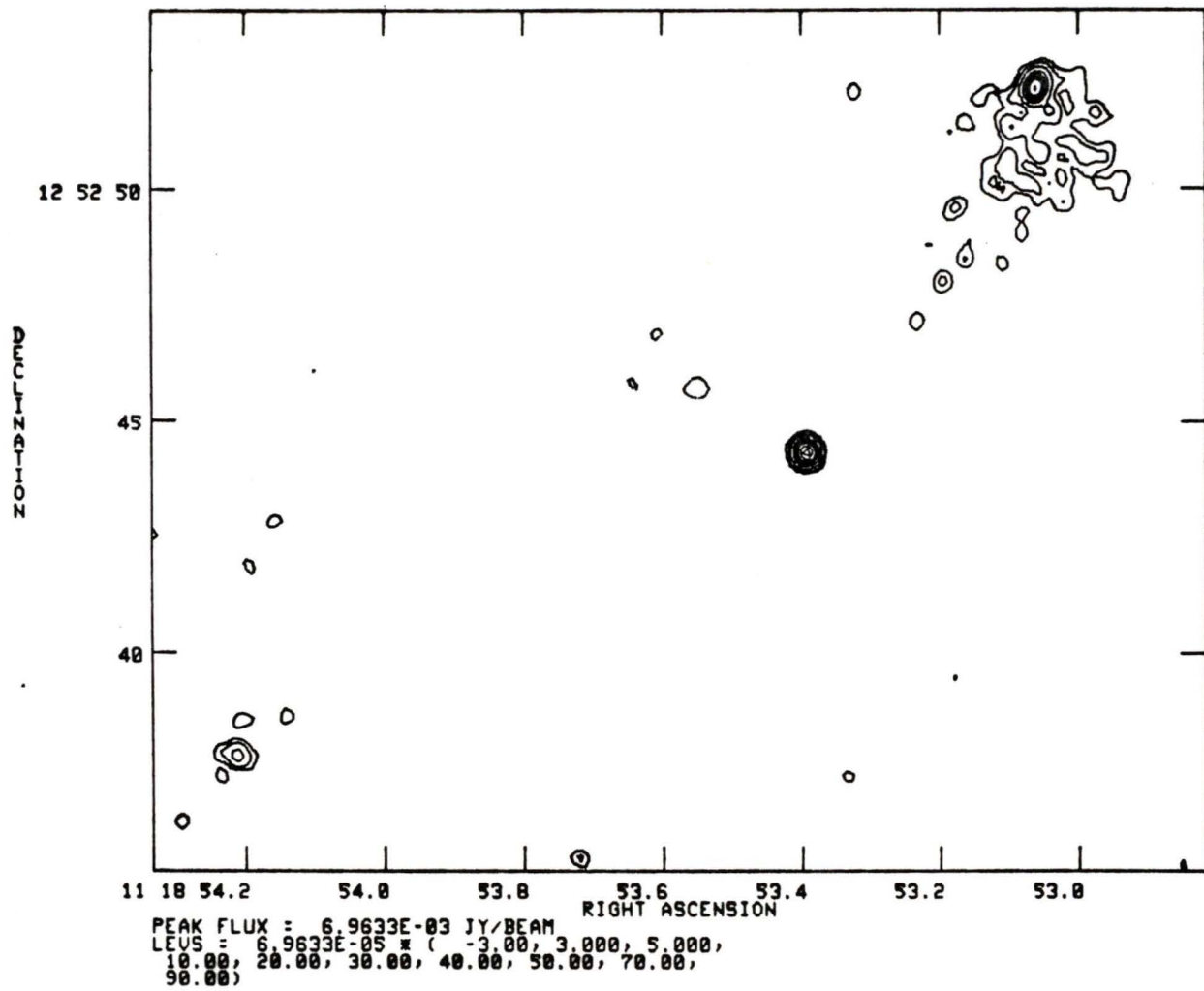




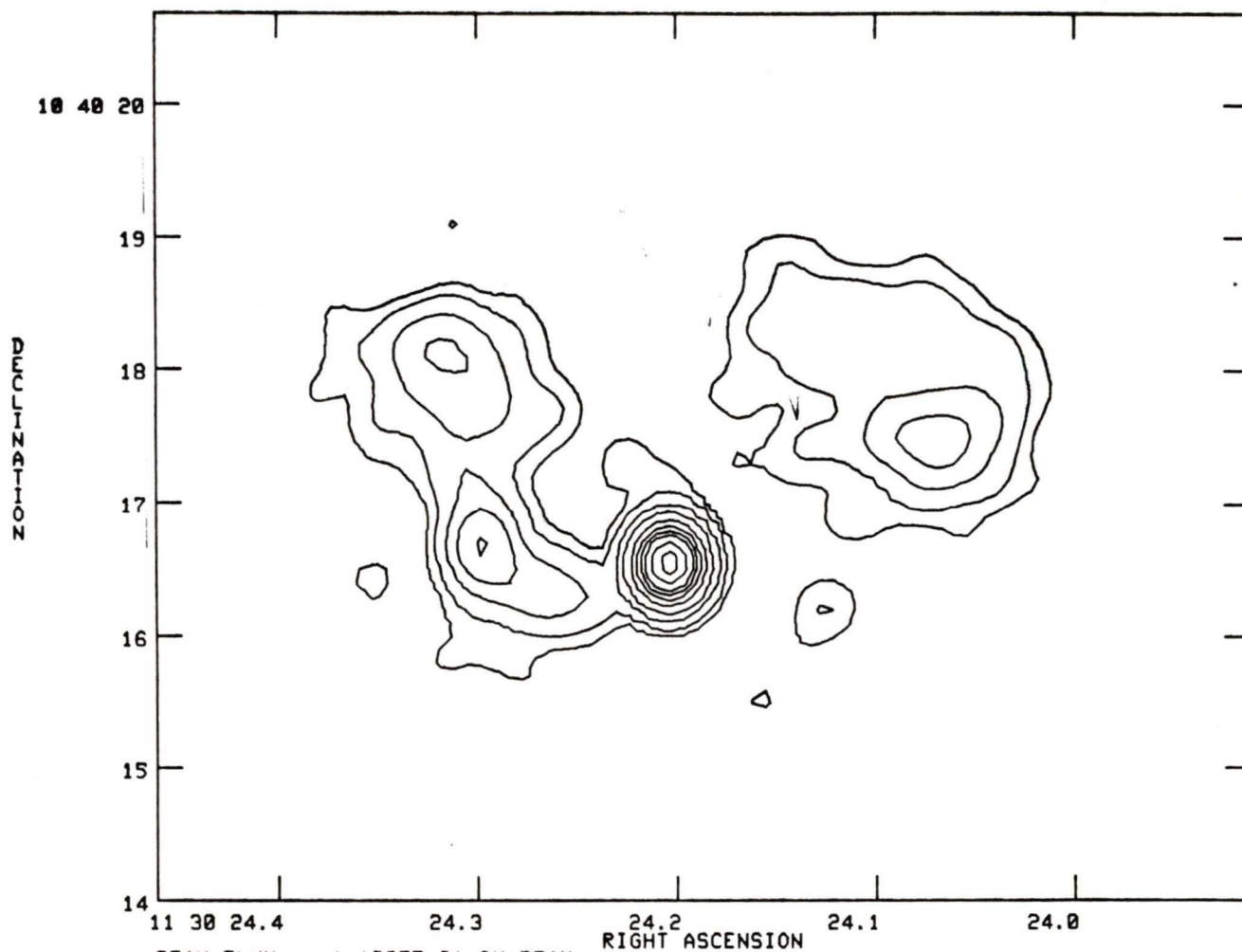
RIGHT ASCENSION
PEAK FLUX = 2.9354E-01 JY/BEAM
LEVS = 2.9354E-03 * (-0.250, 0.250, 0.500,
1.000, 2.000, 5.000, 10.00, 20.00, 30.00,
40.00, 50.00, 70.00, 90.00)



1118+128 6cm

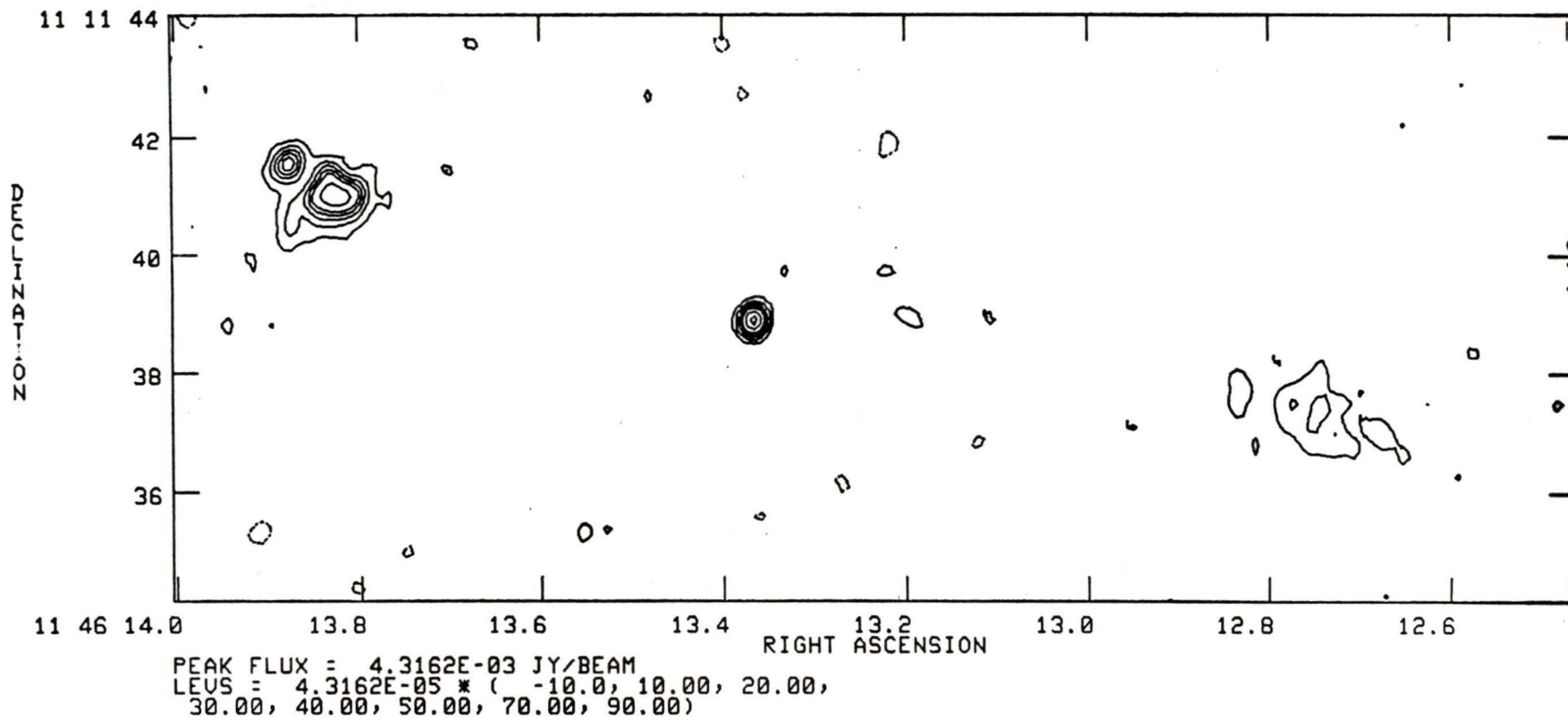


1130+106 6cm

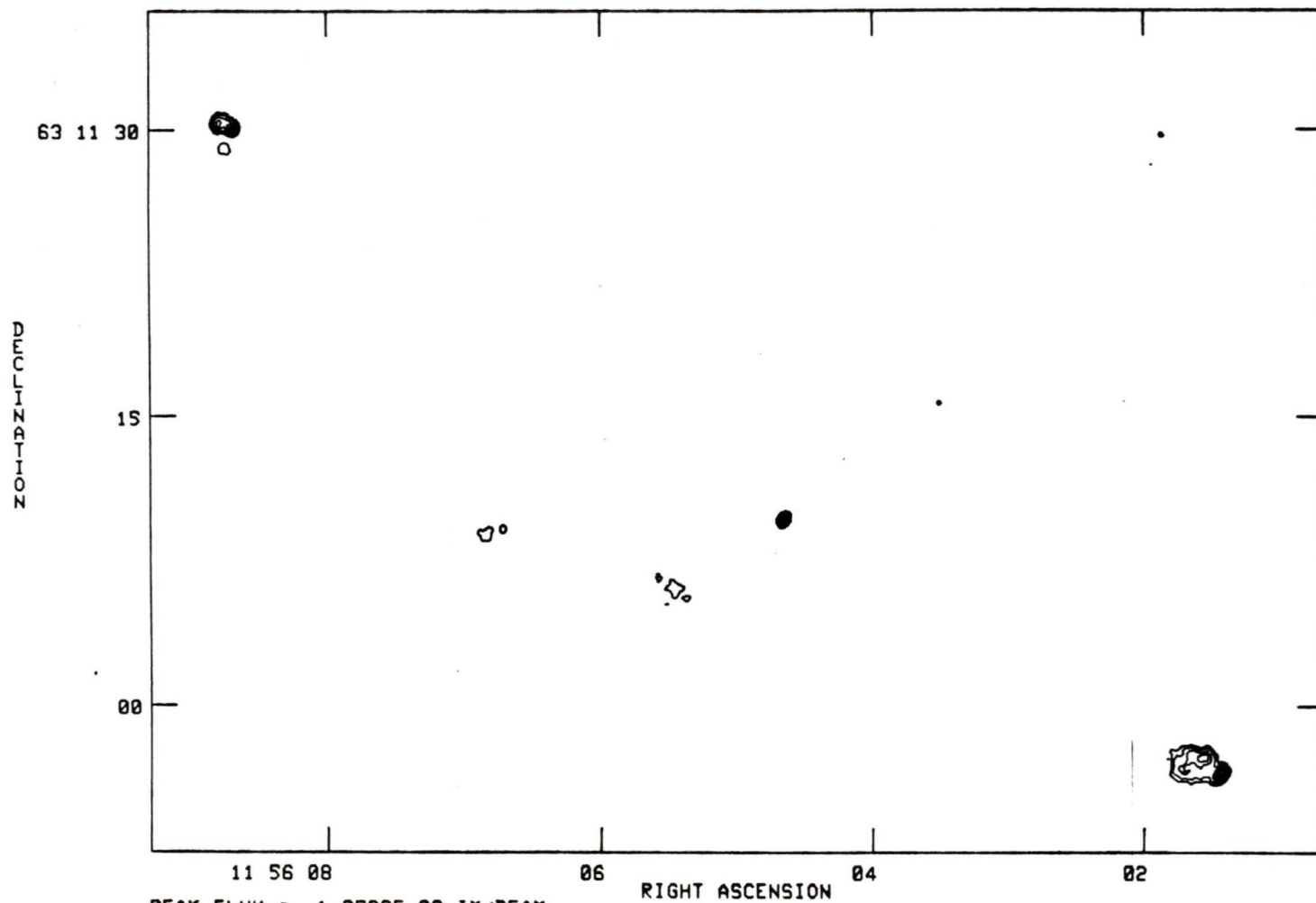


PEAK FLUX = 1.1327E-01 JY/BEAM
LEVS = 1.1327E-03 * (-1.00, 1.000, 2.000,
5.000, 10.00, 20.00, 30.00, 40.00, 50.00,
70.00, 90.00)

1146+111 6cm

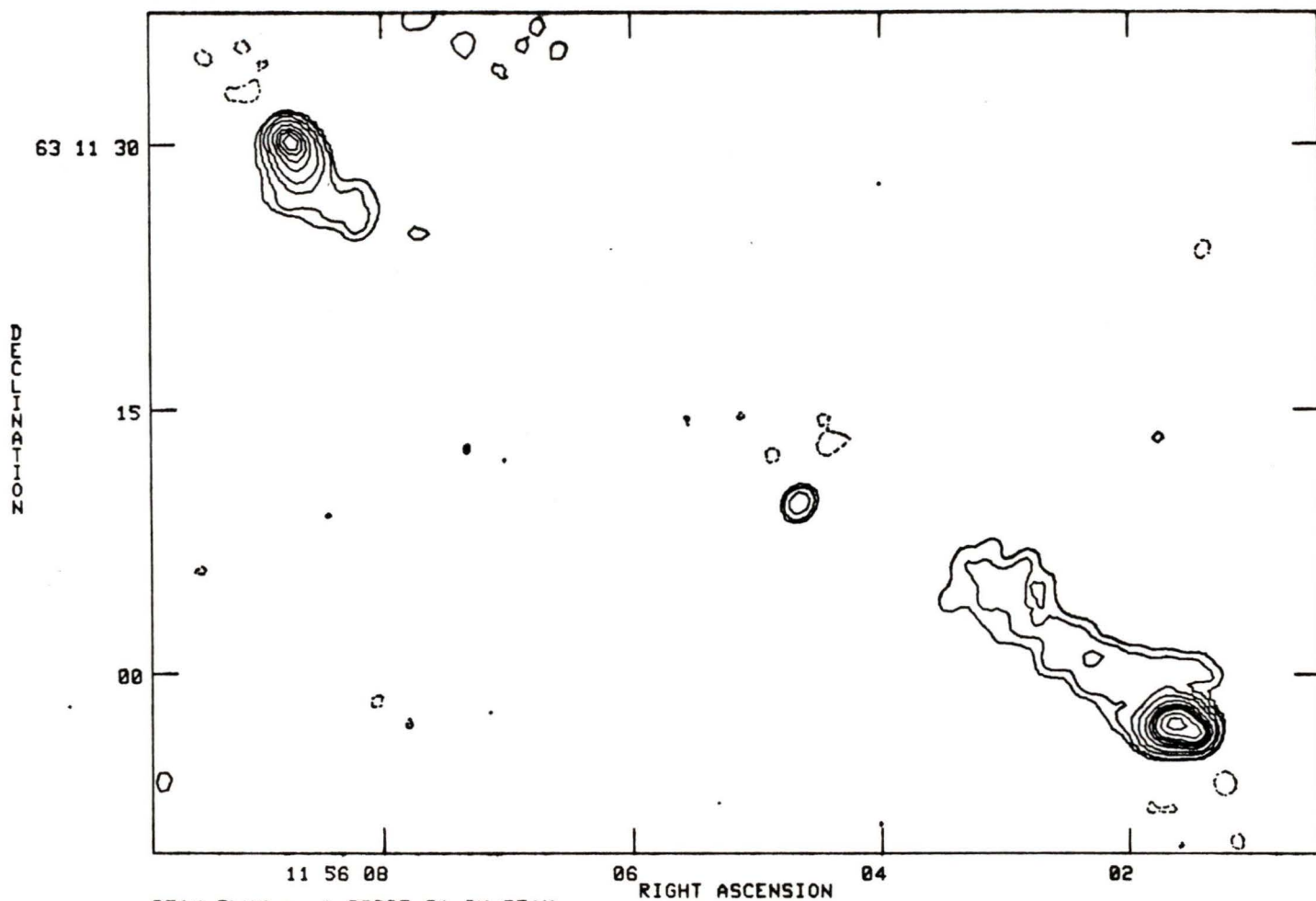


1156+631 6cm



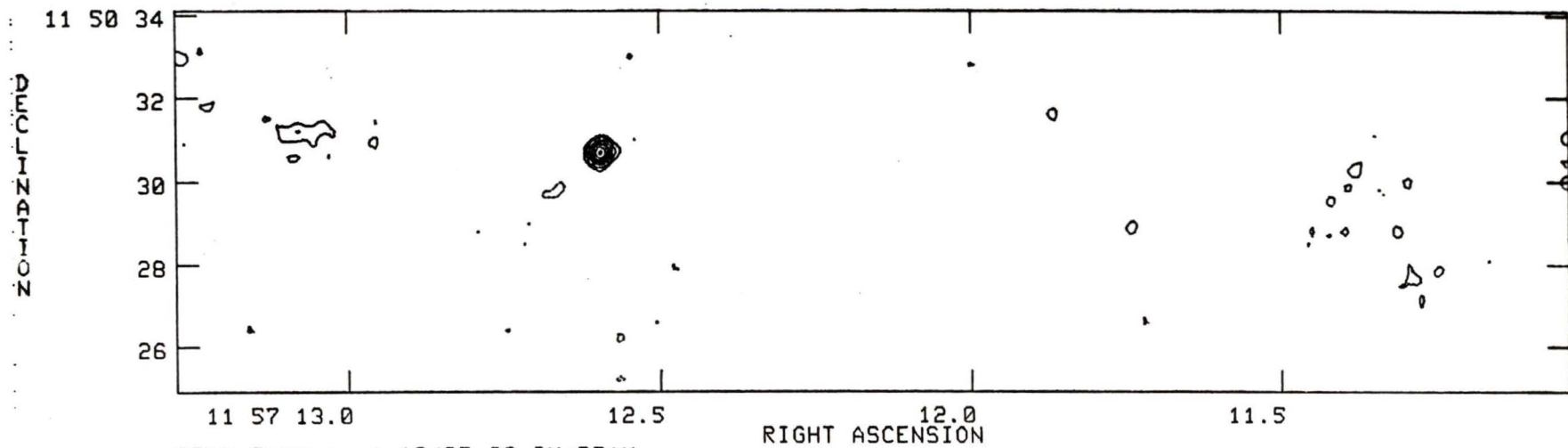
PEAK FLUX = 1.2599E-02 JY/BEAM
LEVS = 1.2599E-04 * (-5.00, 5.000, 10.00,
20.00, 30.00, 40.00, 50.00, 70.00, 90.00)

1156+631 20cm



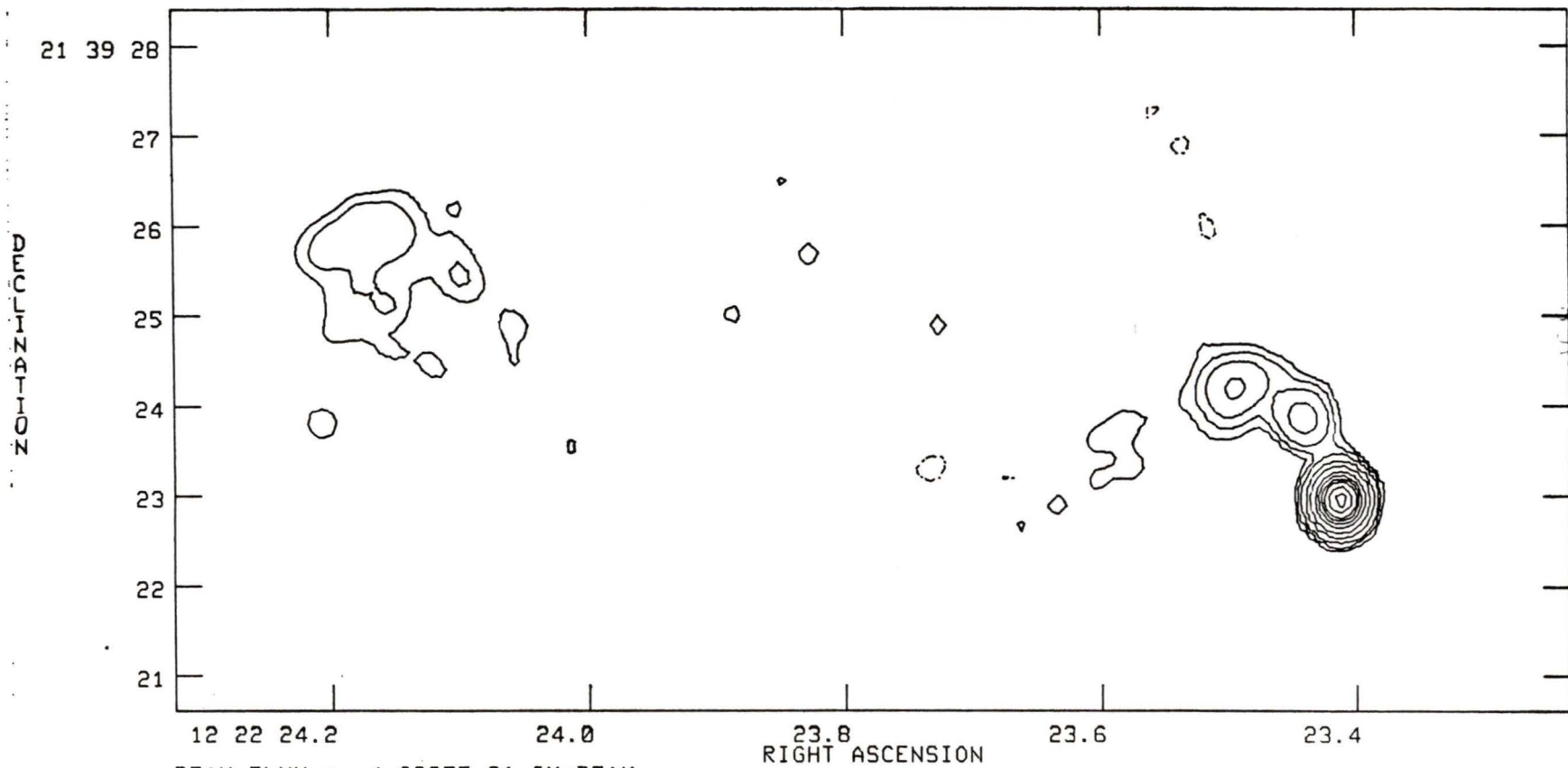
PEAK FLUX = 1.0083E-01 JY/BEAM
LEVS = 1.0083E-03 * (-1.00, 1.000, 2.000,
5.000, 10.00, 20.00, 30.00, 40.00, 50.00,
70.00, 90.00)

1157+118 6cm

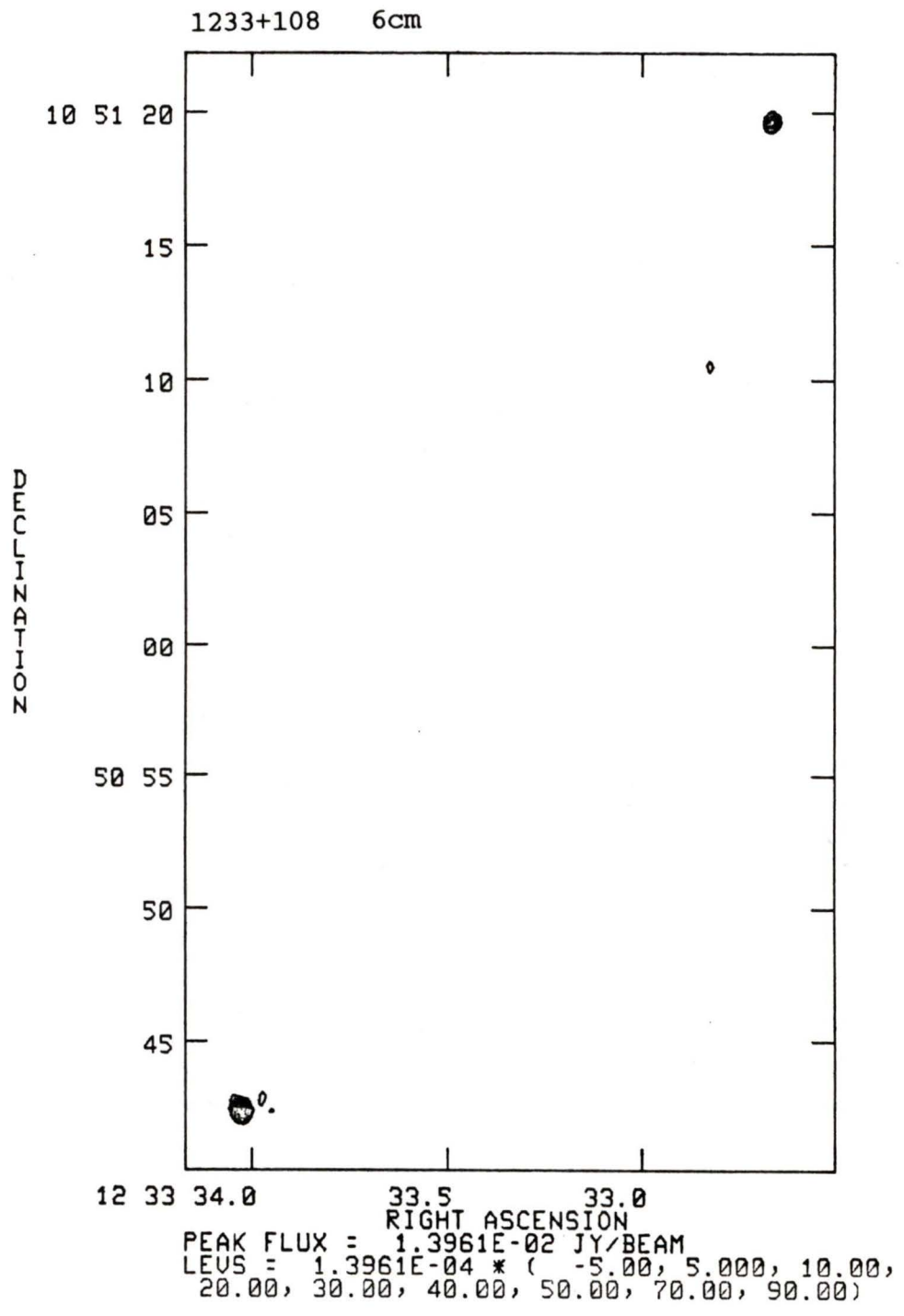


PEAK FLUX = 1.1342E-02 JY/BEAM
LEUS = 1.1342E-04 * (-5.00, 5.000, 10.00,
20.00, 30.00, 40.00, 50.00, 70.00, 90.00)

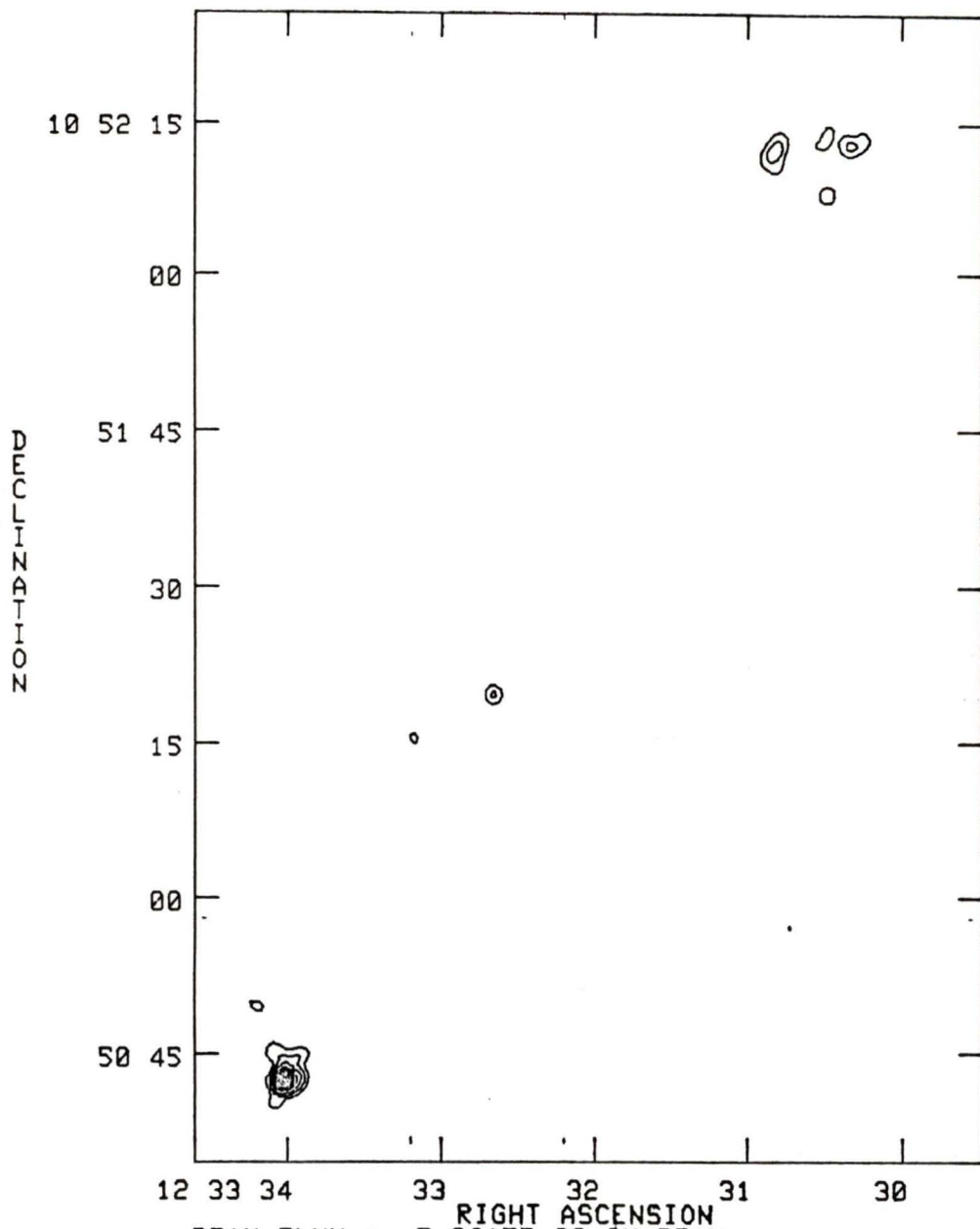
1222+216 6cm



PEAK FLUX = 4.6935E-01 JY/BEAM
LEVS = 4.6935E-03 * (-0.500, 0.500, 1.000,
2.000, 5.000, 10.00, 20.00, 30.00, 40.00,
50.00, 70.00, 90.00)

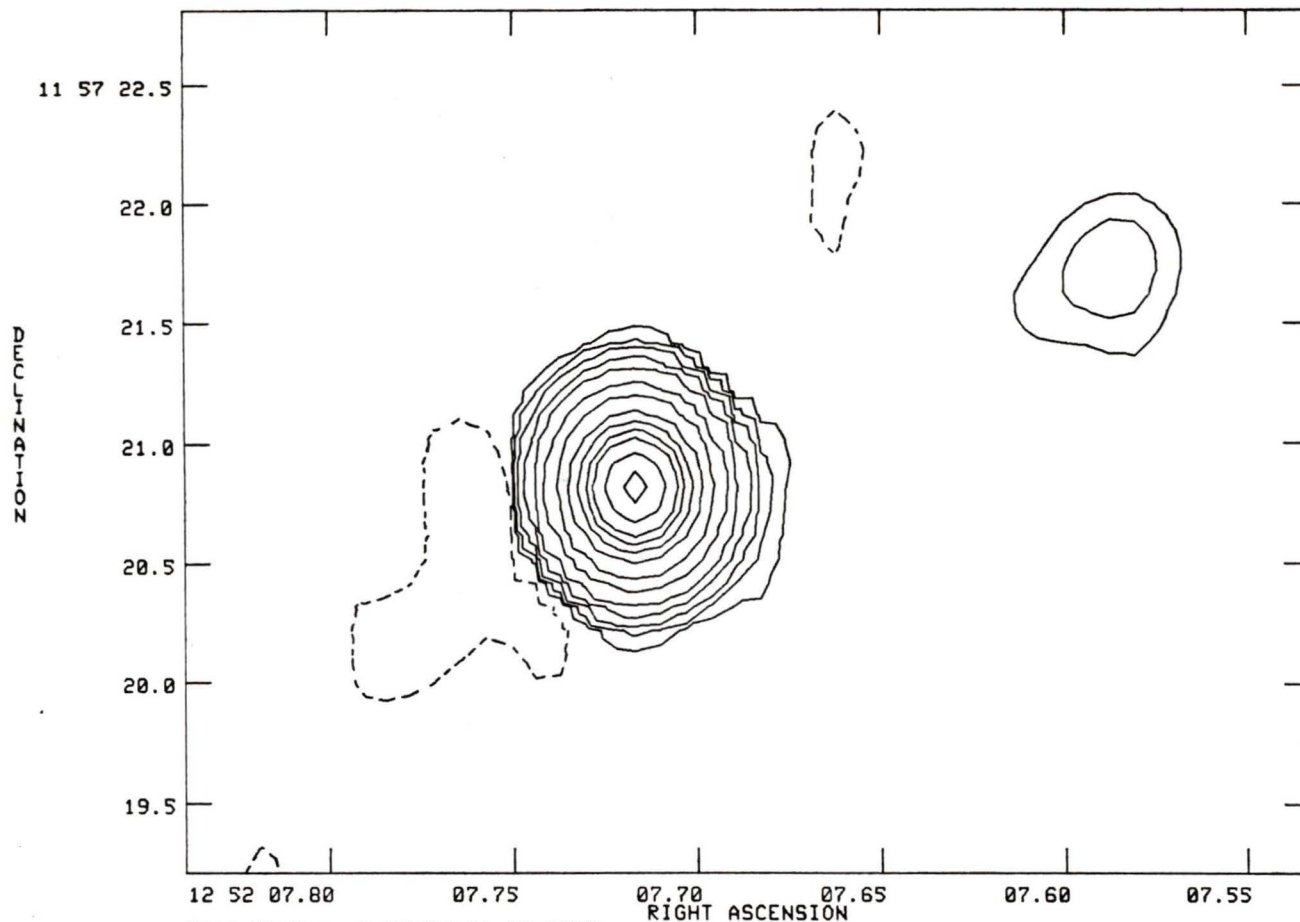


1233+108 20cm



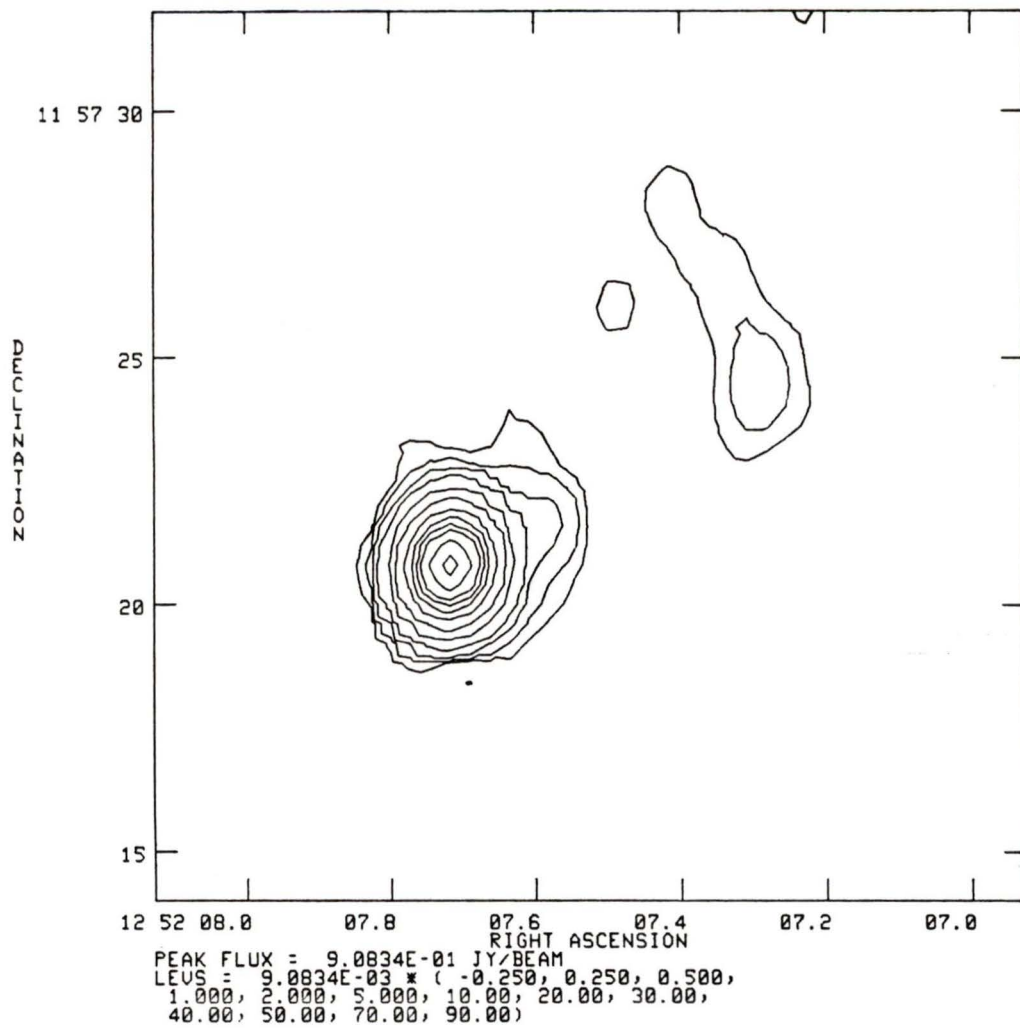
PEAK FLUX = 5.0615E-02 JY/BEAM
 LEVELS = 5.0615E-04 * (-2.00, 2.000, 5.000,
 10.00, 20.00, 30.00, 40.00, 50.00, 70.00,
 90.00)

1252+119 6cm

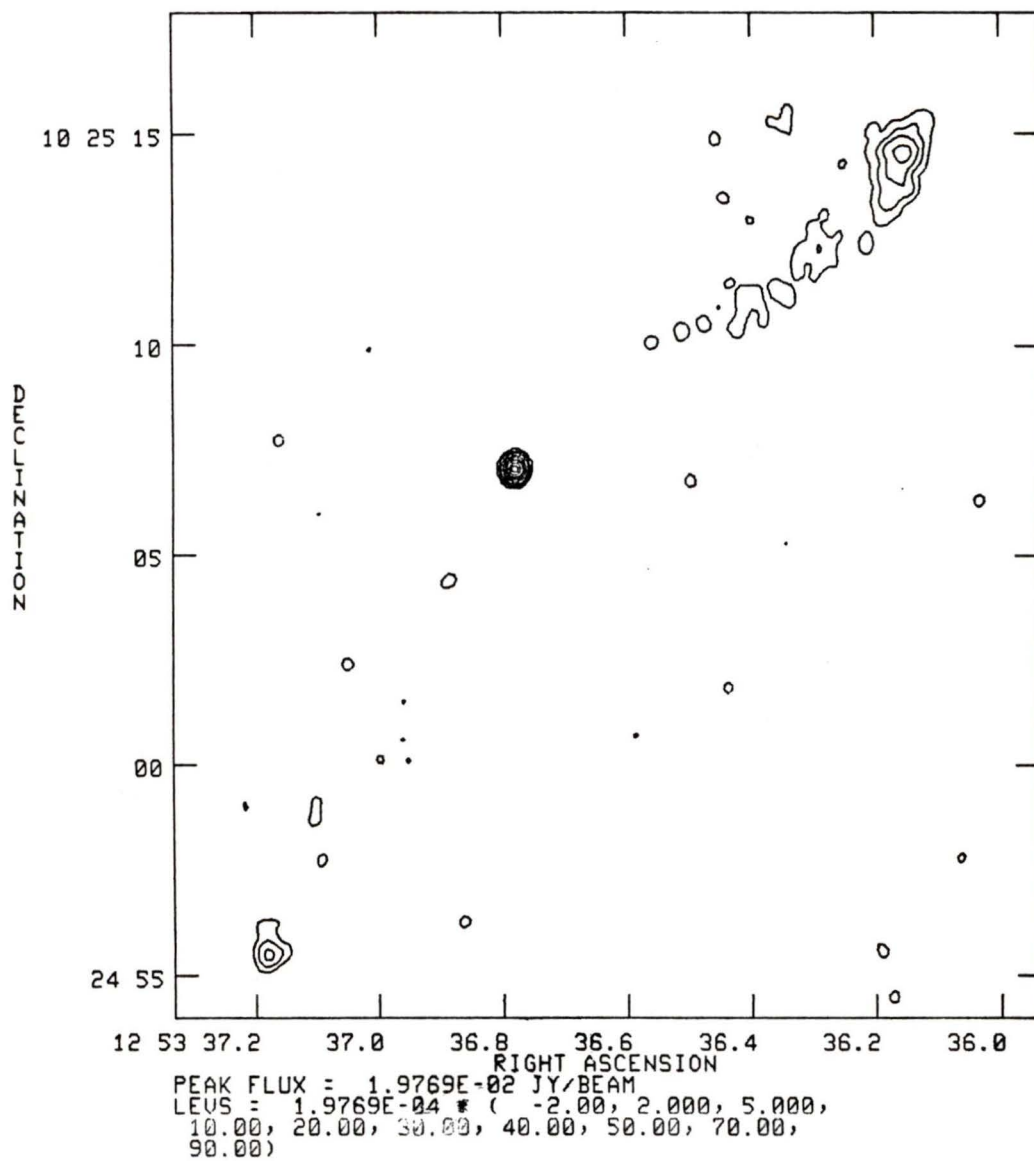


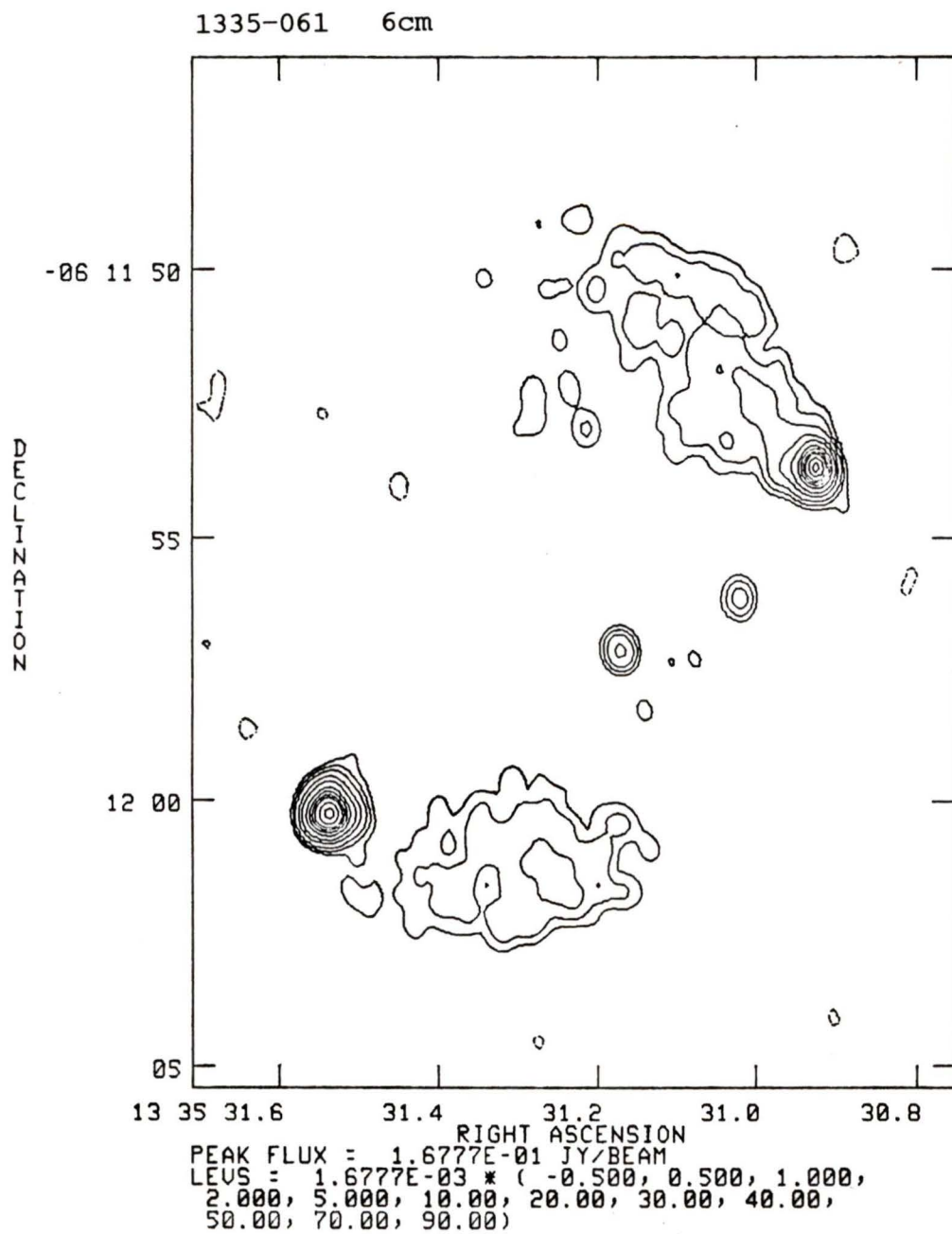
PEAK FLUX = 6.0231E-01 JY/BEAM
LEVS = 6.0231E-03 * (-0.120, 0.120, 0.250,
0.500, 1.000, 2.000, 5.000, 10.00, 20.00,
30.00, 40.00, 50.00, 70.00, 90.00)

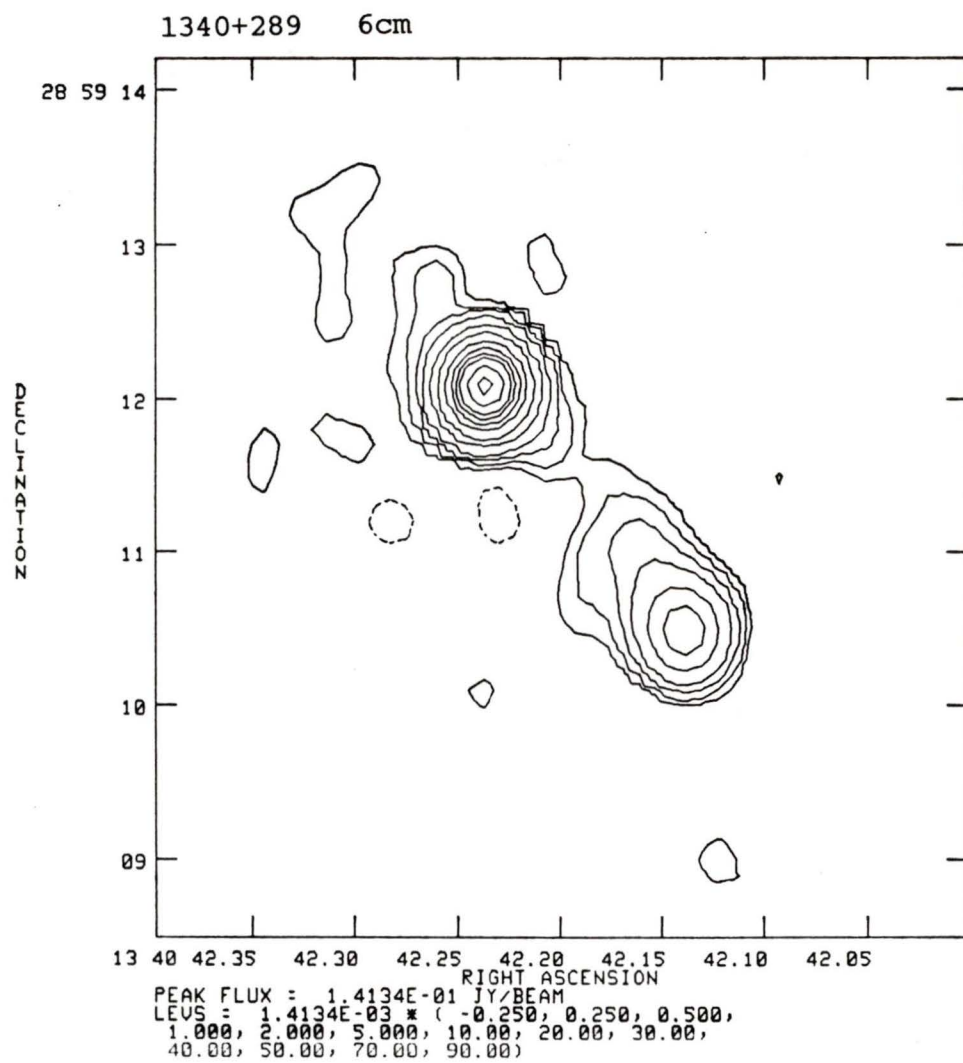
1252+119 20cm

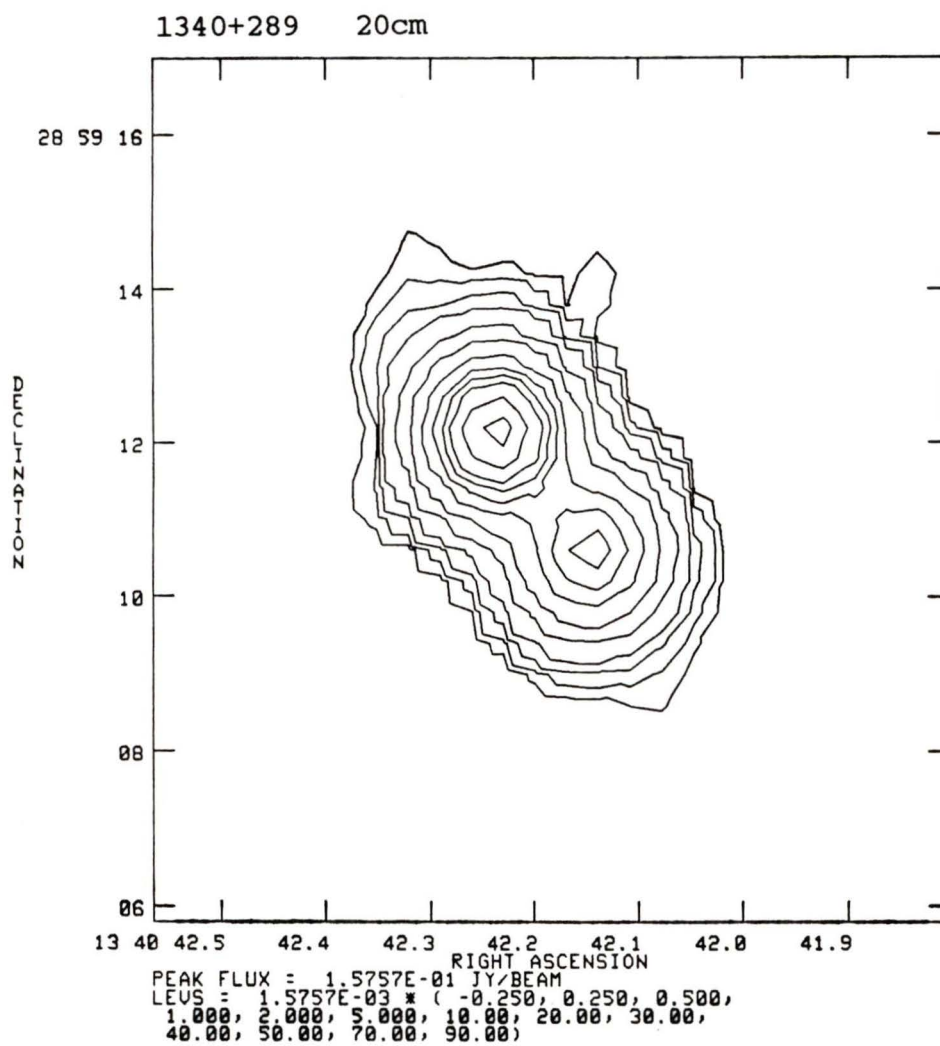


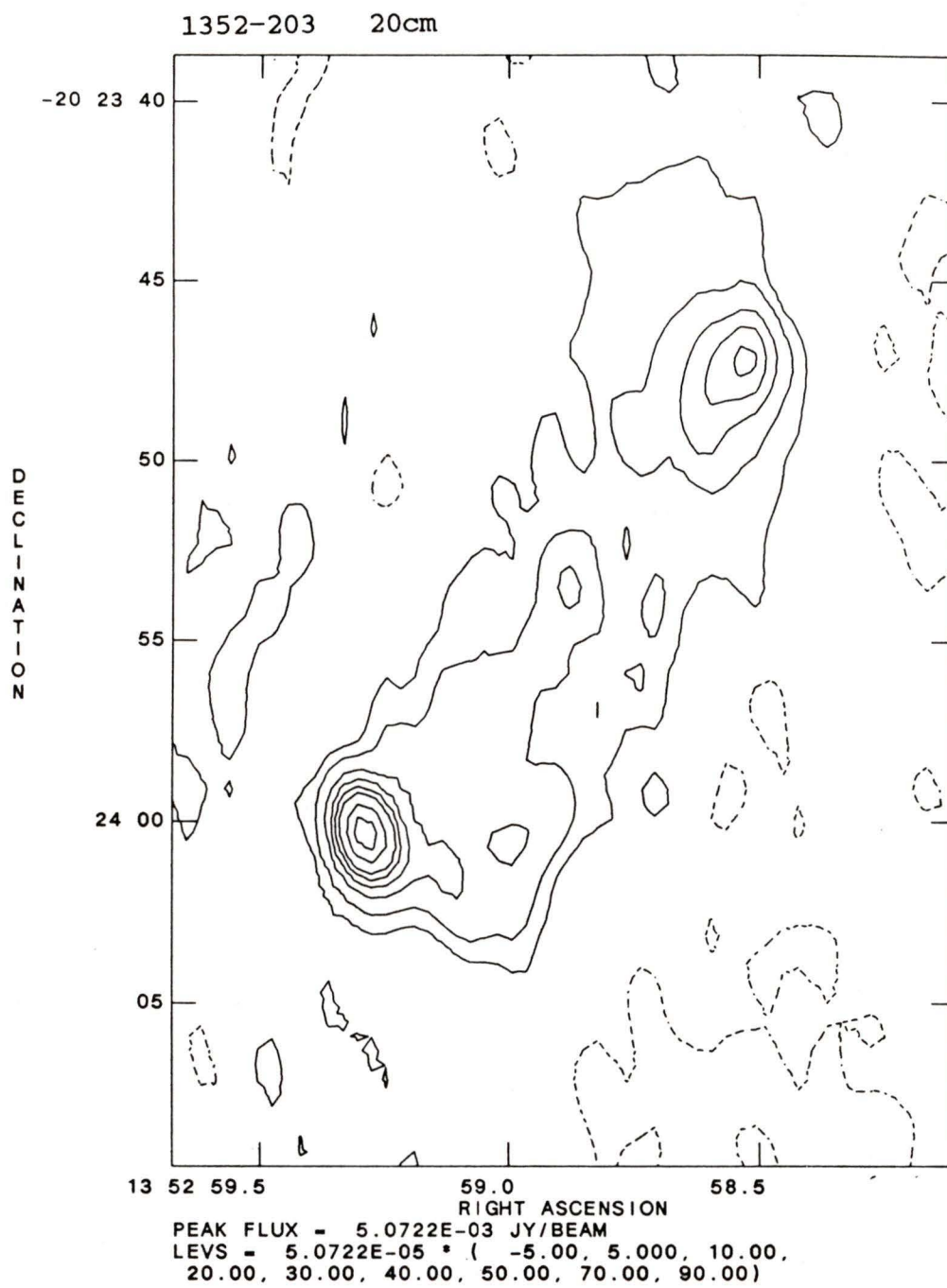
1253+104 6cm



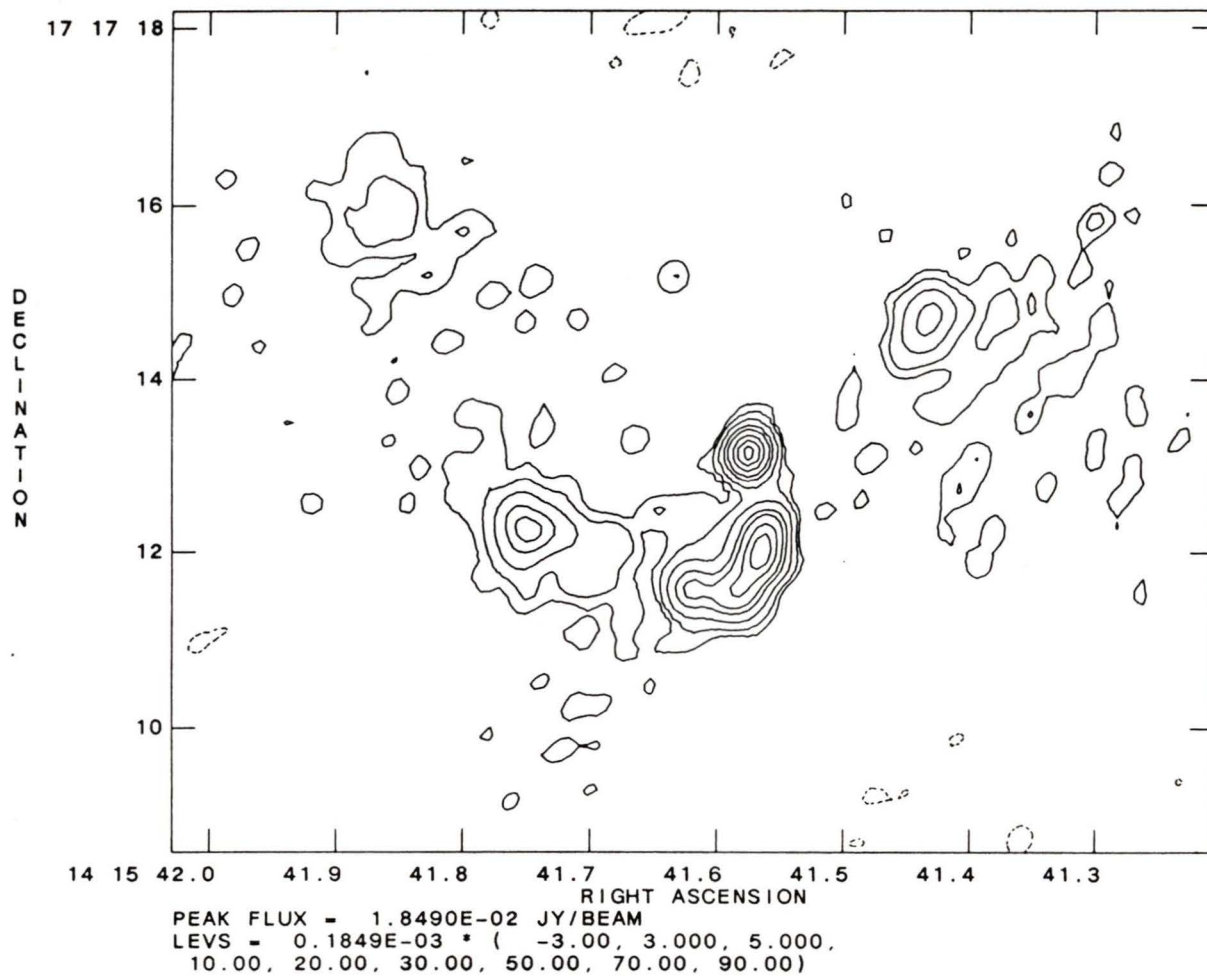




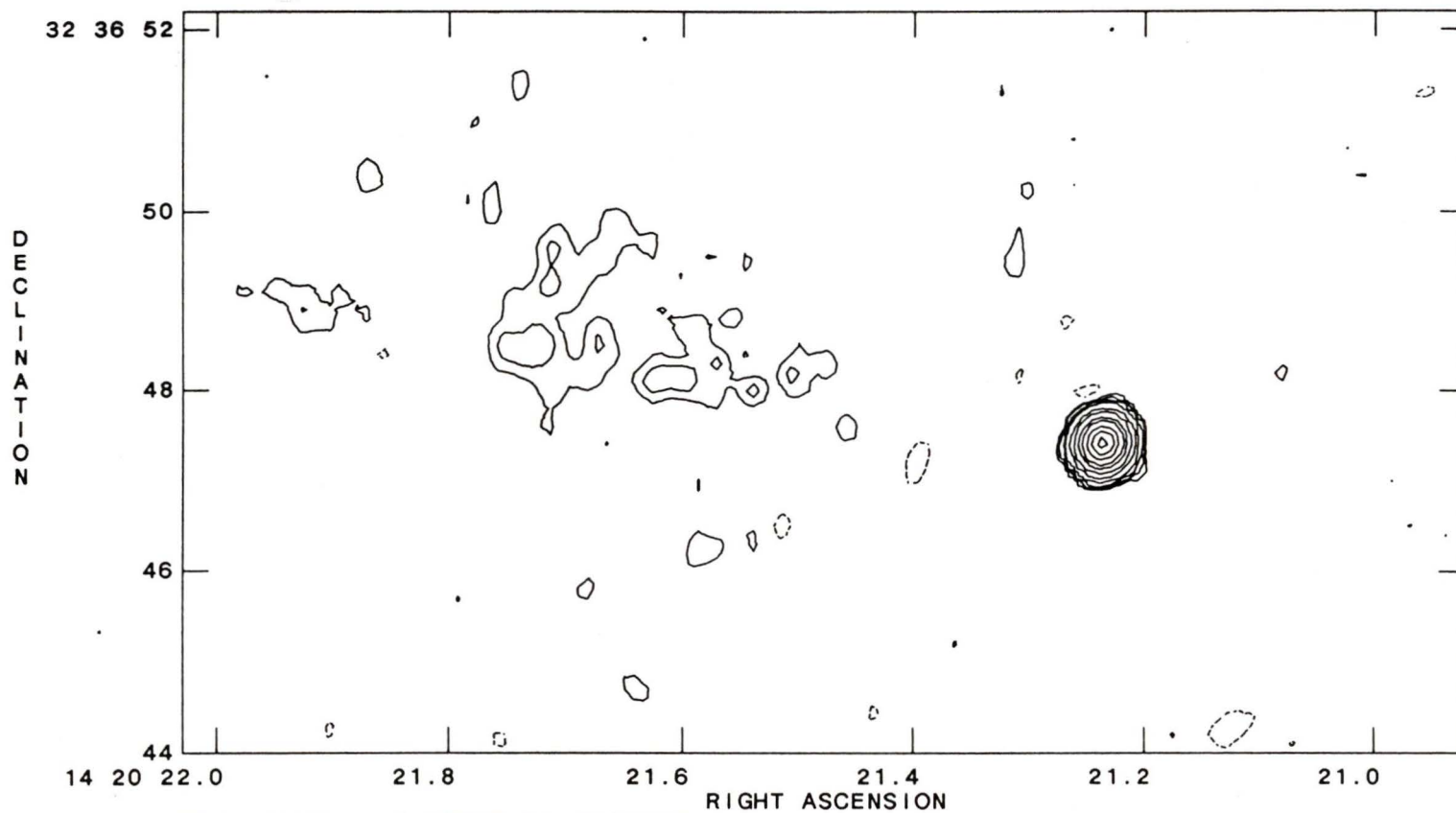




1415+172 6cm

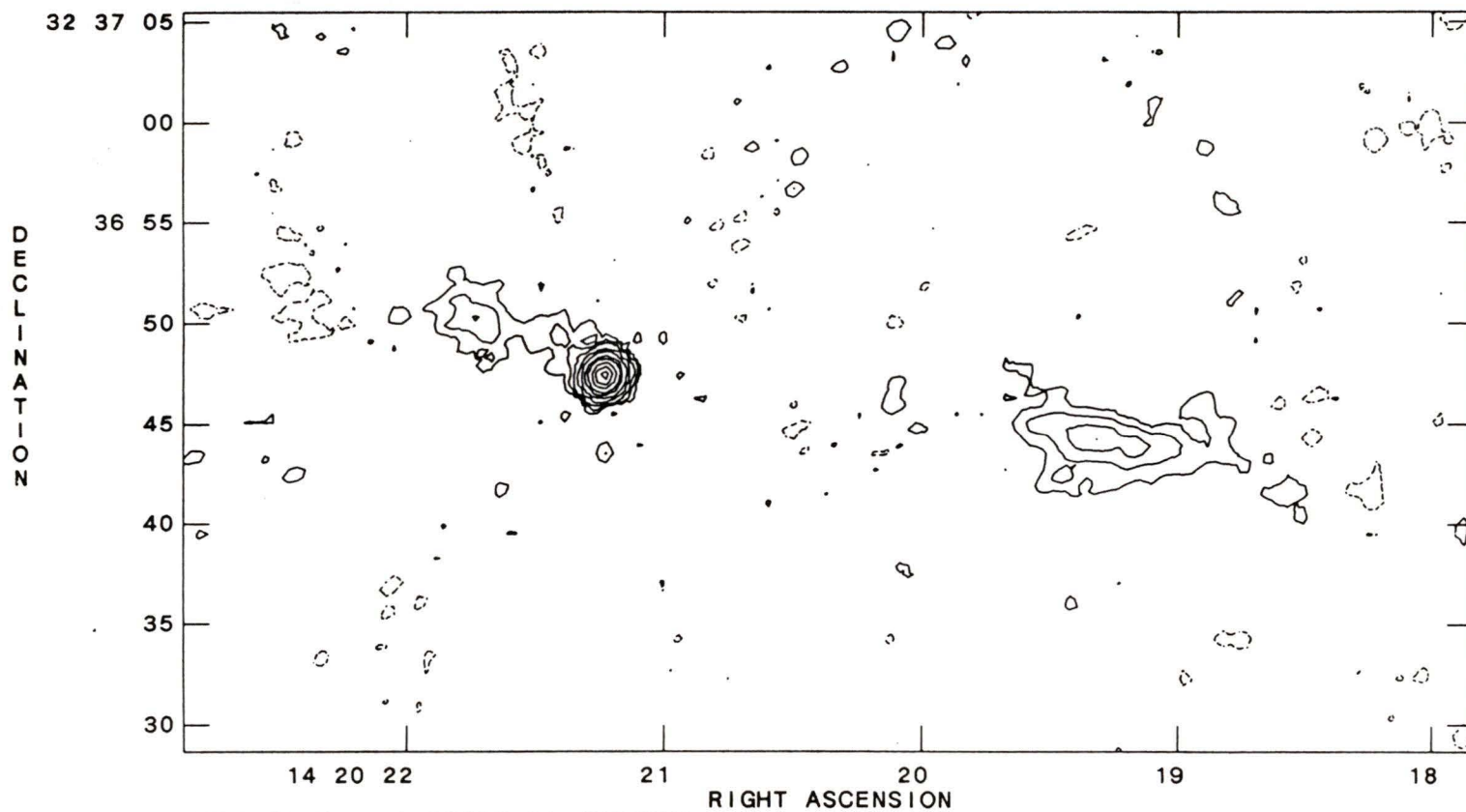


1420+326 6cm



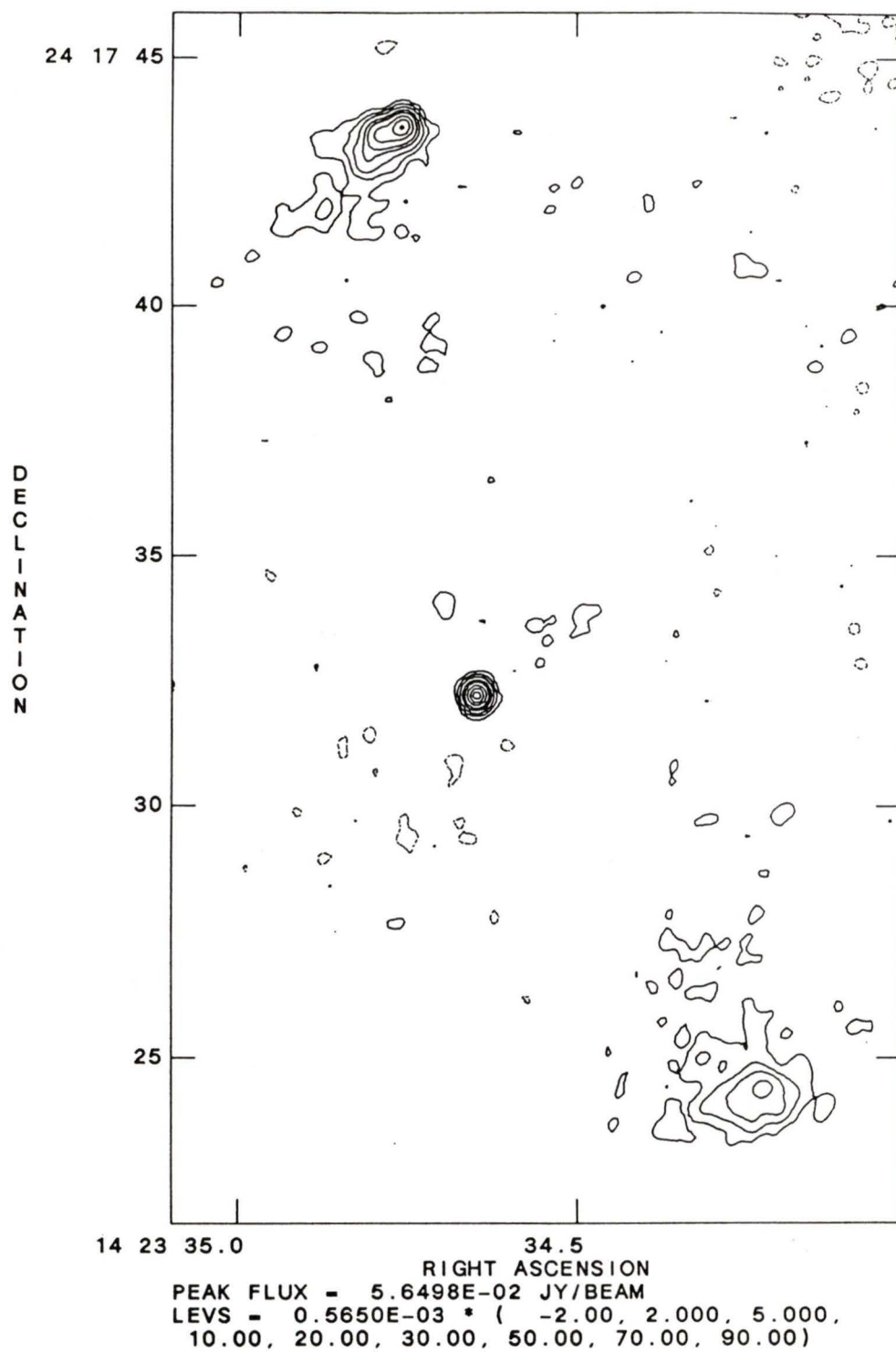
PEAK FLUX = 3.6035E-01 JY/BEAM
LEVS = 0.3604E-02 * (-0.250, 0.250, 0.500,
1.000, 2.000, 5.000, 10.00, 20.00, 30.00,
50.00, 70.00, 90.00)

1420+326 20cm

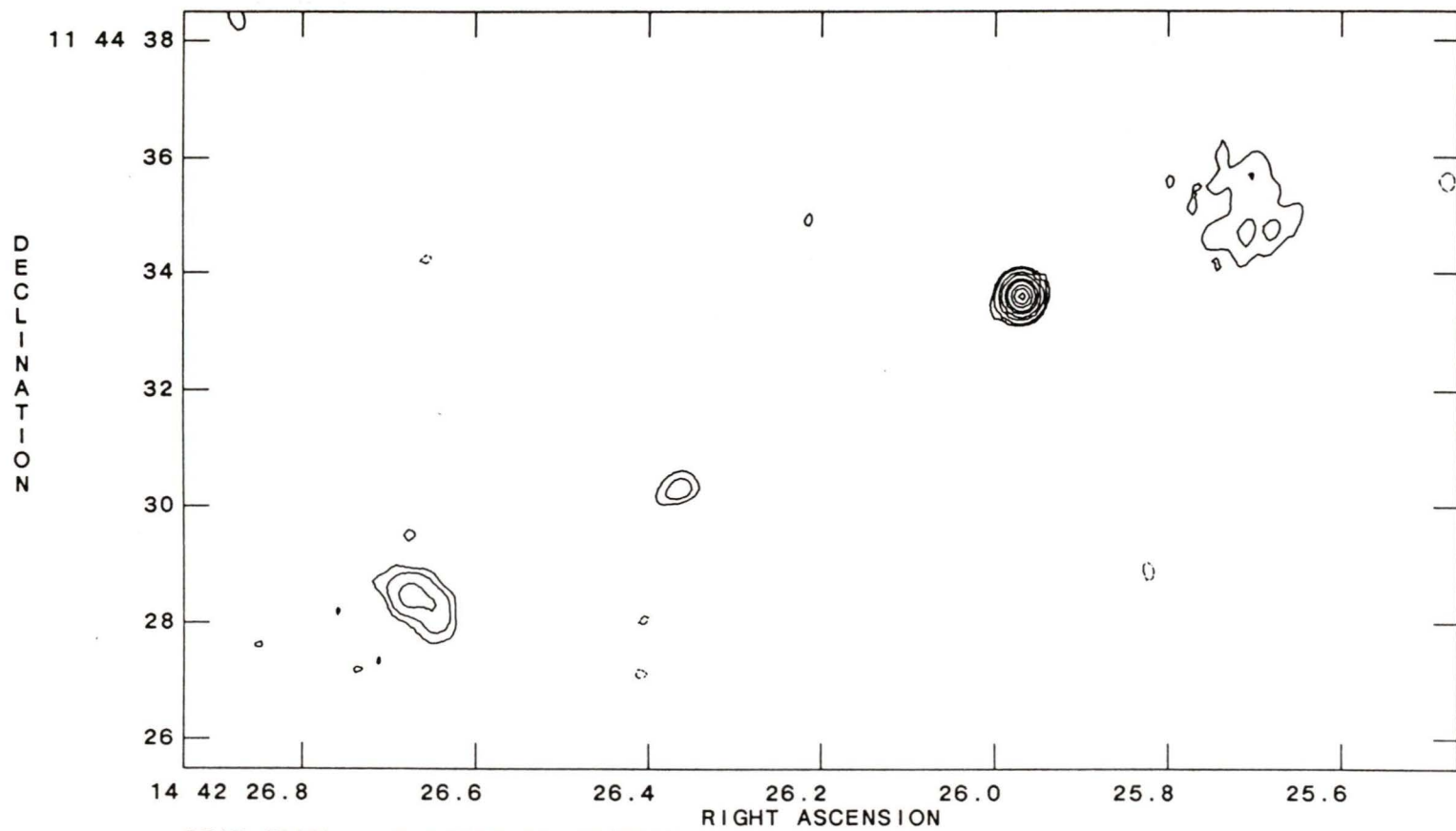


PEAK FLUX = 3.2893E-01 JY/BEAM
LEVS = 0.3289E-02 * (-0.500, 0.500, 1.000,
2.000, 5.000, 10.00, 20.00, 30.00, 50.00,
70.00, 90.00)

1423+242 6cm

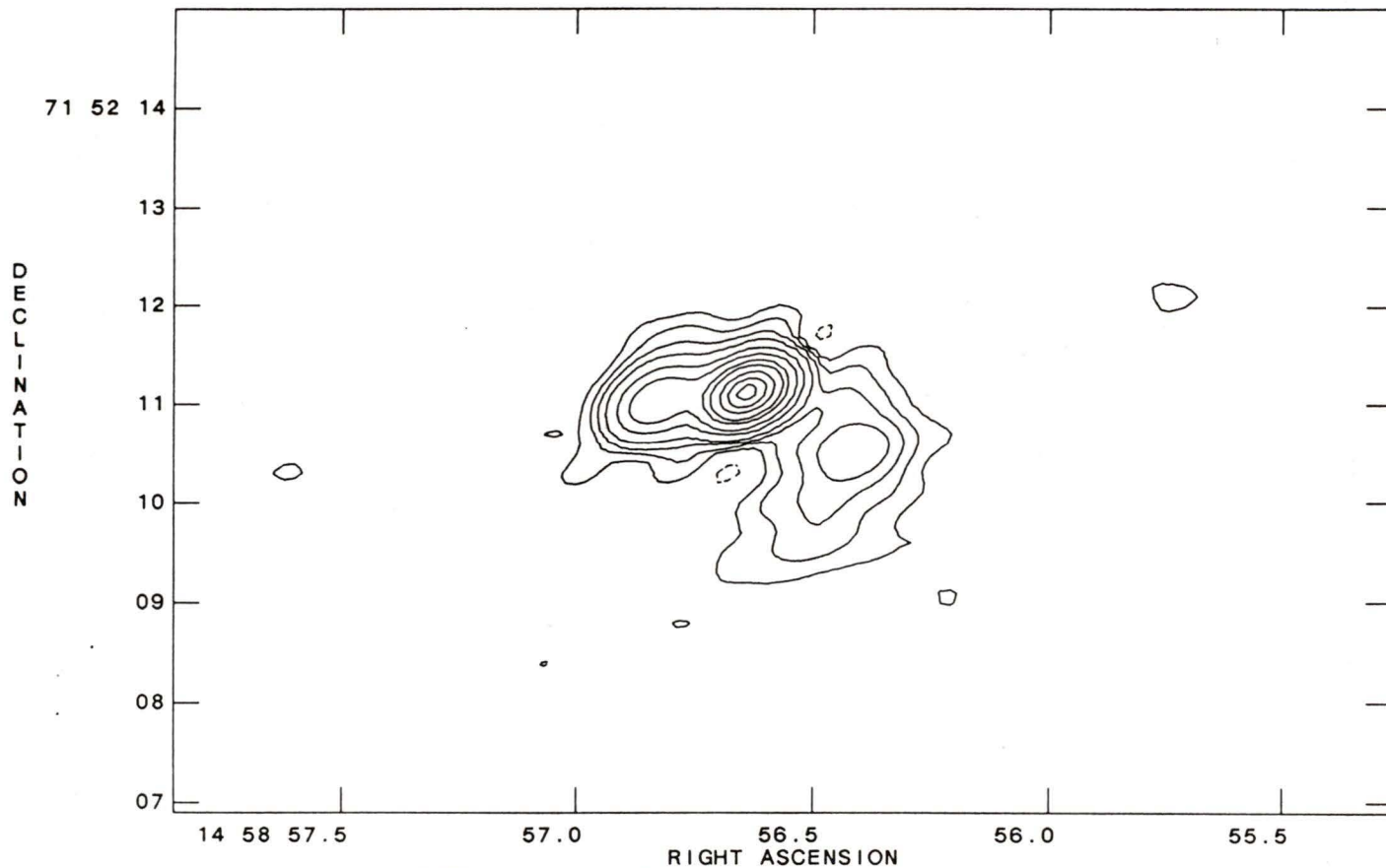


1442+117 6cm



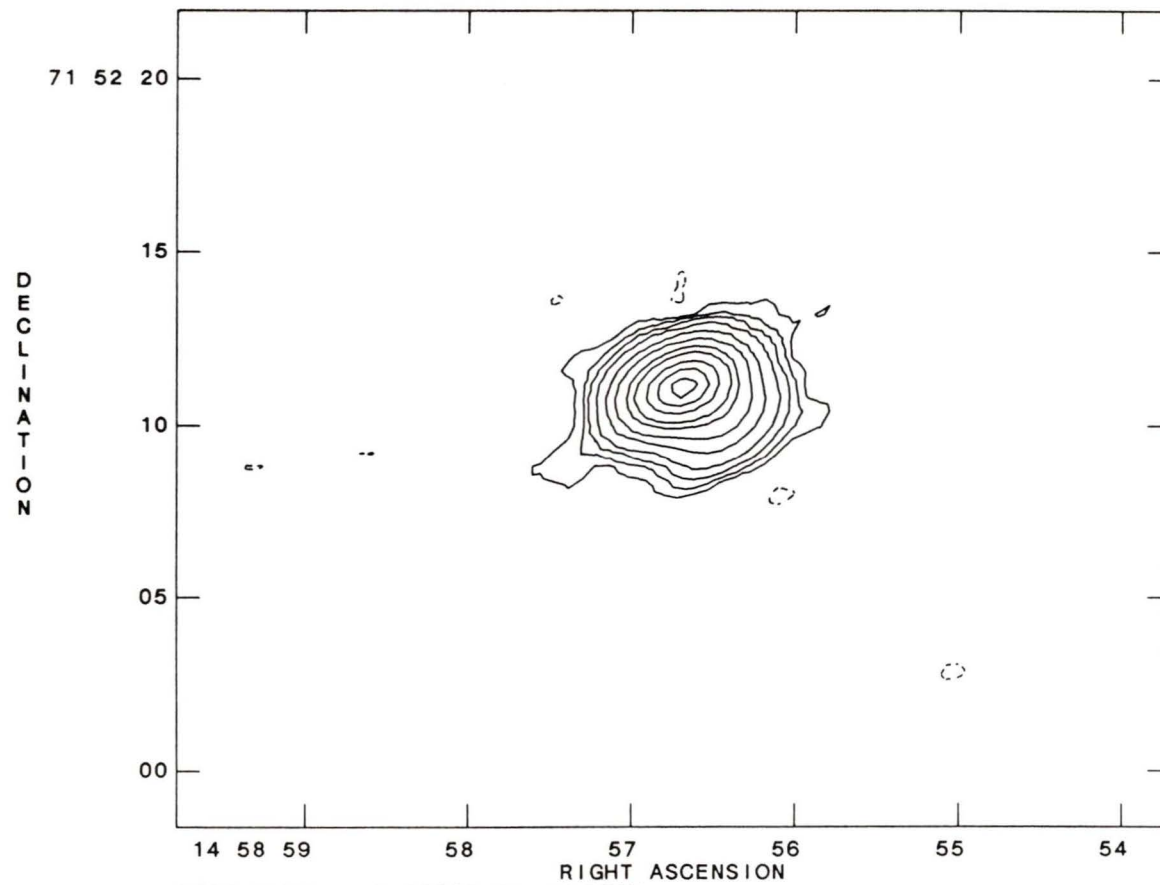
PEAK FLUX = 7.2450E-02 JY/BEAM
LEVS = 0.7245E-03 * (-1.00, 1.000, 2.000,
5.000, 10.00, 20.00, 30.00, 50.00, 70.00,
90.00)

1458+718 6cm



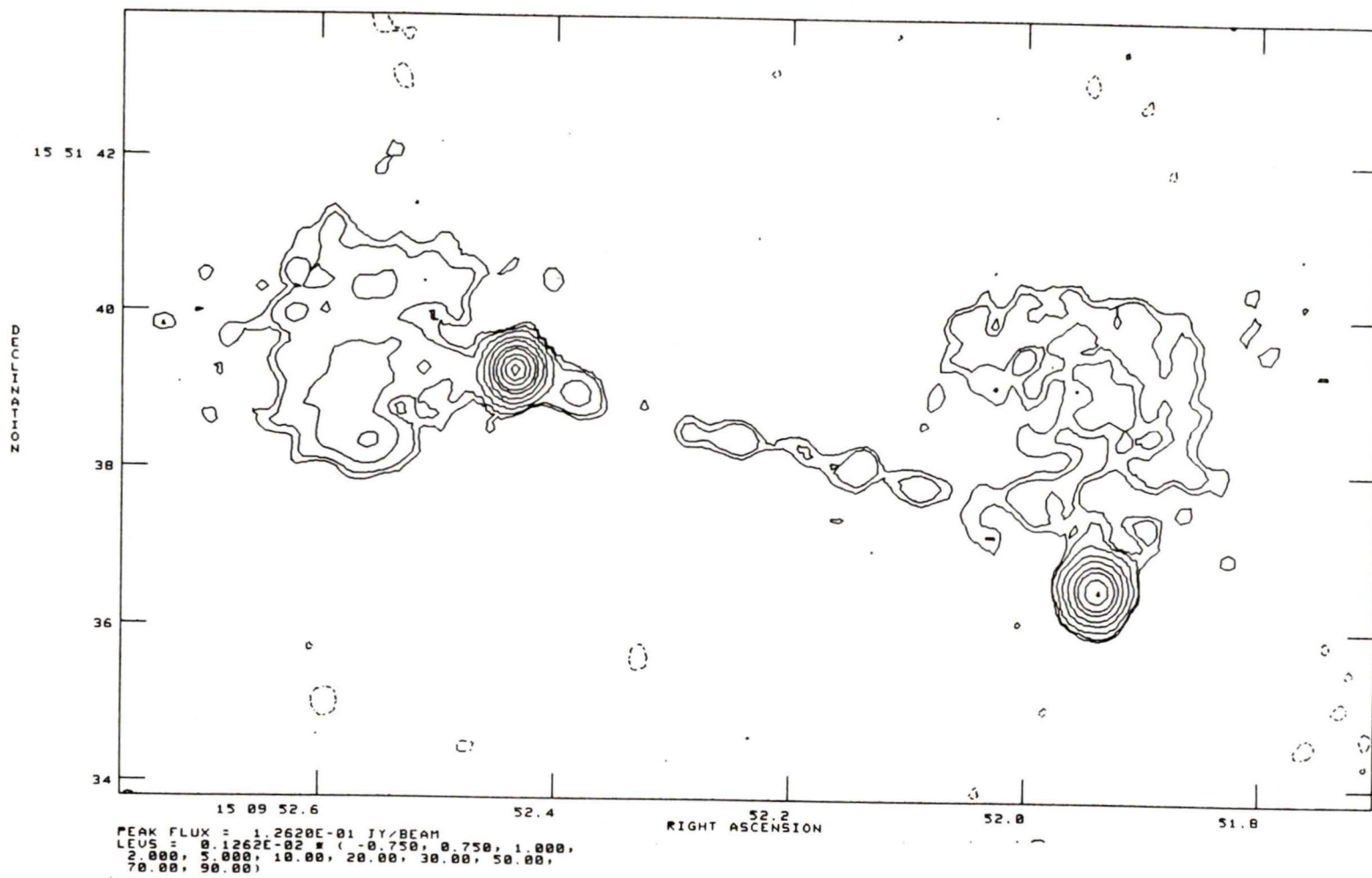
PEAK FLUX = 2.2068E+00 JY/BEAM
LEVS = 0.2207E-01 * (-0.200, 0.200, 0.500,
1.000, 2.000, 5.000, 10.00, 20.00, 30.00,
50.00, 70.00, 90.00)

1458+718 20cm

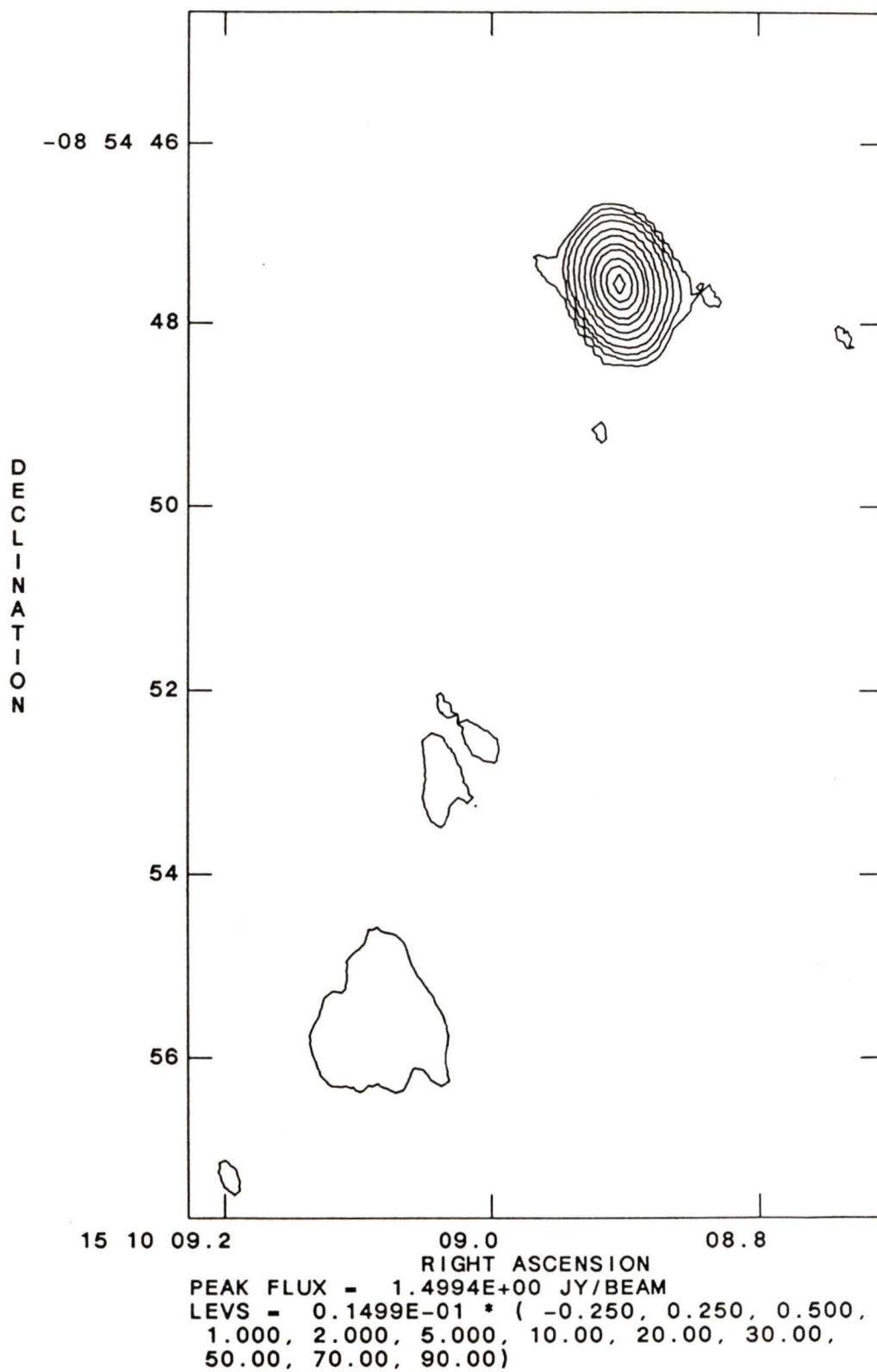


PEAK FLUX = 5.1560E+00 JY/BEAM
LEVS = 0.5156E-01 * (-0.200, 0.200, 0.500,
1.000, 2.000, 5.000, 10.00, 20.00, 30.00,
50.00, 70.00, 90.00)

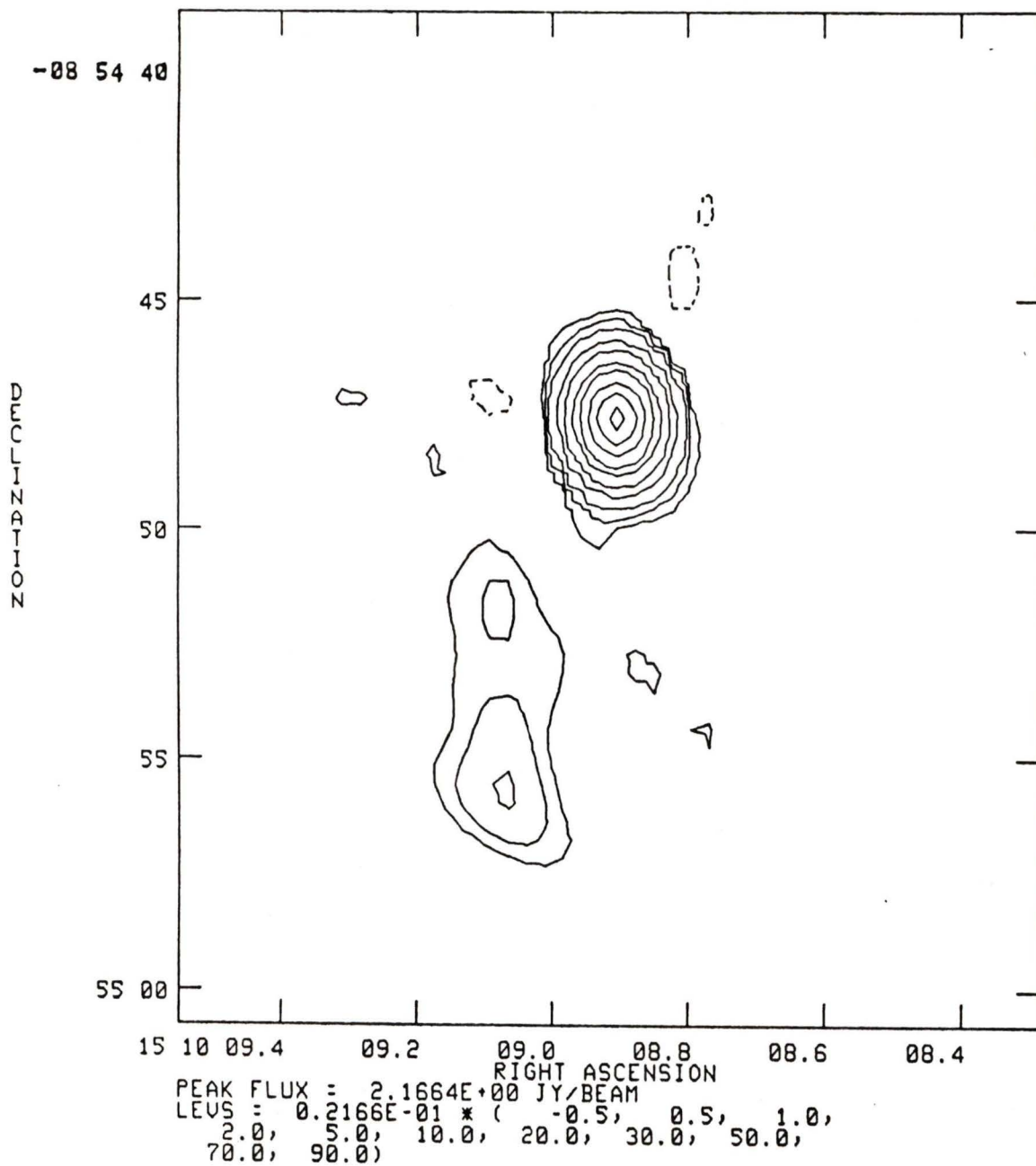
1509+158 6cm



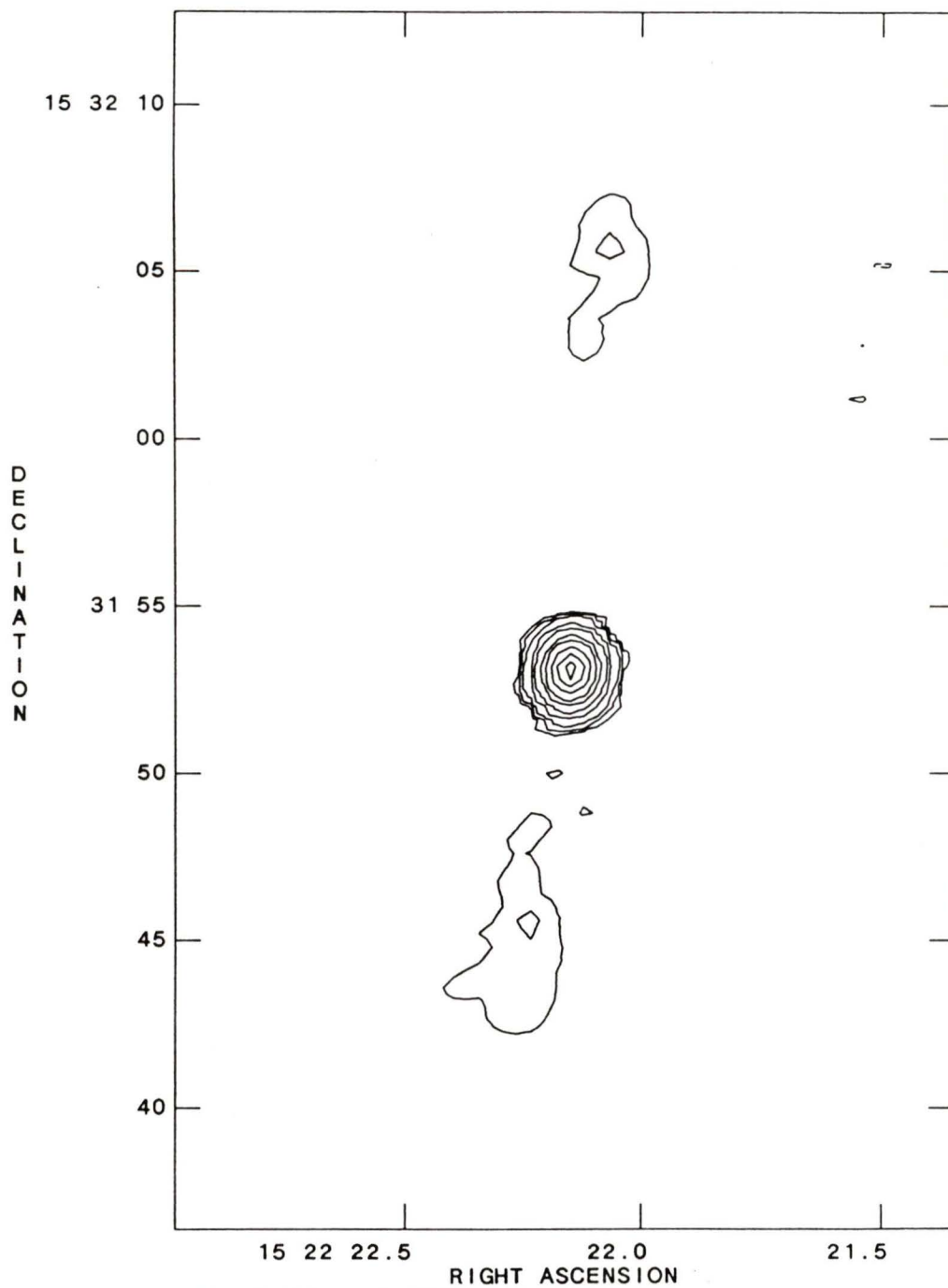
1510-089 6cm



1510-089 20cm

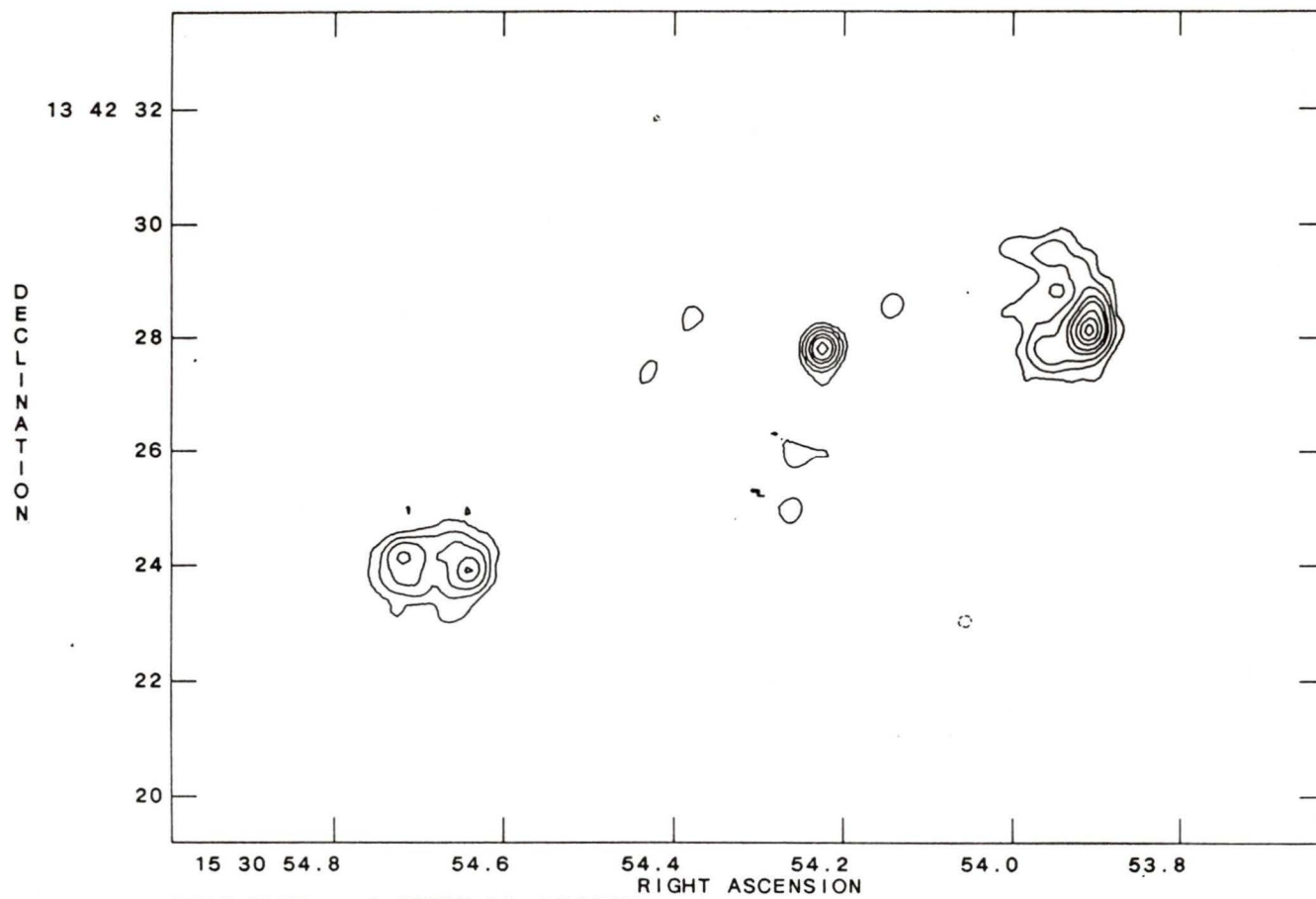


1522+155 20cm

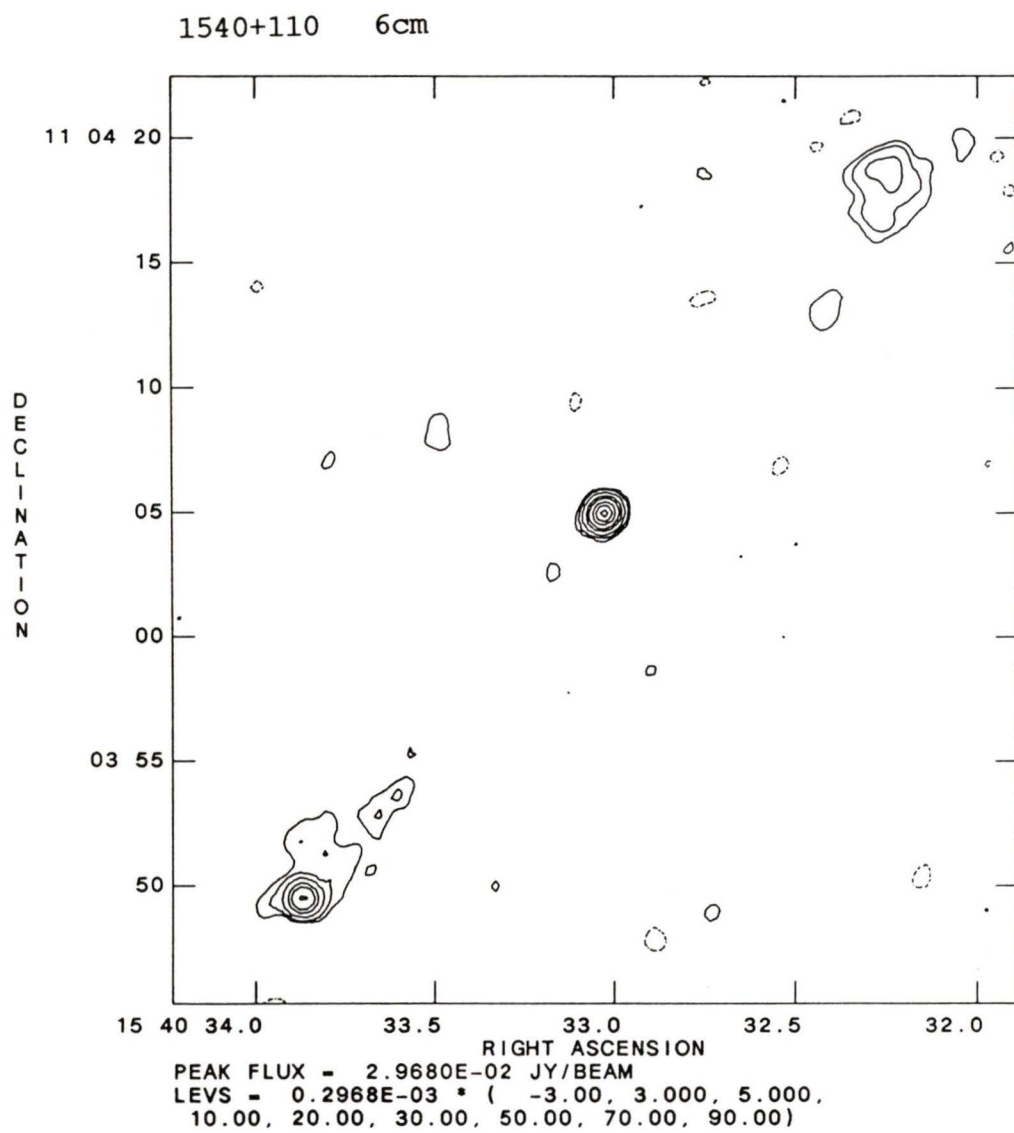


PEAK FLUX = 3.2972E-01 JY/BEAM.
LEVS = 0.3297E-02 * (-0.500, 0.500, 1.000,
2.000, 5.000, 10.00, 20.00, 30.00, 50.00,
70.00, 90.00)

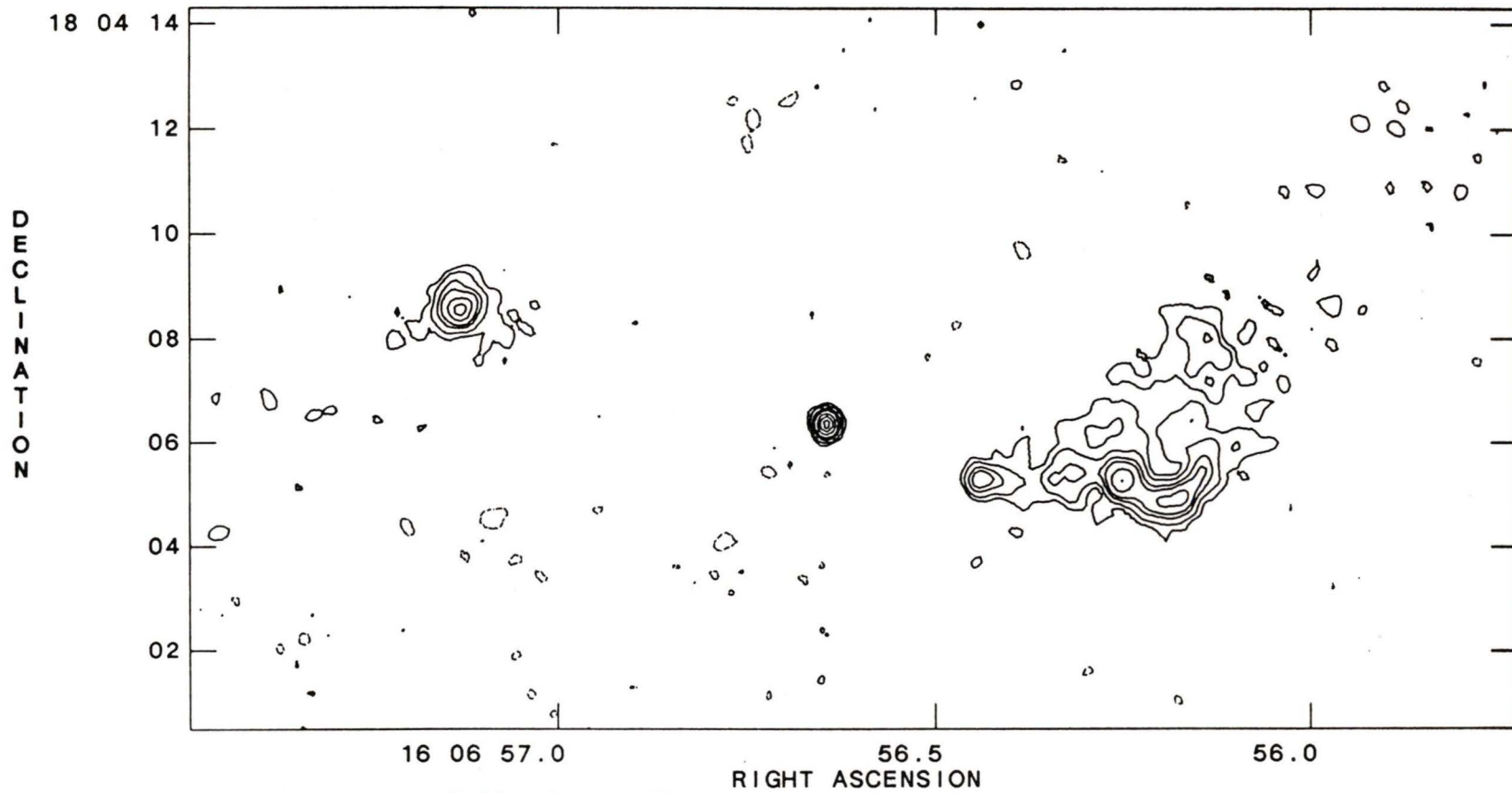
1530+137 6cm



PEAK FLUX = 5.7099E-02 JY/BEAM
LEVS = 0.5710E-03 * (-2.00, 2.000, 5.000,
10.00, 20.00, 30.00, 50.00, 70.00, 90.00)

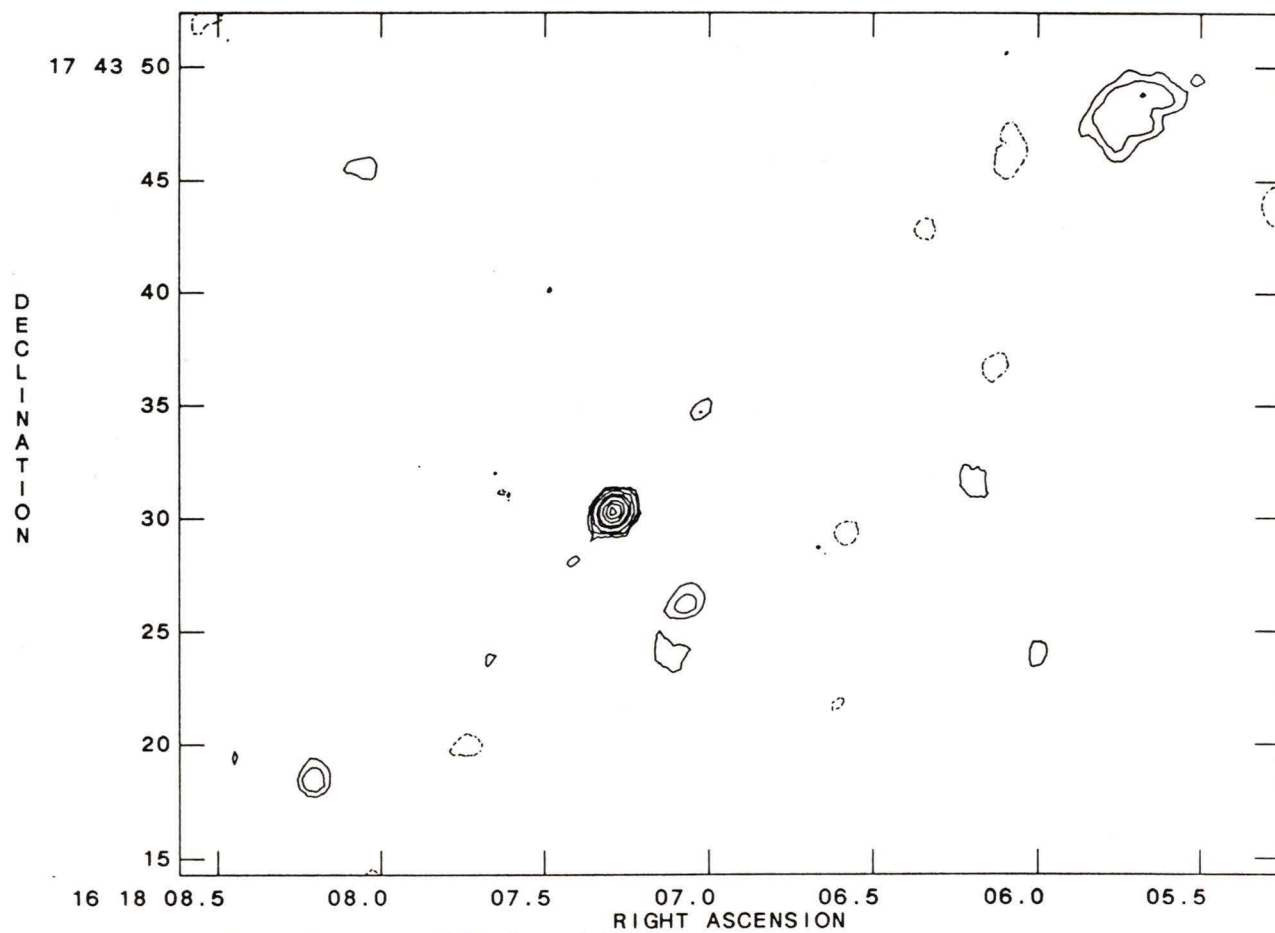


1606+180 6cm



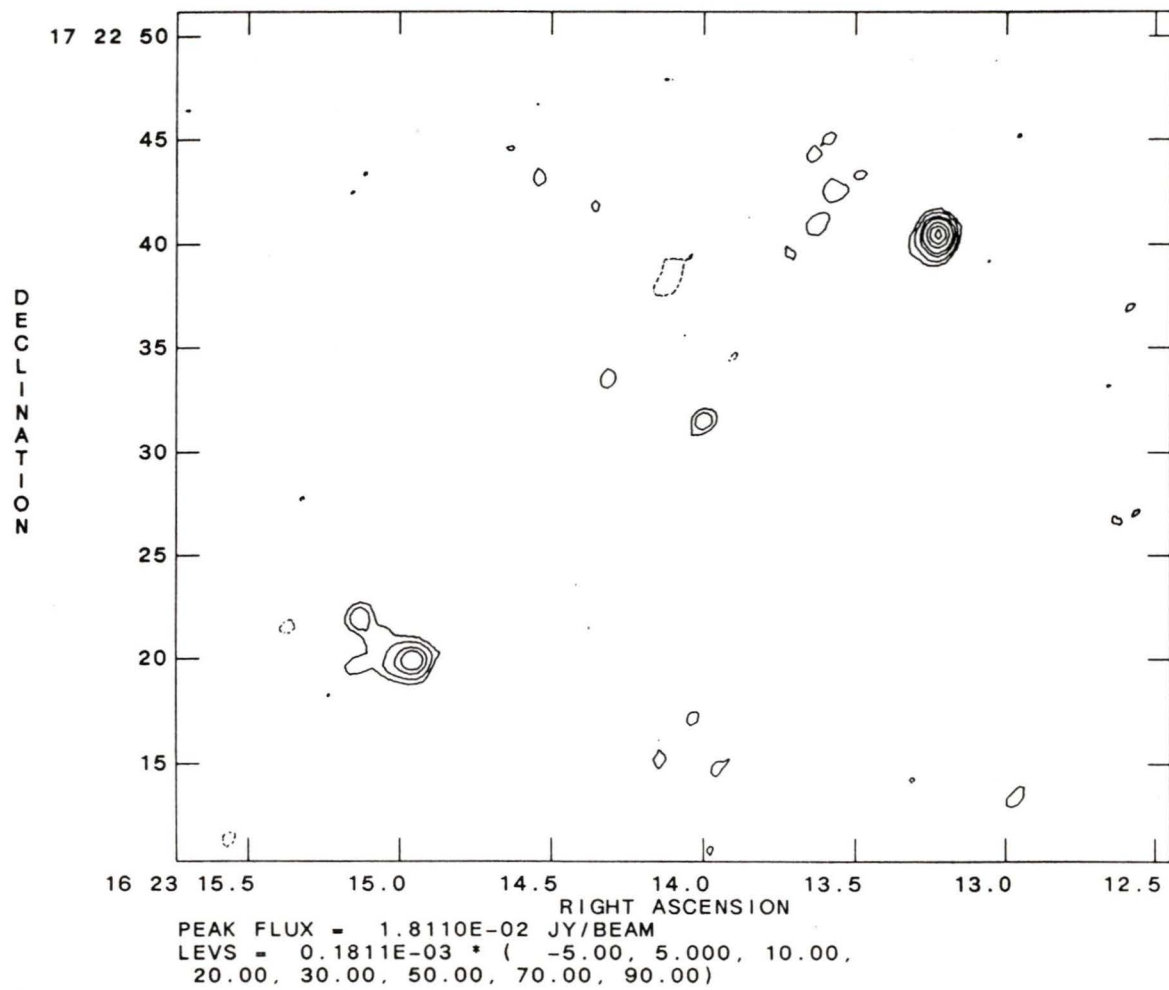
PEAK FLUX = 1.4769E-02 JY/BEAM
LEVS = 0.1477E-03 * (-5.00, 5.000, 10.00,
20.00, 30.00, 50.00, 70.00, 90.00)

1618+177 6cm

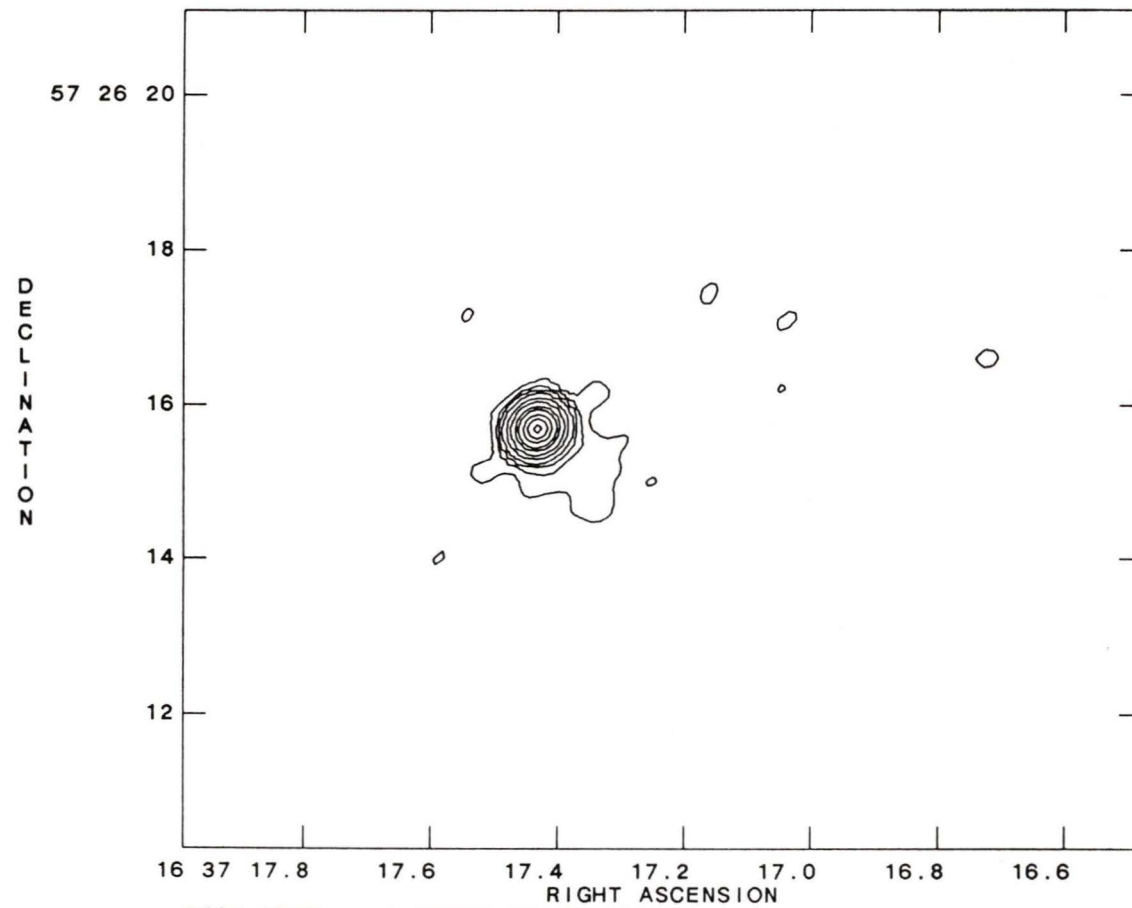


PEAK FLUX = 1.2898E-01 JY/BEAM
LEVS = 0.1290E-02 * (-3.00, 3.000, 5.000,
10.00, 20.00, 30.00, 50.00, 70.00, 90.00)

1623+173 6cm

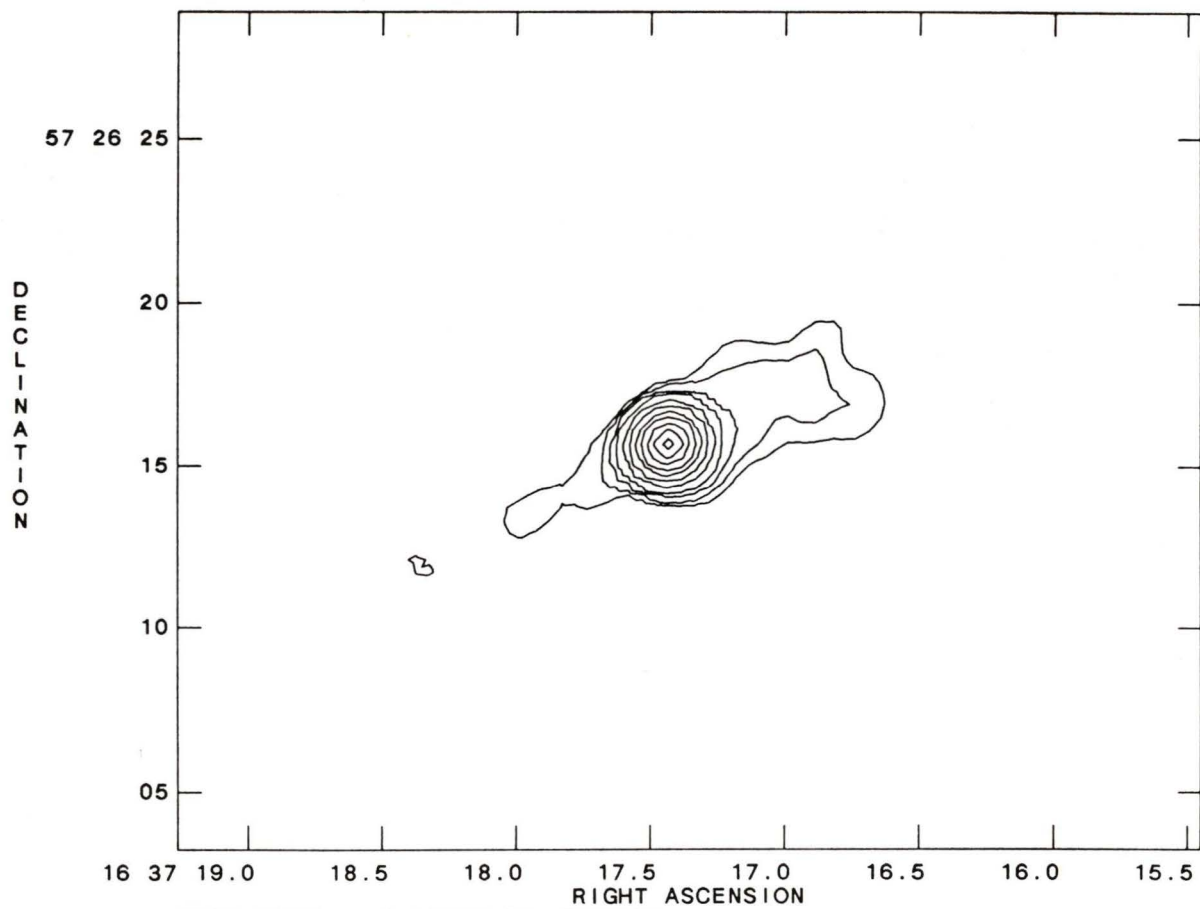


1637+574 6cm

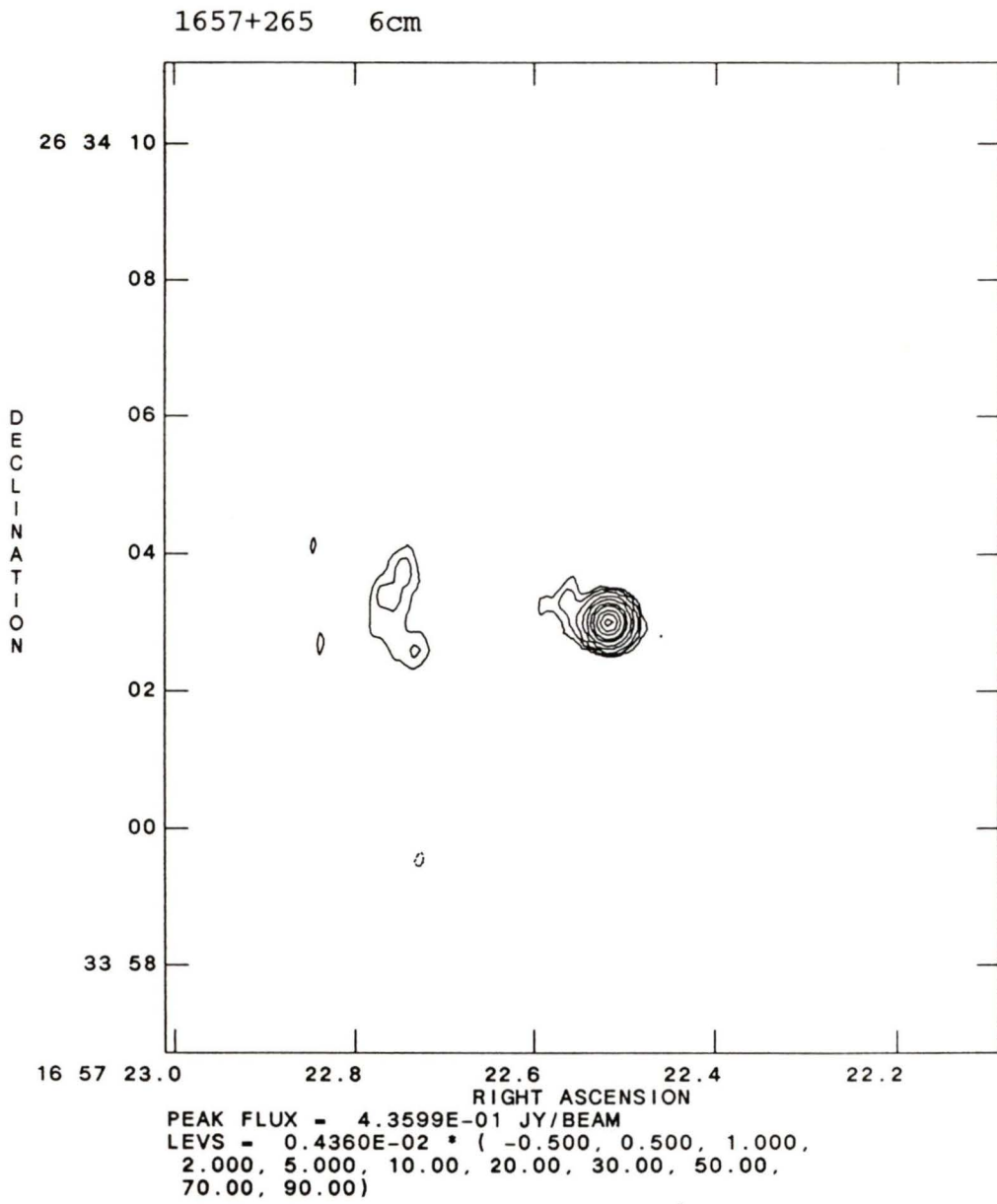


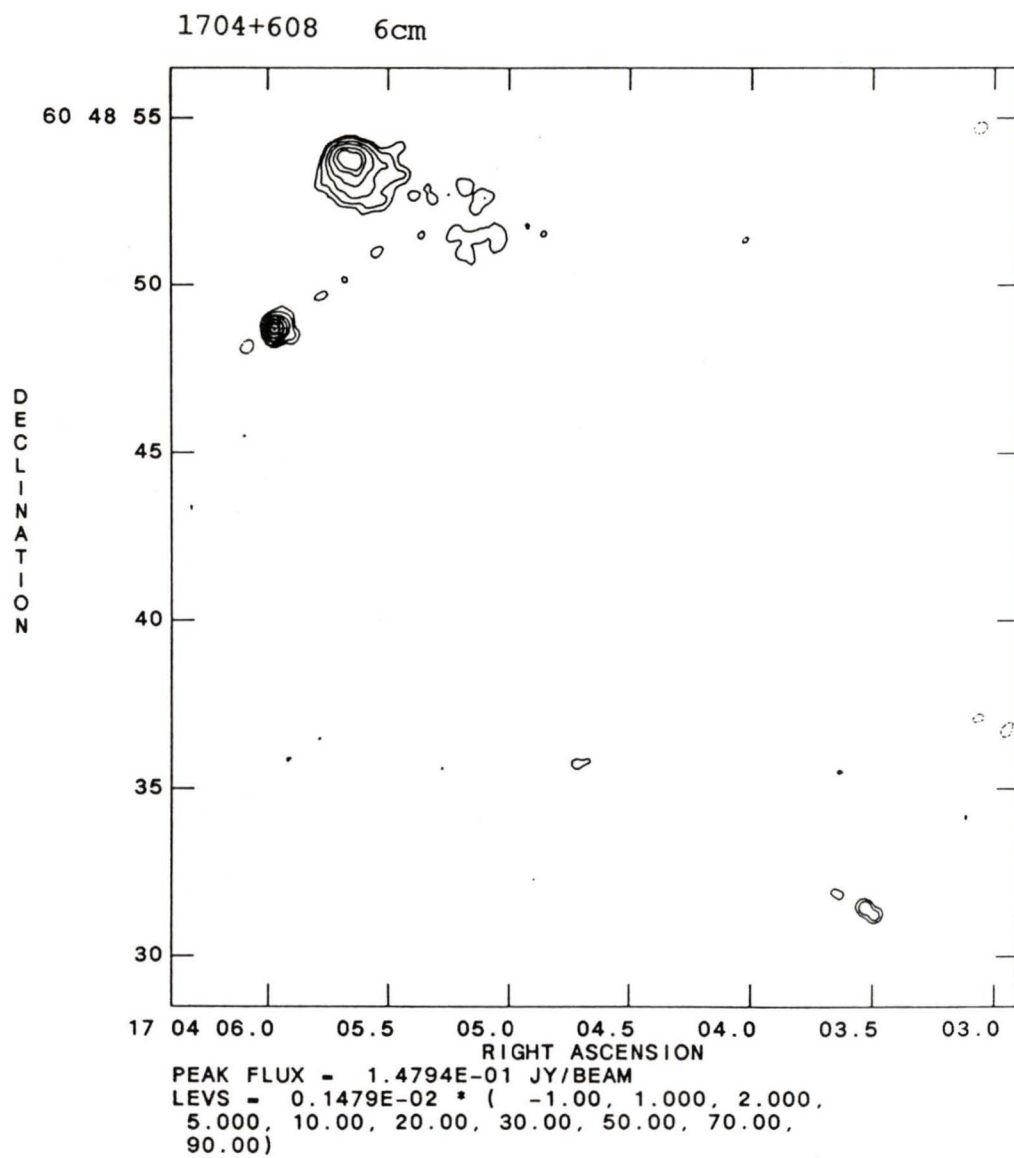
PEAK FLUX = 1.3655E+00 JY/BEAM
LEVS = 0.1365E-01 * (-0.200, 0.200, 0.500,
1.000, 2.000, 5.000, 10.00, 20.00, 30.00,
50.00, 70.00, 90.00)

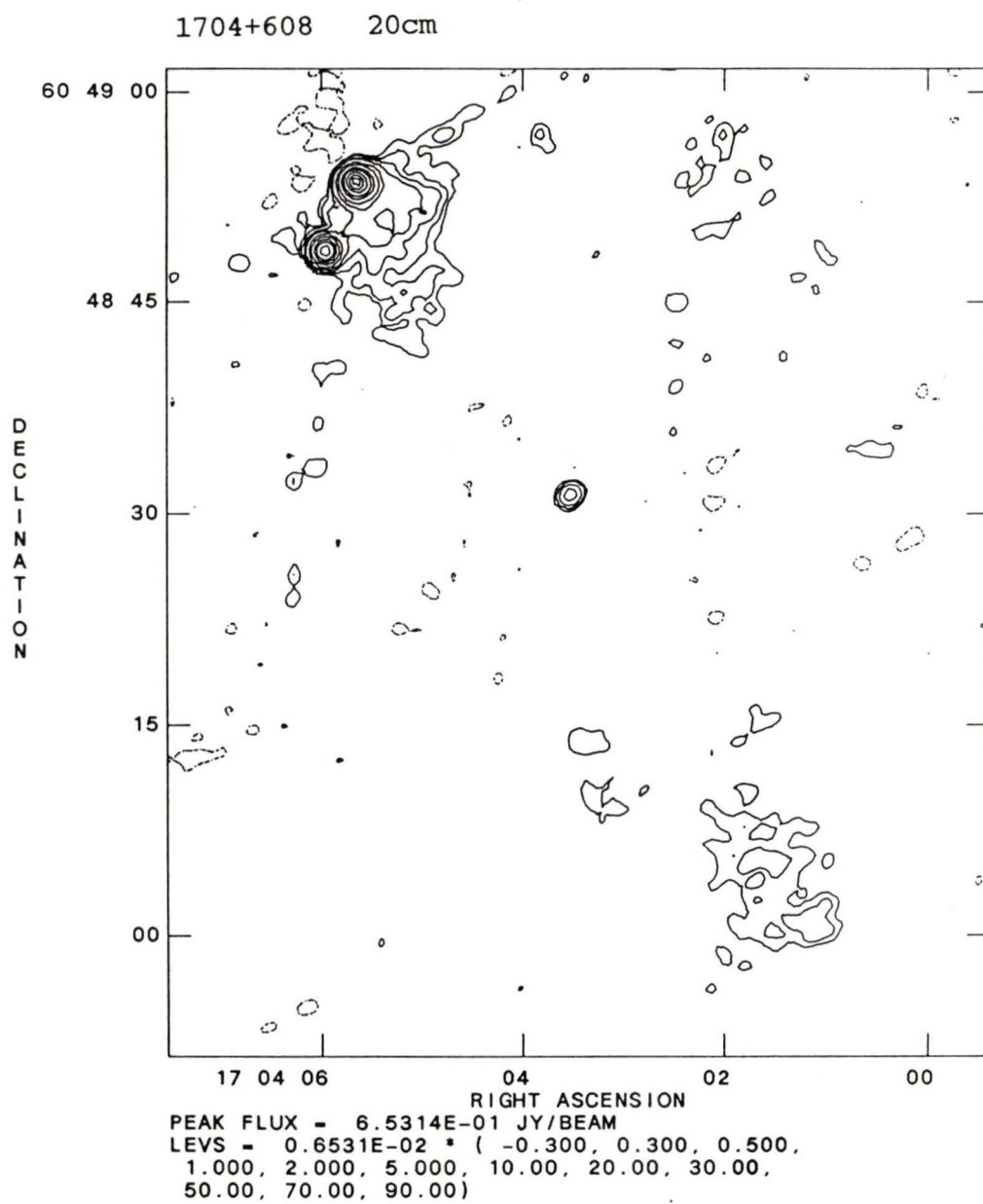
1637+574 20cm

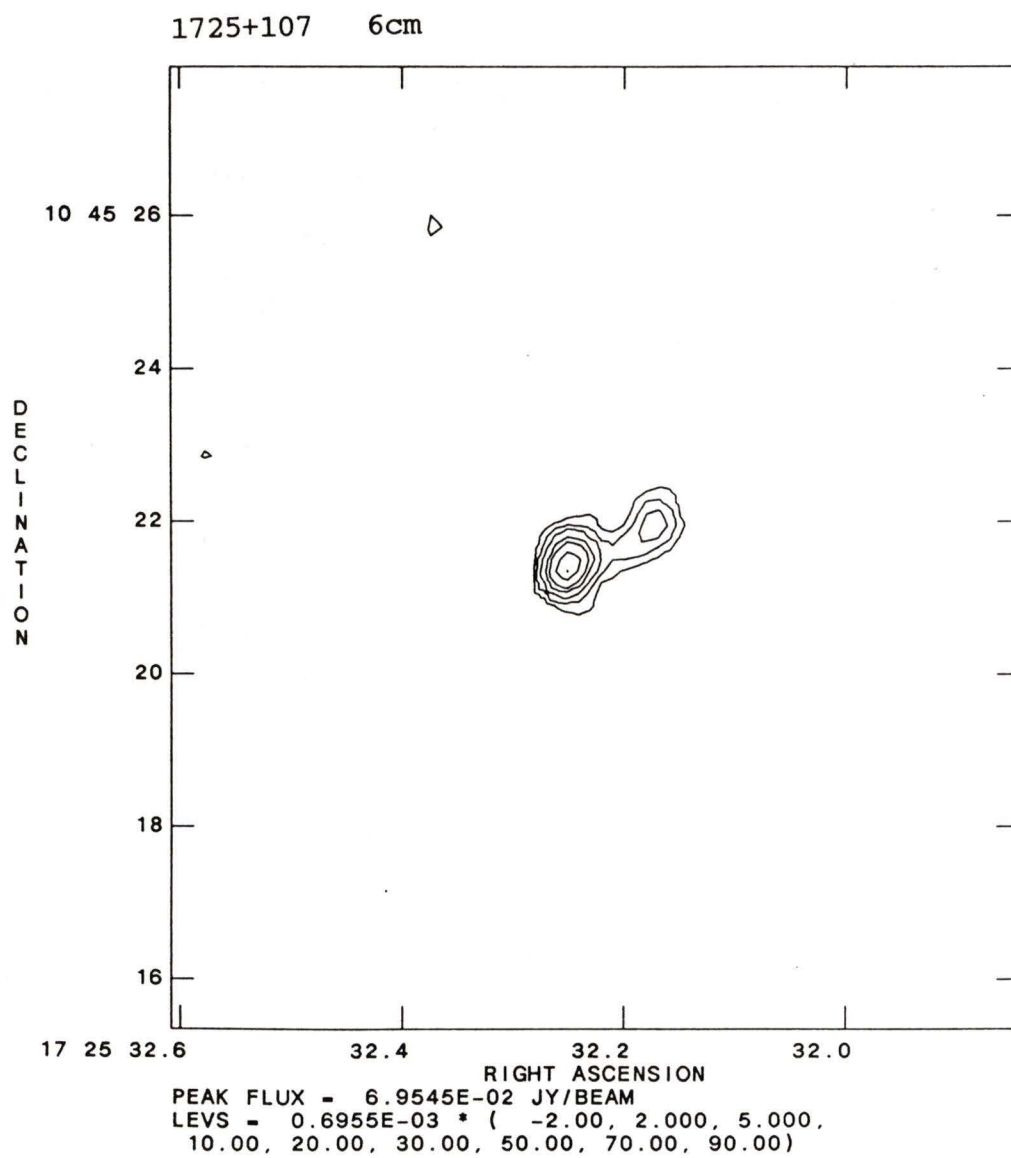


PEAK FLUX = 1.1988E+00 JY/BEAM
LEVS = 0.1199E-01 * (-0.250, 0.250, 0.500,
1.000, 2.000, 5.000, 10.00, 20.00, 30.00,
50.00, 70.00, 90.00)

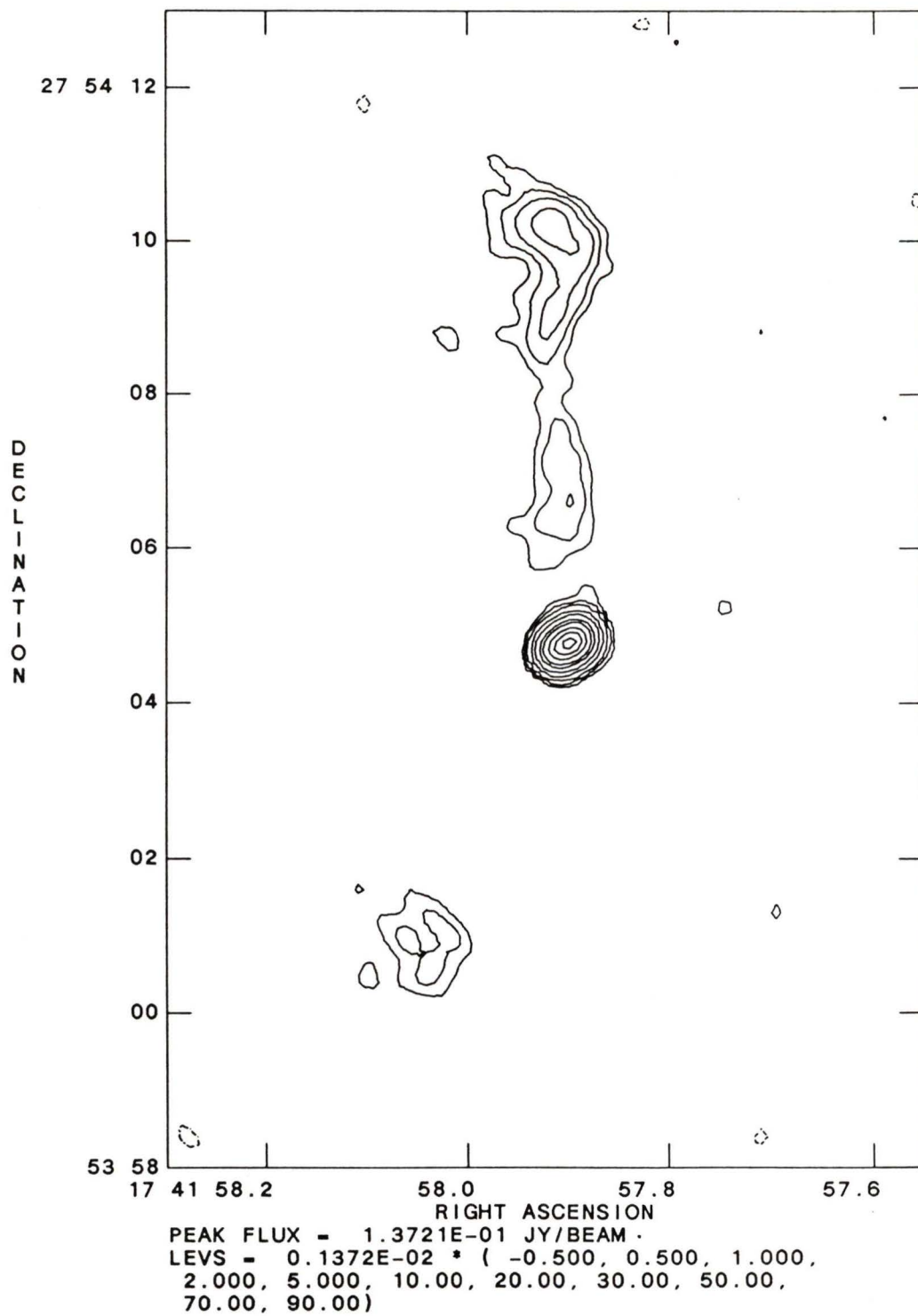




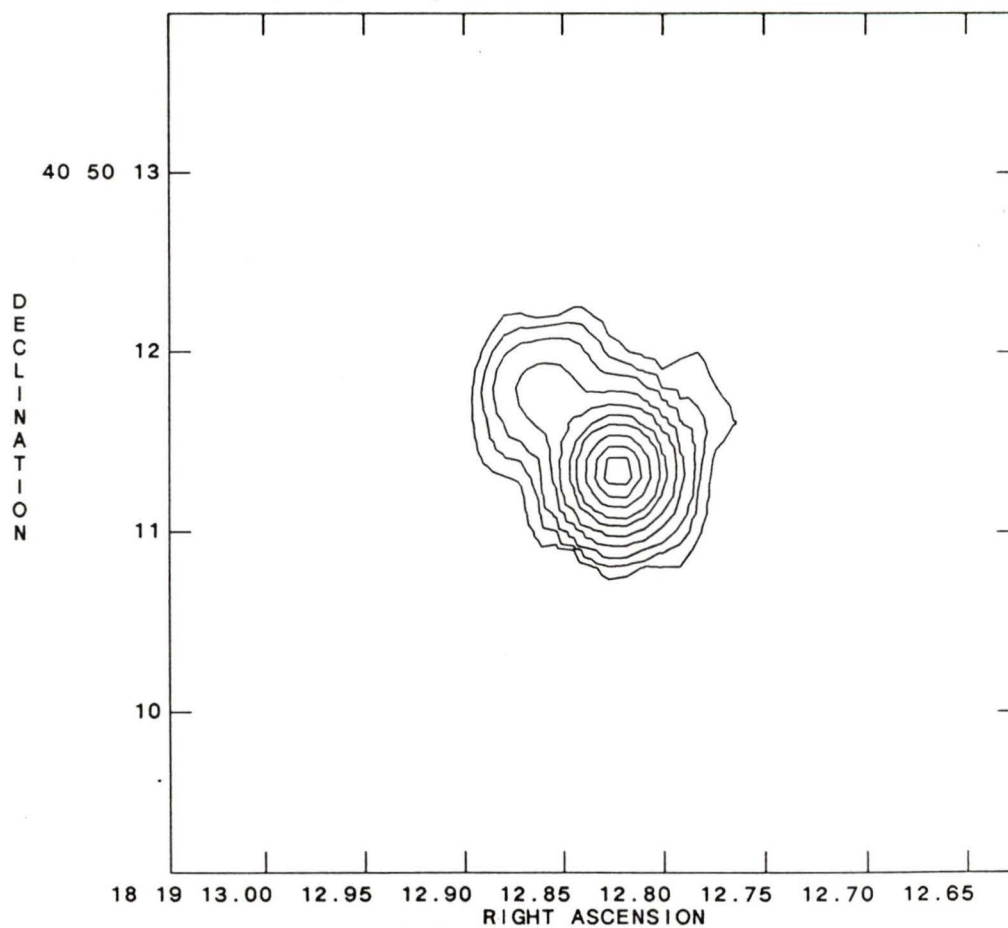




1741+279 6cm



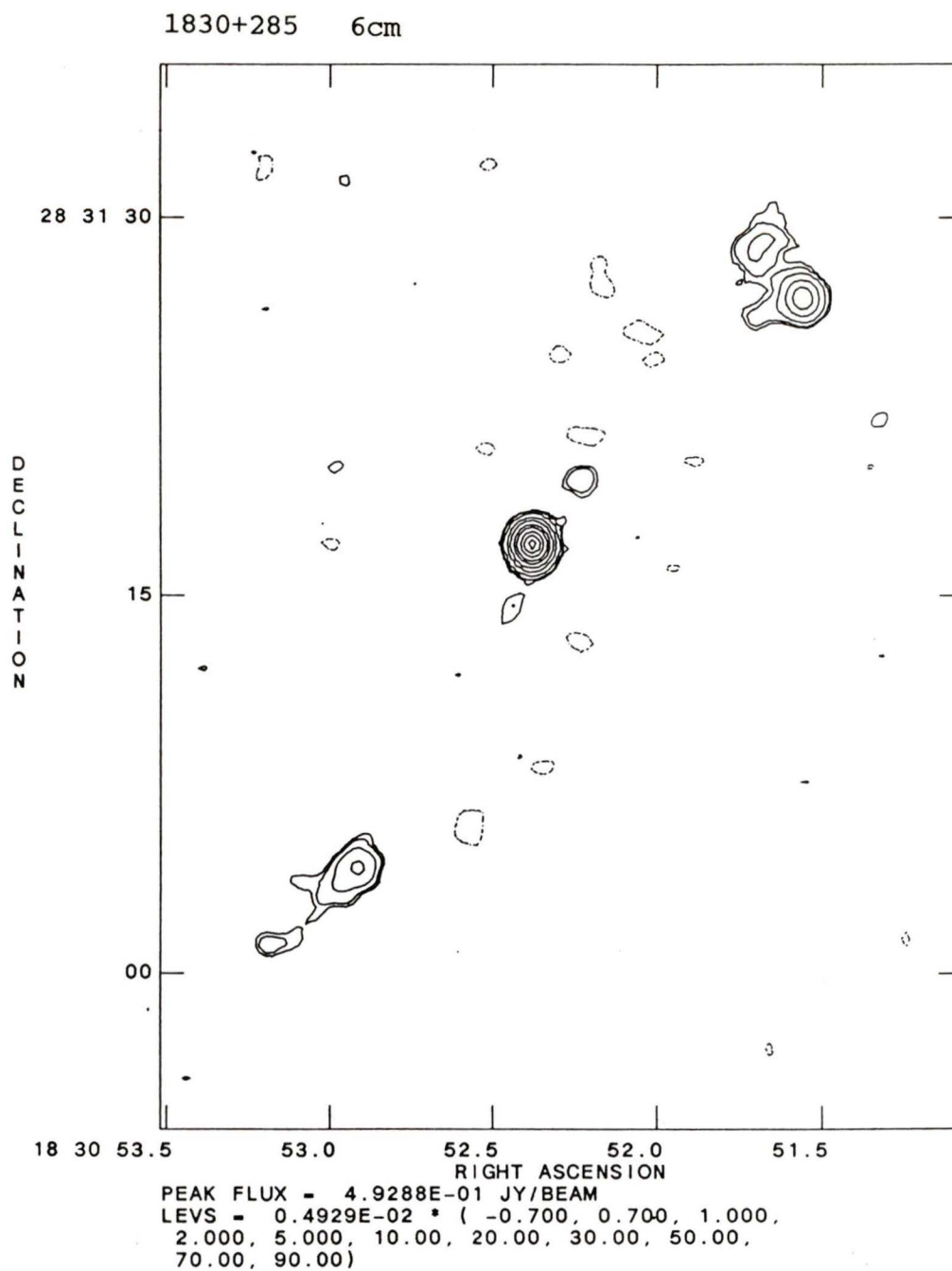
1819+408 6cm



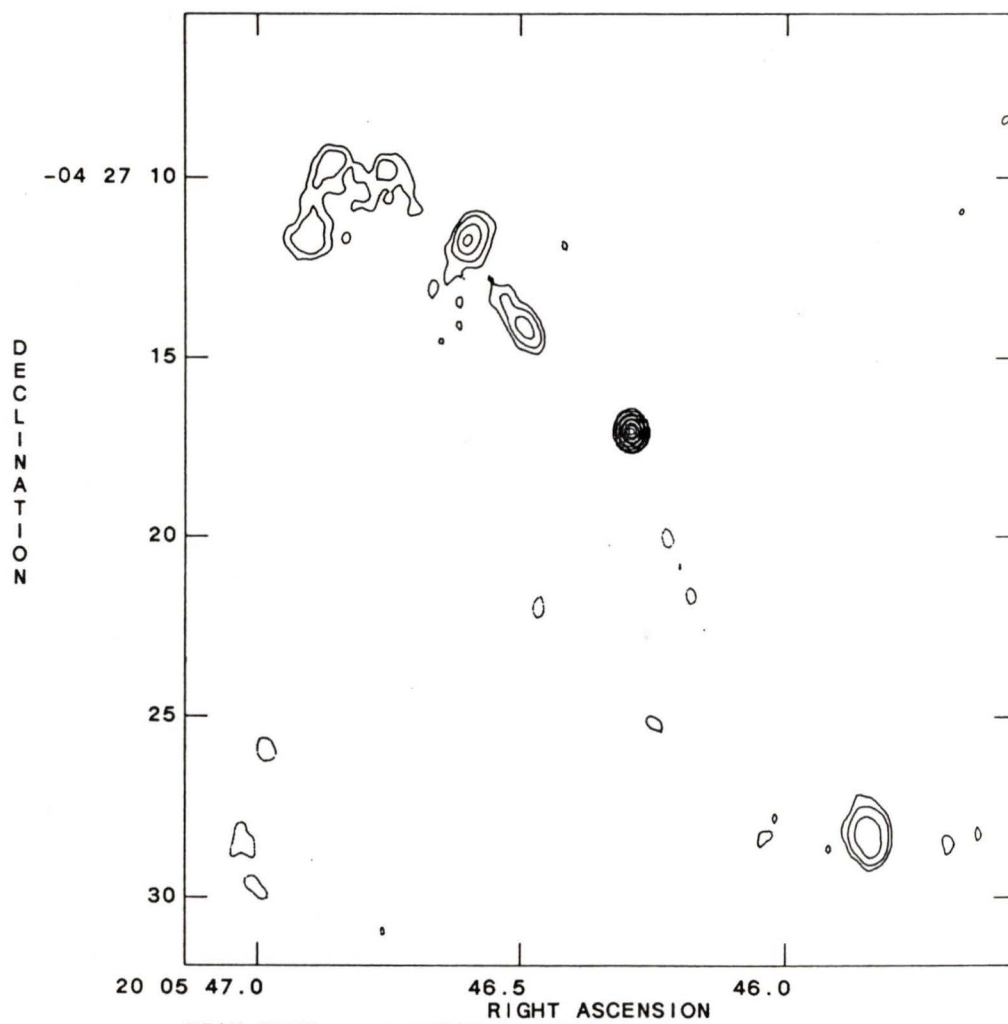
18 19 13.00 12.95 12.90 12.85 12.80 12.75 12.70 12.65

RIGHT ASCENSION

PEAK FLUX = 1.6500E-01 JY/BEAM
LEVS = 0.1650E-02 * (-0.500, 0.500, 1.000,
2.000, 5.000, 10.00, 20.00, 30.00, 50.00,
70.00, 90.00)

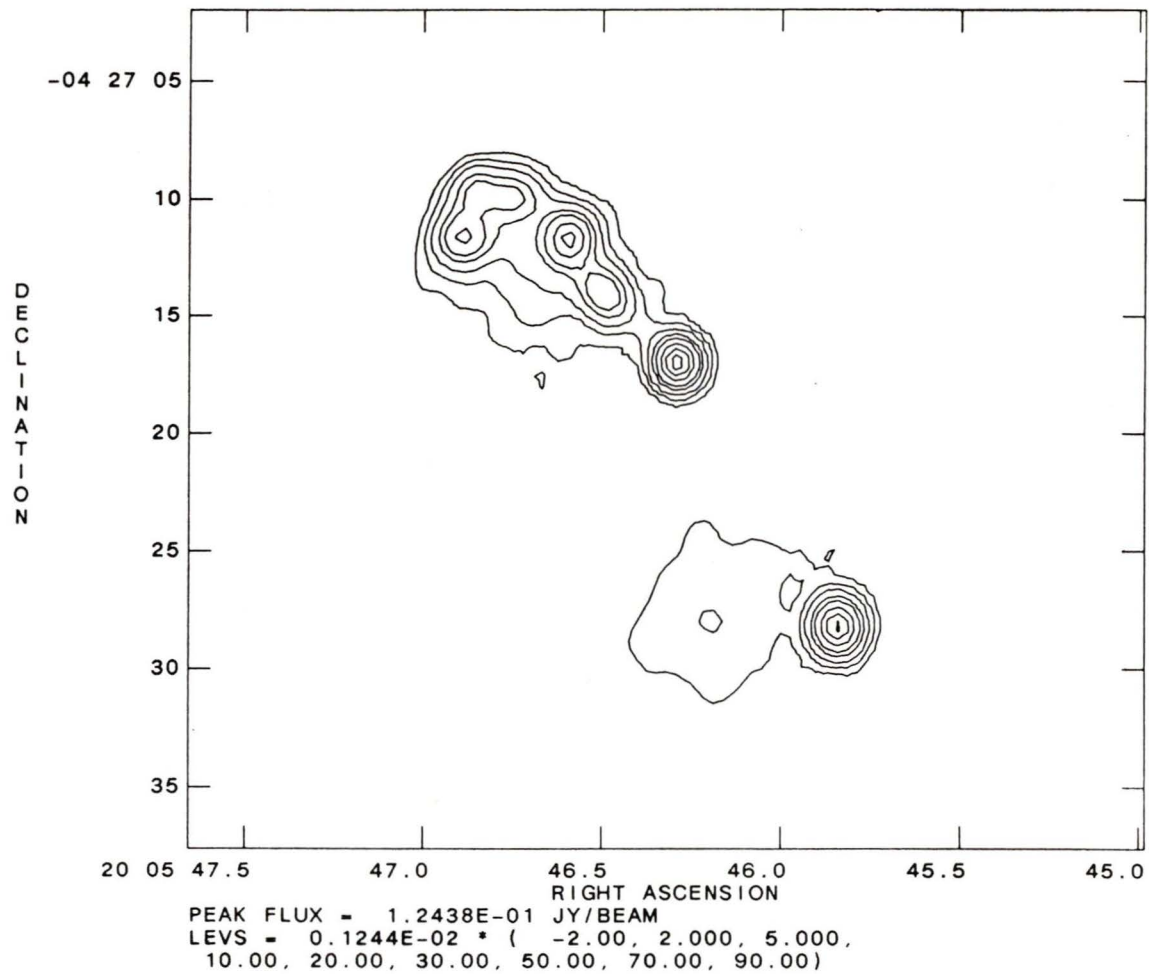


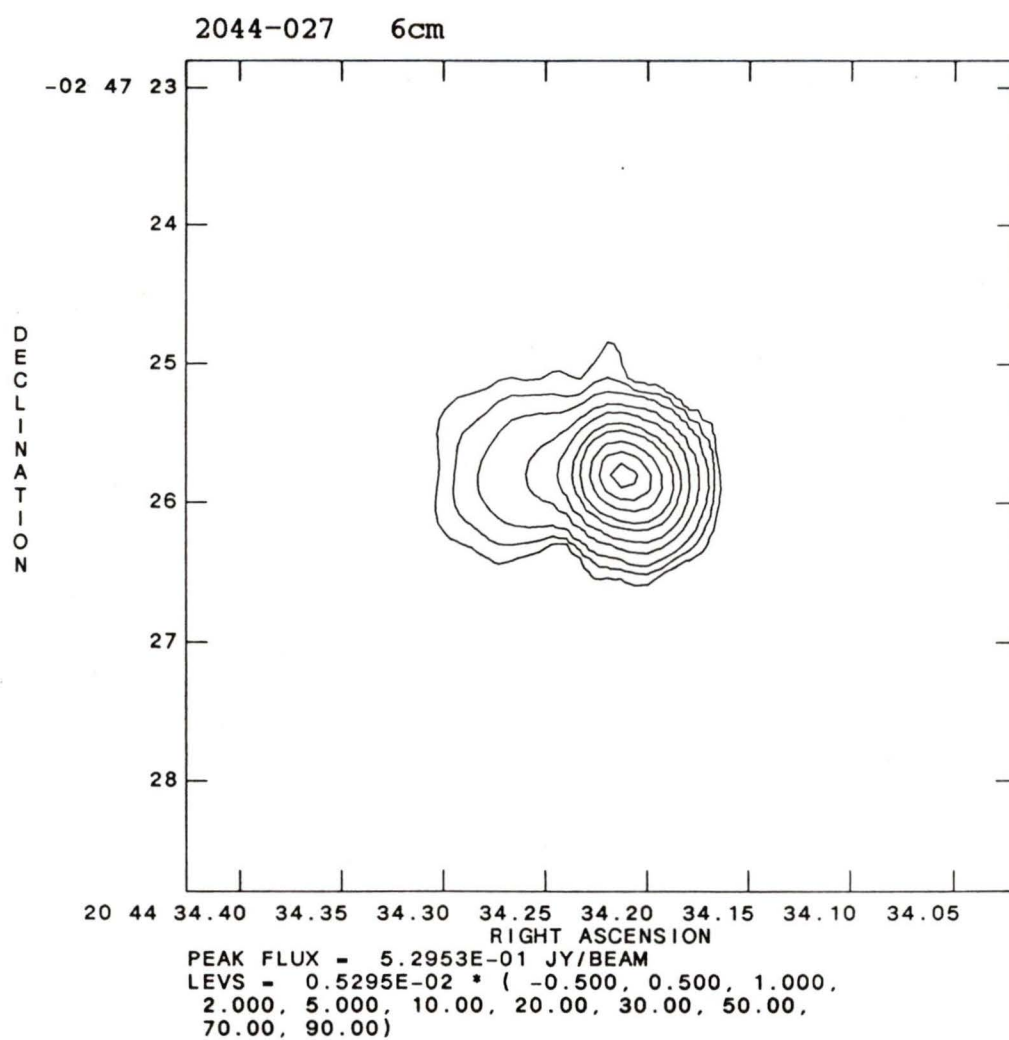
2005-044 6cm

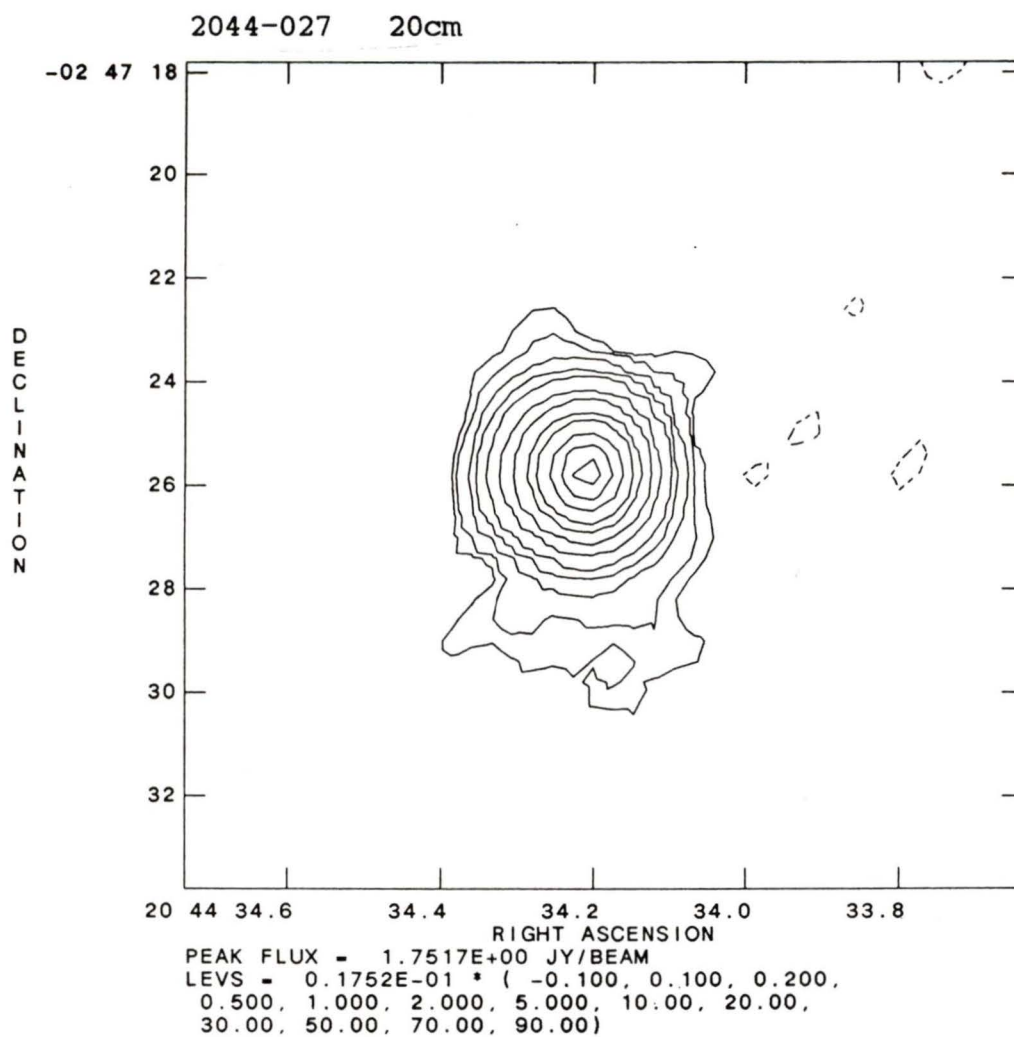


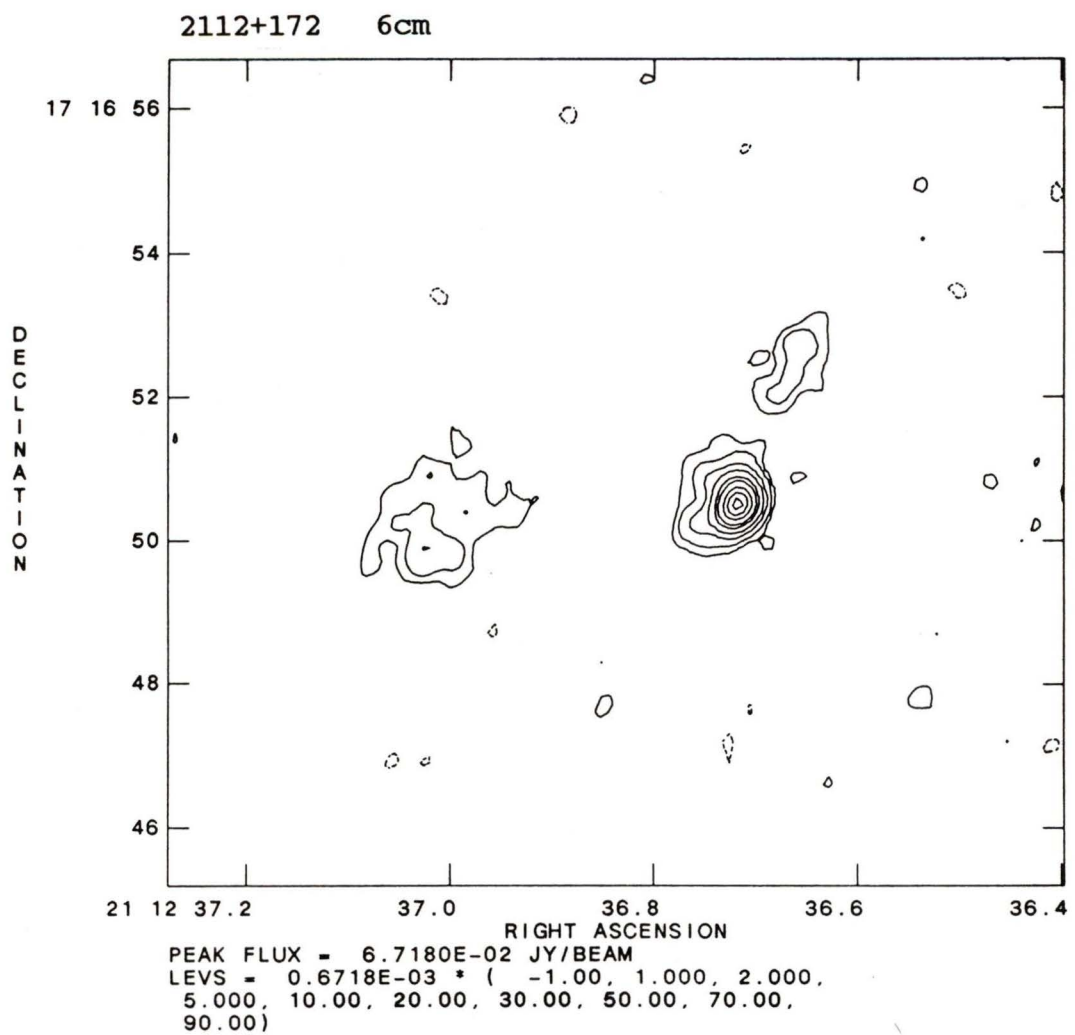
PEAK FLUX = 1.3590E-01 JY/BEAM
LEVS = 0.1359E-02 * (-1.00, 1.000, 2.000,
5.000, 10.00, 20.00, 30.00, 50.00, 70.00,
90.00)

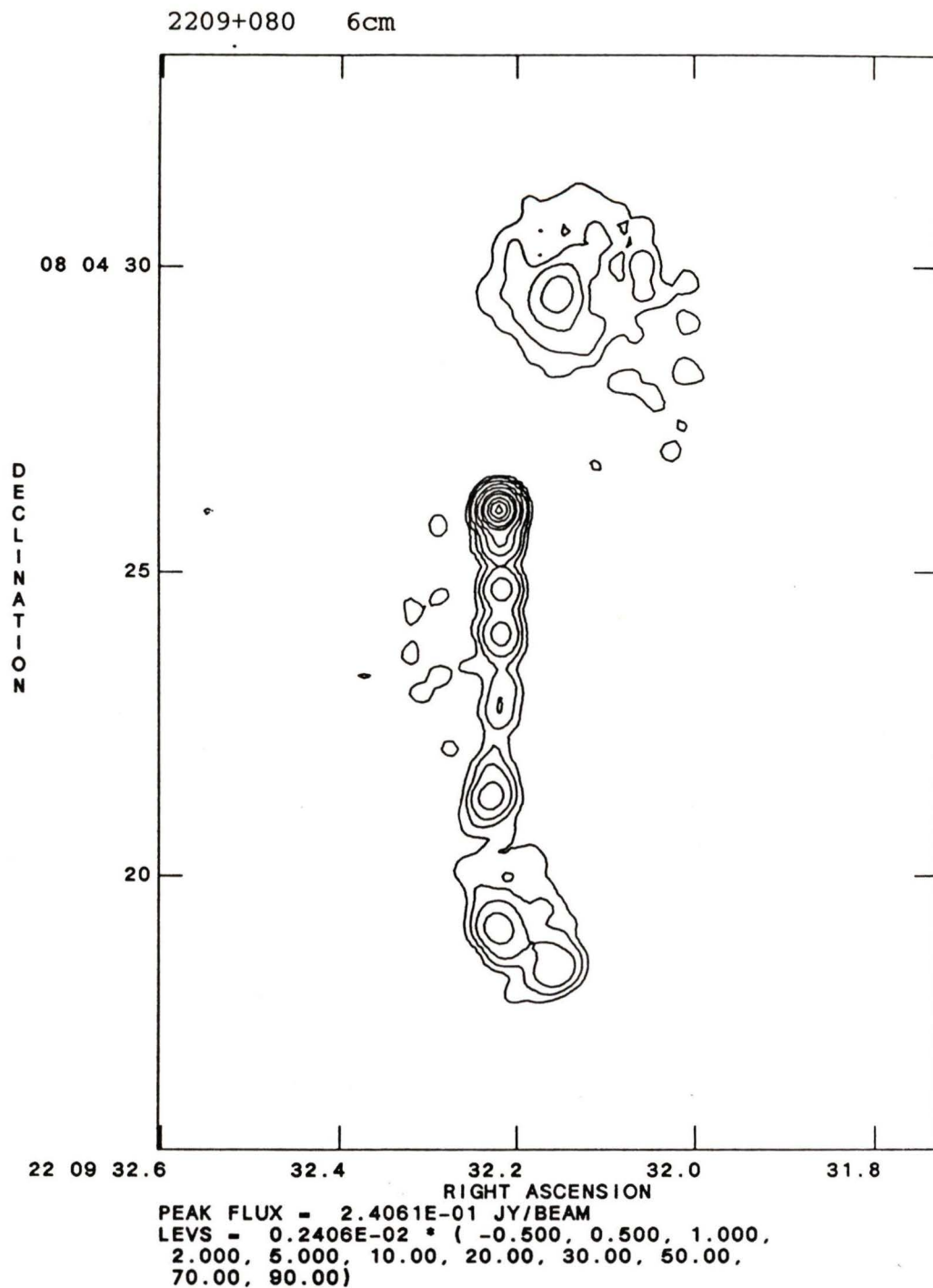
2005-044 20cm



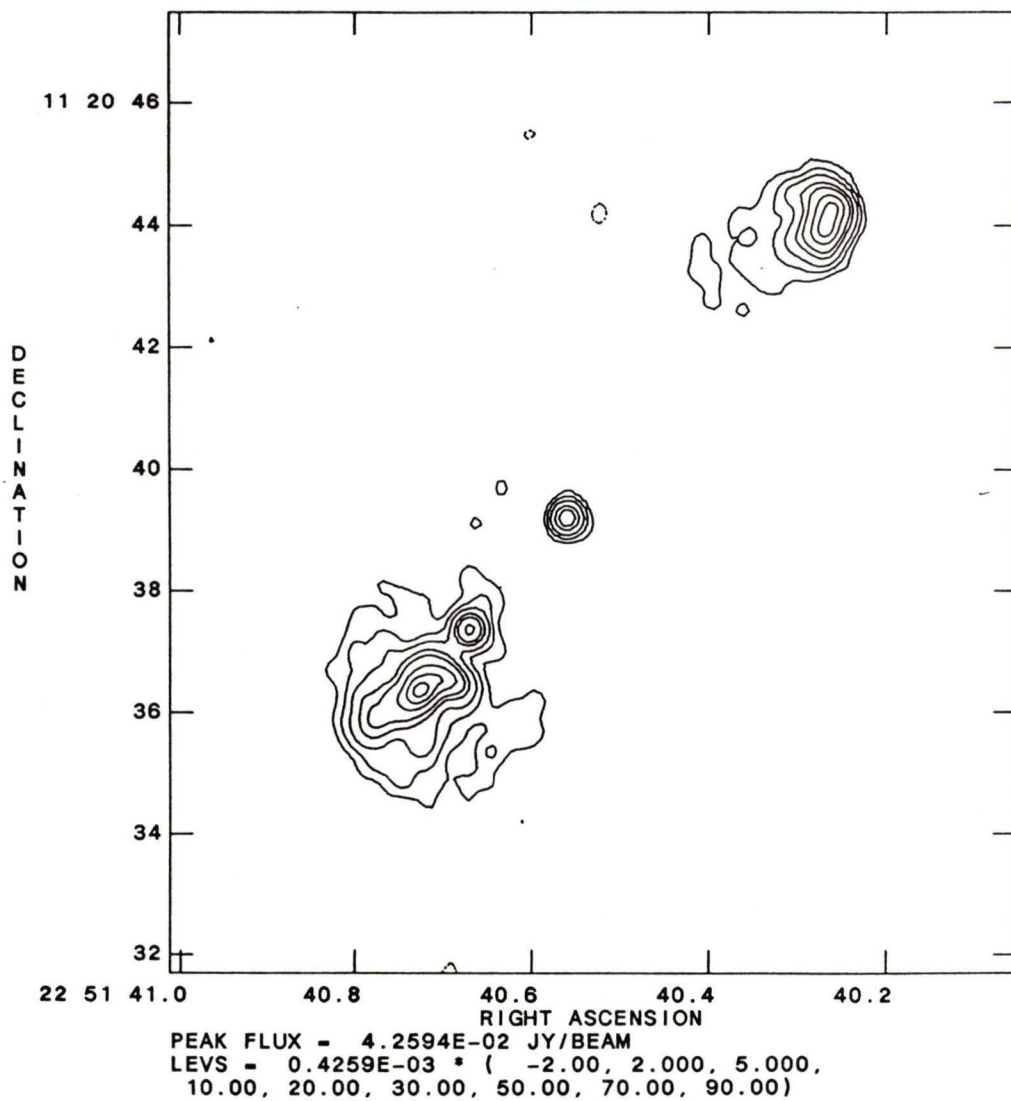




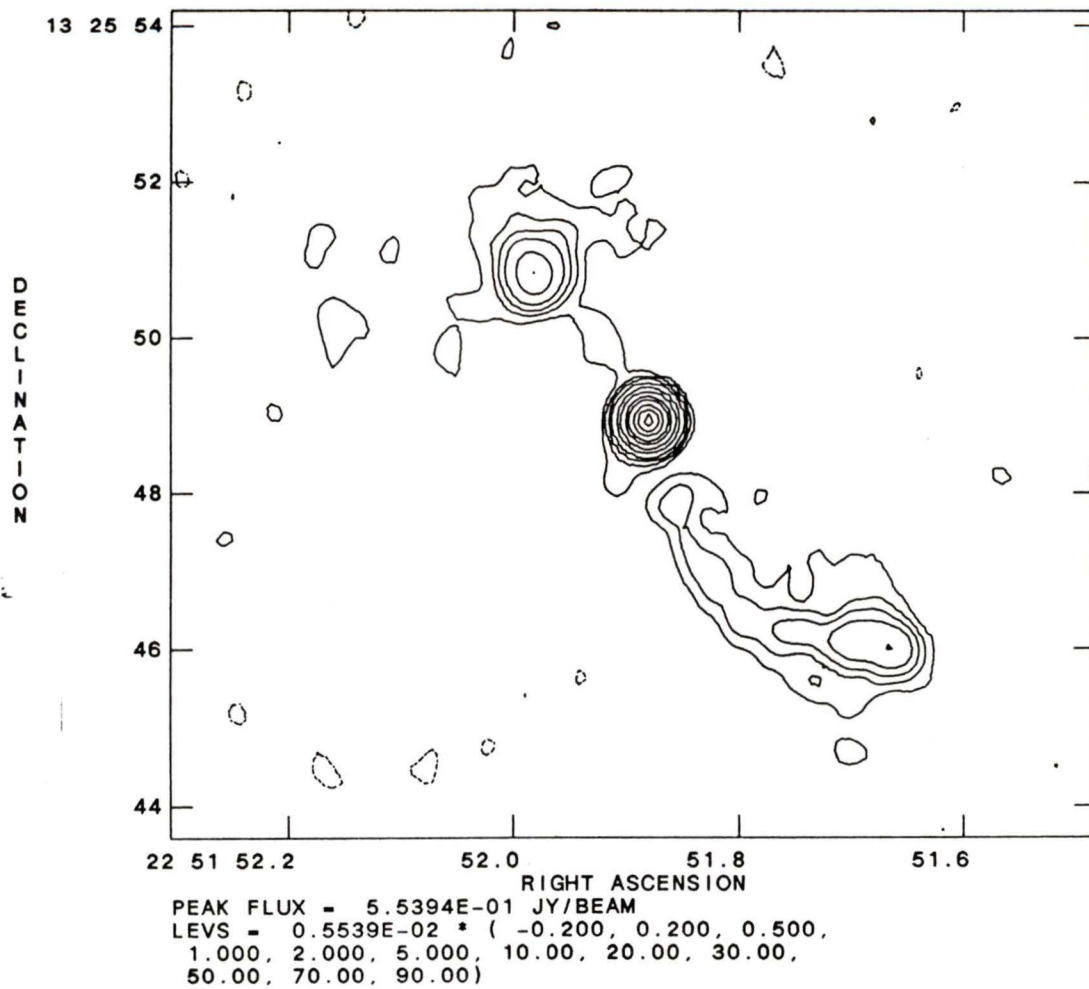




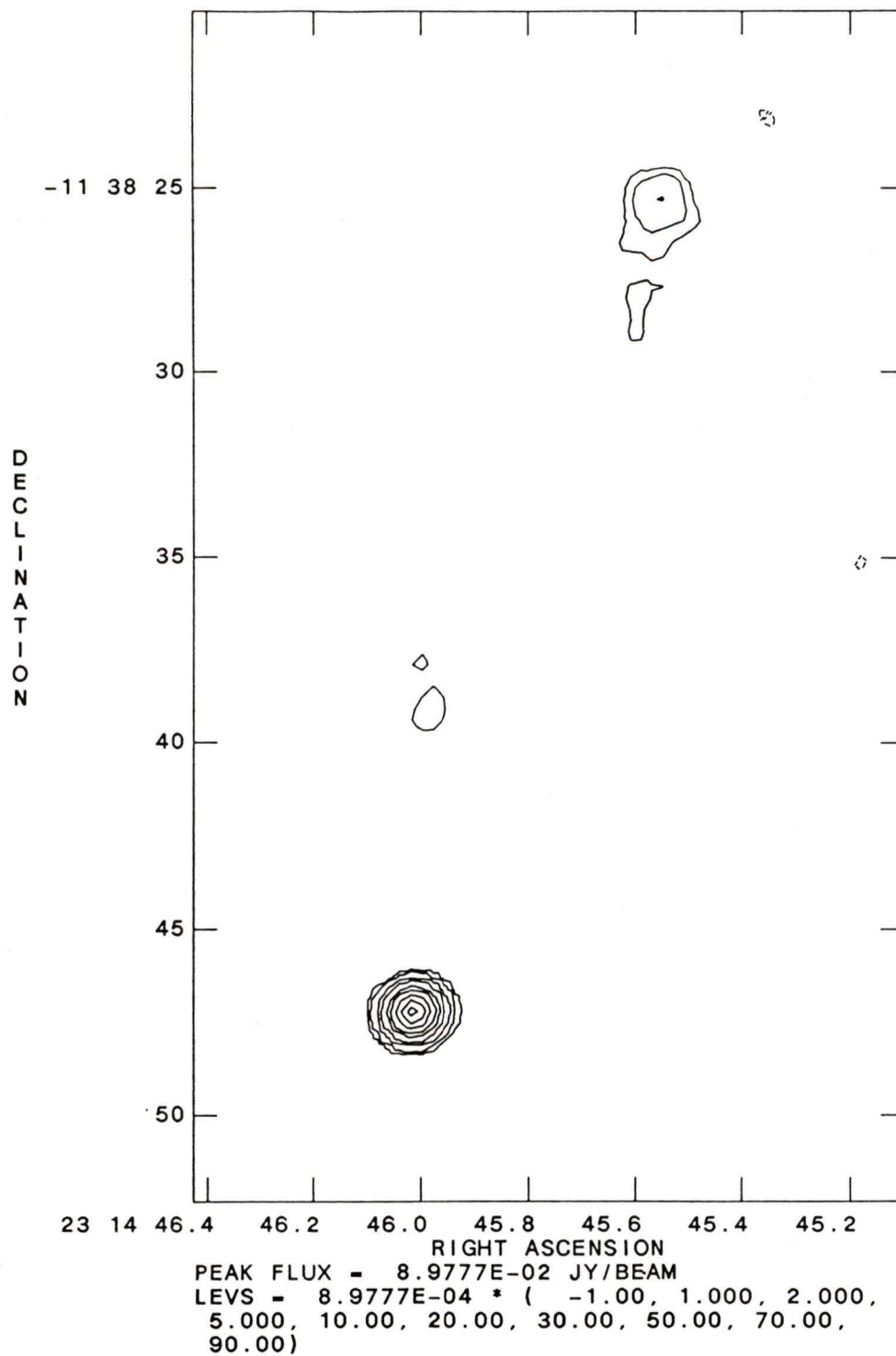
2251+113 6cm



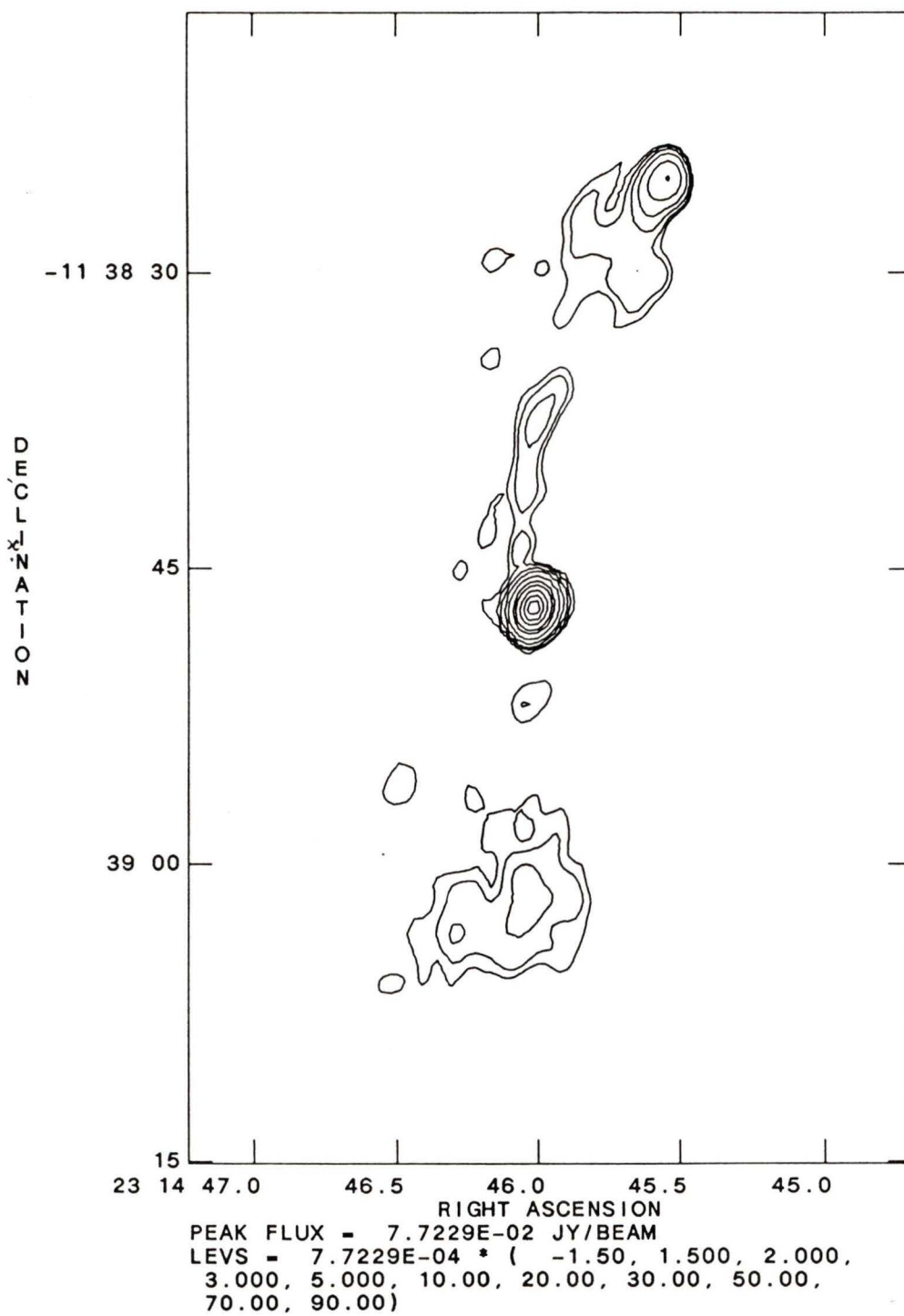
2251+134 6cm

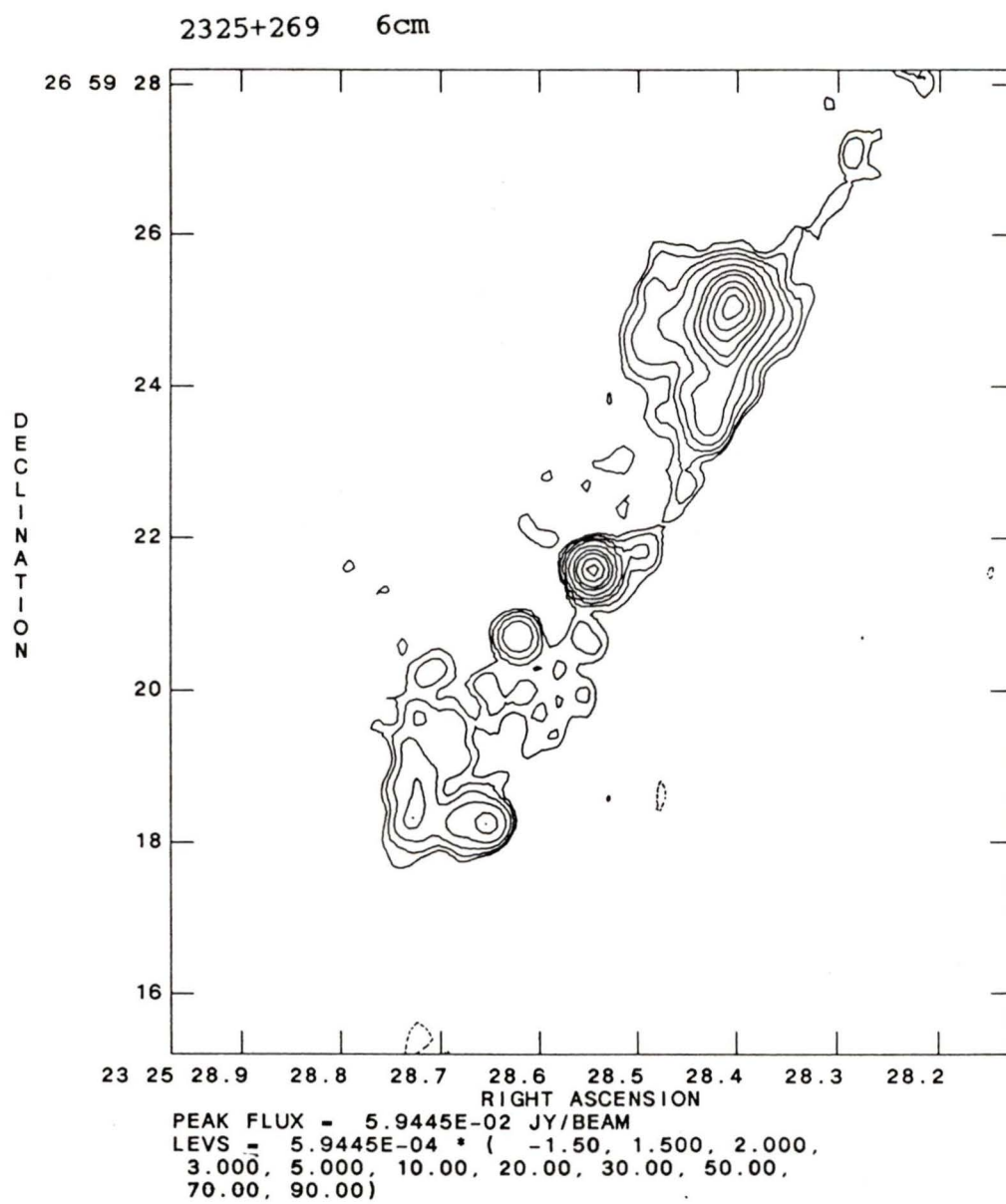


2314-116 6cm

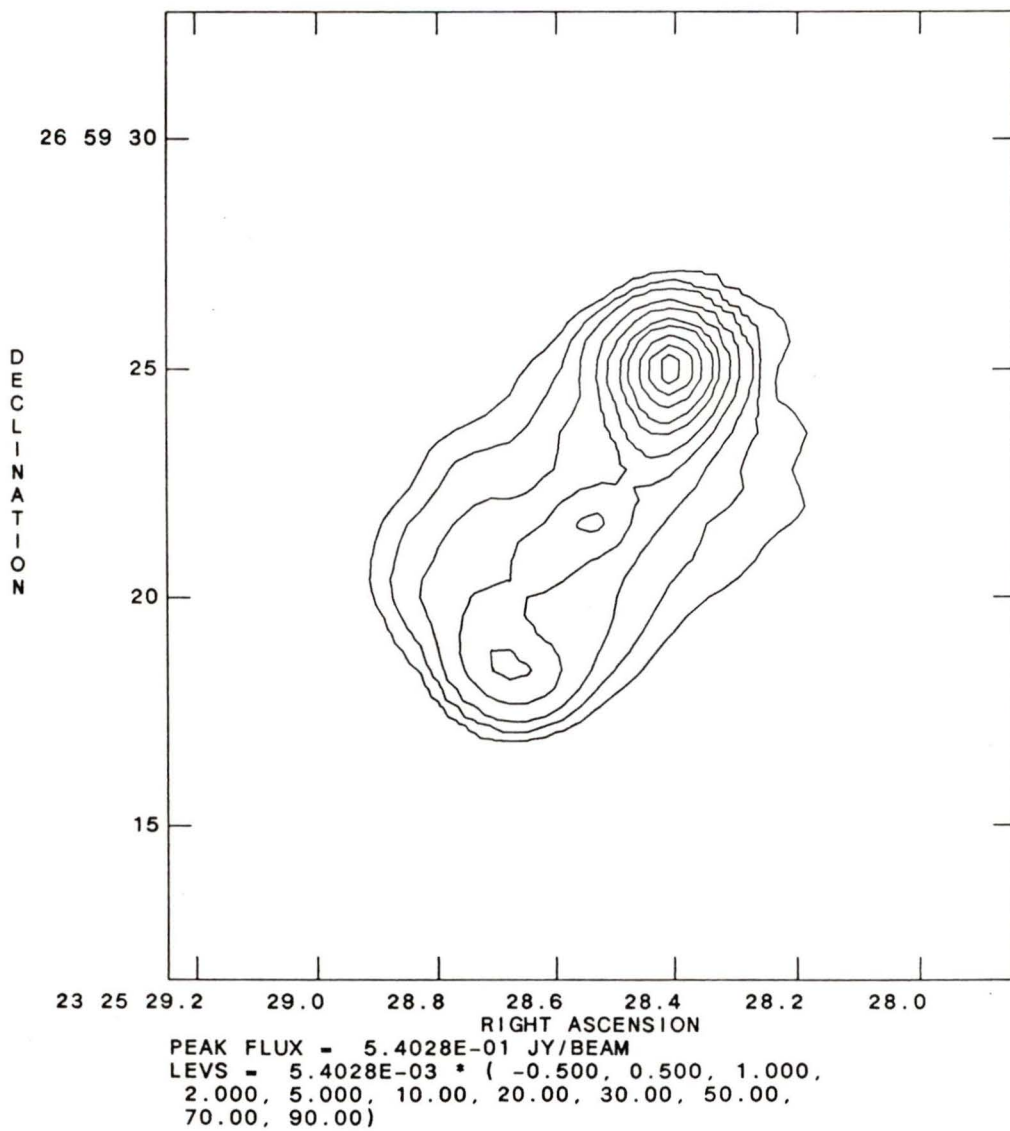


2314-116 20cm

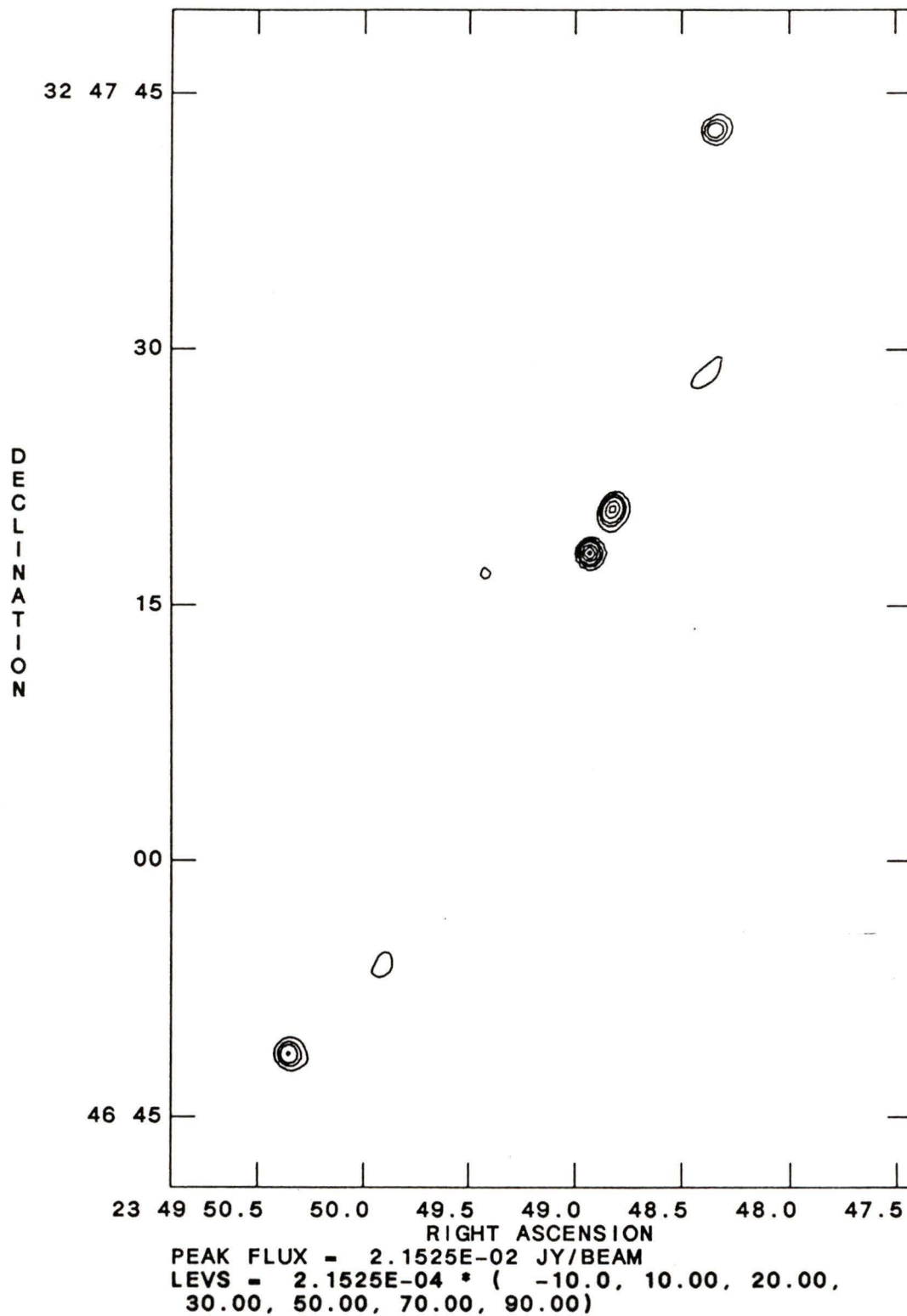




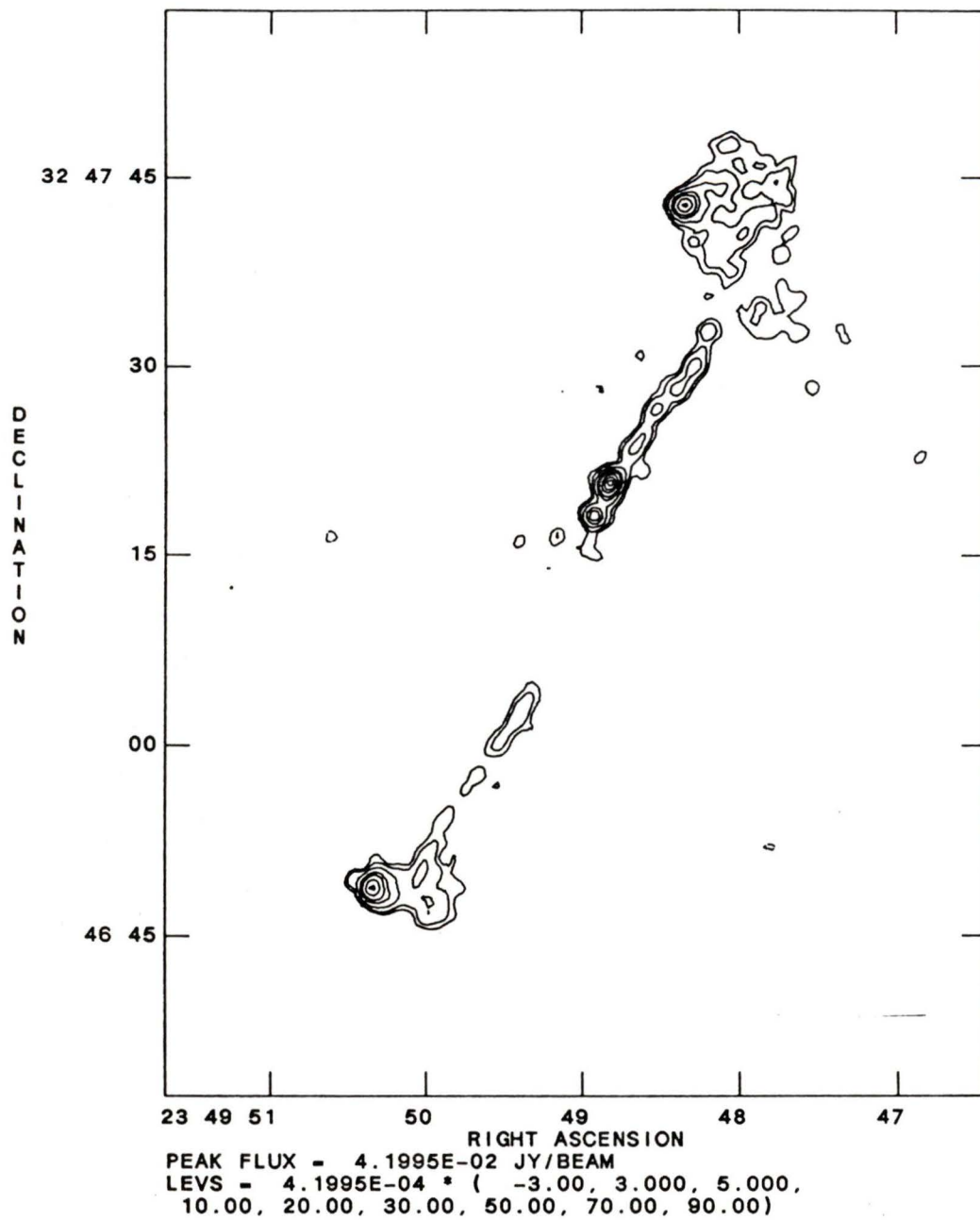
2325+269 20cm

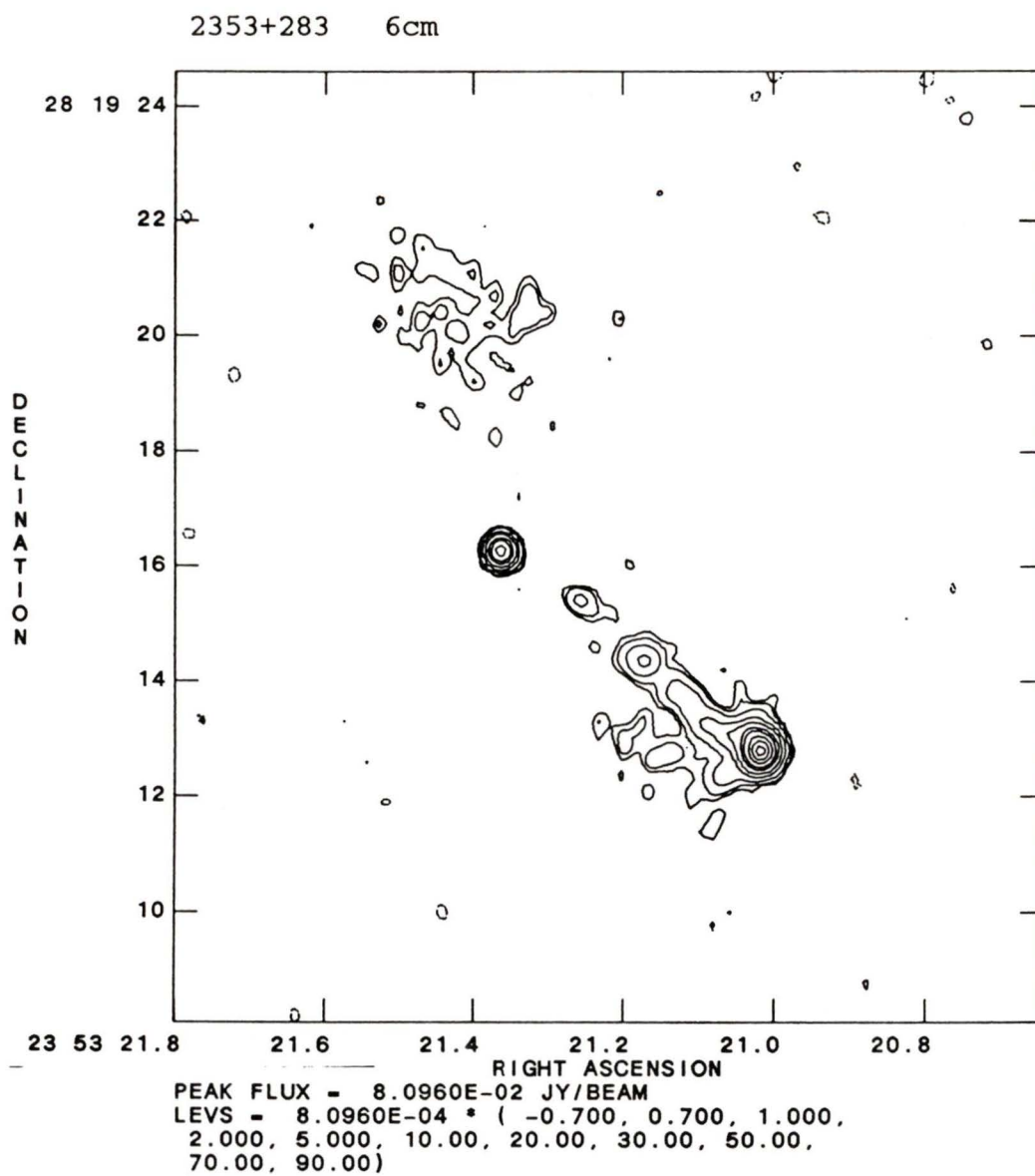


2349+327 6cm



2349+327 20cm





Vita

Surname: **Price**

Given Names: **John Robin**

Place of Birth: **Hamilton, Ontario**

Date of Birth: **October 18, 1959**

Educational Institutions Attended:

University of Prince Edward Island, P.E.I. **1978 to 1979**

Queens University, Ontario **1979 to 1980**

University of Victoria, B.C. **1981 to 1987**

University of New Mexico, U.S.A. **1987 to 1988**

Degrees Awarded:

B.Sc. 1985

University of Victoria

Honors and Awards:

Royal Astronomical Society of Canada Book Prize **1985**

Publications:

21 cm Emission in QSOs and Active Galaxies: J.B. Hutchings, A.C.

Gower, and R. Price 1987, *A.J.* **92**, 6.

Radio Evolution of Quasars at $Z < 1$, J.B. Hutchings, R. Price, A.C.

Gower 1988, *Ap. J.*, **329**, 122.

Partial Copyright License

I hereby grant the right to lend my thesis (the title of which is shown below) to users of the University of Victoria Library, and to make single copies only for such users, or in response to a request from the library of any other university or similar institution, on its behalf or for one of its users. I further agree that permission for extensive copying of this thesis for scholarly purposes may be granted by me or a member of the university designated by me. It is understood that copying or publication of this thesis for financial gain shall not be allowed without my written permission.

Title of Thesis:

**SOME ASPECTS OF THE RADIO MORPHOLOGY
OF QUASARS WITH $Z < 1$**



Author John Robin Price

January 12, 1989



National Library
of Canada

Bibliothèque nationale
du Canada

Canadian Theses Service Service des thèses canadiennes

Ottawa, Canada
K1A 0N4

The author has granted an irrevocable non-exclusive licence allowing the National Library of Canada to reproduce, loan, distribute or sell copies of his/her thesis by any means and in any form or format, making this thesis available to interested persons.

The author retains ownership of the copyright in his/her thesis. Neither the thesis nor substantial extracts from it may be printed or otherwise reproduced without his/her permission.

L'auteur a accordé une licence irrévocable et non exclusive permettant à la Bibliothèque nationale du Canada de reproduire, prêter, distribuer ou vendre des copies de sa thèse de quelque manière et sous quelque forme que ce soit pour mettre des exemplaires de cette thèse à la disposition des personnes intéressées.

L'auteur conserve la propriété du droit d'auteur qui protège sa thèse. Ni la thèse ni des extraits substantiels de celle-ci ne doivent être imprimés ou autrement reproduits sans son autorisation.

ISBN 0-315-50174-X